

Towards a predictive computational growth model for aneurysms

Susanna Sabine Tinkl

Bericht Nr. 29 (2015)
Lehrstuhl für Numerische Mechanik
Professor Dr.-Ing. Wolfgang A. Wall
Technische Universität München

Berichte können bezogen werden über:



Lehrstuhl für Numerische Mechanik
Technische Universität München
Boltzmannstrasse 15
D-85747 Garching bei München
<http://www.lnm.mw.tum.de>

Alle Rechte, insbesondere das der Übersetzung in andere Sprachen, vorbehalten. Ohne Genehmigung des Autors ist es nicht gestattet, dieses Buch ganz oder teilweise auf photomechanischem, elektronischem oder sonstigem Wege zu kommerziellen Zwecken zu vervielfältigen.

All rights reserved. In particular the right to translate the text of this thesis into another language is reserved. No part of the material protected by this copyright notice may be reproduced or utilized in any form or by any means, electronic or mechanical, including photocopying, recording or by any other information storage and retrieval system, without written permission of the author.

TECHNISCHE UNIVERSITÄT MÜNCHEN

Lehrstuhl für Numerische Mechanik

Towards a predictive computational growth model for aneurysms

Susanna Sabine Tinkl

Vollständiger Abdruck der von der Fakultät für Maschinenwesen der Technischen Universität München zur Erlangung des akademischen Grades eines

Doktor-Ingenieurs (Dr.-Ing.)

genehmigten Dissertation.

Vorsitzender: Univ.-Prof. Phaedon-Stelios Koutsourelakis, Ph.D.

Prüfer der Dissertation:

1. Univ.-Prof. Dr.-Ing. Wolfgang A. Wall
2. Univ.-Prof. Dr.-Ing. Michael W. Gee
3. Priv.-Doz. Dr. med. Christian G.H. Reeps
(nur schriftliche Beurteilung)

Die Dissertation wurde am 15. September 2014 bei der Technischen Universität München eingereicht und durch die Fakultät für Maschinenwesen am 19. November 2015 angenommen.

Abstract

The rupture of an abdominal aortic aneurysm (AAA) is the 13th common cause of death in the western world. Approximately 90% of the patients with a ruptured aneurysm die as a consequence of rupture. The prophylactic surgery of an AAA is not without potential risk. Thus, the surgeon has to balance the risk of intervention against the risk of rupture. To assist the decision-making, AAAs have been studied with the help of Finite Element Methods by assessing stresses and strains acting in the AAA wall. These quantities reflect the current state of the aneurysm, but give no information about its further development. To describe the growth of biological tissues, computational growth and remodeling models have also been developed, but they have never been applied to predict growth of a patient-specific aneurysms. The aim of this work is to design a methodology that allows to predict the development of an aneurysm. To the best of the author's knowledge, this is the first method that calibrates the computational growth model not only to accurately reproduce the given growth process but also to predict the future development of a patient-specific aneurysm.

A full three-dimensional computational growth model is developed in order to perform an analysis of a patient-specific geometry. The derived model is utilized to model the formation of an aneurysm and the development of an existing AAA. Normally, the healthy artery is the starting point for growth and remodeling simulations like the formation of an aneurysm. However, the shape of the initial healthy artery is unknown for patient-specific aneurysms. Hence, the computational growth model has to be adapted, when it is started from a patient-specific aneurysmatic aorta. For this purpose, a novel technique to approximate the deformation preceding the initial state is defined.

To characterize the initial state, a reference simulation is computed that reflects the formation of an aneurysm originating from a idealized healthy artery with a local loss of elastin. After a pronounced aneurysm arose, the aneurysmatic geometry is taken as a starting point for a new simulation, where the past deformation is neglected to mimic the patient-specific case. By comparing the results of the reference simulation with the results of this new simulation after another year of growth, the influence of the missing information about the healthy state on the future development of the aneurysm can be characterized.

In order to reproduce the prescribed growth process defined by the reference simulation, the computational growth model has to be calibrated. The growth parameters are computed by solving an optimization problem that aims to minimize the difference in the displacements after one year of growth. To obtain spatially varying parameters, a novel idea of parameterization of the design variables is introduced. The resulting optimization algorithm is successfully applied to reproduce the reference simulation. The final parameters result in a prediction that corresponds to the growth of the reference simulation. Hence, the proposed framework is validated.

Finally, the proposed methodology is applied to a patient-specific example. Two consecutive computed tomography scans of a 62 years old male patient that are recorded in a time span of two years are transformed into a displacement field that describes the deformation resulting from growth. The computational growth model is calibrated with the help of the optimization algorithm to reproduce these measured displacements. The measured displacements are only partially reproduced. The calibrated growth model is utilized to gain insights into the further development of the patient-specific aneurysm and to characterize the predicted state. Due to the latest development of the proposed methodology, a few challenges arising from the patient-

specific application are yet to be resolved, but valuable insights are gained that will be required for future improvements, which are also proposed.

Zusammenfassung

Die Ruptur Abdominaler Aortenaneurysmen (AAA) ist die dreizehnt häufigste Todesursache in der westlichen Welt. In etwa 90% der Patienten mit einem gerissenen Aneurysma sterben in Folge der Ruptur. Die prophylaktische Operation eines AAAs birgt potentielle Risiken, weshalb der Chirurg die Risiken eines Eingriffs gegen die Risiken einer Ruptur abwägen muss. Um die Entscheidungsfindung zu unterstützen, wurden mit Hilfe der Finite-Element-Methode die Spannungen und Dehnungen, die in der Wand eines AAAs wirken, berechnet. Diese Größen spiegeln den momentanen Zustand des Aneurysmas wider, geben aber keine Auskunft über seine weitere Entwicklung. Um das Wachstum von biologischem Gewebe zu beschreiben, wurden numerische Wachstums- und Remodellingmodelle entwickelt, die allerdings nie zur Vorhersage vom Wachstum eines patienten-spezifischen Aneurysmas verwendet wurden. Das Ziel dieser Arbeit ist die Entwicklung einer Methodik, die es erlaubt, die Weiterentwicklung eines Aneurysmas vorherzusagen. Nach bestem Wissen des Autors ist dies die erste Methode, die das numerische Wachstumsmodell kalibriert, nicht nur um einen vorgegebenen Wachstumsprozess akkurat nachzubilden, sondern auch um das zukünftige Wachstum eines patienten-spezifischen Aneurysmas vorherzusagen.

Ein vollständig dreidimensionales numerisches Wachstumsmodell wird entwickelt, um eine patienten-spezifische Geometrie zu untersuchen. Das entwickelte Modell wird verwendet, um die Entstehung eines Aneurysmas und die Entwicklung eines bereits bestehenden AAAs zu modellieren. Normalerweise ist die gesunde Arterie der Startpunkt für Wachstums- und Remodellingsimulationen wie die Entstehung eines Aneurysmas. Allerdings ist die Form der gesunden Arterie für patienten-spezifische Aneurysmen nicht bekannt. Deswegen muss das numerische Wachstumsmodell angepasst werden, wenn die Simulation von einer patienten-spezifischen aneurysmatischen Aorta gestartet wird. Zu diesem Zweck wird eine neue Technik entwickelt, um die Deformation, die dem initialen Zustand vorausgeht, zu approximieren.

Eine Referenzsimulation, die die Entstehung eines Aneurysmas ausgehend von einer idealisierten gesunden Arterie mit einem lokalen Verlust von Elastin widerspiegelt, wird berechnet, um den initialen Zustand zu charakterisieren. Wenn ein ausgeprägtes Aneurysma entstanden ist, wird die aneurysmatische Geometrie als Startpunkt für eine neue Simulation verwendet. In der neuen Simulation wird die vergangene Deformation vernachlässigt, um den patienten-spezifischen Fall nachzubilden. Indem die Ergebnisse der Referenzsimulation mit den Ergebnissen dieser neuen Simulation nach einem Jahr Wachstum verglichen werden, kann der Einfluss der fehlenden Information über den gesunden Zustand auf die weitere Entwicklung des Aneurysmas charakterisiert werden.

Um den durch die Referenzsimulation vorgegebenen Wachstumsprozess zu reproduzieren, muss das numerische Wachstumsmodell kalibriert werden. Die Wachstumsparameter werden berechnet indem ein Optimierungsproblem, das die Differenz der Verschiebungen nach einem Jahr Wachstum minimiert, gelöst wird. Um räumlich variierende Parameter darstellen zu können, wird eine neue Idee der Parametrisierung der Optimierungsparameter eingeführt. Der resultierende Optimierungsalgorithmus wird erfolgreich angewandt, um die Referenzsimulation zu reproduzieren. Die bestimmten Parameter resultieren in eine Vorhersage die mit dem Wachstum der Referenzsimulation übereinstimmen. Mit dieser Übereinstimmung ist die vorgestellte Methodik validiert.

Abschließend wird die vorgestellte Methodik auf ein patienten-spezifisches Beispiel angewandt. Zwei aufeinanderfolgende Computertomographieaufnahmen eines 62 Jahre alten, männlichen Patienten, die in einem Zeitraum von zwei Jahren aufgenommen wurden, werden in ein Verschiebungsfeld transformiert, das die durch das Wachstum entstehende Deformation beschreibt. Das numerische Wachstumsmodell wird mit Hilfe des Optimierungsalgorithmuses kalibriert, um diese gemessenen Verschiebungen zu reproduzieren. Die gemessene Deformation kann nur teilweise nachgebildet werden. Das kalibrierte Wachstumsmodell wird verwendet, um Erkenntnisse über die weitere Entwicklung des Aneurysmas zu erhalten und um den vorhergesagten Zustand zu charakterisieren. Da die vorgestellte Methodik dem neuesten Entwicklungsstand entspricht, müssen noch einzelne Herausforderungen, die durch die patienten-spezifische Anwendung entstehen, gelöst werden. Es werden wertvolle Erkenntnisse erlangt, die für zukünftige Verbesserungen, welche ebenfalls vorgeschlagen werden, notwendig sind.

Danksagung

Während meiner Promotion wurde ich von vielen Personen begleitet, die entscheidend zum Erfolg dieser Arbeit beigetragen haben. An dieser Stelle möchte ich deshalb all diesen Personen meinen ganz herzlichen Dank aussprechen.

Mein besonderer Dank gilt meinem Doktorvater, Prof. Dr. Wolfgang A. Wall, für das in mich gesetzte Vertrauen, die fachliche und persönliche Unterstützung und Förderung, sowie die exzellenten Rahmenbedingungen, die man hier am Lehrstuhl vorfindet. Seine Begeisterung für die Forschung hat mich sehr geprägt und stets motiviert.

Ein weiteres großes Dankeschön möchte ich an Prof. Dr. Michael W. Gee richten. Zum einen bedanke ich mich für die Übernahme des ersten Mitberichts, zum anderen für die geduldige und unermüdliche Unterstützung in allen Phasen meiner Promotion. Das Gefühl, bei kleineren und größeren Fragen stets eine offene Bürotür und ein offenes Ohr vorzufinden, hat mir sehr geholfen und mich immer wieder aufs Neue motiviert.

Bei den weiteren Mitgliedern meiner Prüfungskommission, Herrn PD Dr. Christian Reeps und Herrn Prof. Dr. Phaedon-Stelios Koutsourelakis, bedanke ich mich für die aufgebrauchte Zeit und Mühe im Zusammenhang mit meinem Promotionsverfahren.

Ein ganz besonderes Dankeschön geht auch an meine Kollegen. Die großartige Arbeitsatmosphäre und die vielen spannenden, fachlichen (und nicht-fachlichen) Diskussionen haben für mich die Promotionszeit zu einem unvergesslichen Lebensabschnitt gemacht. Besonders die uneingeschränkte Hilfsbereitschaft, die ich stets erfahren habe, war sehr wichtig für mich. Vor allem Jonas Biehler, Dr. Caroline Danowski, Dr. Florian Henke, Sebastian Kehl, Dr. Ursula Rasthofer und Dr. Shadan Shahmiri möchte ich für die tolle Zusammenarbeit und auch Freundschaft danken. Den fleißigen Korrekturlesern des Manuskripts möchte ich ebenfalls ein großes Dankeschön aussprechen. Sie haben dazu beigetragen die schriftliche Arbeit zu verbessern.

Schließlich danke ich von ganzem Herzen meiner Familie für das in mich gesetzte Vertrauen, die unerschöpfliche Unterstützung und für so manchen Rat und Zuspruch in schwierigen Situationen. Ohne ihren Rückhalt wäre diese Arbeit undenkbar.

München, im Dezember 2015

Susanna Tinkl

Contents

1	Introduction	1
1.1	Motivation	1
1.2	Growth and remodeling	2
1.2.1	Terminology and underlying processes	2
1.2.2	Fundamental computational approaches	3
1.3	Research approach	5
1.4	Outline	7
2	Nonlinear solid mechanics	9
2.1	Nonlinear elasticity	9
2.1.1	Kinematics	9
2.1.2	Stress measures	11
2.1.3	Balance equations	12
2.1.4	Constitutive laws	14
2.2	Finite Element Method	16
2.2.1	Weak form	16
2.2.2	Space discretization	17
3	Growth and remodeling	19
3.1	Introduction to open system thermodynamics	19
3.2	Isotropic growth	21
3.2.1	Model	21
3.2.2	Time discretization and linearization	23
3.2.3	Examples	25
3.3	Constraint mixture	28
3.3.1	Model	28
3.3.2	Time discretization	34
3.3.3	Definition of homeostatic variables	37
3.3.4	Analytic solution of the steady state	41
3.3.5	Hypertension	45
3.3.6	Aging of an artery	46
3.3.7	Exemplary formation of an aneurysm	48
4	Inverse analysis	55
4.1	Optimization algorithm	55
4.1.1	Levenberg-Marquardt algorithm	55
4.1.2	Measured displacements	56

4.2	Parameter distribution	57
4.2.1	Definition of patches	57
4.2.2	Smoothing of patches	58
5	Towards prediction of growth of an aneurysm	61
5.1	Academic setting	61
5.2	Flying start configuration	63
5.2.1	Differences arising from the missing mapping to the homeostatic state at the flying start configuration	64
5.2.2	Influence of history variables	67
5.2.3	Definition of the history	69
5.3	Calibration of growth parameters	72
5.3.1	Uniform parameters	74
5.3.2	Separation of healthy and diseased part	76
5.3.3	Spatially varying parameters	78
5.4	Validation of predicted results	83
6	Patient-specific case	89
6.1	Derivation of a computational model	89
6.2	Challenges of patient-specific geometries	90
6.2.1	Determination of fiber directions	90
6.2.2	Homeostatic variables	93
6.2.3	Stress peaks	94
6.3	Calibration of growth parameters	95
6.3.1	Measured displacement field	97
6.3.2	Uniform parameters	98
6.3.3	Spatially varying parameters with 20 patches	99
6.3.4	Spatially varying parameters with 74 patches	101
6.3.5	Investigation of the diameter	104
6.4	Growth over a longer period of time	105
6.5	Potential modifications in the optimization process	108
7	Summary and outlook	111
A	Appendix	113
A.1	Wall shear stress	113
A.2	Derivatives for the implicit integration within the constraint mixture model . . .	115
A.3	Definition of the elastin degradation area for the formation of an aneurysm . . .	116
	Bibliography	117

Nomenclature

Representation of scalars, tensors and other quantities

q, Q	Scalar quantity
\mathbf{q}	Vector
\mathbf{Q}	Second-order tensor
\mathbb{Q}	Higher-order tensor

Operators and Symbols

$(\cdot)^T$	Transpose of a tensor
$(\cdot)^{-1}$	Inverse of a tensor or mapping
$(\cdot)^{-T}$	Transpose of the inverse of a tensor
$\dot{(\cdot)}$	First time derivative at a fixed reference position
$\hat{(\cdot)}$	Prescribed quantity
$\mathbf{1}$	Identity tensor
det	Determinant
tr	Trace operator
log, ln	Logarithm, natural logarithm
Grad, ∇	Material gradient operator
Div, $\nabla \cdot$	Material divergence operator
Lin	Linearization operator
$\Delta(\cdot)$	Increment, change of (\cdot) in one time step
\times	Cross product
\otimes	Dyadic product
$\delta(\cdot)$	Virtual quantity
δ_{jk}	Kronecker delta

Superscripts and Subscripts

$(\cdot)^{(e)}$	Element
$(\cdot)_h$	Discretized in space with the FEM
$(\cdot)_{gp}$	Gauss point
$(\cdot)_I, (\cdot)_i$	Index in reference and current configuration
$(\cdot)_{int}$	Internal
$(\cdot)_{ext}$	External

$(\cdot)^e$	Elastin
$(\cdot)^m$	Smooth muscle cells
$(\cdot)^c$	Collagen
$(\cdot)^k$	Collagen fiber family k
$(\cdot)^i$	Constituent i (elastin, smooth muscle, collagen fiber family, etc)
$(\cdot)_h, (\cdot)_{hom}$	Homeostatic value

Domains and boundaries

Ω_R	Reference (material) configuration
Ω_0	Initial loaded configuration
Ω_t	Current (spatial) configuration
$\partial\Omega_R$	Boundary in reference configuration
Γ_u	Dirichlet partition of boundary in reference configuration
Γ_σ	Neumann partition of boundary in reference configuration

Kinematics

$\mathbf{e}_{cir}, \mathbf{e}_{axi}, \mathbf{e}_{rad}$	Vectors describing circumferential, axial and radial direction
\mathbf{X}	Position in reference configuration
\mathbf{x}	Position in current configuration
φ_t	Mapping between reference and current configuration
\mathbf{u}	Displacement
\mathbf{F}	Deformation gradient
J	Jacobian, determinant of \mathbf{F}
V, v	Reference and current volume
A, a	Reference and current surface area
\mathbf{N}, \mathbf{n}	Unit normal vector in reference and current configuration
\mathbf{R}, \mathbf{U}	Rotation tensor, right stretch tensor
\mathbf{C}	Right Cauchy–Green deformation tensor
\mathbf{E}	Green–Lagrange strain tensor
I_j, \bar{I}_j	j -th principal invariant, j -th modified invariant
λ_i	Principal stretch
$\check{\mathbf{N}}_i$	Principal axis
$\mathbf{a}_0^k, \mathbf{a}^k$	Fiber direction in reference and current configuration
$\mathbf{A}_0^k, \mathbf{A}^k$	Associated structural tensors

Stresses and constitutive laws

\mathbf{t}	Traction vector in current configuration
\mathbf{t}_0, \mathbf{T}	Pseudo traction vectors
$\boldsymbol{\sigma}$	Cauchy stress tensor
\mathbf{P}	First Piola–Kirchhoff stress tensor
\mathbf{S}	Second Piola–Kirchhoff stress tensor
W	Strain energy function, Helmholtz free-energy function, potential
\mathbb{C}	Constitutive tensor

E	Young's modulus
ν	Poisson's ratio
λ, μ	Lamé parameters (μ also shear modulus)
κ	Bulk modulus
$\alpha, \beta, \beta_1, \beta_2$	Material parameters
k_1, k_2	Anisotropic material parameters

Governing equations

t	Time
m	Mass
ρ_0	Initial reference mass density
ρ	Current mass density
M	Reference mass density
$\hat{\mathbf{b}}_0$	Prescribed body force in reference configuration
$\hat{\mathbf{t}}_0$	Prescribed pseudo-traction in reference configuration
\mathcal{W}	Work

FE space discretization

n_{ele}	Number of elements
n_{nod}	Number of nodes
N_k	FE shape function of node k
p	Polynomial degree of finite element interpolation
ξ	Position in FE parameter space
\mathbf{X}	Discrete nodal positions in reference configuration
\mathbf{x}	Discrete nodal positions in current configuration
\mathbf{d}	Discrete nodal displacements
w_{gp}	Weighting factor for Gauss point
\mathbf{f}	Discrete force vector
\mathbf{r}	Discrete residual vector
\mathbf{K}_{T}	Tangent stiffness matrix
i	Nonlinear iteration index

Growth and remodeling

\mathcal{R}_0	Mass source
\mathcal{R}	Mass flux
\mathbf{h}	History vector
\mathcal{S}_0	Extra entropy source
T	Temperature

Isotropic growth

\mathbf{F}_e	Elastic deformation gradient
\mathbf{F}_g	Growth deformation gradient
(\cdot)	Quantity in the intermediate configuration
ϑ	Isotropic growth stretch
\mathbf{M}	Mandel stress
f_ϑ	Growth law
R_ϑ	Growth residual
\mathbb{C}_{eg}	Constitutive tensor of the growth problem

Constraint mixture

ϕ^i	Mass fraction of constituent i
Ψ^i	Strain energy function of constituent i
$\mathbf{G}_h^i, \lambda_{pre}^i$	Prestretch tensor and scalar prestretch
$\mathbf{F}^k(\tau, t), \lambda^k(\tau, t)$	Deformation gradient and stretch of fibers produced at time τ
$\lambda^k(\tau)$	Stretch at deposition time τ in direction k
$\kappa_n^i(\tau)$	Natural configuration of constituent i produced at time τ
m_0^k	Basal mass density production rate
m_{max}^k	Maximal mass density production rate
$m^k(t)$	Reference mass density production rate
$q^k(\tau, t)$	Survival function
t_{lf}, t_{hl}	Lifetime and half-life of collagen
a_m^k	Mean age
K_g^σ, K_g^τ	Growth factors
σ^k	Scalar growth stress
$\boldsymbol{\sigma}^g, \mathbf{S}^g$	Growth stress tensors
$t_l, \Delta t_l$	Discrete time, time step size
ι^e	Elastin content

Inverse analysis

π	Objective function
\mathbf{p}	Optimization parameters
n_p	Number of optimization parameters
\mathbf{u}^m	Measured displacements
n_m	Number of measured displacements
$\mathbf{u}(\mathbf{p})$	Computed displacements
\mathbf{r}	Residuum
\mathbf{J}	Jacobian matrix
μ	Regularization factor
I_S, I_T	Source and target image
ζ	Mapping between source and target image
$\mathcal{D}(\mathbf{u})$	Similarity measure
$\mathcal{R}(\mathbf{u})$	Elastic regularization
α	Elastic regularization factor

p^{ele}	Element wise optimization parameters
\tilde{P}	Patch matrix
P	Smoothed patch matrix
A	Laplacian matrix
ω	Damping parameter
D	Diagonal matrix

Fluid mechanics

u	Fluid velocity
p	Fluid pressure
μ	Dynamic viscosity
Q	Volumetric flow rate
τ_w	Wall shear stress
r, z, θ	Cylindrical current coordinates
R	Radius in reference configuration

Abbreviations

AAA	Abdominal aortic aneurysm
BVP	Boundary value problem
CT	Computed tomography
DOF	Degree of freedom
EAS	Enhanced assumed strain
ECM	Extracellular matrix
FE	Finite element
FEA	Finite element analysis
FEM	Finite Element Method
FSI	Fluid-structure interaction
GP	Gauss point
HFEF	Helmholtz free-energy function
IA	Inverse analysis
ILT	Intraluminal thrombus
MMP	Matrix metalloproteinase
MULF	Modified updated Lagrangian formulation
PDE	Partial differential equation
PK	Piola-Kirchhoff
PVW	Principle of virtual work
SEF	Strain energy function
WSS	Wall shear stress

1 Introduction

1.1 Motivation

Cardiovascular diseases are a leading cause of death in industrial countries, e.g. 45% of men in the age of 65-74 years die because of cardiovascular incidents (Scott et al. [85]). The rupture of an abdominal aortic aneurysm (AAA) is one of these causes and is fatal in most cases. The elective repair of an AAA is not without potential risk. Hence, it is common practice to balance risk of rupture against risk of intervention. The decision-making is often based on empirical statistics that do not always account for the risks and needs of the individual patients. Consequently, a well established criterion to indicate the necessity of a surgery is e.g. the maximal diameter criterion (Ockert et al. [75]).

In recent years, increasing efforts have been made in interdisciplinary studies of medical and engineering scientists. Computational finite element analyses (FEA) have been utilized to assess the stresses and strains acting in the AAA wall (Reeps et al. [80]). The models have been refined and include several patient-specific aspects like calcifications, intraluminal thrombus, prestress, and patient-specific material properties (Gasser et al. [26], Gee et al. [27], Maier [64], Maier et al. [65], Reeps et al. [81]). As a promising measure to help the decision-making, the rupture potential index has been proposed (Vande Geest et al. [106], Maier et al. [66]).

Since all previous models reflect the current state of the aneurysm, they hold no information about how the aneurysm is going to develop in the future. Even if a second computed tomography (CT) scan exists that was recorded at a later point in time, it is difficult to make a substantiated prediction of the development of the aneurysm, see Figure 1.1. However, in recent studies (Baek et al. [9], Martufi et al. [69]) growth of several AAAs was monitored with follow up scans and related to e.g. the thickness of the intraluminal thrombus (ILT). To model one aspect of the transient behavior of an aneurysm, computational growth and remodeling models can be utilized (Humphrey and Taylor [48]). These models are capable to give further insights into the development of an aneurysm. Therefore, they have to be carefully calibrated and validated. To

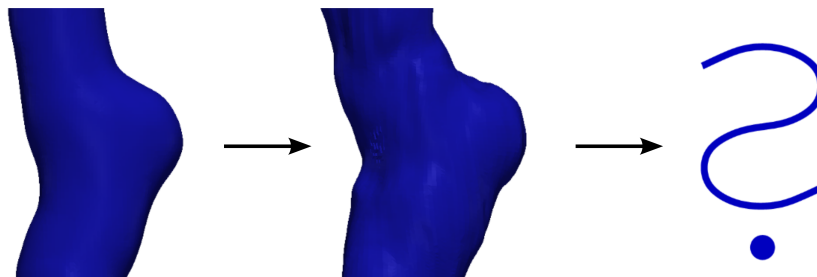


Figure 1.1: Two states of a growing aneurysm are known. How does it develop in the future?

the best of the author's knowledge, there is no established method to predict growth of an existing AAA.

The aim of the presented work is to develop a methodology that allows to predict the development of an existing aneurysm. Therefore, the Finite Element Method (FEM) is combined with a growth and remodeling model that is calibrated to a given growth process. Moreover, a procedure to validate the proposed framework is presented.

1.2 Growth and remodeling

Since growth and remodeling is a fundamental part of this work, a short introduction into this topic is given in this section. First important terms are presented. In the second part, an overview and a literature review of different computational growth models are given.

1.2.1 Terminology and underlying processes

Through the course of this work terms like growth and remodeling appear. Growth and remodeling are often related and cannot be separated. Nevertheless, definitions of these terms are given and underlying processes are presented. Afterwards, a brief introduction to the pathogenesis of AAAs is given.

Growth

Growth is defined as a change of mass and volume, respectively. The change can be positive or negative (atrophy). One distinguishes between two forms of growth: volume (interstitial) and surface (appositional) growth, as described in Taber [92]. In Figure 1.2 one can see sketches of the two forms of growth. During volume growth, the newly deposited mass is created within the original volume. That means within every infinitesimal volume of the body, new and old mass exists. The new mass can be created with cell division, cell enlargement or creation of additional extracellular matrix. Examples of volume growth are swelling and growth of arterial tissue. In surface growth, the new material is deposited at external or internal surfaces of the body, meaning new and old masses are separated. Surface growth takes place during plating, wear and growth of horns or shells. For more details regarding surface growth the reader is referred to Skalak et al. [89].

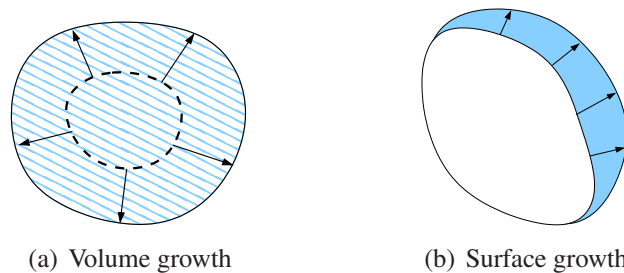


Figure 1.2: Different types of growth, the blue color indicates newly deposited material

There are different ways how growth can occur (Himpel et al. [42]). Either the density is constant or the volume is constant. In the first case, the volume has to adapt to the mass change, in the second case, the density has to adapt to the mass change. A mixture of both variants is also possible. Within this work, only density preserving volume growth is further investigated.

Remodeling

Remodeling describes the change in material properties. This change can stem from a change in the microstructure of the material, like the reorientation of fiber directions or like the change of the internal structure of bones. Within this work, volume growth combined with remodeling will be further investigated.

Pathogenesis of AAAs

It is widely accepted that irreversible enzymatic degradation of structural matrix proteins plays a significant role in the development of AAAs. Thereby, *matrix metalloproteinases* (MMPs) have an important contribution (Choke et al. [17], Kadoglou and Liapis [49], Lehoux et al. [60], Longo et al. [62], Thompson and Parks [97]). A single MMP is capable to induce the degradation of few proteins, but all MMPs together are feasible to degrade the whole extracellular matrix (ECM) (Chase and Newby [16]). Especially MMP 2 and 9 are reported as elevated in AAA tissue. They are two of the four MMPs that are known to degrade elastin (Longo et al. [62]).

Normally, the synthesis of elastin and collagen is balanced by the presence of endogenous inhibitors. The inhibitors of MMPs, like tissue inhibitors of metalloproteinases (TIMPs), nitric oxide (NO) and transforming growth factor- β (TGF- β), play a key role in this equilibrium. It has been reported that the activity level of both, MMPs and TIMPs, is increased in AAA (Kadoglou and Liapis [49], Thompson and Parks [97]). Other studies report that mechanical impulses are able to upregulate the enzymatic activity (Humphrey [45], Newby [74]). Summarizing, the underlying processes are a complex interplay between MMPs and their inhibitors and probably other proteinases. Most of these findings have been reported for already existing AAA, the underlying process of the initiation of the formation of an aneurysm is still part of current research.

1.2.2 Fundamental computational approaches

A classical treatment of growth is the work of D'Arcy Thompson [96]. He described the geometric features of growth. Other early attempts to model growth mathematically are summarized in the review of Cowin [18]. Later Skalak et al. [87] formalized the general description of volumetric and surface growth. In his textbook on biomechanics, Fung [23] presented a stress-growth law that includes several equilibrium states of stress. On the basis of Skalak's work, Rodriguez et al. [82] introduced a continuum theory that accounts for the coupling of stress and growth. They proposed a multiplicative split of the deformation gradient. Growth is transformed into a growth deformation gradient of infinitesimal tissue elements. An elastic deformation gradient ensures compatibility of the whole deformation and leads to residual stresses. This basic concept was applied in several subsequent studies. It is capable to model growth in complex geometries and describes isotropic growth in three dimensions. It can be easily incorporated in an existing finite element code, since it only modifies the relation between stress and strain. Taber and Eggers [94] modeled growth of a two layered artery, Taber [93] additionally included wall shear stress. In Taber and Humphrey [95] the genesis of residual stress in arteries was further investigated.

In Göktepe et al. [30, 31] the model was applied to cardiac growth. Adapted balance equations were investigated in Lubarda and Hoger [63]. They also extended the isotropic growth model to orthotropic and transversal isotropic growth. Ambrosi and Mollica [4] combined the split of the deformation gradient with availability of nutrients that is described with a reaction-diffusion equation to model growth of a tumor. In Ambrosi and Guillou [2] the nutrients were replaced by a biochemical energy concentration. Himpel et al. [42] presented a numerical implementation of the multiplicative split. The basic concept was also used in the incremental growth model of Goriely and Ben Amar [32].

The previous growth model is a single phase model. Since the true tissue consists of several different constituents, mixture models were developed. One of the first mixture growth models was presented in Humphrey and Rajagopal [46, 47], where each constituent grows and remodels individually. Constituents are gradually degraded and simultaneously new tissue is synthesized. The amount of created mass is dependent on mechanical stimuli. The model was developed for axisymmetric membranes and called *constraint mixture* model. There is a wide range of literature about applications and further developments of this model, e.g. growth of saccular (Baek et al. [6], Kroon and Holzapfel [54]) and fusiform aneurysms (Baek et al. [7]). In Valentín et al. [103] the model was extended with active smooth muscle cells. Different aspects and hypotheses were investigated in Valentín and Humphrey [100, 101, 102] and more recently in Valentín and Holzapfel [99]. In Kroon and Holzapfel [55] the influence of more than four collagen fiber families was investigated.

In Figueroa et al. [21] growth of AAA was combined with fluid-structure interaction. Kroon and Holzapfel [56], Cardamone et al. [14], and Sheidaei et al. [86] also included dynamic effects. Zeinali-Davarani et al. [113] investigated the formation of aneurysms after a loss of elastin. Their model is still a membrane model, but they are not restricted to axisymmetry. Karšaj et al. [50] extended the model to three dimensions, but they were restricted to axisymmetric cylinders, since they computed a semi-analytic solution. Valentín et al. [105] recently presented a full three dimensional model. They compared their results to a two dimensional semi-analytical simulation from Valentín et al. [104] and yielded a good agreement. Kwon et al. [57] investigated the adaptation of the tissue after endovascular repair of an AAA. Zeinali-Davarani et al. [112] and Wilson et al. [110] determined material parameters for the healthy human aorta and investigated their influence on developing AAAs. Thorne et al. [98] and Hayenga et al. [38] coupled agent based models with the biomechanical growth model. Alford et al. [1] proposed a combination of the split of the deformation gradient and evolving natural configurations to be able to simulate thick walled vessels.

The methods of Gleason et al. [29], Watton et al. [109] and Martufi and Gasser [68] are also based on collagen turnover, but their implementation is different to the constraint mixture model. For example, the model of Watton et al. [109] is based on the variation of the stress free state of collagen fibers, which is modeled with the help of a recruitment stretch. In Watton and Hill [108], the influence of different parameters of this model was investigated. Another possibility to describe multi-phase growth was presented in Garikipati et al. [25]. In contrast to the other approaches, a fluid phase was included in the growth process. They defined a multiplicative split of the deformation gradient for several phases. The interaction between the different phases was modeled with mass transport. The model was further refined in Narayanan et al. [73].

For a detailed discussion of the biomechanics of growth and the related topics of remodeling and morphology, the reader is referred to the early review of Taber [92]. Garikipati [24] gave a

brief review of the kinematics of biological growth. A recent summary of growth models and perspectives in this field can be found in Ambrosi et al. [3]. A review of mixture models was presented in Ateshian and Humphrey [5]. There exists a wide variety of growth models as shown in the previous paragraphs. But the more complex models are seldom applied to complicated geometries, not to even speak of patient-specific geometries.

1.3 Research approach

The computational models and methodologies that are developed within this work aim at bridging the gap towards the prediction of growth of a patient-specific aneurysm. To achieve this aim, several components have to be combined. The basic concept of how the major components are interrelated to each other, is sketched in Figure 1.3. A computational growth and remodeling approach is calibrated with the help of an inverse analysis to reproduce growth, which is defined by the data from two subsequent CT scans of one patient. The resulting calibrated growth and remodeling model can be utilized to predict the future growth of the aneurysm. Since the predicted state is not known, the proposed procedure has to be validated. In the following, the requirements for each component are investigated in more detail.

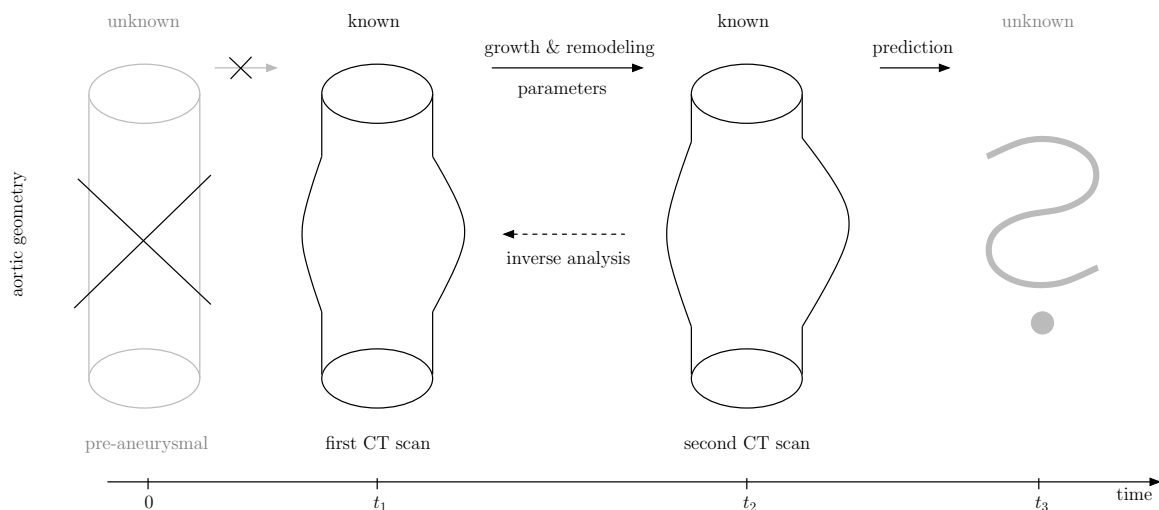


Figure 1.3: Development of an aneurysm: Starting from a healthy artery, two CT scans of the patient depict the development, whereas the healthy state and the further development of the aneurysm are unknown in the patient-specific case

Computational growth and remodeling model

In recent years, a variety of computational models has been developed to model growth and remodeling, as already discussed in Section 1.2.2. The growth and remodeling model that is utilized within this work should not only describe the consequences of growth, but should also aid in the understanding of the underlying processes. Most of these models can reflect the adaption of a homeostatic state to the altered exterior and interior conditions for idealized geometries. Hence, they can model the formation of an aneurysm starting from a healthy artery that is mod-

eled as a straight cylinder. Unfortunately, this starting point is not known for a patient-specific aneurysm, as sketched in Figure 1.3. Thus, the computational model that is applied to the special case here should be able to start a growth and remodeling simulation from any reasonable geometry. Additionally, it should account for the fact that the geometry reflects a grown state. To the best of the author's knowledge, there exists no computational growth and remodeling model that meets all the requirements mentioned above.

Calibration of parameters

Each growth and remodeling approach depends on parameters that have to be chosen. For example, the influence of stress on growth is regulated by such a parameter. In the patient-specific case, these parameters may even vary locally. In the cases considered here, a part of the growth process is known from data of two different CT scans of the same aneurysm at different time points. They can be used to calibrate the developed growth and remodeling model with an inverse analysis. The chosen method for the inverse analysis has to be capable of solving an optimization problem with a partial differential equation (PDE) as constraint and to yield spatially varying parameters. Although the underlying PDE is quasi-static transient effects arise through growth.

Validation of prediction

The calibrated parameters are then utilized for a simulation that gives insights into the subsequent development of the specific aneurysm. Since the future growth of the aneurysm is not known at the time the prediction is made, the quality of the prediction cannot be judged at this point in time. Hence, a methodology has to be developed that validates the proposed framework. The validation process should be as close as possible to a realistic setting.

In the previous paragraphs, the requirements for developing a predictive computational growth model are discussed. To the best of the author's knowledge, there exists no approach in literature to date that meets all the requirements. The important components of this thesis and new scientific aspects it contributes to address these requirements are specified in the following:

- The expansion of an existing complex computational growth model that it is employable in a three dimensional Finite Element Method and that it is applicable to arbitrary geometries.
- The characterization of the consequences from the lacking information of the growth preceding the initial state.
- The definition of a parameterization to yield a spatial distribution of the parameters and the use of an established inverse analysis method to calibrate the growth parameters.
- The methodology to validate the proposed framework for determining the growth parameters by utilizing a known growth process as reference.

In summary, with the combination and extension of existing ingredients, like computational models and optimization strategies, the potential of the growth and remodeling models to reflect growth processes can be extended towards the prediction of growth.

All components of the proposed framework were implemented within the multi-purpose parallel computing platform BACI (Wall and Gee [107]). This flexible finite element software is continuously developed and maintained by the Institute for Computational Mechanics at the Technische

Universität München. The object-oriented code is written in C++ and utilizes powerful open-source libraries of the Trilinos project conducted by Sandia National Laboratories (Heroux et al. [41]). Consequently, existing features such as common finite element formulations, time integration schemes, iterative solution techniques, or inverse analysis schemes are reused within this thesis. All simulation results presented in the following were obtained using BACI.

1.4 Outline

This thesis is organized as follows. First, the basic concepts of structure mechanics, computational growth and remodeling, and optimization are presented. Afterwards, these methods are combined with each other to yield a predictive computational growth model for aneurysms. A more detailed explanation of the structure of this work is given in the following.

The fundamentals of nonlinear solid mechanics are introduced in Chapter 2. The quantities that are required to fully describe a solid are introduced. Subsequently, the basic balance equations that describe a closed system are presented. A brief summary of different material laws utilized within this thesis concludes the continuum mechanics section. The principal of virtual work is utilized to derive a boundary value problem that can be solved with the Finite Element Method. Finally, the Finite Element Method is briefly introduced.

In Chapter 3, the basic equations are adapted to the needs of growth and remodeling. The theory is extended to open system thermodynamics. As the first growth model, the isotropic growth model is introduced. This model is based on the split of the deformation gradient. Its capabilities are shown in illustrating examples. Subsequently, the constraint mixture model is presented and extended to meet the specified requirements. This model is based on the continuous turnover of collagen fibers. It is applied to meaningful examples and further refined. Thereafter, different aspects of the formation of an aneurysm are investigated in more detail. In Appendix A, details for special quantities and functions that are utilized in this chapter are provided.

The method that is utilized to inversely determine the parameters of the growth model is introduced in Chapter 4. The underlying optimization problem is stated and an algorithm to solve the described optimization problem is presented. Afterwards, a brief summary is given of how the data of the two CT scans is converted into a displacement field. Additionally, a parameterization of the parameters is established to be able to identify spatially varying parameters.

The methodology utilized for the validation of the proposed framework is derived in Chapter 5. Therefore, the exemplary formation of an aneurysm is utilized as reference solution. In the validation process, the real setting is replicated. Thus, the healthy artery is assumed as unknown and the simulation is started from a grown aneurysm, as sketched in Figure 1.3. The problems arising from the start of the simulation from a grown body are further investigated and a technique to circumvent some problems is proposed. Subsequently, the growth parameters are calibrated to match the given growth process. Finally, the capability to predict growth is validated by comparing the predicted results with the reference solution.

In Chapter 6, the proposed methodology is applied to a patient-specific example. First, the creation of a computational model is briefly summarized. Afterwards, the challenges arising from patient-specific geometries are addressed and solved. Hence, it is possible to determine growth parameters that can reproduce the growing aneurysm. Different spatial distributions are utilized for the determination of the parameters to characterize their influence. Finally, the determined

parameters are used to compute a simulation over a longer period of time that may provide a prediction of the development.

Chapter 7 concludes with a summary of this work followed by an outlook on future directions.

2 Nonlinear solid mechanics

In this chapter, a brief introduction in continuum mechanics is given. First the quantities to describe a solid are introduced. Subsequently, the balance equations are derived for a closed system. In the last section, the Finite Element Method (FEM) is briefly presented.

2.1 Nonlinear elasticity

Since the deformation in biology is often large and biological tissue commonly behaves nonlinear, a nonlinear theory has to be applied. In solid mechanics typically a *Lagrangian formulation* is used. Within this work cartesian coordinate systems are applied. For a more detailed description of the respective topics, the reader is referred to the corresponding text books, e.g. Bonet and Wood [12], Holzapfel [43], and Zienkiewicz et al. [114].

2.1.1 Kinematics

In this section, the kinematic quantities describing the deformation are introduced. The domain $\Omega_R \subset \mathbb{R}^3$ describes the *reference* or *material* configuration. A material point in this configuration is characterized by the vector \mathbf{X} . One component of the vector is specified by X_I , where $(\cdot)_I$ depicts an index in the reference configuration. The *current* or *spatial* configuration is denoted by Ω_t and a point therein is written as \mathbf{x} . Here, a component is described by x_i with $(\cdot)_i$ being an index in the current configuration. The function φ_t describes the mapping between these configurations, i.e.

$$\varphi_t : \begin{cases} \Omega_R \rightarrow \Omega_t \\ \mathbf{X} \mapsto \mathbf{x} = \varphi_t(\mathbf{X}) . \end{cases} \quad (2.1)$$

The *displacement vector* \mathbf{u} is defined as the difference between current and reference position, i.e.

$$\mathbf{u}(\mathbf{X}) = \mathbf{x} - \mathbf{X} . \quad (2.2)$$

An important kinematic quantity is the so-called *deformation gradient*, it is specified as

$$\mathbf{F} = \frac{d\mathbf{x}}{d\mathbf{X}} = \text{Grad}(\mathbf{x}) = \mathbf{1} + \frac{d\mathbf{u}}{d\mathbf{X}} , \quad (2.3)$$

where Grad denotes the material gradient operator and $\mathbf{1}$ is the second order identity tensor. Since the mapping is invertible, the Jacobian $J = \det(\mathbf{F}) > 0$ has to be larger than zero. The deformation gradient describes the mapping of a referential infinitesimal fiber $d\mathbf{X}$ to its value $d\mathbf{x}$ in the current configuration, i.e.

$$d\mathbf{x} = \mathbf{F} d\mathbf{X} . \quad (2.4)$$

The deformation gradient is a *two-point tensor* F_{jI} . That means one index is related to the spatial coordinate x_j and the other to the material coordinate X_I .

Since the deformation gradient maps a line element, the mapping of an infinitesimal area dA and volume element dV can also be described with the deformation gradient, i.e.

$$\mathbf{n} da = \det(\mathbf{F}) \mathbf{F}^{-T} \mathbf{N} dA, \quad (2.5)$$

$$dv = \det(\mathbf{F}) dV, \quad (2.6)$$

where \mathbf{n} and \mathbf{N} are the unit normal vectors in current and reference configuration, respectively. The deformation gradient can be split into a rotation tensor \mathbf{R} (which contains the rigid body movements) and a symmetric stretch tensor \mathbf{U} , yielding

$$\mathbf{F} = \mathbf{R}\mathbf{U}. \quad (2.7)$$

This decomposition is called *polar decomposition*. The unique rotation tensor \mathbf{R} is an orthogonal tensor that means it fulfills $\mathbf{R}\mathbf{R}^T = \mathbf{R}^T\mathbf{R} = \mathbf{1}$. It follows that $\det(\mathbf{R}) = 1$. The tensor \mathbf{U} is called the *right stretch tensor* and is positive definite, since $\det(\mathbf{U}) = \det(\mathbf{R}^T)\det(\mathbf{F}) = J > 0$. The orthogonal and normalized eigenvectors $\check{\mathbf{N}}_i$ and the corresponding eigenvalues $\check{\lambda}_i$ of \mathbf{U} are defined via

$$\mathbf{U} \check{\mathbf{N}}_i = \check{\lambda}_i \check{\mathbf{N}}_i \quad (2.8)$$

for $i = 1, 2, 3$. The eigenvectors $\check{\mathbf{N}}_i$ are called *principal axes*. The *spectral decomposition* of \mathbf{U} is given as

$$\mathbf{U} = \sum_{i=1}^3 \check{\lambda}_i \check{\mathbf{N}}_i \otimes \check{\mathbf{N}}_i, \quad (2.9)$$

where \otimes denotes the dyadic product. A kinematic quantity solely related to the reference configuration is the *right Cauchy-Green tensor*, it is defined as

$$\mathbf{C} = \mathbf{F}^T \mathbf{F} = \mathbf{U}^2 = \sum_{i=1}^3 \check{\lambda}_i^2 \check{\mathbf{N}}_i \otimes \check{\mathbf{N}}_i. \quad (2.10)$$

Herein, only the stretch part of the deformation gradient is contained, thus it does not include any rigid body movements and is therefore well suited for describing the internal state of a body. Its three principal invariants are defined as follows

$$I_1 = I_1(\mathbf{C}) = \text{tr}(\mathbf{C}) = \check{\lambda}_1^2 + \check{\lambda}_2^2 + \check{\lambda}_3^2, \quad (2.11a)$$

$$I_2 = I_2(\mathbf{C}) = \frac{1}{2} [(\text{tr}(\mathbf{C}))^2 - \text{tr}(\mathbf{C}^2)] = \check{\lambda}_1^2 \check{\lambda}_2^2 + \check{\lambda}_2^2 \check{\lambda}_3^2 + \check{\lambda}_3^2 \check{\lambda}_1^2, \quad (2.11b)$$

$$I_3 = I_3(\mathbf{C}) = \det(\mathbf{C}) = J^2 = \check{\lambda}_1^2 \check{\lambda}_2^2 \check{\lambda}_3^2. \quad (2.11c)$$

The strain measure used within this work is the *Green-Lagrange strain*, which is defined as follows

$$\mathbf{E} = \frac{1}{2} (\mathbf{F}^T \mathbf{F} - \mathbf{1}) = \frac{1}{2} (\mathbf{C} - \mathbf{1}) = \frac{1}{2} \left(\frac{d\mathbf{u}}{d\mathbf{X}} + \left(\frac{d\mathbf{u}}{d\mathbf{X}} \right)^T + \left(\frac{d\mathbf{u}}{d\mathbf{X}} \right)^T \frac{d\mathbf{u}}{d\mathbf{X}} \right). \quad (2.12)$$

For incompressible or nearly incompressible materials, it is useful to split the deformation gradient into an *isochoric* (volume-preserving) and *volumetric* (volume-changing) part, i.e.

$$\mathbf{F} = J^{\frac{1}{3}} \bar{\mathbf{F}}, \quad (2.13)$$

where $J^{\frac{1}{3}} \mathbf{1}$ describes the volume change and $\bar{\mathbf{F}}$ the distortional deformation. Accordingly, the modified Cauchy-Green tensor follows as

$$\bar{\mathbf{C}} = J^{-\frac{2}{3}} \mathbf{C} \quad (2.14)$$

and the modified invariants can be written as

$$\bar{I}_1 = J^{-\frac{2}{3}} I_1, \quad \bar{I}_2 = J^{-\frac{4}{3}} I_2 \quad \text{and} \quad \bar{I}_3 = 1. \quad (2.15)$$

To describe an anisotropic behavior of the solid, additional invariants, i.e. I_4, I_5 , are required. The direction of anisotropy in the reference configuration is denoted by \mathbf{a}_0^k . It often coincides with a fiber direction. The corresponding *structural tensor* is $\mathbf{A}_0^k = \mathbf{a}_0^k \otimes \mathbf{a}_0^k$. The normalized direction of anisotropy in the current configuration is given by $\mathbf{a}^k = \|\mathbf{F} \mathbf{a}_0^k\|^{-1} \mathbf{F} \mathbf{a}_0^k$. For each direction two invariants can be defined as

$$I_4^k = \mathbf{C} : \mathbf{A}_0^k = (\lambda^k)^2, \quad (2.16a)$$

$$I_5^k = \text{tr}(\mathbf{C}^2 \mathbf{A}_0^k), \quad (2.16b)$$

where λ^k is the stretch in fiber direction k . Further invariants can be defined when more directions of anisotropy exist. They describe a connection between the different directions. But they are omitted here, since they are not used within this work.

The modified anisotropic invariants, equivalent to (2.15), are

$$\bar{I}_4^k = J^{-\frac{2}{3}} I_4^k \quad \text{and} \quad \bar{I}_5^k = J^{-\frac{4}{3}} I_5^k. \quad (2.17)$$

2.1.2 Stress measures

The deformation of an elastic body leads to internal stresses. To describe these stresses, the *traction vector* is introduced as

$$\mathbf{t}(\mathbf{n}) = \lim_{\Delta a \rightarrow 0} \frac{\Delta \mathbf{f}}{\Delta a}, \quad (2.18)$$

where Δa is an area element with the unit normal \mathbf{n} in the current configuration and $\Delta \mathbf{f}$ the resultant force on this area. According to Cauchy's stress theorem, an unique second-order stress tensor $\boldsymbol{\sigma}$ exists that fulfills the condition

$$\mathbf{t}(\mathbf{n}) = \boldsymbol{\sigma} \mathbf{n}. \quad (2.19)$$

The tensor $\boldsymbol{\sigma}$ is the so-called *Cauchy stress tensor*. The traction vector (2.18) can be referenced to the initial area element dA . Hence, the *pseudo traction vector* \mathbf{t}_0 is introduced, leading to

$$\mathbf{t} da = \mathbf{t}_0 dA. \quad (2.20)$$

Analogous to the Cauchy theorem, the *1st Piola-Kirchhoff stress* tensor \mathbf{P} is defined with

$$\mathbf{t}_0 = \mathbf{P} \mathbf{N}. \quad (2.21)$$

Utilizing equations (2.5) and (2.20), a relation between \mathbf{P} and $\boldsymbol{\sigma}$ follows

$$\mathbf{P} = \det(\mathbf{F}) \boldsymbol{\sigma} \mathbf{F}^{-\top}. \quad (2.22)$$

Similarly to the pseudo traction \mathbf{t}_0 , another pseudo traction \mathbf{T} can be defined, which represents a purely material quantity

$$\mathbf{T} = \mathbf{F}^{-1} \mathbf{t}_0. \quad (2.23)$$

The *2nd Piola-Kirchhoff stress* tensor \mathbf{S} defines a stress measure purely based on material quantities, illustrated by

$$\mathbf{T} = \mathbf{S} \mathbf{N} \quad (2.24)$$

with

$$\mathbf{S} = \det(\mathbf{F}) \mathbf{F}^{-1} \boldsymbol{\sigma} \mathbf{F}^{-\top}. \quad (2.25)$$

Summarizing, the presented three different stress measures can be transformed to each other with the following relations

$$\mathbf{S} = \mathbf{F}^{-1} \mathbf{P} = \det(\mathbf{F}) \mathbf{F}^{-1} \boldsymbol{\sigma} \mathbf{F}^{-\top}. \quad (2.26)$$

2.1.3 Balance equations

Balance equations are the basis to describe continuum mechanics physically. They can be stated either globally, i.e. in an integral form, or locally, i.e. at a specific point. In the following, only the material point of view is considered. In this section, the equations for a closed system are derived. In Chapter 3.1, they are extended to open systems, since in growth mass changes.

Conservation of mass

The total mass m is defined as follows

$$m = \int_{\Omega_R} M \, dV = \int_{\Omega_t} \rho \, dv \quad (2.27)$$

with M denoting the reference mass density and ρ the current mass density. It follows that $M = J\rho$. In a closed system, the total mass m is constant that means in a global form

$$0 = \frac{dm}{dt} = \frac{d}{dt} \int_{\Omega_R} M \, dV = \int_{\Omega_R} \dot{M} \, dV, \quad (2.28)$$

where the superscript $(\dot{\cdot})$ denotes the first time derivative at a fixed reference position. In a local form this reads

$$\dot{M} = 0. \quad (2.29)$$

It follows that $M = \rho_0$ with ρ_0 being the initial reference density.

Balance of linear momentum

For a detailed description of the pressure applied to the inner wall of an artery, a fluid-structure interaction (FSI) problem has to be solved. Since growth happens in a time scale of months, which is much larger than the time scale of one heartbeat, a pure structural *quasi-static* formulation with mean values for the boundary conditions is applied. For more details concerning the coupling of a dynamic FSI simulation with growth and remodeling, the reader is referred to Figueroa et al. [21] and Baek et al. [8]. The assumption of quasi-static leads to a global balance of linear momentum in the following form

$$\mathbf{0} = \int_{\Omega_R} \hat{\mathbf{b}}_0 \, dV + \int_{\partial\Omega_R} \hat{\mathbf{t}}_0 \, dA, \quad (2.30)$$

where $\hat{\mathbf{b}}_0$ is an external body force and $\hat{\mathbf{t}}_0$ an external traction vector. The superscript hat ($\hat{\cdot}$) denotes prescribed quantities. With the help of the Gauss' divergence theorem and the definition of the 1st Piola-Kirchhoff stress (2.21), equation (2.30) can be transformed into

$$\mathbf{0} = \int_{\Omega_R} \hat{\mathbf{b}}_0 \, dV + \int_{\Omega_R} \text{Div}(\mathbf{P}) \, dV = \int_{\Omega_R} \hat{\mathbf{b}}_0 \, dV + \int_{\Omega_R} \text{Div}(\mathbf{F} \mathbf{S}) \, dV \quad (2.31)$$

with Div denoting the material divergence operator. The local form reads

$$\hat{\mathbf{b}}_0 + \text{Div}(\mathbf{F} \mathbf{S}) = \mathbf{0}. \quad (2.32)$$

Balance of angular momentum

In the static case, the external moments acting on a body have to be balanced. For simplicity only the moments around the origin are considered, leading to

$$0 = \int_{\Omega_R} \mathbf{x} \times \hat{\mathbf{b}}_0 \, dV + \int_{\partial\Omega_R} \mathbf{x} \times \hat{\mathbf{t}}_0 \, dA. \quad (2.33)$$

With the help of the Gauss' divergence theorem and some algebra, the symmetry of the 2nd Piola-Kirchhoff stress tensor can be shown, i.e.

$$\mathbf{S}^T = \mathbf{S}. \quad (2.34)$$

Accordingly, for the Cauchy stress tensor follows

$$\boldsymbol{\sigma}^T = \boldsymbol{\sigma}. \quad (2.35)$$

Clausius-Planck inequality

For a purely mechanical problem, the *second law of thermodynamics* reduces to the following form of the Clausius-Planck inequality

$$\frac{1}{2} \mathbf{S} : \dot{\mathbf{C}} - \dot{W}(\mathbf{C}) \geq 0, \quad (2.36)$$

where the scalar quantity W is the strain energy function (SEF) of the tissue.

2.1.4 Constitutive laws

To prescribe a relation between the deformation and stress, the SEF W has to be specified. Since we only consider *hyperelastic* materials, the SEF solely depends on the current state of deformation, i.e. $W = W(\mathbf{F})$. The SEF has to be objective that means it is independent of rigid body translations and rotations. Hence, it only depends on the stretch part \mathbf{U} , see (2.7). Since \mathbf{C} and \mathbf{E} can be written in terms of the stretch tensor \mathbf{U} , the SEF can be expressed in these two quantities too, leading to

$$W(\mathbf{F}) = W(\mathbf{U}) = W(\mathbf{C}) = W(\mathbf{E}) = W(I_1, I_2, I_3). \quad (2.37)$$

Similar to the split of the deformation gradient (2.13), the SEF can be split into an isochoric and a volumetric part according to (2.15), leading to

$$W(\mathbf{C}) = W_{iso}(\bar{I}_1, \bar{I}_2) + W_{vol}(J). \quad (2.38)$$

This split is especially reasonable for compressible materials, for which the volumetric deformation behaves differently compared to the isochoric deformation. Furthermore, for the case of nearly incompressible materials, the volumetric term can be interpreted as a penalty term. To obtain a relation between stress and strain, the Clausius-Planck inequality (2.36) is applied. Therefore, the time derivative of the SEF is necessary, i.e.

$$\dot{W}(\mathbf{C}) = \frac{\partial W(\mathbf{C})}{\partial \mathbf{C}} : \dot{\mathbf{C}}. \quad (2.39)$$

Inserting this relation into the Clausius-Planck inequality (2.36), this leads to the well known constitutive law for the 2nd Piola-Kirchhoff stresses

$$\mathbf{S} = 2 \frac{\partial W(\mathbf{C})}{\partial \mathbf{C}} = \frac{\partial W(\mathbf{E})}{\partial \mathbf{E}}. \quad (2.40)$$

For the solution of the nonlinear problem (2.32), the *constitutive tensor* \mathbb{C} is required. The fourth-order tensor is defined as

$$\mathbb{C} = 2 \frac{d\mathbf{S}}{d\mathbf{C}} = 4 \frac{\partial^2 W(\mathbf{C})}{\partial \mathbf{C} \partial \mathbf{C}}. \quad (2.41)$$

Since stress and constitutive tensor are both defined through the SEF, it is sufficient to specify a SEF to describe the material behavior. In the following some SEFs utilized throughout this work are summarized. The main focus of this work is to model the arterial wall. Hence, elastic and anisotropic functions are presented.

Neo-Hooke

The Neo-Hooke material is a very simple and widely used isotropic material with the SEF

$$W = \frac{\mu}{2} (I_1 - 3) + \frac{\mu}{2\beta} \left(I_3^{-\beta} - 1 \right), \quad (2.42)$$

where $\mu = E/2(1 + \nu)$ is the shear modulus and $\beta = \nu/(1 - 2\nu)$ a dimensionless parameter. The scalar ν is the Poisson's ratio and E the Young's modulus.

Log-Neo-Hooke

Another coupled isotropic material law is defined as

$$W = \frac{\mu}{2} (I_1 - 3) - \mu \ln J + \frac{\lambda}{2} (\ln J)^2, \quad (2.43)$$

where $\lambda = E\nu/[(1 + \nu)(1 - 2\nu)]$ is the first Lamé parameter and \ln the natural logarithm. Furthermore, the shear modulus μ is also known as the second Lamé parameter.

Raghavan & Vorp

A material law especially designed for the wall of an abdominal aortic aneurysm (AAA) is given in Raghavan and Vorp [77] using the SEF

$$W = \alpha (I_1 - 3) + \beta_1 (I_1 - 3)^2, \quad (2.44)$$

where α and β_1 are stress-like parameters.

Sussman-Bathe

A pure volumetric SEF is defined in Sussman and Bathe [91] by

$$W = \frac{\kappa}{2} (J - 1)^2, \quad (2.45)$$

where κ is the bulk modulus.

Ogden

Another pure volumetric SEF for rubber-like material is defined in Ogden [76] as

$$W = \kappa \beta_2^{-2} (\beta_2 \ln J + J^{-\beta_2} - 1), \quad (2.46)$$

where $\beta_2 \geq 0$ is a dimensionless parameter.

Holzappel-Gasser-Ogden

The following material was first presented in Holzappel et al. [44] for arterial walls. It is an anisotropic material for cylindrical structures. The directions of anisotropy correspond to two collagen fiber directions, which are oriented tangentially to the arterial wall as follows

$$\mathbf{a}_0^1 = \cos \gamma \mathbf{e}_{\text{cir}} + \sin \gamma \mathbf{e}_{\text{axi}}, \quad (2.47a)$$

$$\mathbf{a}_0^2 = \cos \gamma \mathbf{e}_{\text{cir}} - \sin \gamma \mathbf{e}_{\text{axi}}, \quad (2.47b)$$

where \mathbf{e}_{axi} is the axial direction, \mathbf{e}_{cir} the circumferential direction and γ the fiber angle. The SEF of the anisotropic part is defined as

$$W = \frac{k_1}{2k_2} \sum_{k=1}^2 \left[\exp \left(k_2 (I_4^k - 1)^2 \right) - 1 \right] \quad (2.48)$$

with $k_1 > 0$ represents a stress-like parameter and k_2 a dimensionless parameter. This material can easily be extended to more than two fibers. For example Cardamone et al. [13] use four fiber directions, where two additional fibers are oriented in circumferential and axial direction.

2.2 Finite Element Method

To solve the nonlinear solid mechanics problem defined in Section 2.1, in particular equations (2.32) and (2.40), the *Finite Element Method* (FEM) is used. In the following, a brief introduction to the FEM is given.

2.2.1 Weak form

The balance of linear momentum (2.32) leads to the following *boundary value problem* (BVP)

$$\hat{\mathbf{b}}_0 + \text{Div}(\mathbf{F} \mathbf{S}) = \mathbf{0} \quad (2.49a)$$

with the boundary conditions

$$\mathbf{u} = \hat{\mathbf{u}} \quad \text{on } \Gamma_u, \quad (2.49b)$$

$$\mathbf{P} \mathbf{N} = \hat{\mathbf{t}}_0 \quad \text{on } \Gamma_\sigma. \quad (2.49c)$$

The first condition (2.49b) is a *Dirichlet* boundary condition and the second condition (2.49c) a *Neumann* boundary condition. The corresponding boundaries Γ_u and Γ_σ are disjoint sets of the whole boundary $\partial\Omega_R$, i.e.

$$\Gamma_u \cup \Gamma_\sigma = \partial\Omega_R, \quad \Gamma_u \cap \Gamma_\sigma = \emptyset. \quad (2.50)$$

To solve the BVP (2.49) with the FEM, the weak form is required, i.e.

$$\int_{\Omega_R} (\hat{\mathbf{b}}_0 + \text{Div}(\mathbf{F} \mathbf{S}))^\top \mathbf{w} \, dV + \int_{\Gamma_\sigma} (\hat{\mathbf{t}}_0 - \mathbf{P} \mathbf{N})^\top \mathbf{w} \, dA = 0, \quad (2.51)$$

where \mathbf{w} is a weighting function, which fulfills $\mathbf{w} = \mathbf{0}$ on Γ_u . The weighting function can be interpreted as virtual displacements $\mathbf{w} = \delta\mathbf{u}$. Applying the Gauss' divergence theorem and inserting the definition of the weighting function leads to the *principle of virtual work* (PVW)

$$\delta\mathcal{W} = \int_{\Omega_R} (\text{Grad}(\delta\mathbf{u}))^\top : (\mathbf{F} \mathbf{S}) \, dV - \int_{\Omega_R} \delta\mathbf{u}^\top \hat{\mathbf{b}}_0 \, dV - \int_{\Gamma_\sigma} \delta\mathbf{u}^\top \hat{\mathbf{t}}_0 \, dA = 0. \quad (2.52)$$

Using the symmetry of \mathbf{S} (2.35) and the relation $\delta\mathbf{E} = \frac{1}{2} \left[(\mathbf{F}^\top \text{Grad} \delta\mathbf{u})^\top + \mathbf{F}^\top \text{Grad} \delta\mathbf{u} \right]$ the PVW can be written as

$$\delta\mathcal{W} = \underbrace{\int_{\Omega_R} \delta\mathbf{E} : \mathbf{S} \, dV}_{-\delta\mathcal{W}_{\text{int}}} - \underbrace{\int_{\Omega_R} \delta\mathbf{u}^\top \hat{\mathbf{b}}_0 \, dV - \int_{\Gamma_\sigma} \delta\mathbf{u}^\top \hat{\mathbf{t}}_0 \, dA}_{-\delta\mathcal{W}_{\text{ext}}} = 0, \quad (2.53)$$

which is the basis for the FEM. The total virtual work $\delta\mathcal{W}$ can be split into an internal virtual work $\delta\mathcal{W}_{\text{int}}$ and an external virtual work $\delta\mathcal{W}_{\text{ext}}$.

2.2.2 Space discretization

In order to solve the weak form (2.53) numerically, the equation has to be discretized in space. For this purpose, the FEM method is used throughout this work. The continuous displacements are approximated by an interpolation of discrete displacements at discrete nodes. The variables \mathbf{X}_k and \mathbf{x}_k describe the position of node k in the reference and current configuration, respectively. The vector \mathbf{d}_k denotes the discrete displacement of node k . The interpolated quantities are indicated with the index $(\cdot)_h$. Several nodes are connected to form elements, which leads to a partition of the domain

$$\Omega_R \approx \bigcup_{e=1}^{\text{nele}} \Omega_R^{(e)}, \quad (2.54)$$

where the subdomains (*elements*) $\Omega_R^{(e)}$ are non-overlapping. Each element is mapped to the parameter space described by the coordinate $\boldsymbol{\xi}$. This mapping depends on the number of nodes (nnod) of the element. For an hexahedral element typically the cube $[-1, 1] \times [-1, 1] \times [-1, 1]$ is used. The element displacements $\mathbf{u}^{(e)}$ are discretized as follows

$$\mathbf{u}^{(e)}(\boldsymbol{\xi}, t) \approx \mathbf{u}_h^{(e)}(\boldsymbol{\xi}, t) = \sum_{k=1}^{\text{nnod}^{(e)}} N_k(\boldsymbol{\xi}) \mathbf{d}_k(t), \quad (2.55)$$

where N_k is a polynomial of order p . The exact form of the polynomial depends on the chosen element type dependent on the requirements of the given problem.

In this work, the *isoparametric concept* is applied, i.e. the geometry is discretized equally to the displacements (2.55), leading to

$$\mathbf{X}_h^{(e)}(\boldsymbol{\xi}) = \sum_{k=1}^{\text{nnod}^{(e)}} N_k(\boldsymbol{\xi}) \mathbf{X}_k, \quad (2.56)$$

$$\mathbf{x}_h^{(e)}(\boldsymbol{\xi}, t) = \sum_{k=1}^{\text{nnod}^{(e)}} N_k(\boldsymbol{\xi}) \mathbf{x}_k(t). \quad (2.57)$$

The virtual displacements $\delta \mathbf{u}$ are also interpolated with the same shape functions, yielding

$$\delta \mathbf{u}_h^{(e)}(\boldsymbol{\xi}, t) = \sum_{k=1}^{\text{nnod}^{(e)}} N_k(\boldsymbol{\xi}) \delta \mathbf{d}_k(t). \quad (2.58)$$

This approach is often referred to as the *Bubnov-Galerkin* approach. The integration over the domain Ω_R is carried out element-wise on each element domain $\Omega_R^{(e)}$ using *Gauss quadrature*, i.e.

$$\int_{\Omega_R^{(e)}} f(\mathbf{X}) dV \approx \sum_{\text{gp}} w_{\text{gp}}^{(e)} f(\mathbf{X}_{\text{gp}}^{(e)}), \quad (2.59)$$

where $w_{\text{gp}}^{(e)}$ are the weights of the Gauss points and $\mathbf{X}_{\text{gp}}^{(e)}$ their positions. Thus, the quantities in equation (2.53) are evaluated at the Gauss points. Afterwards, the local quantities are sorted into

global vectors based on the so-called assembly operator \mathbf{A} , leading to

$$\int_{\Omega_R} (\cdot) \, dV \approx \mathbf{A} \int_{\Omega_R^{(e)}} (\cdot) \, dV. \quad (2.60)$$

This leads to the discrete version of the PVW in the following form

$$\delta \mathcal{W}_h = \delta \mathbf{d}^T (\mathbf{f}_{\text{int}}(\mathbf{d}) - \mathbf{f}_{\text{ext}}) = 0. \quad (2.61)$$

This equation has to be fulfilled for all admissible virtual displacements. Consequently, it is equivalent to the following discrete system of nonlinear equations

$$\mathbf{r} = \mathbf{f}_{\text{int}}(\mathbf{d}) - \mathbf{f}_{\text{ext}} = \mathbf{0}, \quad (2.62)$$

where \mathbf{r} is called the residuum. For solving this system of nonlinear equations, the *Newton* scheme is used. Hence, the linearized form of (2.62) is solved iteratively, i.e.

$$\text{Lin } \mathbf{r} = \mathbf{r}(\mathbf{d}^i) + \underbrace{\frac{\partial \mathbf{r}(\mathbf{d})}{\partial \mathbf{d}} \Big|_{\mathbf{d}^i}}_{\mathbf{K}_T} \Delta \mathbf{d}^{i+1} = \mathbf{0} \quad (2.63)$$

with the stiffness matrix \mathbf{K}_T and the iteration index $(\cdot)^i$. The updated displacements are defined in the following way

$$\mathbf{d}^{i+1} = \mathbf{d}^i + \Delta \mathbf{d}^{i+1}. \quad (2.64)$$

3 Growth and remodeling

To model growth and remodeling, the theory established in Section 2.1 has to be extended. This extended theory is presented in the first section of this chapter. In the next two sections, two approaches to model growth and remodeling in three dimensions are introduced. The first approach models isotropic volumetric growth and is based on the consequences of growth on the macroscopic level. Whereas, the second approach models growth and remodeling of individual constituents and describes growth on a smaller scale. Thus, the first can be used to study large scale results and the second to study underlying mechanisms (Ambrosi et al. [3]). For both approaches, representative examples are presented to illustrate the behavior of the respective model.

3.1 Introduction to open system thermodynamics

During growth and remodeling, the mass of the solid body changes. The mass can increase (*growth*) or decrease (*atrophy*). Since the mechanical behavior of the body is defined through the solid phase, it is meaningful to model only this phase. The other phases are omitted in the following. Hence, the solid phase has to be treated as an *open system*, where the mass can vary. In the following section, a brief introduction to open system thermodynamics is given. For a more detailed explanation of this topic, the reader is referred to Epstein and Maugin [20] and for the theory for more than one species to Garikipati et al. [25].

Due to the creation of mass, the balance equations have to be adapted. The total mass is still defined as follows

$$\mathfrak{m} = \int_{\Omega_R} M \, dV = \int_{\Omega_t} \rho \, dv. \quad (3.1)$$

It follows that $M = J\rho$. The mass balance equation reads now

$$\frac{d}{dt} \int_{\Omega_R} M \, dV = \int_{\Omega_R} \mathcal{R}_0 \, dV + \int_{\partial\Omega_R} \mathbf{N}^\top \mathcal{R} \, dA, \quad (3.2)$$

where \mathcal{R}_0 is the mass source and \mathcal{R} the mass flux over the boundary. The vector \mathbf{N} has already been introduced as unit normal in the reference configuration. Applying the Gauss' divergence theorem to equation (3.2) leads to

$$\frac{d}{dt} \int_{\Omega_R} M \, dV = \int_{\Omega_R} \mathcal{R}_0 \, dV + \int_{\Omega_R} \text{Div}(\mathcal{R}) \, dV. \quad (3.3)$$

From this equation, the local form can be derived, i.e.

$$\dot{M} = \mathcal{R}_0 + \text{Div}(\mathcal{R}). \quad (3.4)$$

Since in the problems considered within this work, the mass flux is zero, it is omitted in the following. This assumption and the fact that a quasi-static analysis (see Section 2.1.3) is performed result in simplified equations. The function W is no longer called a strain energy function, but a *Helmholtz free-energy function* (HFEF) since the deformation leaves the elastic regime. Thus, the HFEF depends not only on the actual deformation, i.e. $W \neq W(\mathbf{C})$, but also on the history of the deformation, e.g. $W = W(\mathbf{C}(\mathbf{h}), \mathbf{h})$. The *history vector* \mathbf{h} describes a collection of variables, which may be history variables or quantities that describe the inelastic behavior. The exact form of \mathbf{h} depends on the chosen growth model. The summands of the HFEF may be strain energy functions or potentials.

The balance of linear momentum has the same form as in equation (2.32) and from the balance of angular momentum still follows the symmetry of the stresses. An extra entropy source \mathcal{S}_0 arises to satisfy the second law of thermodynamics (Himpel et al. [42]). Hence, the Clausius-Planck inequality (2.36) has to be adapted. It now reads

$$\frac{1}{2} \mathbf{S} : \dot{\mathbf{C}} - \dot{W} + \frac{\mathcal{R}_0}{M} W - T M \mathcal{S}_0 \geq 0, \quad (3.5)$$

where T denotes the constant temperature. Since $\dot{W}(\mathbf{C}(\mathbf{h}), \mathbf{h})$ depends on the chosen growth model, the relation between stress and strain cannot be given in general in contrast to the elastic case. Often, the Cauchy-Green tensor \mathbf{C} is independent of the history vector \mathbf{h} , i.e. $W = W(\mathbf{C}, \mathbf{h})$. Hence, the time derivative of the HFEF is defined as follows

$$\dot{W}(\mathbf{C}, \mathbf{h}) = \frac{\partial W}{\partial \mathbf{C}} : \dot{\mathbf{C}} + \left(\frac{\partial W}{\partial \mathbf{h}} \right)^\top \dot{\mathbf{h}}. \quad (3.6)$$

Since the Cauchy-Green tensor is independent of \mathbf{h} , it follows from equations (3.5) and (3.6) that

$$\mathbf{S} = 2 \frac{\partial W(\mathbf{C}, \mathbf{h})}{\partial \mathbf{C}}. \quad (3.7)$$

This relation between stress and strain is nearly identical to the constitutive law of the elastic case (2.40), only the dependency on \mathbf{h} is different. The history vector \mathbf{h} is treated as a local quantity that is defined at each Gauss point independently. Hence, to incorporate growth into an existing finite element code, the constitutive equations have to be adapted, i.e. a new material law with the local variable \mathbf{h} has to be implemented. Since the balance of linear momentum is the same as in (2.32), the same boundary value problem as in the elastic case (2.49) has to be solved. Thus, the weak form (2.53) remains the same and the finite element formulation does not have to be adapted.

Inserting equations (3.6) and (3.7) into the Clausius-Planck inequality (3.5) yields for the extra entropy source \mathcal{S}_0 the following relation

$$\mathcal{S}_0 = \frac{1}{TM} \left[\frac{\mathcal{R}_0}{M} W - \left(\frac{\partial W}{\partial \mathbf{h}} \right)^\top \dot{\mathbf{h}} \right]. \quad (3.8)$$

The exact form of (3.8) is derived in the following chapters for the presented growth and remodeling approaches.

3.2 Isotropic growth

The following method to model growth was first presented in Rodriguez et al. [82]. First, the basic concept is introduced. Subsequently, some details needed for the implementation are given, and finally, illustrating results are presented. Part of the notation and basic equations are taken from Himpel et al. [42].

3.2.1 Model

The basic idea of this model stems from plasticity (Lee [59]). The deformation gradient (2.3) is split into two parts, a growth deformation \mathbf{F}_g and an elastic deformation \mathbf{F}_e , yielding

$$\mathbf{F} = \mathbf{F}_e \mathbf{F}_g. \quad (3.9)$$

The growth deformation does not have to be compatible, since the elastic deformation ensures compatibility of the whole deformation. Thus, growth can lead to residual stresses in the growing body (Skalak et al. [88]). With the split of the deformation gradient an intermediate configuration is defined. Quantities in this configuration are marked with $\check{(\cdot)}$, like the density $\check{\rho}$, the stretch tensor $\check{\mathbf{C}}$, and the stress $\check{\mathbf{S}}$.

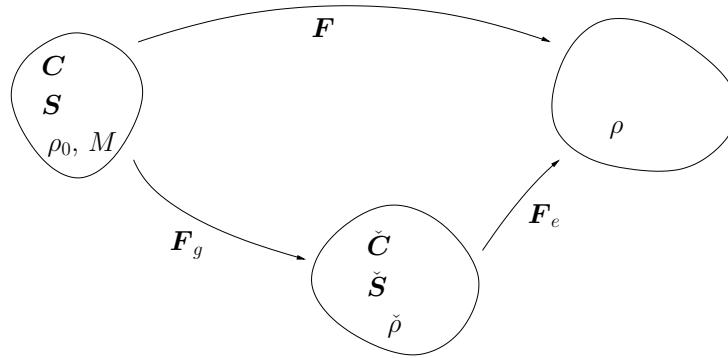


Figure 3.1: Multiplicative split of the deformation gradient \mathbf{F} into a growth part \mathbf{F}_g and an elastic part \mathbf{F}_e

In Figure 3.1 a graphical summary of the different configurations and the mappings between them is given. It is assumed that the pure growth deformation does not create any stresses. Thus, the HFEF only depends on the intermediate stretch $\check{\mathbf{C}}$, i.e. $W = W(\check{\mathbf{C}})$. The intermediate stretch is defined as follows

$$\check{\mathbf{C}} = \mathbf{F}_e^T \mathbf{F}_e. \quad (3.10)$$

The Cauchy-Green stretch (2.10) is related to the intermediate stretch in the following way $\mathbf{C} = \mathbf{F}_g^T \check{\mathbf{C}} \mathbf{F}_g$. The stress $\check{\mathbf{S}}$ in the intermediate configuration is defined through the transformation of the 2nd Piola-Kirchhoff stress \mathbf{S} (2.24) into the intermediate configuration, i.e.

$$\check{\mathbf{S}} = \mathbf{F}_g \mathbf{S} \mathbf{F}_g^T. \quad (3.11)$$

With the intermediate configuration an additional density $\check{\rho}$ arises. The different densities are related as follows

$$\check{\rho} = J_e \rho, \quad M = J \rho = J_g \check{\rho} \quad (3.12)$$

with $J_e = \det(\mathbf{F}_e)$ and $J_g = \det(\mathbf{F}_g)$. For an incompressible material, the densities in the intermediate and current configuration are the same $\check{\rho} = \rho$. During the growth process the density is constant, i.e. when the mass is increased, the volume is increased relatively with the same amount. For the density, this means that $\check{\rho} = \rho_0 = M(t=0)$ and $M = J_g \rho_0$. For isotropic growth, the growth deformation gradient can be written as

$$\mathbf{F}_g = \vartheta \mathbf{1}, \quad (3.13)$$

where ϑ is the *growth stretch*. Formulas for orthotropic and transversely isotropic growth can be found in Lubarda and Hoger [63]. Here, only the isotropic growth model is further investigated. In this case, the history vector \mathbf{h} consists only of the growth stretch ϑ . Since the growth stretch ϑ is a local variable, it is treated as a secondary variable. That means for every deformation state a matching growth stretch is computed and the deformation itself is treated as independent of the growth stretch at this stage. In the general case, all components of the growth deformation gradient \mathbf{F}_g would be part of the history vector.

Since the Cauchy-Green tensor is independent of the growth stretch, the HFEF can be described in terms of both quantities in the following way $W = W(\mathbf{C}, \vartheta)$. Thus, the assumption for equation (3.7) is fulfilled, i.e. the 2nd Piola-Kirchhoff stress is defined as

$$\mathbf{S} = 2 \frac{\partial W}{\partial \mathbf{C}}. \quad (3.14)$$

From the definition of the intermediate stress $\check{\mathbf{S}}$ (3.11) follows the constitutive law

$$\check{\mathbf{S}} = \mathbf{F}_g \mathbf{S} \mathbf{F}_g^\top = 2 \mathbf{F}_g \frac{\partial W}{\partial \mathbf{C}} \mathbf{F}_g^\top = 2 \frac{\partial W}{\partial \check{\mathbf{C}}}. \quad (3.15)$$

In order to compute the stresses, the growth stretch has to be defined. Therefore, the following differential equation is used

$$\frac{d\vartheta}{dt} = \dot{\vartheta} = f_\vartheta(\vartheta, \check{\mathbf{C}}, \check{\mathbf{S}}) = f_\vartheta(\vartheta, \mathbf{C}). \quad (3.16)$$

The last relation holds, since the intermediate stretch $\check{\mathbf{C}}$, and thus $\check{\mathbf{S}}$, can be expressed in terms of ϑ and \mathbf{C} . Equation (3.16) is solved at every Gauss point for a given Cauchy-Green tensor. One possibility for the growth differential equation is proposed by Lubarda and Hoger [63] as

$$\dot{\vartheta} = k_\vartheta(\vartheta) (\text{tr} \check{\mathbf{M}} - \check{M}_{hom}), \quad (3.17)$$

where $\check{\mathbf{M}} = \check{\mathbf{C}} \check{\mathbf{S}}$ is the *Mandel stress* and \check{M}_{hom} the trace of its homeostatic value. The factor in front of the stress term is defined as

$$k_\vartheta(\vartheta) = \begin{cases} k_{\vartheta 0}^+ \left[\frac{\vartheta^+ - \vartheta}{\vartheta^+ - 1} \right]^{m_\vartheta^+} & \text{for } (\text{tr} \check{\mathbf{M}} - \check{M}_{hom}) > 0 \\ k_{\vartheta 0}^- \left[\frac{\vartheta - \vartheta^-}{1 - \vartheta^-} \right]^{m_\vartheta^-} & \text{for } (\text{tr} \check{\mathbf{M}} - \check{M}_{hom}) < 0 \end{cases} \quad (3.18)$$

with ϑ^+ denoting the maximal value of ϑ and ϑ^- the minimal value. Hence, the growth stretch ϑ is restricted to the interval $[\vartheta^-, \vartheta^+]$. The dimensionless constants m_ϑ^+ and m_ϑ^- describe the

influence of the limiting values. The constants $k_{\vartheta_0}^+$ and $k_{\vartheta_0}^-$ scale the overall behavior and are measured in $(\text{Pa s})^{-1}$.

For the sake of completeness formulas for the mass source \mathcal{R}_0 and the extra entropy source \mathcal{S}_0 are derived. Since the reference mass density is defined as $M = \vartheta^3 \rho_0$ for the isotropic growth defined in equation (3.13), the mass source can be computed from the local balance of mass (3.4), leading to

$$\mathcal{R}_0 = \dot{M} = 3\vartheta^2 \dot{\vartheta} \rho_0. \quad (3.19)$$

To compute the extra entropy source (3.8) the time derivative of the HFEF (3.6) is needed, it is defined as

$$\dot{W}(\check{\mathbf{C}}) = \frac{\partial W}{\partial \mathbf{C}} : \dot{\mathbf{C}} + \frac{\partial W}{\partial \mathbf{F}_g} : \dot{\mathbf{F}}_g = \frac{\partial W}{\partial \mathbf{C}} : \dot{\mathbf{C}} - \left(2\check{\mathbf{C}} \frac{\partial W}{\partial \check{\mathbf{C}}} \mathbf{F}_g^{-\top} \right) : \dot{\mathbf{F}}_g. \quad (3.20)$$

Inserting this equation into the Clausius-Planck inequality (3.5) leads to

$$\frac{1}{2} \mathbf{S} : \dot{\mathbf{C}} - \frac{\partial W}{\partial \mathbf{C}} : \dot{\mathbf{C}} + \left(2\check{\mathbf{C}} \frac{\partial W}{\partial \check{\mathbf{C}}} \mathbf{F}_g^{-\top} \right) : \dot{\mathbf{F}}_g + \frac{3\vartheta^2 \dot{\vartheta} \rho_0}{M} W - T M \mathcal{S}_0 \geq 0. \quad (3.21)$$

Inserting the two equations (3.14) and (3.15) into (3.21) gives

$$\underbrace{(\check{\mathbf{C}} \check{\mathbf{S}})}_{\check{\mathbf{M}}} : \underbrace{(\dot{\mathbf{F}}_g \mathbf{F}_g^\top)}_{\check{\mathbf{L}}_g} + \frac{3\vartheta^2 \dot{\vartheta} \rho_0}{M} W - T M \mathcal{S}_0 \geq 0. \quad (3.22)$$

The Mandel stress is work conjugate to the growth velocity gradient $\check{\mathbf{L}}_g$. Hence, it is reasonable to choose $\text{tr}(\check{\mathbf{M}})$ as the driving force of growth. With $\check{\mathbf{L}}_g = \frac{\dot{\vartheta}}{\vartheta} \mathbf{1}$, the extra entropy source is defined as

$$\mathcal{S}_0 = \frac{\dot{\vartheta}}{T \rho_0 \vartheta^4} (\text{tr}(\check{\mathbf{M}}) + 3W). \quad (3.23)$$

3.2.2 Time discretization and linearization

In order to solve the growth problem, one needs to discretize the growth differential equation (3.16) and to linearize the stress, this is done as proposed in Himpel et al. [42]. The differential equation is solved with an implicit Euler scheme in the following way

$$\vartheta = \vartheta_n + f_\vartheta(\vartheta, \check{\mathbf{C}}, \check{\mathbf{S}}) \Delta t, \quad (3.24)$$

where ϑ_n is the stretch value of the previous time step and ϑ the value of the current time step. To solve this equation a local Newton iteration is used. The residual is

$$R_\vartheta = \vartheta_n - \vartheta + f_\vartheta(\vartheta, \check{\mathbf{C}}, \check{\mathbf{S}}) \Delta t. \quad (3.25)$$

The first derivative of the residual with respect to the growth stretch reads

$$\frac{dR_\vartheta}{d\vartheta} = -1 + \frac{df_\vartheta}{d\vartheta} \Delta t = -1 + \frac{\partial f_\vartheta}{\partial \vartheta} \Delta t + \left(\frac{\partial f_\vartheta}{\partial \check{\mathbf{C}}} + \frac{\partial f_\vartheta}{\partial \check{\mathbf{S}}} : \frac{\partial \check{\mathbf{S}}}{\partial \check{\mathbf{C}}} \right) : \frac{\partial \check{\mathbf{C}}}{\partial \vartheta} \Delta t. \quad (3.26)$$

The derivative of $\check{\mathbf{C}}$ with respect to ϑ can be easily computed as

$$\frac{\partial \check{\mathbf{C}}}{\partial \vartheta} = \frac{\partial (\mathbf{F}_g^{-1} \mathbf{C} \mathbf{F}_g^{-\top})}{\partial \vartheta} \stackrel{(3.13)}{=} -2\vartheta^{-3} \mathbf{C} = -\frac{2}{\vartheta} \check{\mathbf{C}}. \quad (3.27)$$

The relation between stress $\check{\mathbf{S}}$ and strain $\check{\mathbf{C}}$ is defined through the constitutive law (3.15). The intermediate constitutive matrix $\check{\mathbb{C}}_e$ is defined as $\check{\mathbb{C}}_e = 2 \frac{\partial \check{\mathbf{S}}}{\partial \check{\mathbf{C}}}$. Using the proposed growth law (3.17) the derivative of the residual can be computed, it reads

$$\frac{dR_\vartheta}{d\vartheta} = -1 + \frac{\partial k_\vartheta(\vartheta)}{\partial \vartheta} (\text{tr}(\check{\mathbf{M}}) - \check{M}_{hom}) \Delta t - \frac{2k_\vartheta(\vartheta)}{\vartheta} \left(\text{tr}(\check{\mathbf{M}}) + \frac{1}{2} \check{\mathbf{C}} : \check{\mathbb{C}}_e : \check{\mathbf{C}} \right) \Delta t. \quad (3.28)$$

When the local Newton iteration converged, a growth stretch ϑ that fulfills $R_\vartheta = 0$ is found.

For the linearization of the discrete residual (2.63), the derivative of the stress \mathbf{S} with respect to \mathbf{C} is needed, it follows

$$\mathbb{C}_{eg} = 2 \frac{d\mathbf{S}}{d\mathbf{C}} = 2 \left(\frac{\partial \mathbf{S}}{\partial \mathbf{C}} + \frac{\partial \mathbf{S}}{\partial \vartheta} \otimes \frac{d\vartheta}{d\mathbf{C}} \right). \quad (3.29)$$

The first term yields the elasticity matrix $\mathbb{C}_e = 2 \frac{\partial \check{\mathbf{S}}}{\partial \check{\mathbf{C}}} = \mathbf{F}_g^{-1} \mathbf{F}_g^{-1} \check{\mathbb{C}}_e \mathbf{F}_g^{-\top} \mathbf{F}_g^{-\top}$. The second term $\frac{\partial \mathbf{S}}{\partial \vartheta}$ can be computed as

$$\begin{aligned} \frac{\partial \mathbf{S}}{\partial \vartheta} &= \frac{\partial}{\partial \vartheta} (\mathbf{F}_g^{-1} \check{\mathbf{S}} \mathbf{F}_g^{-\top}) = \frac{\partial (\mathbf{F}_g^{-1})}{\partial \vartheta} \check{\mathbf{S}} \mathbf{F}_g^{-\top} + \mathbf{F}_g^{-1} \left(\frac{\partial \check{\mathbf{S}}}{\partial \check{\mathbf{C}}} : \frac{\partial \check{\mathbf{C}}}{\partial \vartheta} \right) \mathbf{F}_g^{-\top} + \mathbf{F}_g^{-1} \check{\mathbf{S}} \frac{\partial (\mathbf{F}_g^{-\top})}{\partial \vartheta} \\ &\stackrel{(3.13), (3.27)}{=} -\frac{2}{\vartheta} \left(\mathbf{S} + \frac{1}{2} \mathbb{C}_e : \mathbf{C} \right). \end{aligned} \quad (3.30)$$

The third term $\frac{d\vartheta}{d\mathbf{C}}$ needs further considerations. To obtain it, one can differentiate the residual of the growth equation for the final ϑ , yielding

$$\frac{dR_\vartheta}{d\mathbf{C}} = \frac{dR_\vartheta}{d\vartheta} \frac{d\vartheta}{d\mathbf{C}} + \frac{\partial f_\vartheta}{\partial \mathbf{C}} \Delta t = \mathbf{0} \quad \Rightarrow \quad \frac{d\vartheta}{d\mathbf{C}} = - \left(\frac{dR_\vartheta}{d\vartheta} \right)^{-1} \frac{\partial f_\vartheta}{\partial \mathbf{C}} \Delta t. \quad (3.31)$$

To compute the derivative the following relation is required

$$\frac{\partial f_\vartheta}{\partial \mathbf{C}} \stackrel{(3.17)}{=} k_\vartheta(\vartheta) \left(\mathbf{S} + \frac{1}{2} \mathbf{C} : \mathbb{C}_e \right). \quad (3.32)$$

Inserting all derivatives into equation (3.29) yields the growth constitutive tensor

$$\mathbb{C}_{eg} = \mathbb{C}_e + \frac{4}{\vartheta} k_\vartheta(\vartheta) \left(\frac{dR_\vartheta}{d\vartheta} \right)^{-1} \left(\mathbf{S} + \frac{1}{2} \mathbf{C} : \mathbb{C}_e \right) \otimes \left(\mathbf{S} + \frac{1}{2} \mathbf{C} : \mathbb{C}_e \right) \Delta t, \quad (3.33)$$

which can be used to compute the tangential stiffness matrix \mathbf{K}_T .

3.2.3 Examples

To show how the presented growth model works, several simulations are performed. First a cylindrical tube is stretched and compressed and compared to results from literature to validate the implementation of the model. Second hypertension is simulated and the third example is growth of a patient-specific aneurysm.

Tension and compression of a cylinder

The following example is taken from Himpel et al. [42]. A thick cylindrical tube, as depicted in Figure 3.2, with inner radius 0.5 mm, outer radius 1.0 mm and axial length 2.0 mm is stretched or compressed in axial direction by a quarter of its length. There is no Neumann boundary condi-

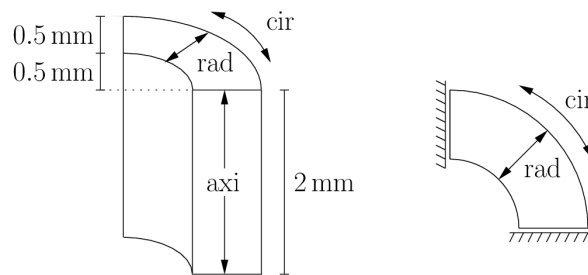


Figure 3.2: Reference geometry for compression and tension with symmetric boundary conditions, sketch of important directions for cylindrical geometries: axial, circumferential, and radial direction

tion applied. Since the problem is symmetric in circumferential direction, only one quarter of the cylinder with symmetric boundary conditions is simulated. It is discretized with four elements in radial direction, eight elements in circumferential direction and eight elements in axial direction. As elastic material the Log-Neo-Hooke material law (2.43) with parameters $E = 3 \text{ N/mm}^2$ and $\nu = 0.3$ is used. For the growth law the following parameters are prescribed $\tilde{M}_{hom} = 0 \text{ Pa}$, $\vartheta^+ = 1.5$, $\vartheta^- = 0.5$, $k_{\vartheta 0}^+ = 0.5 \frac{1}{\text{Pa d}}$, $k_{\vartheta 0}^- = 0.25 \frac{1}{\text{Pa d}}$, $m_{\vartheta}^+ = 4.0$ and $m_{\vartheta}^- = 5.0$. The time step

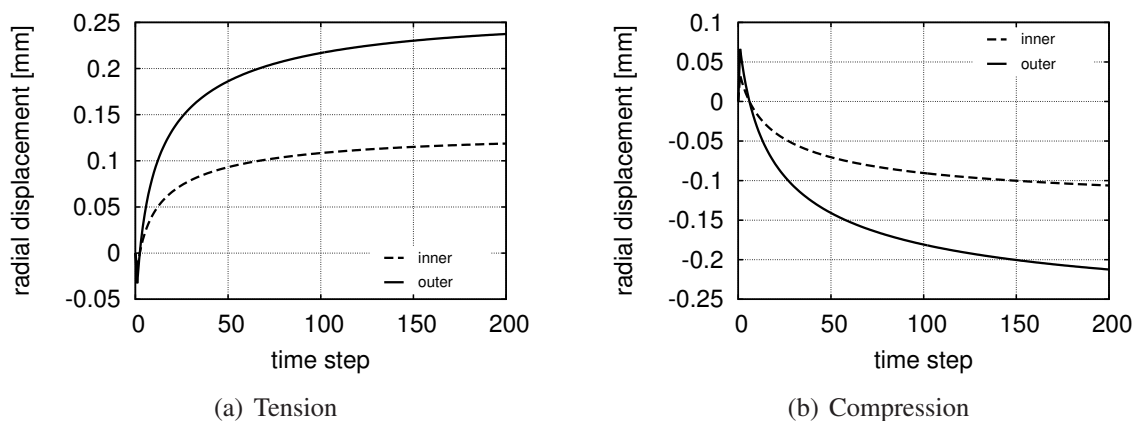


Figure 3.3: Tension and compression of a cylinder, evolution of the radial displacement over time at a point at the inner and outer surface

size is $\Delta t = 0.1$ d. In Figure 3.3 one can see the evolution of the radial displacement at a point at the inner surface and a point at the outer surface. The growth model reacts quickly and compensates the change of the geometry. After 100 time steps growth gets less, since an equilibrium is nearly reached. Due to the choice of growth parameters, the adaptation takes longer in the case of compression. The results from literature (Himpel et al. [42]) can be reproduced.

Hypertension

In a second example, the inner pressure of a thin walled cylinder is increased. This imitates hypertension. The cylinder has an inner radius of 10 mm, an outer radius of 12 mm and a length of 10 mm, see Figure 3.4, what coincides with the dimensions of an artery. Again only one quarter of the cylinder is simulated. The mesh consists of one element in radial, twelve in circumferential and eight in axial direction. The same material and growth parameters as in the previous example are used.

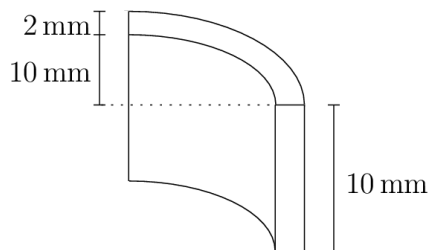


Figure 3.4: Reference geometry for hypertension

During the first five time steps (t_1) the pressure is increased linearly to its initial value of 0.01 Pa. This leads to a homeostatic stress of $\bar{M} = 0.061573$ Pa. The linear increase is visible in the time course of the mandel stress, the displacements and the thickness of the wall, see Figure 3.5(b)-(d). After the tenth time step (t_2) the pressure is increased by a factor of 1.5 and growth starts. This leads to a jump in the stresses, see Figure 3.5(b). An equilibrium is achieved after about 80 time steps, see Figure 3.5(a)-(b). The trace of the mandel stress reaches its homeostatic value and the growth stretch converges to $\vartheta \approx 1.01172$. The radial displacements also reach a maximal value. The inner radius cannot be restored, what would be expected for arteries (Matsumoto and Hayashi [70], Fridez et al. [22]). Nevertheless, the thickness of the cylinder increases due to growth. Summarizing, the growth model cannot reproduce the behavior of an artery that suffers from hypertension.

Aneurysm

The third example is the growth of an aneurysm of a 67 years old male patient. As elastic material the material of Raghavan and Vorp (2.44) with parameters $\alpha = 52.3$ kPa and $\beta = 3.12$ MPa is used with the modified invariants (2.15) and for the volumetric part the Ogden function (2.46) with $\kappa = 5.23$ MPa and $\beta_2 = -2$ (Maier [64]). The diastolic pressure of 11598.84 Pa is applied while using the modified updated Lagrangian formulation (MULF, Gee et al. [27, 28]). At $t = 0.3$ y, growth starts with $\bar{M}_{hom} = 50$ kPa. The other growth parameters are nearly the same as in the previous examples, only the two following values are adapted to the different homeostatic stress: $k_{\vartheta 0}^+ = 0.5 \cdot 10^{-6} \frac{1}{\text{Pa} \cdot \text{y}}$ and $k_{\vartheta 0}^- = 0.25 \cdot 10^{-6} \frac{1}{\text{Pa} \cdot \text{y}}$. During growth the end surfaces at the top and bottom are fixed.

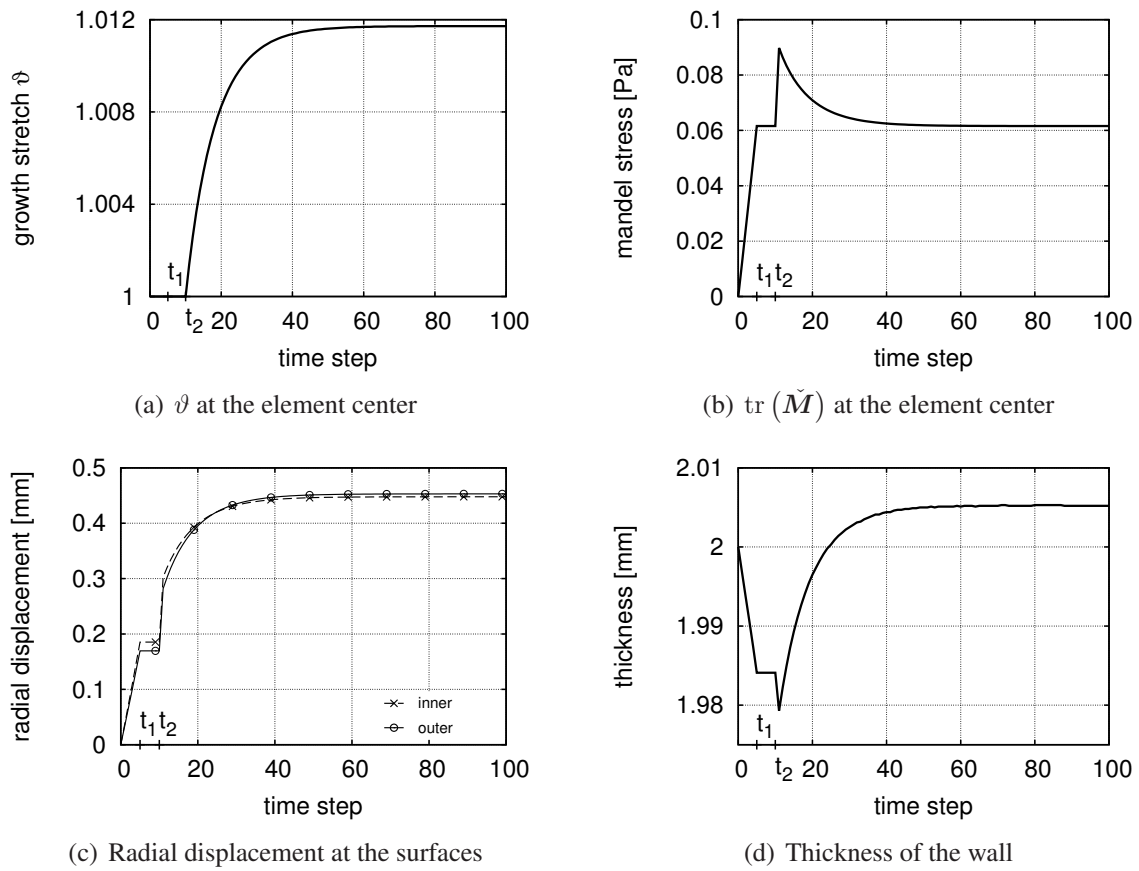


Figure 3.5: Time course of important quantities of a cylinder with increased inner pressure

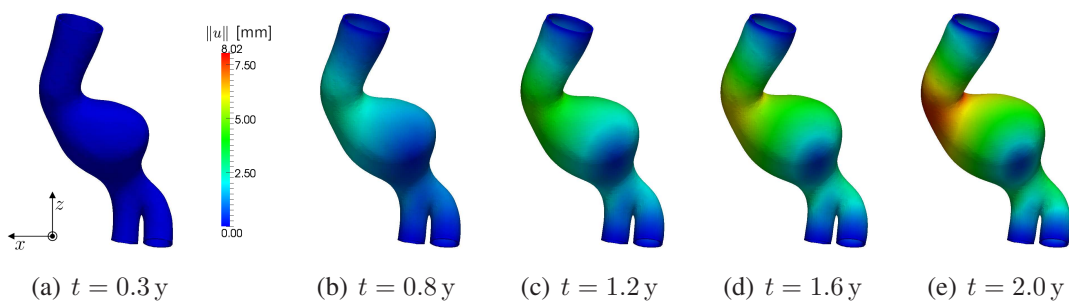


Figure 3.6: Deformed geometry of a growing aneurysm at different time steps, colors depict the magnitude of the displacements

In Figure 3.6 one can see the growth of the aneurysm until $t = 2.0$ y. The largest deformation can be seen at the transition between the healthy aorta and the aneurysm, where the existing kink is amplified. The diameter of the aneurysm increases, in Figure 3.7(c) one can see its evolution over time. The diameter is measured by the distance between the two points marked in the figure. It has not reached its maximal value at the end of the simulation. The peak mandel stress at the final state is one order of magnitude higher than the homeostatic value. The maximal growth stretch is 1.15, i.e. the aneurysm can still grow until the limit of 1.5 is reached. As one can see, the stress at the center of the aneurysm sac is quite low compared to the rest of the aneurysm. Thus, the growth stretch is low, too. Due to the fixation of the aneurysm atrophy occurs close to the boundaries.

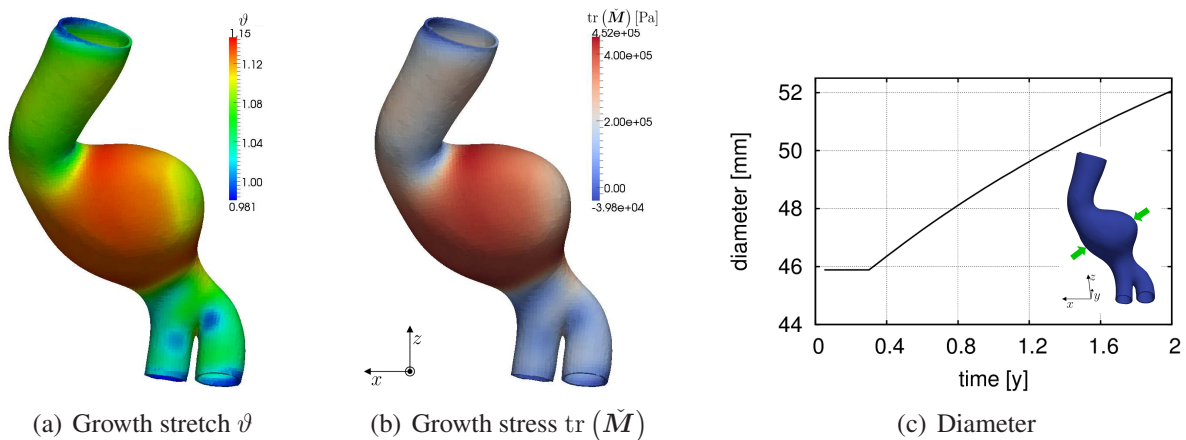


Figure 3.7: Growth variables at the final state and evolution of the diameter over time

3.3 Constraint mixture

Contrary to the previous model, this model distinguishes between different constituents of the soft tissue and their behavior. It was first presented in Humphrey and Rajagopal [46, 47]. In the following, the model is introduced and extended to three dimensions. Then, the temporal discretization is presented. Afterwards, the homeostatic state is examined in more detail. While investigating a steady state, some details regarding the driving force of growth arise. In the end, the reaction of the model to two diseases and altered conditions is tested. The first disease is hypertension, during aging the structure of the artery changes and the second disease is the formation of an aneurysm.

3.3.1 Model

The constraint mixture model is especially designed for arterial tissue. The tissue consists of several constituents like elastin, collagen fibers and smooth muscle cells. The basis of the model is that all constituents are compatible in the spatial configuration (thus *constraint* mixture), but they can grow and remodel individually. The following notation and formulas have been adapted

from the two dimensional case in Baek et al. [6]. The fraction of the total mass of constituent i defines its mass fraction ϕ^i . The sum of all mass fractions has to be one, i.e. $\phi^e + \phi^c + \phi^m = 1$. Constituent i has a SEF Ψ^i . For elastin a Neo-Hooke material (2.42) is used. The collagen fiber families and the passive part of the smooth muscle cells are modeled with a Holzapfel-Gasser-Ogden material (2.48). The SEF of the mixture in the elastic case is defined as the sum of the SEFs of all constituents multiplied with their mass fraction ϕ^i . Additionally, a volumetric SEF W^{vol} (2.45) is added, leading to

$$W = \phi^e \Psi^e + \phi^c \sum_{k=1}^4 \Psi^k + \phi^m \Psi^m + W^{vol} = W^e + \sum_{k=1}^4 W^k + W^m + W^{vol}, \quad (3.34)$$

where collagen is modeled with four fiber families, which are oriented tangential to the wall, as shown in Figure 3.8. The first two fiber families point in axial and circumferential direction of the vessel. The last two fiber families are oriented diagonally to the first two directions.

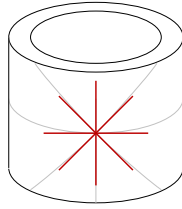


Figure 3.8: Fiber directions of an artery

The total density is the sum of the densities of the different constituents, i.e.

$$M = M^e + \sum_{k=1}^4 M^k + M^m. \quad (3.35)$$

Elastin has a half-life comparable to the lifespan of an animal. Thus, it normally does not grow and remodel during maturity. Whereas, collagen has a half-life between weeks and month (Langille [58]). Hence, it continuously turns over. Smooth muscle cells have a similar half-life as collagen. To model smooth muscle cells correctly, a passive and an active contribution have to be modeled. Since the time scale of growth is months, the active response of the muscle cells has to be averaged. In arteries, the muscle cells only have an influence in circumferential direction. Since the major goal of this work is to model growth of abdominal aortic aneurysms (AAAs) and their wall does not contain much smooth muscle cells (He and Roach [39]), smooth muscle cells are neglected in the following.

To get a better understanding of the model, the underlying processes are examined separately. First, remodeling is investigated in more detail, later it will be complemented with growth. In Figure 3.9 one can see a sketch of the process of remodeling for one collagen fiber family. The fiber family is represented by three fibers that are oriented in horizontal direction. In the undeformed geometry, all fibers have the same stretch λ_{pre}^c . This is the preferred stretch state of all collagen fibers and called *prestretch*. To show how remodeling works, the biological tissue is continually stretched in fiber direction. At time t_1 , one collagen fiber has been degraded and is replaced by a newly generated fiber. This new fiber is deposited at its preferred stretch. Hence,

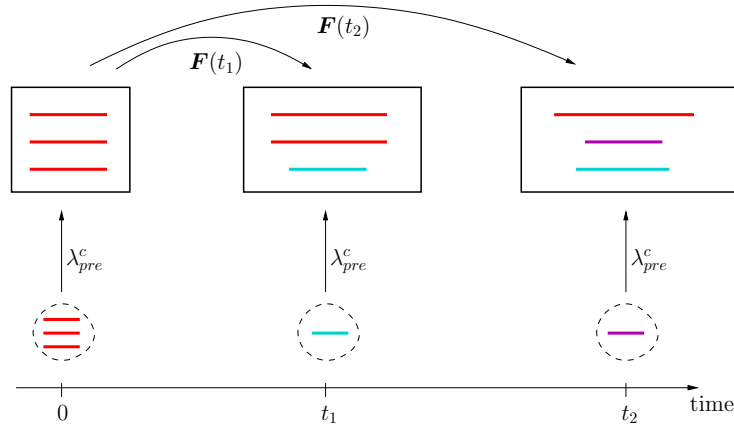


Figure 3.9: Sketch of remodeling of one collagen fiber family, — original collagen fibers, — newly produced fibers

it has a lower stretch than the old fibers. The direction of the new fiber is the same as the one of the old fibers. At time t_2 , the second fiber is replaced by a new one. The oldest fiber is stretched with the whole deformation of the body, the newest fiber is only prestretched and the middle aged fiber feels parts of the deformation. Thus, a variety of stretch states exist within one fiber family, if the tissue is continually deformed.

In the following, this process is described more generally, as shown in Figure 3.10. The prestretch of constituent i is defined by the prestretch tensor \mathbf{G}_h^i . For elastin it corresponds to an isotropic tensor $\mathbf{G}_h^e = \lambda_{pre}^e \mathbf{1}$. The collagen fibers are prestretched in fiber direction, i.e. $\mathbf{G}_h^k = \lambda_{pre}^k \mathbf{a}^k \otimes \mathbf{a}^k$. The stress free configuration $\kappa_n^i(\tau)$ of constituent i that is deposited at time τ is called *natural configuration*. This configuration is a pure virtual configuration, since the body never passes through this configuration.

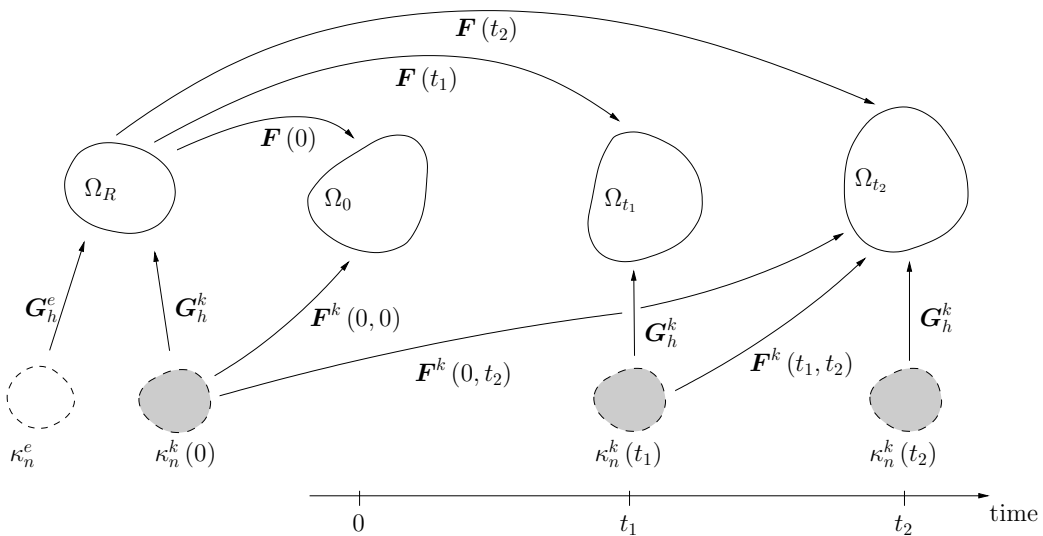


Figure 3.10: Remodeling: scheme of different configurations and kinematic quantities

In the beginning, elastin and collagen are directly deposited in the reference configuration Ω_R , which is identical to the prescribed geometry. Due to the prestretch of the constituents, the reference configuration is not stress free. Hence, it deforms. Together with the applied loads this leads to a second configuration, the so-called *initial loaded configuration* Ω_0 . When prestretch and load are balanced perfectly, reference and initial loaded configuration coincide, but most often they are slightly different.

Since elastin behaves like an elastic material, its deformation gradient is defined as $\mathbf{F}^e = \mathbf{F}(t) \mathbf{G}_h^e$. It follows for the SEF W^e that $W^e = \phi^e \Psi^e(\mathbf{F}(t) \mathbf{G}_h^e)$. The deformation of the collagen fiber deposited at time τ is defined as

$$\mathbf{F}^k(\tau, t) = \mathbf{F}(t) \mathbf{F}(\tau)^{-1} \mathbf{G}_h^k, \quad (3.36a)$$

$$\lambda^k(\tau, t) = \lambda^k(t) \lambda^k(\tau)^{-1} \lambda_{pre}^k. \quad (3.36b)$$

Hence, the SEF of this fiber only depends on this deformation, i.e. $\Psi^k = \Psi^k(\mathbf{F}^k(\tau, t)) = \Psi^k(\lambda^k(\tau, t))$. Since every fiber is potentially in a different stretch state, an integration over time has to be performed to get the total potential of the whole fiber family, i.e.

$$W^k(t) = \int_{-\infty}^t \frac{m_0^k}{\rho_0} q^k(\tau, t) \Psi^k(\mathbf{F}^k(\tau, t)) d\tau \quad (3.37)$$

with m_0^k denoting the *basal mass density production rate* and $q^k(\tau, t)$ the *survival function*. The basal mass density production rate can be computed from the total density of the fiber family, since during remodeling the density is constant. It follows

$$M^k(t) = \int_{-\infty}^t m_0^k q^k(\tau, t) d\tau = M^k(0) \quad \Rightarrow \quad m_0^k = \frac{M^k(0)}{\int_{-\infty}^t q^k(\tau, t) d\tau}. \quad (3.38)$$

The survival function $q^k(\tau, t)$ describes the amount of collagen produced at time τ that still exists at time t . At least three different forms of this function can be found in literature (cf. Humphrey and Rajagopal [46], Baek et al. [6], and Valentín et al. [103]) :

$$q_{lin}^k(\tau, t) = \begin{cases} 1 & \text{for } t - \tau \leq t_{lf}^{lin} \\ 0 & \text{for } t_{lf}^{lin} < t - \tau \end{cases}, \quad (3.39a)$$

$$q_{cos}^k(\tau, t) = \begin{cases} 1 & \text{for } t - \tau < 0.2 t_{lf}^{cos} \\ \frac{1}{2} \left[\cos \left(\frac{\pi}{0.8 t_{lf}^{cos}} (t - \tau - 0.2 t_{lf}^{cos}) \right) + 1 \right] & \text{for } 0.2 t_{lf}^{cos} \leq t - \tau \leq t_{lf}^{cos} \\ 0 & \text{for } t_{lf}^{cos} < t - \tau \end{cases}, \quad (3.39b)$$

$$q_{exp}^k(\tau, t) = \begin{cases} \exp \left(- \int_{\tau}^t \frac{\ln(2)}{t_{hl}^{exp}} d\tilde{\tau} \right) & \text{for } t - \tau \leq t_{lf}^{exp} \\ 0 & \text{for } t_{lf}^{exp} < t - \tau \end{cases} \quad (3.39c)$$

with t_{hl} denoting the half-life and t_{lf} the lifetime of collagen. These time values have to be chosen for each function such that the *mean age* $a_m^k = \int_0^{t_{lf}} q^k(0, \tilde{\tau}) d\tilde{\tau}$ of the collagen fiber

family is independent of the choice of the survival function. This leads to the following relations for lifetime and half-life of the different survival functions

$$\frac{t_{hl}^{\exp}}{\ln(2)} \left[\exp \left(-\frac{\ln(2)}{t_{hl}^{\exp}} t_{lf}^{\exp} \right) - 1 \right] = 0.6 t_{lf}^{\cos} = t_{lf}^{\text{lin}}. \quad (3.40)$$

With a half-life of 50 days and cutting off the exponential function after 300 days (Wilson et al. [110]) this leads to $t_{lf}^{\cos} = 118$ d and $t_{lf}^{\text{lin}} = 71$ d. In Figure 3.11 one can see the time course of $q^k(0, t)$ for these parameters. The linear (lin) survival function is the simplest choice. But it is not reasonable that all collagen fibers that were deposited at time τ are degraded at once. The cos function smooths this transition and is thus more reasonable. Most degradation processes in nature are described by an exponential function. Hence, this choice would be the most reasonable. But in this case, half of the collagen fibers are already degraded after 50 days, whereas the lifetime of the collagen fibers is up to 300 days. This means that a large amount of collagen is already degraded shortly after its production. Additionally, a lot of time steps have to be stored for this long period of time, since a small time step is not admissible, due to the steep decrease in the beginning. Hence, within this work the cos function is used when not stated otherwise.

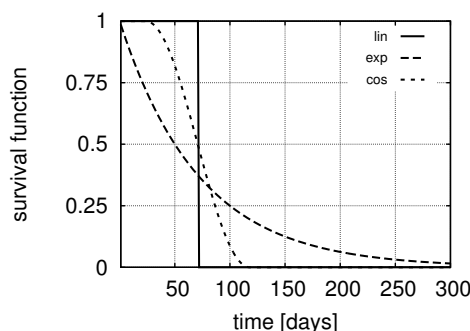


Figure 3.11: Different survival functions $q^k(0, t)$

Since the remodeling process has been fully described, the model is extended with growth. The mass of a collagen fiber family is no longer constant. That means the amount of newly produced collagen is not anymore the basal rate m_0^k , but a variable mass density production rate $m^k(\tau)$. The total density of one collagen fiber family has to be adapted as follows

$$M^k(t) = \int_{-\infty}^t m^k(\tau) q^k(\tau, t) d\tau. \quad (3.41)$$

The production rate is defined as

$$m^k(t) = m_0^k \left[1 + K_g^\sigma \left(\frac{\sigma^k(t)}{\sigma_h} - 1 \right) - K_g^\tau \left(\frac{\tau_w(t)}{\tau_{w;h}} - 1 \right) \right] \quad (3.42)$$

with σ^k denoting a scalar driving stress for growth, τ_w wall shear stress (WSS), σ_h and $\tau_{w;h}$ their homeostatic values, and K_g^σ and K_g^τ growth factors for the respective terms. For more details regarding WSS, the reader is referred to Appendix A.1. More details regarding the homeostatic

variables are given in Section 3.3.3. The density production rate has to be positive, since newly produced fibers cannot have a negative mass. A mass decrease is described with $m^k(t) < m_0^k$. For stability reasons it is sometimes useful to bound the density production rate, e.g. when stress peaks occur. Thus, the production rate $m^k(t)$ is restricted to the interval $[0, m_{max}^k]$. The scalar stress measure σ^k is evaluated in the current configuration. It is defined as the amount of the growth stress $\boldsymbol{\sigma}^g$ in fiber direction, yielding

$$\sigma^k(t) = \|\boldsymbol{\sigma}^g(t) \mathbf{a}^k\| = \frac{\|\mathbf{F} \mathbf{S}^g \mathbf{C} \mathbf{a}_0^k\|}{\lambda^k(t) \det(\mathbf{F})}, \quad (3.43)$$

where the second term describes σ^k in quantities defined in the reference configuration. The growth stress can be chosen as the total Cauchy stress $\boldsymbol{\sigma}$, the stress of the fiber family $\boldsymbol{\sigma}^k$ or the sum of the stress of elastin and collagen $\boldsymbol{\sigma}^e + \boldsymbol{\sigma}^c$, where the volumetric stress is omitted. Some hints about the choice of the growth stress can be found in Section 3.3.4. Inserting the variable mass production (3.42) into equation (3.37) leads to

$$W^k(t) = \int_{-\infty}^t \frac{m^k(\tau)}{\rho_0} q^k(\tau, t) \Psi^k(\mathbf{F}^k(\tau, t)) d\tau. \quad (3.44)$$

Growth occurs such that the density remains constant $\rho_0 = \rho$. That means the volume has to change relatively in the same amount as the mass changes. In the two dimensional growth model proposed by Humphrey, the membrane thickness is adapted during post processing (Baek et al. [6]). This is not possible in this fully three-dimensional model, the volume change has to be enforced differently. Since the volumetric potential (2.45) prescribes the volume change J , it has to be adapted. Since the mass change can be described with the change of the reference density, the adaptation is done in the following way

$$W^{vol}(t) = \frac{\kappa}{2} \left(J - \frac{M(t)}{M(0)} \right)^2 = \frac{\kappa}{2} \left(J - \frac{M(t)}{\rho_0} \right)^2. \quad (3.45)$$

With this last ingredient, the HFEF W of the mixture (3.34) is defined and a relation between stress and strain can be derived. Since the potential of the collagen fiber families (3.44) contains an integral over the history of the deformation, the HFEF cannot be written in the form $W = W(\mathbf{C}(\mathbf{h}), \mathbf{h})$. Hence, the constitutive law (3.7) derived in Section 3.1 cannot be applied. Thus, to get a relation for stress the Clausius-Planck inequality (3.5) has to be evaluated. The mass source (3.4) is defined through the time derivative of the density. Equations (3.35) and (3.41) lead to the following mass source

$$\mathcal{R}_0 = \frac{d}{dt} \left(\sum_{k=1}^4 \int_{-\infty}^t m^k(\tau) q^k(\tau, t) d\tau \right) = \sum_{k=1}^4 \left[m^k(t) + \int_{-\infty}^t m^k(\tau) \frac{\partial q^k(\tau, t)}{\partial t} d\tau \right], \quad (3.46)$$

where the first term represents the density production and the second term its degradation. The time derivative of the HFEF defined in equations (3.34), (3.44) and (3.45) is also required, it

reads

$$\begin{aligned} \dot{W} = & \frac{\partial W^e}{\partial \mathbf{C}(t)} : \dot{\mathbf{C}}(t) + \sum_{k=1}^4 \left[\frac{m^k(t)}{\rho_0} \Psi^k(\mathbf{F}^k(t, t)) + \int_{-\infty}^t \frac{m^k(\tau)}{\rho_0} \frac{\partial q^k(\tau, t)}{\partial t} \Psi^k(\mathbf{F}^k(\tau, t)) d\tau \right] \\ & + \sum_{k=1}^4 \left[\int_{-\infty}^t \frac{m^k(\tau)}{\rho_0} q^k(\tau, t) \frac{d\Psi^k(\mathbf{F}^k(\tau, t))}{d\mathbf{C}(t)} d\tau \right] : \dot{\mathbf{C}}(t) \\ & + \frac{\partial W^{vol}}{\partial \mathbf{C}(t)} : \dot{\mathbf{C}}(t) - \kappa \left(J - \frac{M(t)}{\rho_0} \right) \frac{\mathcal{R}_0}{\rho_0}. \end{aligned} \quad (3.47)$$

Inserting this equation into the Clausius-Planck inequality (3.5) and separating the terms with $\dot{\mathbf{C}}$ leads to the following stress-strain relation

$$\mathbf{S}(t) = 2 \left(\frac{\partial W^e}{\partial \mathbf{C}(t)} + \sum_{k=1}^4 \left[\int_{-\infty}^t \frac{m^k(\tau)}{\rho_0} q^k(\tau, t) \frac{d\Psi^k(\mathbf{F}^k(\tau, t))}{d\mathbf{C}(t)} d\tau \right] + \frac{\partial W^{vol}}{\partial \mathbf{C}(t)} \right). \quad (3.48)$$

How this integral can be evaluated is discussed in the following section. For the sake of completeness the extra entropy source \mathcal{S}_0 is also given

$$\begin{aligned} \mathcal{S}_0 = & -\frac{1}{TM} \sum_{k=1}^4 \left[\frac{m^k(t)}{\rho_0} \Psi^k(\mathbf{F}^k(t, t)) + \int_{-\infty}^t \frac{m^k(\tau)}{\rho_0} \frac{\partial q^k(\tau, t)}{\partial t} \Psi^k(\mathbf{F}^k(\tau, t)) d\tau \right] \\ & + \frac{1}{TM} \left(\frac{\mathcal{R}_0}{M} W + \kappa \left(J - \frac{M(t)}{\rho_0} \right) \frac{\mathcal{R}_0}{\rho_0} \right). \end{aligned} \quad (3.49)$$

3.3.2 Time discretization

In order to compute the stress, one has to evaluate equation (3.48). In the form given in the previous section, this is not possible, since the integral over time cannot be evaluated analytically. Hence, the integral is replaced by a numerical approximation, a quadrature formula. This approximation is done in two different ways: in an explicit and an implicit way, as depicted in Figure 3.12. These two possibilities are presented in the following sections.

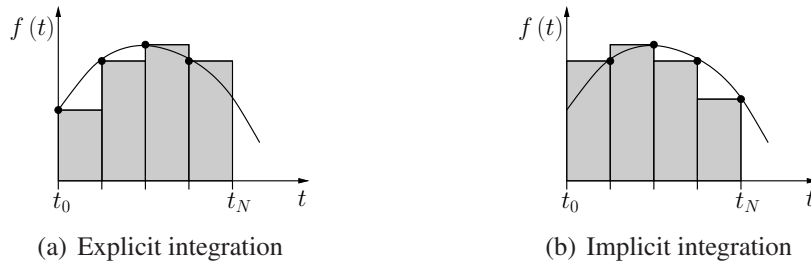


Figure 3.12: Schemes of numerical integration over time

3.3.2.1 Explicit integration

In this section, the so-called explicit integration is presented. Why it is called explicit can be seen later. Since $q^k(\tau, t)$ is zero for fibers older than t_{lf} , the infinite integral $\int_{-\infty}^t (\cdot) d\tau$ reduces to a finite integral $\int_{t-t_{lf}}^t (\cdot) d\tau$. The time interval $[t - t_{lf}, t]$ is split into N discrete intervals $[t_l, t_{l+1}[$ for $l = 0, \dots, N - 1$ with $t_0 = t - t_{lf}$ and $t_N = t$. On the discrete intervals, the function that is integrated, is approximated by a constant value. In case of the explicit integration the value at time t_l is chosen for the interval $[t_l, t_{l+1}[$, see Figure 3.12(a). The reference density of one collagen fiber family is computed by a sum over discrete time steps leading to

$$M^k(t) = \sum_{l=0}^{N-1} m^k(t_l) q^k(t_l, t) \Delta t_{l+1}, \quad (3.50)$$

where $\Delta t_{l+1} = t_{l+1} - t_l$ is the time step size. Since the previously computed time steps are used for the discrete times t_l , one does not need extra interpolation points. Just in the beginning N time steps have to be initialized. Normally, this is done with the homeostatic values and artificial time values t_l . During the simulation, a finite number of time steps has to be stored. To be precisely: for every Gauss point, $m^k(t_l)$ and $\mathbf{F}(t_l)$ have to be stored for each fiber family for N time steps to be able to compute the stress. The 2nd Piola-Kirchhoff stress is approximated in the same way as the density, yielding

$$\mathbf{S}^k(t) = 2 \sum_{l=0}^{N-1} \frac{m^k(t_l)}{\rho_0} q^k(t_l, t) \frac{\partial \Psi^k(I_4^k(t_l, t))}{\partial I_4^k(t_l, t)} \left(\frac{\lambda_{pre}^k}{\lambda^k(t_l)} \right)^2 \mathbf{A}_0^k \Delta t_{l+1}. \quad (3.51)$$

One possibility to memorize the history of the deformation would be to store the complete deformation gradient $\mathbf{F}(t_l)$. Since the deformation gradient is not symmetric, nine scalar values would have to be recorded for each time step. This is not necessary, since only the stress of the collagen fibers depends on the past deformation. Since the fourth invariant can be expressed in terms of the stretch in fiber direction, i.e. $I_4^k(t_l, t) = (\lambda_{pre}^k \lambda^k(t) / \lambda^k(t_l))^2$ it is sufficient to store just $\lambda^k(t_l)$. This leads to four scalar values contrary to the nine values for the deformation gradients. Hence, less storage is required. Since every summand in (3.51) depends through $\Psi^k(I_4^k(t_l, t))$ nonlinearly on the current deformation state, the summation can not be simplified. That means always N time steps have to be summed up. This can be very expensive, when e.g. small time step sizes are required or the exponential survival function is used. This way of integration is called explicit, since it can be evaluated directly at time t . The production rate $m^k(t)$ can be computed with equation (3.42). It does not influence $\mathbf{S}(t)$ as it is not included in the sum.

3.3.2.2 Implicit integration

In case of the implicit integration the value at time t_{l+1} instead of t_l is used to approximate the function in the interval $]t_l, t_{l+1}]$, see Figure 3.12(b). This leads to the following equations for the density and the stress

$$M^k(t) = \sum_{l=0}^{N-1} m^k(t_{l+1}) q^k(t_{l+1}, t) \Delta t_{l+1}, \quad (3.52)$$

$$\mathbf{S}^k(t) = 2 \sum_{l=0}^{N-1} \frac{m^k(t_{l+1})}{\rho_0} q^k(t_{l+1}, t) \frac{\partial \Psi^k(I_4^k(t_{l+1}, t))}{\partial I_4^k(t_{l+1}, t)} \left(\frac{\lambda_{pre}^k}{\lambda^k(t_{l+1})} \right)^2 \mathbf{A}_0^k \Delta t_{l+1}. \quad (3.53)$$

Now, the production rate $m^k(t)$ is part of the sum. It depends on $\mathbf{S}^k(t)$. Thus, equation (3.53) cannot be evaluated directly as in the explicit case. Additionally, the volumetric stress $\mathbf{S}^{vol}(t)$ also depends on $m^k(t)$ for $k = 1, \dots, 4$.

To get a shorter notation (t) is omitted in the following. The growth stress \mathbf{S}^g is a function of the mass production rates and can hence be expressed as follows

$$\mathbf{S}^g = \mathbf{g}(m^1, m^2, m^3, m^4) \stackrel{\text{e.g.}}{=} \mathbf{S}^e + \sum_{k=1}^4 \mathbf{S}^k + \mathbf{S}^{vol}. \quad (3.54)$$

Here, exemplary the function is given for the whole stress as growth stress. Similarly, the density production rate can be written as a function of stress leading to

$$m^k = f^k(\mathbf{S}^g) = m_0^k \left[1 + K_g^\sigma \left(\frac{\sigma^k(\mathbf{S}^g)}{\sigma_h} - 1 \right) - K_g^\tau \left(\frac{\tau_w}{\tau_{w;h}} - 1 \right) \right]. \quad (3.55)$$

All equations together, i.e. equations (3.54) and (3.55) lead to a system of nonlinear equations in \mathbf{S}^g and m^k , which reads

$$\begin{aligned} \mathbf{S}^g - \mathbf{g}(m^1, m^2, m^3, m^4) &= \mathbf{0} \\ m^1 - f^1(\mathbf{S}^g) &= 0 \\ m^2 - f^2(\mathbf{S}^g) &= 0 \\ m^3 - f^3(\mathbf{S}^g) &= 0 \\ m^4 - f^4(\mathbf{S}^g) &= 0. \end{aligned} \quad (3.56)$$

It is not reasonable to solve these equations together in a large nonlinear equation, since they have different units and orders of magnitude. In aortic tissue, the stresses are in the range of 10^5 Pa and the density production in the range of $10^{-3} \frac{\text{g}}{\text{mm}^3}$. The density production rate is a local quantity that is defined for each Gauss point. Thus, the density production rates are condensed out and only one independent variable \mathbf{S}^g and one equation remains. The equation is defined as

$$\mathbf{S}^g - \mathbf{g}(f^1(\mathbf{S}^g), f^2(\mathbf{S}^g), f^3(\mathbf{S}^g), f^4(\mathbf{S}^g)) = \mathbf{0}. \quad (3.57)$$

This nonlinear equation is solved with a local Newton iteration. That means the following linear equation is solved iteratively

$$\mathbf{S}^{g;i} - \mathbf{g}(\mathbf{S}^{g;i}) + \Delta \mathbf{S}^{g;i+1} - \left. \frac{d\mathbf{g}}{d\mathbf{S}^g} \right|_{\mathbf{S}^{g;i}} : \Delta \mathbf{S}^{g;i+1} = \mathbf{0}. \quad (3.58)$$

Hence, the following derivative is required

$$\frac{d\mathbf{g}}{d\mathbf{S}^g} = \sum_{k=1}^4 \frac{\partial \mathbf{g}}{\partial m^k} \frac{df^k}{d\mathbf{S}^g}. \quad (3.59)$$

The exact form of the derivatives on the right hand side are given in Appendix A.2.

To solve the linearized residuum (2.63) of the structural equations, the derivative of the stress with respect to \mathbf{C} is required, it defines the constitutive matrix $\mathbb{C} = 2 \, d\mathbf{S}/d\mathbf{C}$. The growth stress has to be treated specially as it depends on the density production rate that depends on the strain too. It follows for the growth constitutive tensor \mathbb{C}^g that

$$\mathbb{C}^g = 2 \frac{d\mathbf{S}^g}{d\mathbf{C}} = 2 \frac{\partial \mathbf{S}^g}{\partial \mathbf{C}} + 2 \sum_{k=1}^4 \frac{\partial \mathbf{S}^g}{\partial m^k} \left(\frac{\partial m^k}{\partial \mathbf{C}} + \frac{\partial m^k}{\partial \mathbf{S}^g} \frac{d\mathbf{S}^g}{d\mathbf{C}} \right). \quad (3.60)$$

Moving the last term of the right hand side to the left, a linear equation for \mathbb{C}^g arises. It reads

$$\left(\mathbb{I} - \sum_{k=1}^4 \frac{\partial \mathbf{S}^g}{\partial m^k} \frac{\partial m^k}{\partial \mathbf{S}^g} \right) \mathbb{C}^g = 2 \frac{\partial \mathbf{S}^g}{\partial \mathbf{C}} + 2 \sum_{k=1}^4 \frac{\partial \mathbf{S}^g}{\partial m^k} \frac{\partial m^k}{\partial \mathbf{C}} \quad (3.61)$$

with $\mathbb{I}_{ijn\alpha} = \frac{1}{2} (\delta_{in} \delta_{j\alpha} + \delta_{i\alpha} \delta_{jn})$. The derivative $2 \frac{\partial \mathbf{S}^g}{\partial \mathbf{C}}$ results in the normal constitutive matrix depending on the chosen potentials. The missing derivatives, like $\frac{\partial \mathbf{S}^g}{\partial m^k}$, $\frac{\partial m^k}{\partial \mathbf{S}^g}$, and $\frac{\partial m^k}{\partial \mathbf{C}}$, are given in Appendix A.2. The other parts of \mathbb{C} , like $2 \frac{d\mathbf{S}^e}{d\mathbf{C}}$, can be computed normally.

This way of integration is more complex than the explicit way. At each Gauss point, a local Newton iteration has to be solved. This local iteration can influence the convergence of the global iteration, since equation (3.57) is not fulfilled exactly. Especially close to the solution, when the error of the local iteration prohibits a higher accuracy of the global iteration. Since the results for both methods are nearly similar (the explicit integration reacts one time step later to changes in the surroundings), the explicit integration is used in the following.

3.3.3 Definition of homeostatic variables

Since the homeostatic state is the starting point for nearly all simulations that start with a healthy artery, it will be further examined in this section. In literature, it is often stated that the simulations start from the homeostatic state, but how it is achieved is not described in detail.

Patient-specific geometries stem from medical imaging. These geometries represent the prestressed current configuration. Hence, techniques have been developed to imprint these prestresses into the reference configuration (Gee et al. [27, 28]). In this model, a prestress is already introduced with the prestretch of the constituents. Thus, no special techniques have to be used to imprint it. Nonetheless, the reference configuration and the initial loaded configuration should be identical to represent the desired geometry. Therefore, homeostatic variables and geometric quantities like the thickness of the wall shall be chosen carefully.

To examine the homeostatic state, a thin walled cylinder with inner pressure is analyzed. To save computational time only one quarter of the cylinder is modeled with symmetric boundary conditions. In Figure 3.13(a) one can see a sketch of the geometry. The parameters used for the material laws and the growth model are summarized in Table 3.1. They are taken from Wilson et al. [110] of a 47 year old male patient, but the muscles cells are not modeled here. The cylinder is meshed with one element in radial direction, twelve elements in circumferential and eight elements in axial direction. As inner pressure a orthopressure of $P = 13.322 \text{ kPa}$ is applied to the current inner surface. This corresponds to a mean value of the diastolic and systolic pressure of a healthy patient. As one can see in Figure 3.13(b), the initial loaded configuration is quite close to the reference configuration. The maximal radial displacement is $u_r = 0.068 \text{ mm}$. In

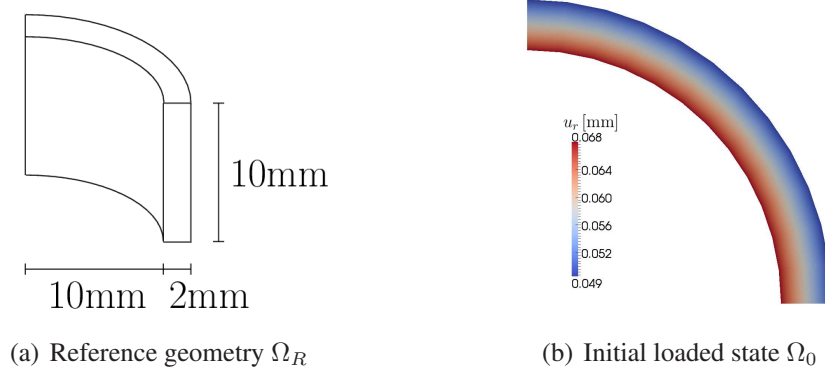


Figure 3.13: Reference and initial loaded configuration for a thin walled cylinder

Elastin	$\mu = 77.7 \text{ kPa}, \nu = 0.49, \phi^e = 0.3, \lambda_{pre}^e = 1.3$
Collagen	$k_1 = 917.175 \text{ kPa}, k_2 = 10.6, \phi^k = 0.1375, \lambda_{pre}^k = 1.05$
Volumetric	$\kappa = 10.0 \text{ MPa}$
Growth	$\rho_0 = 0.00105 \frac{\text{g}}{\text{mm}^3}, t_{lf} = 118.0 \text{ d}, \Delta t = 1.0 \text{ d}, \sigma_h = 66.61 \text{ kPa}, \boldsymbol{\sigma}^g = \boldsymbol{\sigma}$
Geometry	$R_i = 10.0 \text{ mm}, H = 2.0 \text{ mm}, L = 10.0 \text{ mm}$
Pressure	$P = 13.322 \text{ kPa}$

Table 3.1: Parameters for a healthy artery of a 47 year old male patient (Wilson et al. [110])

the following, it will be shown that theoretical considerations predict a higher deviation. For the example considered here the *Kesselformel* gives an approximation for the circumferential stress, yielding

$$\sigma_{cir} = \frac{PR_i}{H} \quad (3.62)$$

with R_i denoting the inner radius and H the wall thickness. For the given geometry, this leads to $\sigma_{cir} = 66.61 \text{ kPa}$. To get a better understanding how this value is distributed over the constituents, the stresses of the constituents are computed analytically in the reference configuration for the ideal case, i.e. $\mathbf{F}(0) = \mathbf{1}$. The volumetric stress is zero since $J = 1$. For elastin one gets $\boldsymbol{\sigma}^e = 39.39 \text{ kPa} \cdot \mathbf{1}$ and for a collagen fiber family $\boldsymbol{\sigma}^k \approx 31.86 \text{ kPa} \cdot \mathbf{A}_0^k$. Hence, the total stress in circumferential direction is $\sigma_{cir} \approx 116.3 \text{ kPa}$, which is much higher than the value that stems from the *Kesselformel*. If the corresponding inner pressure $P = 23.26 \text{ kPa}$ that is derived from the *Kesselformel* is applied to the vessel, even larger radial displacements ($u_r^{max} = 0.408 \text{ mm}$) arise. The question is where this difference stems from. The material is not an incompressible material, but a slightly compressible one. Hence, it leads to small variations in the volume, i.e. $J \approx 0.996$. Due to the high bulk modulus κ , see Table 3.1, this variation leads to a high volumetric stress of about $\sigma^{vol} \approx -39.84 \text{ kPa}$, what corresponds to the main part of the difference. This slight variation of the volume cannot be predicted. Due to the high influence of the volumetric stress, it is difficult to compute σ_{cir} in advance and thus, to define the proper thickness of the wall, when the inner radius is preset.

In the following, the effect of this small deviation between initial loaded and reference configuration is investigated. After the pressure is applied, growth and remodeling starts. It is expected that the model reacts and finds a steady state close to the original state. This is not true, as one can see in Figure 3.14 for different growth parameters. For high values of the growth factors, the simulation reaches a steady state, for low values, a steady state is not even achieved. In both cases, the results are slightly better when the shear stress term is included in the density production, since it controls the inner radius. The density changes most, when high growth factors for both terms in the density production are used. In this case, the inner radius changes the least. Overall, the model is not able to compensate quickly the variation between the two configurations.

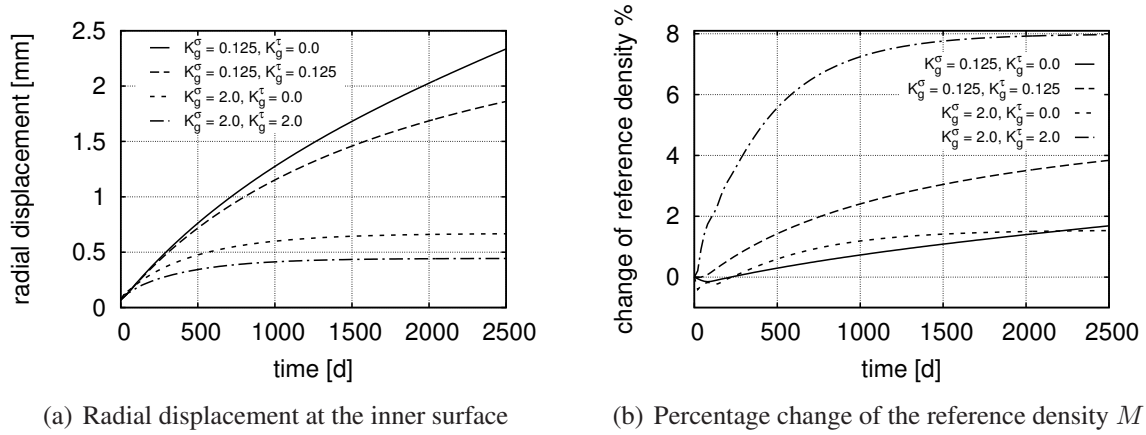


Figure 3.14: Time course of the radial displacements and the change of the reference density for different combinations of growth parameters

In the most cases, the homeostatic state is the starting point for further investigations, i.e. it should be simple and cheap to get. It is not feasible to perform a long simulation to get a steady state, before the actual simulation starts. Furthermore, one has no control of the geometry of the steady state. Thus, in the beginning of the simulation, a new prestretch and homeostatic stress are defined in order to get a stable homeostatic state. This is done in the following way

$$\lambda_{pre}^k := \lambda_{pre}^{k;old} \lambda^k(0) \quad \text{and} \quad \sigma_h^k := \sigma^k(0). \quad (3.63)$$

To get the same stress as before, the stretches at deposition time have to be adapted too, i.e. $\lambda^k(\tau) := \lambda^k(0)$. Moreover, the homeostatic inner radius, which is needed to compute the WSS is adapted to the initial radius. Altogether, that means that the collagen fibers are deposited with an adapted prestretch in the initial loaded configuration as sketched in Figure 3.15 contrary to the sketch in Figure 3.10, where they were deposited in the reference configuration. This methodology makes only sense, when initial loaded and reference configuration are close together. Otherwise the newly computed prestretches differ a lot from the original values and are not in a physiological range anymore. To guarantee that the initial loaded configuration matches the initial geometry, this approach can be combined with the modified updated Lagrangian formulation.

To get a better impression of the distribution of the homeostatic variables, a simulation with three elements in radial direction has been performed. In Figure 3.16(a) one can see the distribution of the circumferential prestretch over the radius. It decreases from the inner to the outer

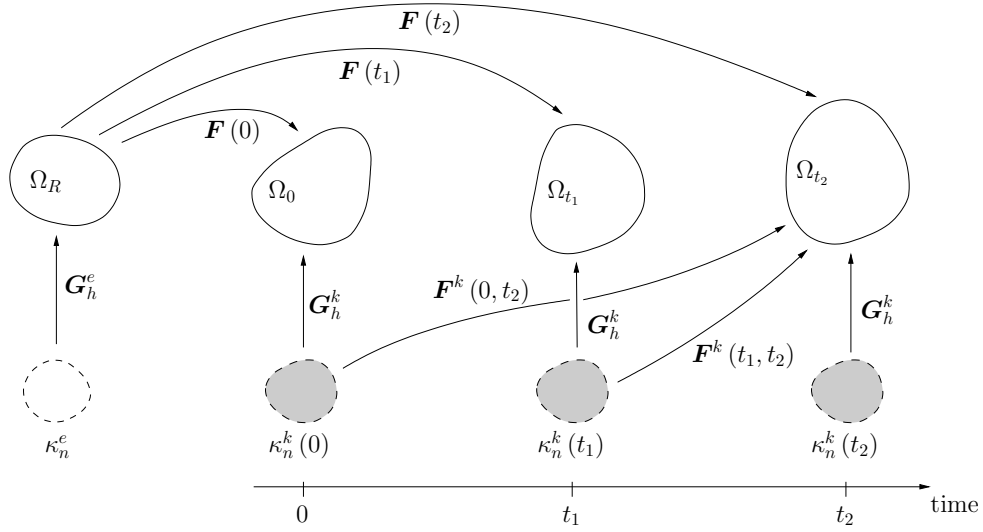


Figure 3.15: Different configurations and kinematic quantities after the adaptation of the homeostatic variables

surface. The homeostatic stress varies a lot over the radius, as shown in Figure 3.16(b). It decreases within an element, but the mean over each element increases with increasing radius. Since the elastin stress is nearly constant over the radius and the stress of the collagen fibers is defined through the prestretch, which does not oscillate, see Figure 3.16(a), the volumetric stress is the only portion of the growth stress that can generate this oscillation. The hexahedral elements have a trapezoidal shape due to the curvature of the cylinder. This distortion causes shear locking. Additionally, volumetric locking is present due to the nearly incompressible behavior of the tissue. Both locking effects mainly influences the volumetric stress. To circumvent locking, two element technologies are used, the Fbar method (de Souza Neto et al. [19]) and enhanced assumed strains (EAS, Zienkiewicz et al. [114]). As one can see in Figure 3.16(b) the variation

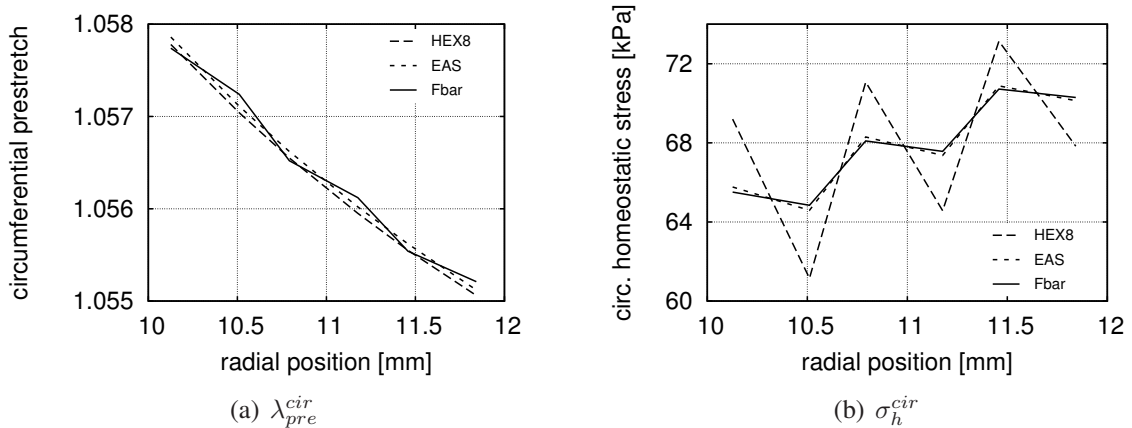


Figure 3.16: Variation over the radius of prestretch and homeostatic stress in circumferential direction

within an element gets better, but does not completely vanish. The Fbar method leads to small

oscillations in the prestretch, see Figure 3.16(a). Since the variations do not vanish and element technologies cannot always be applied, a growth stress that includes only the contributions of elastin and collagen was proposed in Section 3.3.1.

To test the stability of the homeostatic state, two different simulations have been performed. First the pressure is held constant for a long time, second the pressure is increased by a factor of 1.3 for a short time period and then reduced to its original value. With the constant pressure no alteration in the displacements can be seen after 10000 days. In Figure 3.17 one can see the results for an increase in pressure for one week. The growth model responds quickly to the disturbance and the collagen mass is increased. When the pressure decreases again, the mass still increases, but with a lower amount. After about 50 days the collagen mass decreases too. It takes long until the homeostatic state is restored, but the radial displacement as well as the reference density of the collagen fiber families converge to the homeostatic state. Thus, the stability of the homeostatic state is shown.

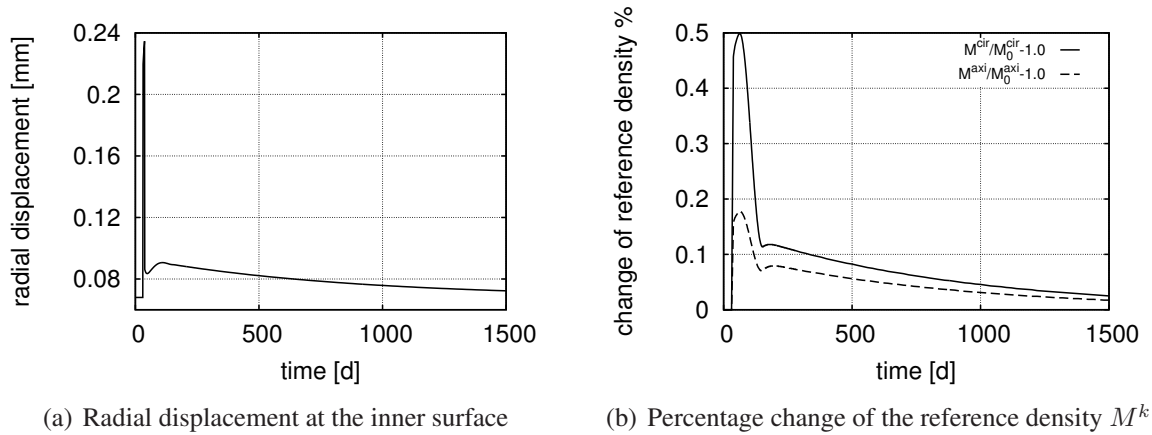


Figure 3.17: Radial displacements and change of the reference density of the axial and circumferential fiber families for a one week jump in pressure

To show the applicability to more complex geometries, a short patient-specific segment of the aorta is simulated. The thickness of the vessel wall is determined by the relation $H = \frac{PR_i}{\sigma_{cir}} \approx 0.2 R_i$, where the values of the straight cylinder have been inserted. In Figure 3.18(a) one can see the displacements after applying the inner pressure. The maximal value is 0.56 mm, the mean value of the nodal displacements is 0.14 mm. This is just a small deviation, since the inner radius is approximately 10 mm. In Figure 3.18(b) one can see the constant maximal displacement magnitude for a long period of time. This means the proposed definition of the homeostatic state is stable. In Figures 3.18(c)-(d) one can see the distribution of the new prestretch values of the circumferential and axial fibers. Their values are still in a physiological range.

3.3.4 Analytic solution of the steady state

Normally, the human body is in the healthy homeostatic state, but it can react to alterations of the environment. For example, patients with an elevated blood pressure have a thicker wall of the arteries (Matsumoto and Hayashi [70]). Thus, the body is able to react to changes and to maintain the resulting altered state. This state is a steady state and will be investigated in the

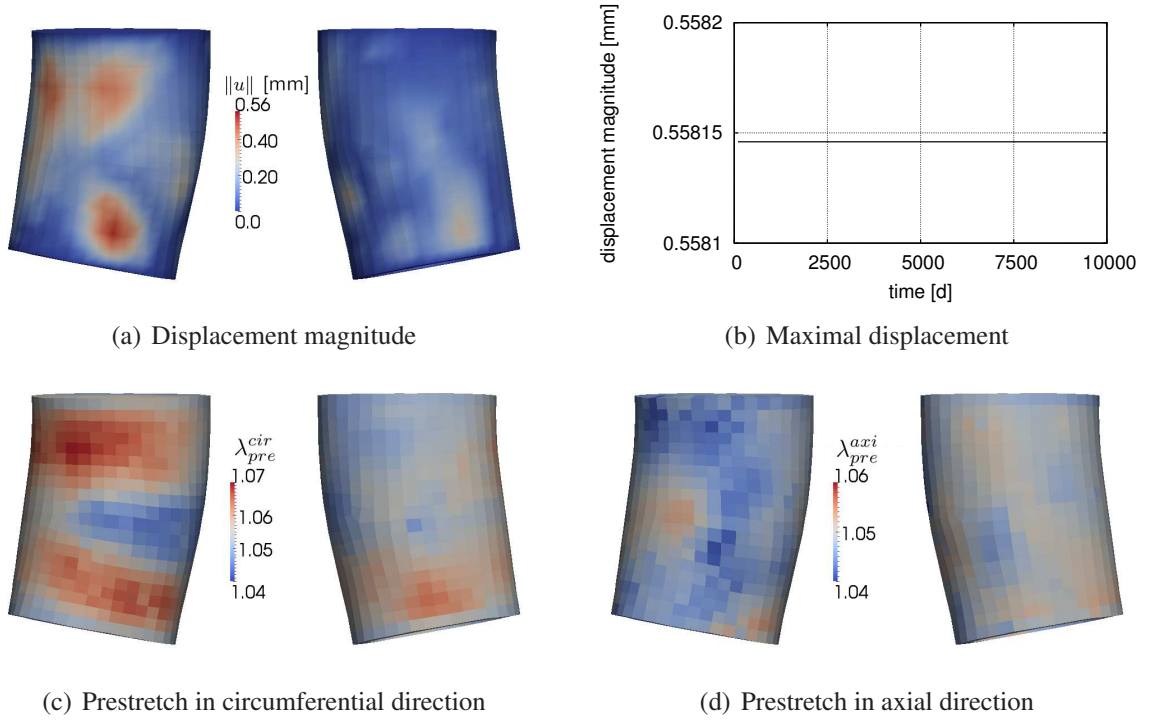


Figure 3.18: Radial displacements and prestretches for a patient-specific artery, view from two different sides

following. Therefore, an analytic solution is computed. To be able to do so, wall shear stress (WSS) is neglected. Furthermore, it is assumed that the volume change equals the mass change, i.e. the volumetric potential (3.45) is zero. Starting point of the considerations is the homeostatic state, which corresponds to the undeformed state. The homeostatic stress of one fiber family in fiber direction is with equations (2.48), (3.38), and (3.51) defined as

$$S_h^k = \phi^k (\lambda_{pre}^k)^2 2k_1 \left((\lambda_{pre}^k)^2 - 1 \right) e^{k_2 \left((\lambda_{pre}^k)^2 - 1 \right)^2}. \quad (3.64)$$

In a steady state the displacements are constant. Hence, the stretch in fiber direction is constant $\lambda^k(\tau) = \lambda^k(t) =: \lambda^k$. That means the actual stretch of the collagen fibers is their prestretch, i.e. $\lambda^k(\tau, t) = \lambda_{pre}^k$. Since the density production depends on the deformation, it is also constant, leading to

$$m^k(\tau) = m^k(t) = m_0^k \left[1 + K_g^\sigma \left(\frac{\sigma^k}{\sigma_h^k} - 1 \right) \right] \quad \forall \tau : q^k(\tau, t) \geq 0, \quad (3.65)$$

where σ^k is the constant scalar growth stress (3.43). It follows for the reference density of the collagen fiber family that

$$M^k(t) = m^k(t) \int_{-\infty}^t q^k(\tau, t) d\tau \stackrel{(3.38)}{=} \frac{m^k(t)}{m_0^k} M^k(0) \stackrel{(3.65)}{=} \left[1 + K_g^\sigma \left(\frac{\sigma^k}{\sigma_h^k} - 1 \right) \right] M^k(0). \quad (3.66)$$

Since the volume change is defined through the density change (3.45), it leads to the following equation for the determinant of the deformation gradient

$$J = \frac{M(t)}{M(0)} = \frac{\sum_{k=1}^4 (M^k(t) - M^k(0)) + M(0)}{M(0)} = 1 + \sum_{k=1}^4 K_g^\sigma \left(\frac{\sigma^k}{\sigma_h^k} - 1 \right) \phi^k. \quad (3.67)$$

The stress of the fiber family in the steady state can be expressed with the help of their homeostatic stress (3.64), yielding

$$\mathbf{S}^k = \frac{m^k(t)}{m_0^k} \frac{S_h^k}{(\lambda^k)^2} \mathbf{A}_0^k. \quad (3.68)$$

In order to determine the density production rate, one needs to define the growth stress σ^g . In the following, the different possibilities are presented.

Fiber stress as growth stress, i.e. $\sigma^g = \sigma^k$

As first growth stress, the stress of the fiber family itself is chosen. The homeostatic stress is defined by the fiber stress in fiber direction $\sigma_h^k = S_h^k$, as defined in equation (3.64). To compute σ^k the Cauchy stress of the fiber family is required, it reads

$$\boldsymbol{\sigma}^k = \frac{1}{J} \mathbf{F} \mathbf{S}^k \mathbf{F}^\top \stackrel{(3.68)}{=} \frac{\sigma_h^k}{J} \frac{m^k(t)}{m_0^k} \mathbf{A}^k, \quad (3.69)$$

where the relation $\|\mathbf{F} \mathbf{a}_0^k\| = \lambda^k$ and the definition of the fiber direction in Section 2.1.1 have been used. This yields the scalar growth stress σ^k that is defined in equation (3.43), as follows

$$\sigma^k = \|\boldsymbol{\sigma}^k \mathbf{a}^k\| = \frac{\sigma_h^k}{J} \frac{m^k(t)}{m_0^k} \stackrel{(3.65)}{=} \frac{\sigma_h^k}{J} \left[1 + K_g^\sigma \left(\frac{\sigma^k}{\sigma_h^k} - 1 \right) \right]. \quad (3.70)$$

Inserting equation (3.67) into equation (3.70) multiplied with J leads to a system of nonlinear equations in the following form

$$\left[1 + \sum_{k=1}^4 K_g^\sigma \left(\frac{\sigma^k}{\sigma_h^k} - 1 \right) \phi^k \right] \sigma^k = \sigma_h^k \left[1 + K_g^\sigma \left(\frac{\sigma^k}{\sigma_h^k} - 1 \right) \right] \text{ for } k = 1, \dots, 4. \quad (3.71)$$

The two solutions of this equations are

$$\sigma^k = \sigma_h^k \text{ for } k = 1, \dots, 4 \quad \text{and} \quad \sigma^k = \frac{K_g^\sigma - 1}{K_g^\sigma \phi^k} \sigma_h^k \text{ for } k = 1, \dots, 4. \quad (3.72)$$

For $K_g^\sigma \leq 1$ the second solution makes no sense, since $\sigma^k \leq 0$. Both solutions are independent of the applied forces, since ϕ^k , K_g^σ and σ_h^k are defined through the chosen parameters. Thus, the density, see equation (3.65), and therefore the volume in the steady state are independent of the applied boundary conditions. That means in the case of hypertension the final density and volume of the vessel wall are independent of the amount of increase of the blood pressure. The model predicts the same volume change of the vessel wall for patients with low hypertension and patients with high hypertension. The shape of the adapted vessel is different, since it is defined

through the elastic properties of the wall. But the vessel wall of the patient with the higher blood pressure should have a thicker wall and therefore a higher volume, than the one of the patient with the slightly elevated blood pressure. Hence, it is not reasonable to use only the stress of the fiber family as growth stress, when WSS is excluded.

Other growth stresses

For the other growth stresses, it is not possible to compute the value of σ^k generally, since the relations are more complex. Since elastin does not remodel, its Cauchy stress σ^e depends on the final deformation. Additionally, the volumetric Cauchy stress σ^{vol} depends in a complex way on J . These two stresses lead to additional summands in equation (3.70). Thus, the terms depending on the boundary conditions do not cancel out. Hence, the adapted volume depends on the boundary conditions.

To illustrate the obtained results, a simulation has been performed. The example of the previous section is used, see Figure 3.13(a) and Table 3.1. The lifetime of collagen has been reduced to $t_{lf} = 50$ d to get a faster convergence to the steady state. Once the pressure is increased by a factor of 1.05 and once it is decreased by a factor of 0.95. In Figure 3.19 one can see the resulting displacements and the change of the reference density for $\sigma^g = \sigma^k$ and $\sigma^g = \sigma$. The simulation with the elevated pressure and the total stress as growth stress has not reached a steady state after 1500 days of growth, all other simulations reach a steady state. The displacement is the highest, when the total stress is chosen as growth stress. When the fiber stress is chosen as growth stress, the reference density nearly converges to its original value. The difference to the original value stems from the fact that a numerical solution was computed, e.g. equation (3.67) is not fulfilled exactly. In the case of the total stress as growth stress, the density is increased when the pressure is increased and decreased when the pressure decreases. Thus, the volume of the steady state depends on the applied force.

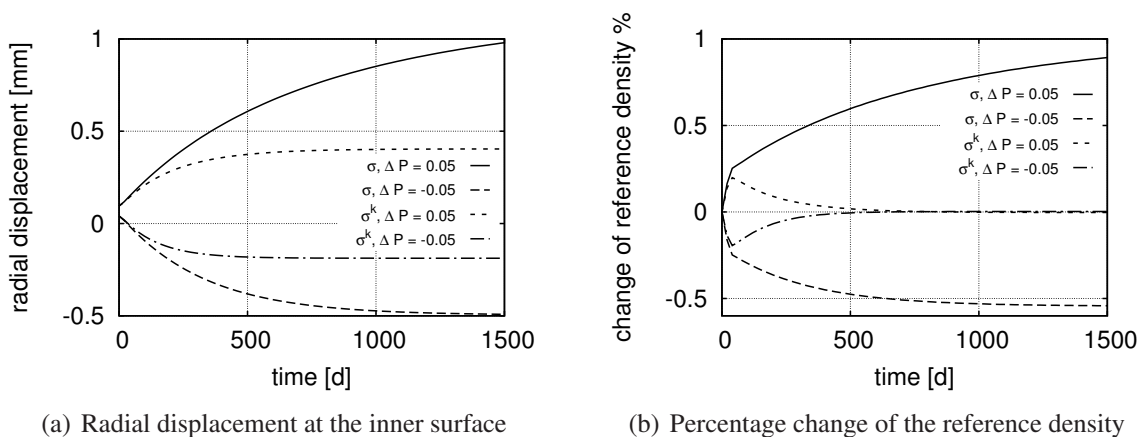


Figure 3.19: Radial displacements and change of the reference density after an increase and decrease of pressure

3.3.5 Hypertension

High blood pressure is a common disease. The arteries adapt to the altered pressure such that the inner radius is restored and the arterial wall gets thicker (Matsumoto and Hayashi [70], Fridez et al. [22]). In this section, hypertension of a thin walled cylinder is modeled. Again the same geometry as before, see Figure 3.13(a) and Table 3.1, is used. The mesh consists of 5 elements in radial direction, 24 elements in circumferential direction and 16 elements in axial direction. The pressure is increased by 30 percent. Since the segment of the artery is fixed in axial direction, the vessel cannot expand in this direction. Thus, the increase in volume only leads to expansion in the other directions and the grown tissue is compressed in axial direction. This leads to artificial negative volumetric stresses in the axial direction. Hence, the stress in axial direction is smaller than the homeostatic stress and will lead to degradation of the axial fibers, if the volumetric stress is included in the growth stress. Thus, the volumetric stress is excluded from the growth stress and only the stress of elastin and the collagen fibers is used, i.e. $\sigma^g = \sigma^e + \sigma^c$.

Since the pressure jump is large, the deformation is large too. Hence, the difference between fibers that are deposited before the pressure jump and the fibers that are deposited afterwards is significant. This effect has an influence on the results depending on the choice of the survival function. When the oldest fibers are degraded, the younger fibers have to carry the load. If this transition is too fast or discontinuous, it may affect the results. The exponential survival function smooths this out. For the other functions it is visible in the results, see Figure 3.20. The linear survival function leads to kinks after 70 d and 140 d of growth in the time course of the inner radius. For the cosine survival function one can see a small oscillation with a period of approximately 120 d. Since the exponential survival function does not show oscillations, it is used within this section.

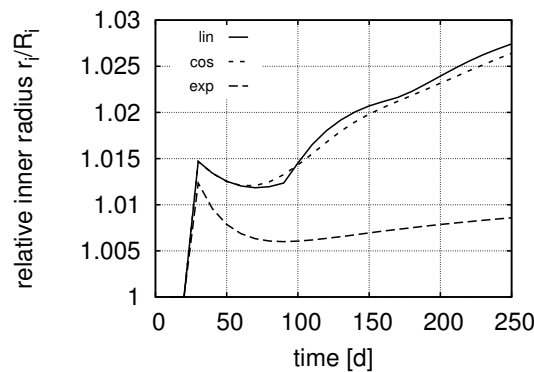


Figure 3.20: Time course of the relative inner radius for the cylinder with increased inner pressure for different survival functions, the growth factors are $K_g^\sigma = 3.0$ and $K_g^\tau = 5.0$

In Figure 3.21 one can see the evolution of the inner radius and the thickness of the vessel wall for different growth factors. At first, the inner radius decreases after the increase due to the pressure jump. Later, the inner radius increases again. For lower values of the growth factor K_g^σ for stress, growth cannot compensate the pressure jump and the inner radius increases nearly from the beginning. The radius increases again as more and more fibers that were deposited before the pressure jump are degraded. Recall that the half-life of collagen is chosen as 50 days. For all chosen parameters the thickness of the wall increases. For the highest value, it reaches a

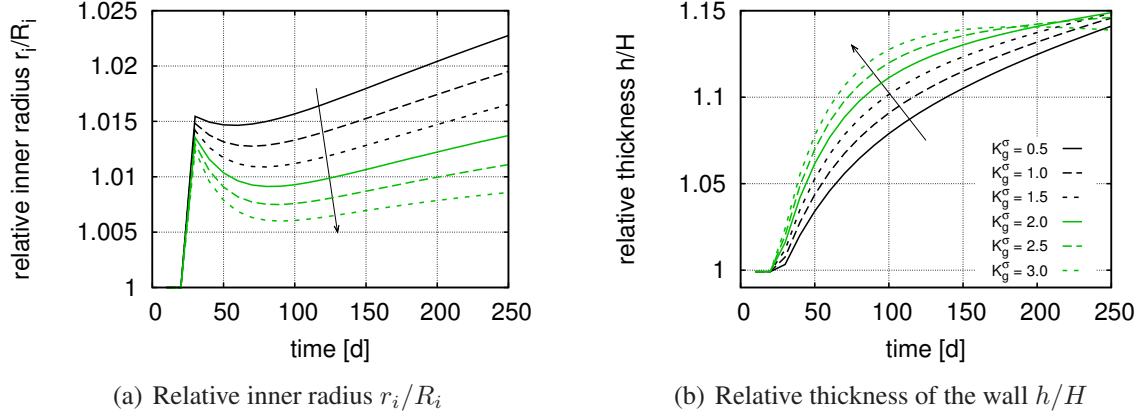


Figure 3.21: Evolution of the relative inner radius and the relative thickness of the cylinder with increased inner pressure for different growth factors for stress, the growth factor for WSS is fixed to $K_g^\tau = 5.0$

maximal value and slightly decreases afterwards. Compared to the observations in literature, the model can predict a thickening of the wall, whereas the inner radius is not completely restored.

3.3.6 Aging of an artery

To validate the implemented growth and remodeling model, it is compared to results in literature. In Valentín et al. [105], a three dimensional constraint mixture model is proposed. One example in this paper is aging of an artery. A cylinder consistent of two layers (media and adventitia) is modeled, see Figure 3.22 and Table 3.2. For simplicity only one element in axial direction is used and movement in axial direction is prohibited. The mesh consists of 49 elements in circumferential direction and 18 elements in radial direction.

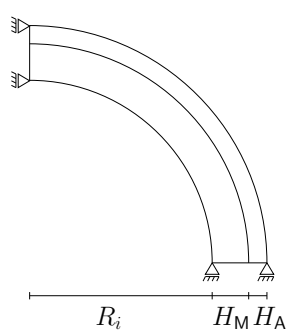


Figure 3.22: Geometry

Geometry	$R_i = 6.25 \text{ mm}$, $H_M = 0.6 \text{ mm}$, $H_A = 0.3 \text{ mm}$, $P = 12.399 \text{ kPa}$
Growth	$\rho_0 = 0.00105 \frac{\text{g}}{\text{mm}^3}$, $K_g^\sigma = K_g^\tau = 1.0$, $\sigma_h = 65.0 \text{ kPa}$, $\sigma^g = \sigma^k$, $t_{hl} = 70 \text{ d}$
Elastin	$\mu = 125 \text{ kPa}$, $\nu = 0.49$, $\lambda_{pre}^e = 1.3$
Collagen	$k_1 = 74.9 \text{ kPa}$, $k_2 = 20.0$, $\lambda_{pre}^k = 1.08$
Media	$\phi^e = 0.55$, $\phi^k = 0.25$, $\phi^m = 0.2$
	$k_1^m = 10.0 \text{ kPa}$, $k_2^m = 1.0$
Adventitia	$\phi^e = 0.05$, $\phi^k = 0.95$

Table 3.2: Material parameters of the arterial segment

During aging of arteries, elastin is degraded over time. Hence, the following relation $\mu(t) = \exp(-t \ln(2)/(14600 \text{ d})) \mu(0)$ is used for the elastin stiffness. This is a long term degradation. Thus, the adaptation is only small within month. In order to model the example, a variable

degradation of collagen fibers has been implemented. It reads

$$q_{\text{expvar}}^k(\tau, t) = \exp\left(-\int_{\tau}^t \hat{K}_q^k(\tilde{t}) d\tilde{t}\right) \quad (3.73)$$

with

$$\hat{K}_q^k(\tilde{t}) = \left(\left[\frac{\frac{\partial \Psi^k}{\partial \lambda^k}(\lambda^k(\tau, \tilde{t}))}{\frac{\partial \Psi^k}{\partial \lambda^k}(\lambda_{pre}^k)} - 1.0 \right]^2 + 1.0 \right) \frac{\ln(2)}{t_{hl}^{\text{exp}}}. \quad (3.74)$$

Thus, the total collagen mass can decrease even when the mass production is elevated. Additionally, a different dependency of the density production rate on the growth stress and WSS is used, leading to

$$m^k(t) = \frac{m_0^k}{2} \left[\chi\left(\frac{\sigma^k}{\sigma_h^k} - 1\right) + \chi\left(-\frac{\tau_w}{\tau_{w;h}} + 1\right) \right] \quad (3.75)$$

with

$$\chi(\cdot) = \begin{cases} 0 & \text{for } (\cdot) \in (-\infty, -\frac{\pi}{2K_g}) \\ \frac{1}{2} [1 + \cos(2K_g(\cdot))] & \text{for } (\cdot) \in [-\frac{\pi}{2K_g}, 0) \\ \frac{1}{2} [6.0 - 4.0 \cos(\frac{1}{2}K_g(\cdot))] & \text{for } (\cdot) \in [0, \frac{2\pi}{K_g}) \\ 5 & \text{for } (\cdot) \in [\frac{2\pi}{K_g}, \infty) \end{cases}. \quad (3.76)$$

In a small area close to the homeostatic values, the density production is nearly constant. That means that small deviations from the homeostatic state are not penalized. Within this example, the values are close to this area. Thus, the density production is only elevated marginally, as one can see in Figures 3.23(c)-(d).

In Figure 3.23(a) one can see the evolution of the change of the inner radius over time for two years of aging. The maximal value is about half of the value reported in Valentín et al. [105]. There are several explanations for this difference. First, the treatment of the smooth muscle cells is different, since within this work smooth muscle cells are excluded from growth and remodeling. Hence, they lead to an additional resistance to the widening of the artery. Second, in Valentín et al. [105] they use a split of the deformation gradient and a different volumetric potential, which also leads to differences.

The total mass decrease is so low that it cannot be seen in the volume, since the enforcement of the volume change through the volumetric potential is not exact enough. Hence, the volume change cannot be compared with the volume change of the reference solution in Valentín et al. [105]. Other quantities have to be compared with the volume change. The sum of the densities of all constituents gives no reasonable results, since the change in each density is very small and cancellations lead to errors within the summation. Thus, the density of the circumferential collagen fibers is examined. In Figure 3.23(b) one can see its decrease. The decrease is one order of magnitude lower than the local volume change in the reference solution. The reduction is the highest at the inner surface and decreases in outward direction. A jump occurs at the transition between Media and Adventitia, since the material properties are different there. The increase in collagen density production rates in circumferential and diagonal fiber direction, as shown in Figures 3.23(c)-(d), is also one order of magnitude lower. The jump between Media and Adventitia can be seen again. Also the decrease within each layer is visible.

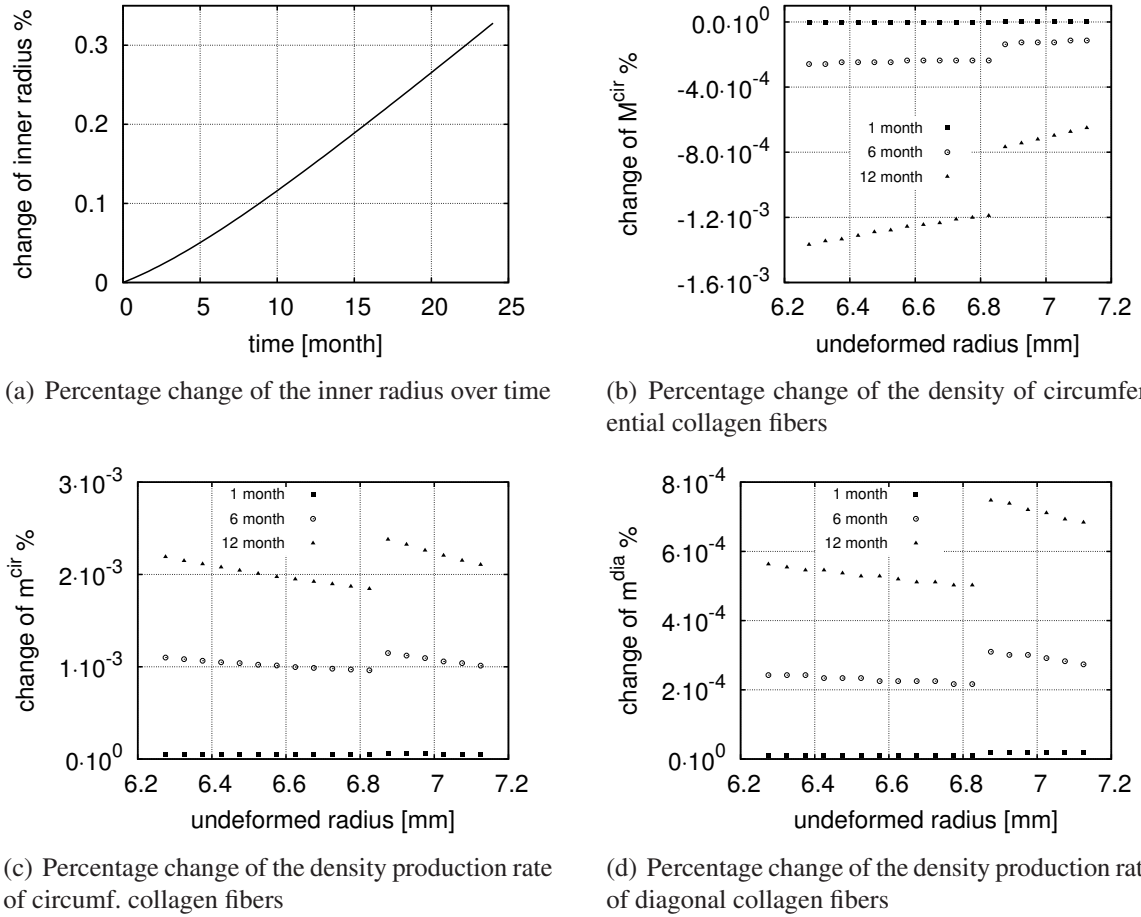


Figure 3.23: Time course of the inner radius, distribution of the change of density and density production rates over the radius at different times for aging of an artery

The values of the measured quantities are all too low compared to the results in literature (Valentín et al. [105]). But their trend can be reproduced, this means the results are qualitatively correct. The differences in the results stem from different model assumptions, as has been explained already.

3.3.7 Exemplary formation of an aneurysm

Degradation of elastin is often regarded as an initial step in AAA formation (He and Roach [39], Carmo et al. [15] and Sakalihan et al. [83]). In the following section, the ability of the constraint mixture model to reflect the genesis of an AAA is tested. Therefore, a long thin cylinder is used as a starting point. The cylinder has the same properties as given in Table 3.1, only the axial length is increased to 150 mm and κ is reduced to 1 MPa. As growth factor for the growth stress $K_g^\sigma = 1.0$ is used. To initiate growth of an aneurysm, elastin is degraded in some regions. That means the elastin stiffness μ is reduced as follows

$$\mu(\mathbf{X}) = \iota^e(\mathbf{X}) \mu_0, \quad (3.77)$$

where ι^e describes the *elastin content* and μ_0 the initial stiffness. In the first section, different forms of aneurysms are created, in the second section, one form is investigated in more detail, in the third section, the influence of the value of the growth factor on the development of the aneurysm is shown, and in the fourth section, a mesh study is performed.

3.3.7.1 Different forms

To investigate the influence of elastin degradation on the formation of an aneurysm, the elastin stiffness is reduced in certain regions to trigger the growth of an aneurysm. In Figure 3.24 one can see three different shapes of these regions. To smooth the transition, \cos functions have been used. The functions that define the degradation area only depend on the axial position z and the azimuthal angle ϕ . The exact definition of the degradation area can be found in Appendix A.3.

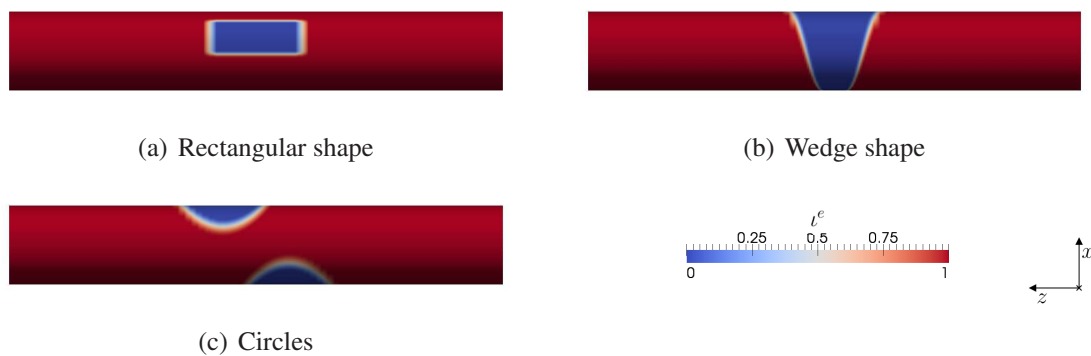


Figure 3.24: Different patterns of elastin content ι^e

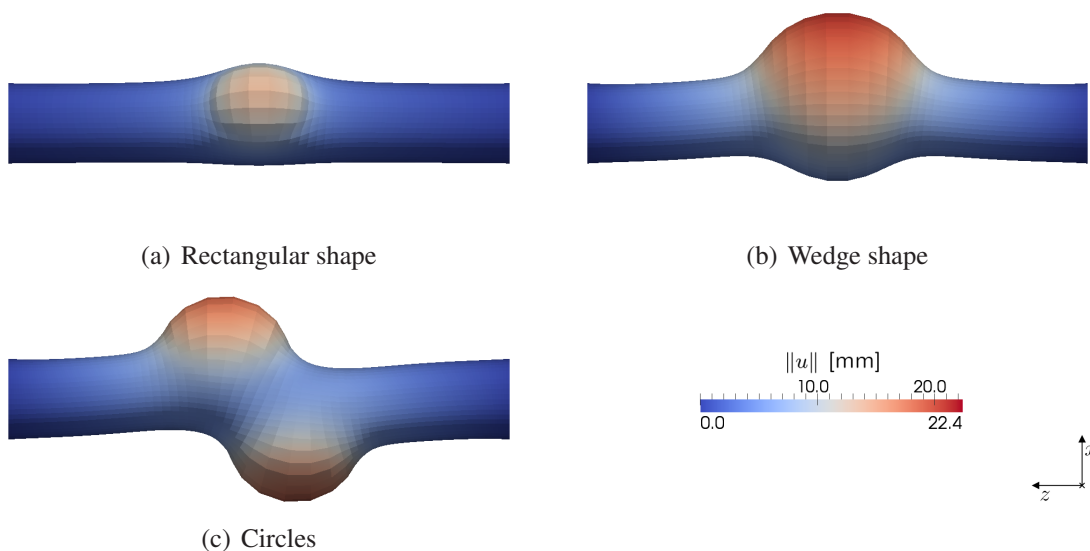


Figure 3.25: Resulting aneurysms after 7700 (rectangle), 3300 (wedge) and 4400 (circles) days of growth for different patterns of elastin content ι^e

All three shapes lead to a formation of an aneurysm. In Figure 3.25 one can see the resulting shapes of the aneurysms. It is obvious that the form of the elastin degradation influences the shape of the final aneurysm. The rectangle aneurysm results in a saccular aneurysm (cerebral aneurysm), whereas the wedge shape leads to a fusiform aneurysm (AAA). The healthy part of the artery is in all cases stable and the region, where the aneurysm bulges out, is close to the region, where the elastin has been degraded. The rectangular shape takes the longest to evolve an aneurysm, since the region of elastin damage is the smallest.

3.3.7.2 The rectangular shape in more detail

To get a deeper insight into the development of the aneurysms, the rectangular region is further investigated. When the elastin stiffness is decreased, the stress decreases too. Thus, the mass of the collagen fibers decreases, see Figure 3.26(b) and the wall gets thinner. This leads to a further weakening of the wall, it starts to bulge out. In the beginning, the wall is able to nearly compensate this effects, the increase in diameter is quite small, see Figure 3.26(a). When a certain threshold is reached, the aneurysm develops abruptly. The aneurysm wall gets very thin, as shown in Figure 3.27, since the mass increase is not high enough to compensate the expansion. This extreme thinning of the wall has not been observed in reality. The presented approach only models the turnover of the load bearing collagen fibers. Other processes occurring during the creation of an aneurysm, like inflammation, are not considered. Hence, the wall is artificially thinner.

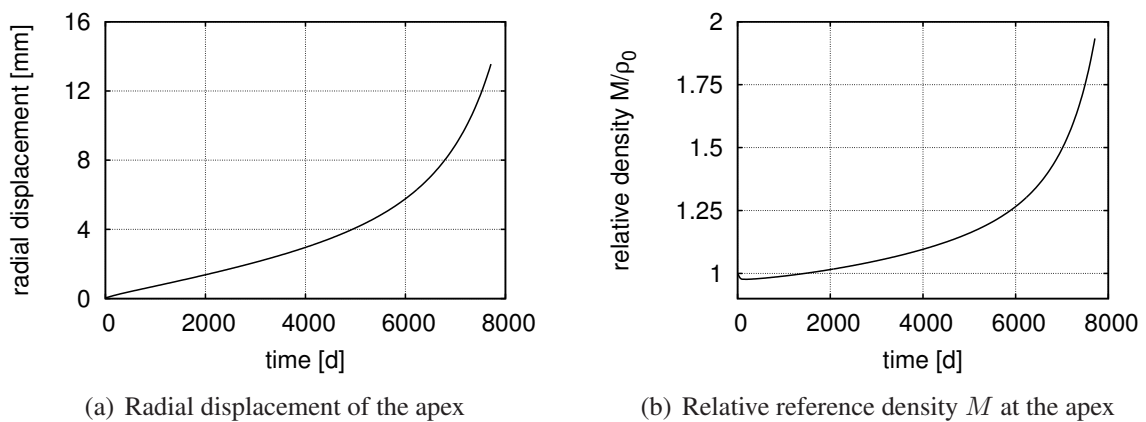


Figure 3.26: Evolution over time of the aneurysm for a rectangular degradation of elastin

To characterize the developed aneurysm despite the shape, the von Mises stress and the reference density are shown in Figure 3.28 for the final state. Both distributions are similar, the maximal value is located at the apex. The von Mises stress in the apex is approximately three times higher than the stress in the healthy part of the artery, as shown in Figure 3.28(a). The increase in the reference density is not as high, see Figure 3.28(b). It is defined through an integral over time over the stresses (see equations (3.35), (3.41), and (3.42)). Hence, the density change is defined by the average stress change over a fixed time interval and not only by the maximal value at the end time. Throughout the aneurysm sac, the reference density is elevated. Whereas in the healthy part, the density is slightly decreased.

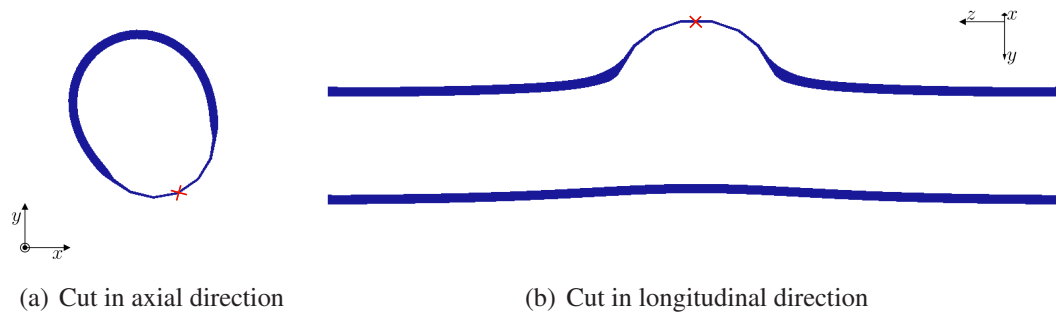


Figure 3.27: Slices of the developed aneurysm and position of the apex \times

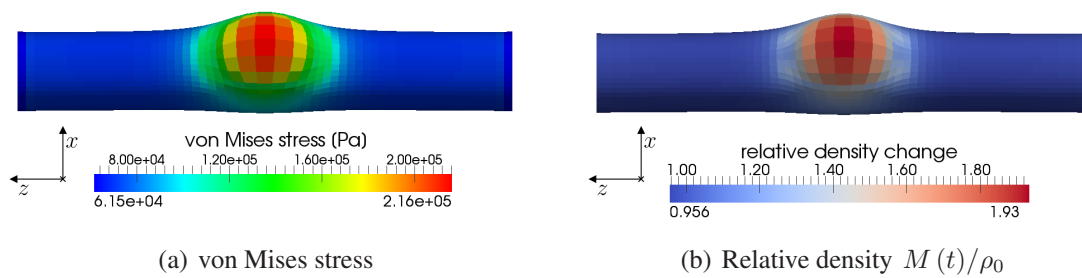


Figure 3.28: Distribution of von Mises stress and relative density $M(t)/\rho_0$ at the final state

To get a better insight into the effects leading to this density distribution, the relative densities of the different collagen fiber families are investigated separately in Figure 3.29. The final distributions of the relative densities of the different fiber directions are drawn over lines through the apex in axial direction in Figure 3.29(a), and in circumferential direction in Figure 3.29(b). The position of the degradation area is indicated with strokes at the x axis. Again the locality of the aneurysm is visible. There is a discontinuity at the border of the degradation area for all

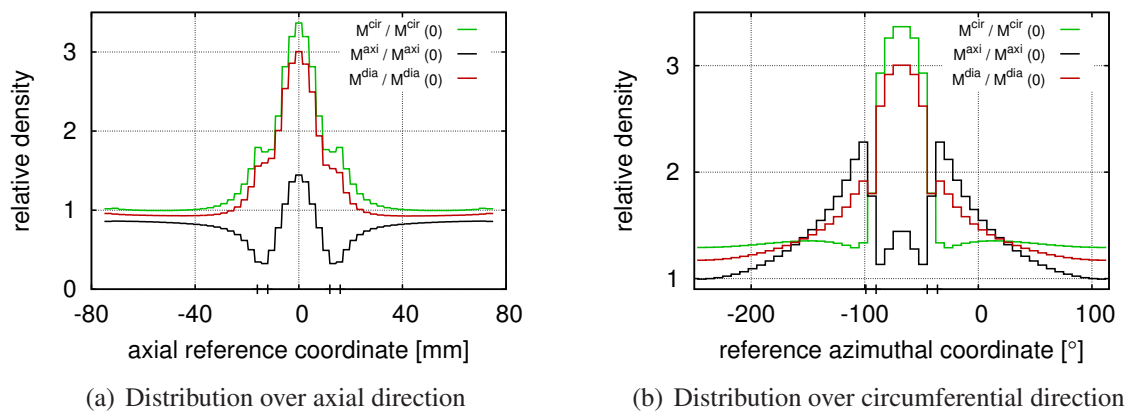


Figure 3.29: Distribution of relative fiber densities at the final state over lines through the apex in axial and circumferential direction

fiber directions. The fibers in axial direction behave different than the other fiber directions. The degradation of elastin is pronounced in axial direction. Hence, the distortion is distributed over a larger region. This leads to smaller stresses in the axial direction. Thus, the increase in mass is the smallest. The cylinder is fixed in axial direction at the boundary. This leads to compression in the healthy part and consequently to a decrease in mass. The maximal increase in density in the axial direction is next to the degradation. This effect stabilizes the healthy part, since the resistance is increased.

3.3.7.3 Influence of growth factors

The growth factor K_g^σ plays an important role in the mass production defined in equation (3.42). It determines how stress influences growth. To investigate the influence of the growth factor on the formation of an aneurysm, its value was varied within $[0.125, 1.5]$. Elastin has been degraded in the rectangular area. Higher values of the growth factor were not used, as numerical problems occurred. The transition at the border of the degradation was too abrupt and led to stability problems in this area. In Figure 3.30 one can see the resulting displacement and density time curves for four different values of the growth factor. The highest value of the growth factor did not lead to an aneurysm, since a thickening of the wall increased its stability, see Figure 3.31. In this case, the decrease of the density at the beginning is the highest.

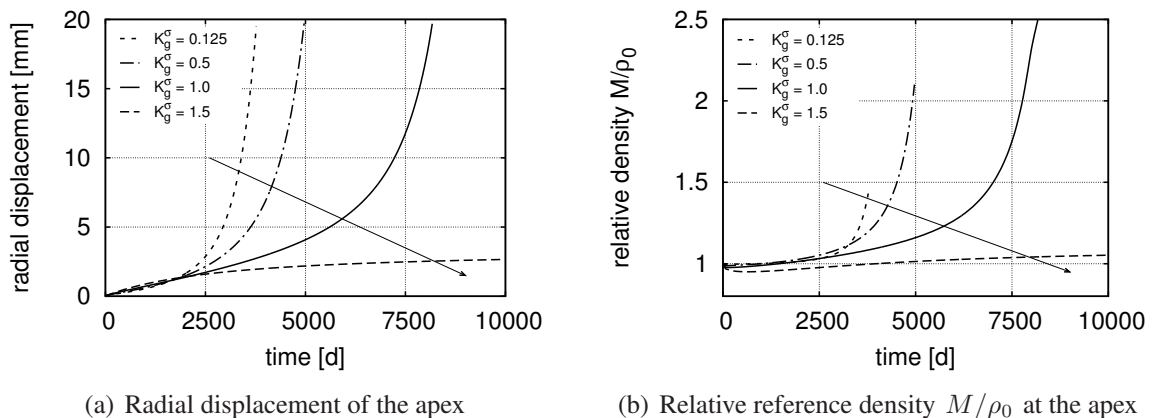


Figure 3.30: Evolution of important quantities of the aneurysm for different values of the growth factor, the arrow indicates increasing K_g^σ

The other simulations have been terminated, when the aneurysms had approximately the same size. The density increase is the smallest for the smallest K_g^σ . Thus, it has the thinnest wall, but all three aneurysms have a very thin wall, as shown in Figure 3.31. The locality of the aneurysm increases with increasing growth factor. The higher the growth factor the later an aneurysm evolves. When the aneurysm arises, the thickening of the wall cannot compensate the weakening of the wall that stems from remodeling. During enlargement the highly stretched older fibers are replaced by new fibers with less resistance, since they are deposited at their preferred stretch state. Hence, the resistance of the fibers decreases. With higher growth factors, the tissue adapts more to the changes in the environment. Thus, the point, where the mass increase cannot compensate the loss of the resistance, is later. Hence, it takes longer until an aneurysm evolves.

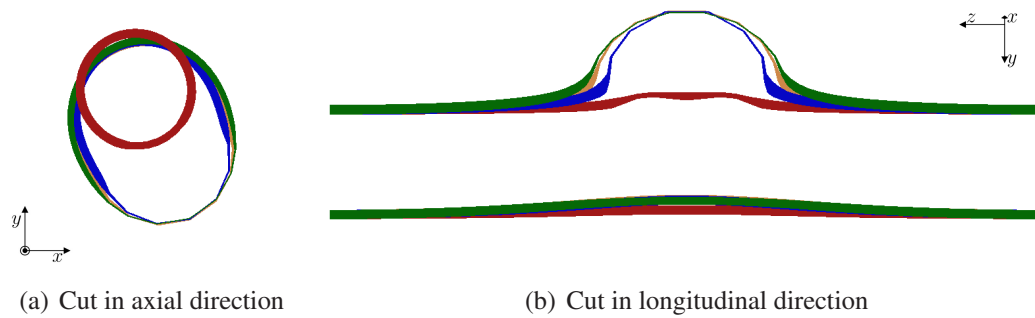
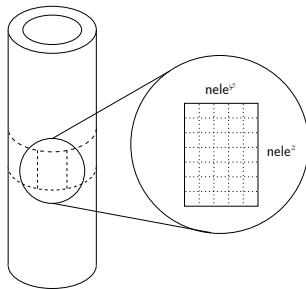


Figure 3.31: Slices of the developed aneurysm for different growth factors, green: $K_g^\sigma = 0.125$, orange: $K_g^\sigma = 0.5$, blue: $K_g^\sigma = 1.0$, and red: $K_g^\sigma = 1.5$

3.3.7.4 Mesh refinement

In this section, the influence of the mesh is investigated. since the diameter increases, the elements at the degradation zone are getting larger. Additionally, the thickness of the wall decreases. This leads to huge distorted elements at the end of the simulation. To get rid of these elements, either an adaptive mesh refinement can be performed or the mesh is very fine from the start of the simulation. The second approach is applied within this section. Therefore the number of elements was increased in the rectangular degradation area, as depicted in Figure 3.32. The exact number of elements in the refined area for the different meshes is listed in Table 3.3. In the other regions the mesh was adapted, but not as much refined. A smaller growth factor $K_g^\sigma = 0.125$ has been chosen to get a faster development of the aneurysm, since the simulation is quiet costly for the finer meshes (mesh 5 consists of approximately 90,000 elements).



	$nele^z$	$nele^\phi$
mesh 1	11	8
mesh 2	18	12
mesh 3	36	24
mesh 4	72	48
mesh 5	144	96

Figure 3.32: Area of mesh refinement Table 3.3: Number of elements in the refined region for the different meshes

In Figure 3.33 one can see the evolution of the radial displacement of the apex and in Table 3.4 the list of its final values for the different meshes. The coarse meshes lead to smaller aneurysms. This is reasonable, since locking is higher for these meshes. The difference increases with increasing time, since the distortion of the elements increases during the development of the aneurysm. The results converge to the solution of the finest mesh with increasing mesh size. The difference between the two finest meshes at the final shape is negligible (about 1.6 %).

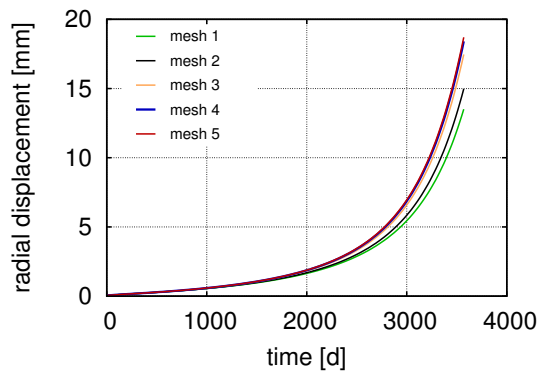


Figure 3.33: Evolution of the radial displacement at the apex

	u_r	rel. error
mesh 1	13.51 mm	-27.78%
mesh 2	14.98 mm	-19.92%
mesh 3	17.46 mm	-6.65%
mesh 4	18.41 mm	-1.58%
mesh 5	18.70 mm	-

Table 3.4: Final values of u_r for the different meshes

4 Inverse analysis

In this chapter, the method, which is used to determine the growth parameters, is introduced. First, the basic concept of the method is given. In the second part, a possible re-parameterization is presented.

4.1 Optimization algorithm

Optimization is a popular field of interest in mathematics. For a wide variety of problems, optimization algorithms exist, which are adapted to the needs of the particular problem (Haftka and Gürdal [35]). Within this work, optimal growth parameters \mathbf{p} are searched to be able to reproduce the growth process of an abdominal aortic aneurysm (AAA). Since the growth problem cannot be solved analytically, it is not possible to determine analytic derivatives of the objective function. Thus, the derivatives have to be approximated by *Finite Differences*. Since the computation of higher order derivatives with Finite Differences is expensive, the optimization algorithm should if at all require the gradient. The objective function π for the given problem can be written in the following form

$$\pi(\mathbf{p}) = \|\mathbf{u}^m - \mathbf{u}(\mathbf{p})\|^2 = \sum_{j=1}^{n_m} (u_j^m - u_j(\mathbf{p}))^2 = \mathbf{r}^T \mathbf{r}, \quad (4.1)$$

where \mathbf{u}^m are the measured displacements, $\mathbf{u}(\mathbf{p})$ the computed displacements for given parameters \mathbf{p} and \mathbf{r} the residuum. n_m is the number of measured quantities. The displacement vectors are composed of the displacements of the nodes of interest in directions of interest. That means not every node is evaluated and not all displacement components in a monitored node have to be measured. The choice of the objective function (4.1) leads to a *least squares* optimization problem as follows

$$\min_{\mathbf{p} \in \mathbb{R}^{n_p}} \pi(\mathbf{p}), \quad (4.2)$$

where n_p corresponds to the number of optimization parameters. For the existence of an unique optimal solution, it is necessary that the number of measured quantities is larger than the number of parameters, i.e. $n_m \geq n_p$. This condition is not sufficient. An efficient method to solve this type of problems is the *Levenberg-Marquardt algorithm*. An adapted version is implemented in BACI and has been used to fit material properties for lung parenchyma (Rausch et al. [79], Rausch [78], and Bel-Brunon et al. [10]).

4.1.1 Levenberg-Marquardt algorithm

The origin of this method goes back to Levenberg [61] and Marquardt [67]. It bears resemblance to Newton's method for solving a nonlinear equation. The optimal parameters are computed

iteratively, leading to

$$\mathbf{p}^{i+1} = \mathbf{p}^i + \Delta \mathbf{p}^{i+1}. \quad (4.3)$$

A formula for the increment can be derived from the linearization of the displacements with respect to the parameters, i.e. $\text{Lin } \mathbf{u} = \mathbf{u}(\mathbf{p}^i) + \mathbf{J} \Delta \mathbf{p}^{i+1}$, where \mathbf{J} is the Jacobian matrix of the displacements \mathbf{u} with respect to \mathbf{p} . This linearization is inserted into the objective function and leads in combination with an additional regularization to the following form of the increment

$$\Delta \mathbf{p}^{i+1} = [\mathbf{J}^\top \mathbf{J} + \mu \text{diag}(\mathbf{J}^\top \mathbf{J})]^{-1} \mathbf{J}^\top \mathbf{r}. \quad (4.4)$$

The scalar variable μ is a regularization factor, which is updated corresponding to the pseudo transient continuation method (Kelley et al. [53]). The Jacobian matrix can be approximated by a Finite Difference, yielding

$$J_{jl} = \frac{\partial u_j}{\partial p_l} \doteq \frac{u_j(\mathbf{p} + \boldsymbol{\varepsilon}^l) - u_j(\mathbf{p})}{\|\boldsymbol{\varepsilon}^l\|}, \quad (4.5)$$

where $\boldsymbol{\varepsilon}^l$ is a small perturbation of the following form $\varepsilon_k^l = \delta_{lk} \varepsilon$. This means for each optimization step, $n_p + 1$ forward simulation have to be computed. The $n_p + 1$ simulations are composed of one unperturbed and n_p perturbed simulations. These simulation can be computed parallel to each other, since the algorithm is implemented with nested parallelization. Hence, one optimization step takes the time of one forward simulation if enough resources are available. The optimization algorithm is terminated, when the error of the gradient is smaller than the prescribed tolerance ε , e.g. $\varepsilon = 10^{-5} \text{ mm}^2$. When no descent direction is found, the algorithm is stopped too.

4.1.2 Measured displacements

To be able to evaluate the objective function defined in equation (4.1), the measured displacements have to be computed at the nodes of interest. The measured displacements stem from computed tomography (CT) data of follow up scans. These two CT scans have to be mapped to each other to get a displacement field \mathbf{u} . To simplify this procedure, the CT images are converted to binary pictures. The new images only include the luminal volume that is colored white and the intraluminal thrombus (ILT) that is colored gray. The rest of the image is colored black. Based on these images a similar image registration as in Bel-Brunon et al. [10] is performed. For more details regarding image registration the reader is referred to Modersitzki [71] and Haber et al. [34]. The basic concept is introduced in the following.

In Figure 4.1 one can see one slice of the first CT scan, the *source image* I_S , that is mapped by ζ to one slice of the second scan, the *target image* I_T . To quantify the quality of the mapping, the following similarity measure is used

$$\mathcal{D}(\mathbf{u}) = \int_{\Omega} [I_S(\mathbf{x}) - I_T(\zeta(\mathbf{x}))]^2 dx \quad (4.6)$$

with $\zeta(\mathbf{x}) = \mathbf{x} + \mathbf{u}(\mathbf{x})$ and Ω the domain of the CT scans. The final displacement field \mathbf{u} is defined by a minimization problem in the following form

$$\min_{\mathbf{u} \in L^2(\Omega)} (\mathcal{D}(\mathbf{u}) + \alpha \mathcal{R}(\mathbf{u})) \quad (4.7)$$

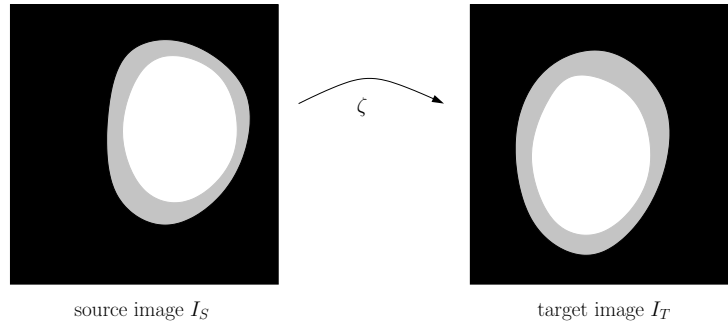


Figure 4.1: Mapping between the source image (left) and the target image (right)

with an elastic regularization $\mathcal{R}(\mathbf{u})$ (Modersitzki [71]) and a regularization parameter α . The elastic regularization is added to ensure the well-posedness of the optimization problem. The minimization problem is solved with a Gauss-Newton optimization scheme combined with a multiresolutional approach (Haber and Modersitzki [33]). The resulting displacement field \mathbf{u} is specified on the grid that is defined by the pixels of the CT images. Hence, it has to be interpolated to evaluate the measured displacements \mathbf{u}^m in the objective function (4.1) at the respective nodes.

4.2 Parameter distribution

To get a spatial distribution of the optimization parameters, they have to be parameterized. A discrete element wise description is too expensive with the Levenberg-Marquardt algorithm combined with Finite Differences. Thus, the parameter space is reduced. The parameterization should be applicable to complex geometries, since the optimization approach shall be used for patient-specific geometries. In the following sections, a method for the parameterization based on ideas from multigrid techniques is presented.

4.2.1 Definition of patches

In a first step, the geometry is divided into patches, on which a constant optimization parameter is prescribed. The following procedure to define patches is especially designed for tube like structures with a centerline. The structure is split into slices with cutting planes orthogonal to the centerline. Each slice can be cut into several patches in circumferential direction. In Figure 4.2 one can see twenty patches for the aneurysm that results from the wedge shaped degradation of elastin. The straight parts at the endings of the aneurysm are treated separately, since they represent a healthy region. This region is only of minor interest. Hence, the resolution of the optimization parameter is very low there. To get a relation between the constant optimization parameters \mathbf{p} on the patches and the discrete element wise parameters \mathbf{p}^{ele} , a *patch matrix* $\tilde{\mathbf{P}}$ is introduced. It is defined in the following way

$$\tilde{P}_{ij} = \begin{cases} 1 & \text{if element } i \text{ belongs to patch } j \\ 0 & \text{else} \end{cases} . \quad (4.8)$$

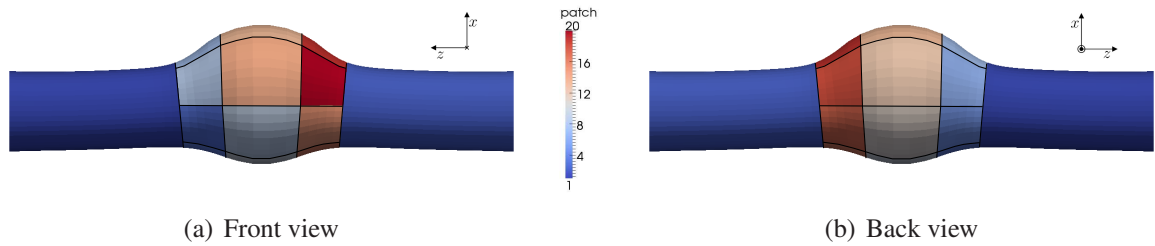


Figure 4.2: Possible patches for the aneurysm that is depicted in Figure 3.25(b)

The patch matrix fulfills the following condition $\sum_j \tilde{P}_{ij} = 1$. The relation between optimization parameters and element wise parameters is defined as follows

$$\mathbf{p}^{\text{ele}} = \tilde{\mathbf{P}} \mathbf{p}. \quad (4.9)$$

In the context of multigrid methods, the matrix $\tilde{\mathbf{P}}$ would be called a *prolongation operator*. This parameterization is discontinuous at the patch boundaries, jumps will occur there. This leads to artificial discontinuities in the stresses of the solution of the Finite Element problem and may also influence the convergence of the optimization algorithm. Thus, a smoothing technique is presented in the following section.

4.2.2 Smoothing of patches

To be able to smooth the jumps between elements, a graph of neighboring elements is build. Neighboring elements are defined in the following way: two elements are neighbors, if they share a node. The element graph contains only those elements, who are included in the optimization. In aneurysms for example the elements of the thrombus are excluded. As a positive side effect, this graph could be used to define patches with a partitioning algorithm from a third-party library like ParMETIS (Karypis and Kumar [51]). This library is already used in BACI for distributing the node graph over different processors. To smooth the transition between the patches, the *Laplacian matrix* \mathbf{A} (Mohar [72]), of the element graph is required. It is defined as

$$A_{ij} = \begin{cases} \deg(v_j) & \text{for } i = j \\ -1 & \text{if element } i \text{ is a neighbor of element } j, \\ 0 & \text{else} \end{cases}, \quad (4.10)$$

where $\deg(v_j)$ is the degree of the graph vertex v_j . In the special case here, it corresponds to the number of neighboring elements of element j . The Laplacian fulfills the condition $\sum_j A_{ij} = 0$ and is symmetric. To illustrate the presented quantities, a small two dimensional example is given in Figure 4.3. In the left picture one can see a mesh that consists of seven elements. The corresponding element graph is sketched in the middle. The Laplacian matrix is given on the right. As one can see, elements two and five are neighbors, even if they do not share an edge, since they share a node.

As smoothing technique the Jacobi method (Smith et al. [90]) is used. The smoothing matrix has the following form $(\mathbf{1} - \omega \mathbf{D}^{-1} \mathbf{A})$ with damping parameter $\omega = \frac{2}{3}$ and the diagonal matrix

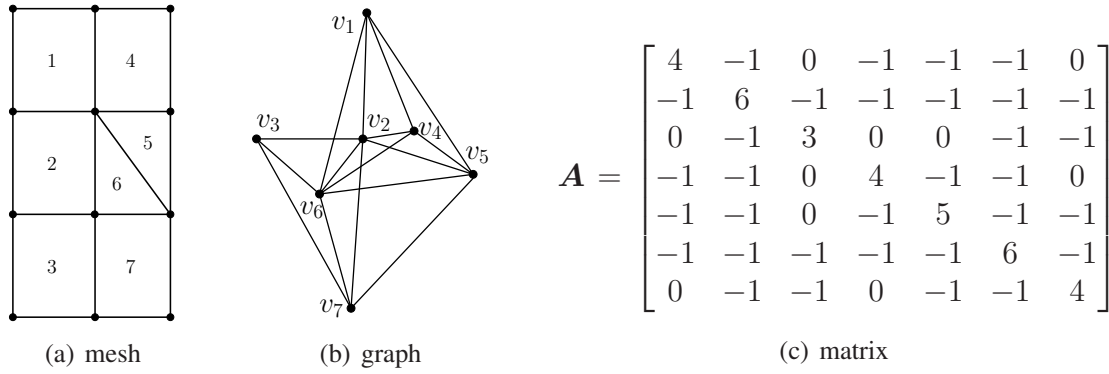


Figure 4.3: Example for the Laplacian matrix

$\mathbf{D} = \text{diag}(\mathbf{A})$. The damping parameter is fixed here for simplicity reasons, generally it can vary in the interval $]0, 2[$. Another choice could be $\omega = \frac{4}{3\lambda_{\max}(\mathbf{A})}$. In this case the maximal eigenvalue of \mathbf{A} is needed, which can be approximated for large matrices. The smoothing matrix can be applied several times (n_{smo}). The smoothed patch matrix \mathbf{P} is defined as

$$\mathbf{P} = \left[\prod_{n_{\text{smo}}} (1 - \omega \mathbf{D}^{-1} \mathbf{A}) \right] \tilde{\mathbf{P}}. \quad (4.11)$$

The sum of all elements of a row remains one ($\sum_j P_{ij} = 1$), since \mathbf{A} has a zero line sum. An additional feature is the preservation of the sum of each column $\sum_i P_{ij} = \sum_i \tilde{P}_{ij}$. That means the influence of each patch remains constant, if all elements are treated as equal to each other. The relation between element-wise and patch-wise parameters is defined as

$$\mathbf{p}^{\text{ele}} = \mathbf{P} \mathbf{p}. \quad (4.12)$$

In Figure 4.4 one can see the influence of the smoothing on a parameter distribution with four patches. If one smoothing step is applied, the parameters in one element row on each side of

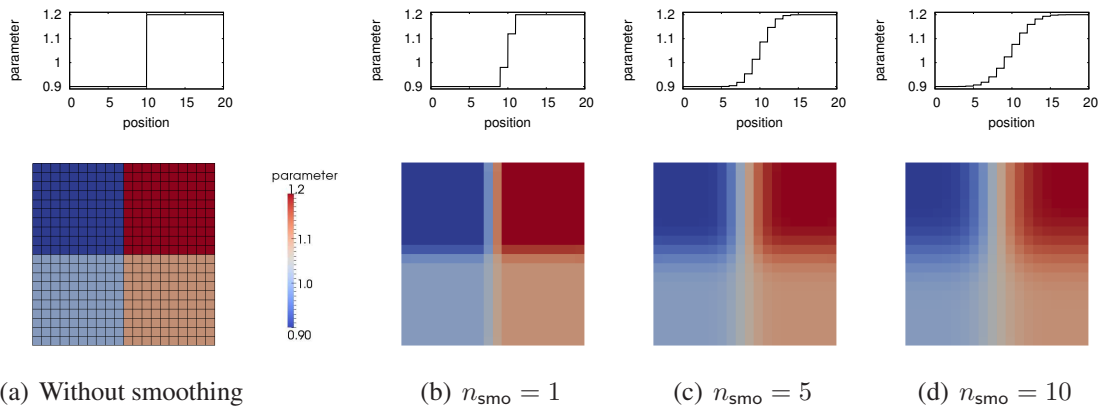


Figure 4.4: Influence of smoothing on the parameter distribution of a square with four patches, top row: plot over a line at the top of the square

the boundary are altered. With more smoothing steps, the influence of the parameters on the neighboring patches gets larger. After ten smoothing steps, the values in the corners are slightly altered, since each patch consists of ten elements in each direction. The values are further altered, when more smoothing steps are applied. Thus, the optimization parameter has a different value than all elements corresponding to its patch. In this case, the maximal (or minimal) value of the optimization parameters p is not identical to the maximal (or minimal) value of the element wise parameters p^{ele} . Hence, the number of smoothing steps has to be limited, when the extreme values shall be restored. If there are more patches, the limit of smoothing steps decreases even more, since there will be patches that are smoothed from two sides. Hence, the number of maximal smoothing steps reduces to half of the element number. The smoothing of the parameter between the patches is not linear, as can be seen in the top row of Figure 4.4.

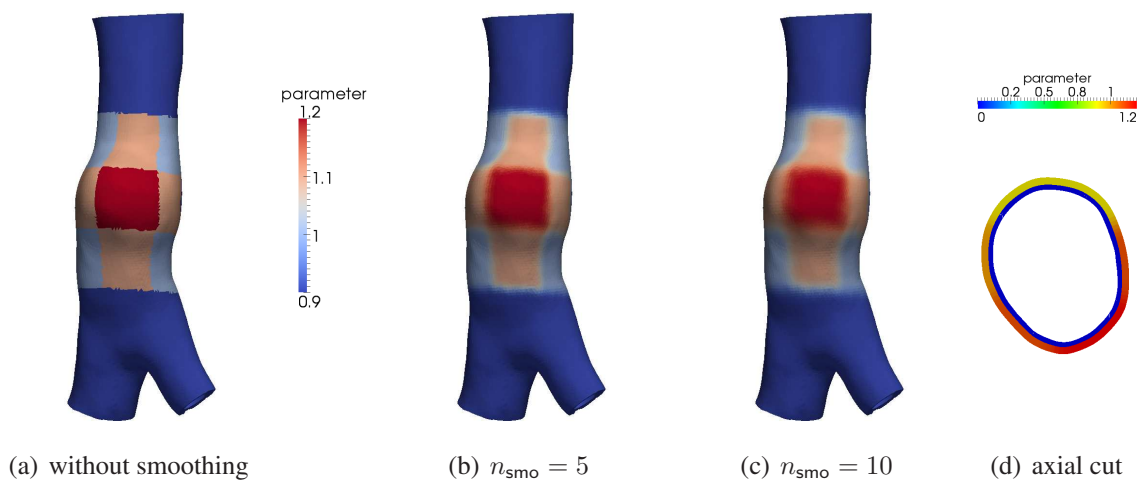


Figure 4.5: Influence of smoothing on the parameter distribution of a patient-specific aneurysm

In Figure 4.5 one can see the effect of smoothing for a patient-specific geometry. Thus, the presented method is applicable to complex geometries. The smoothing occurs only locally at the boundaries of the patches, in the rest of the patches the original value is restored. In Figure 4.5(d) one can see that the Thrombus (blue) is handled separately and does not influence the smoothing of the wall (yellow to red). Hence, a technique has been developed that is able to provide a spatial distribution of parameters with a reduced number of variables and that is applicable to patient-specific geometries.

5 Towards prediction of growth of an aneurysm

One aim of this work is to find a growth simulation that is able to reproduce the growth between two known states of an aneurysm. To develop a methodology to accomplish this goal, an academic setting is defined. It is well suited to validate the proposed framework, since the growth process is known. In the first section, the academic setting is introduced. In the second, an important configuration that is defined in the following section is investigated in more detail. Afterwards, the growth parameters are determined by inverse analysis. In the end, the predicted results are compared to the reference solution to quantify the error.

5.1 Academic setting

When elastin is degraded in a section of a straight cylinder, the formation of an aneurysm can be simulated (see Section 3.3.7). Hence, the complete process of the formation of this special aneurysm with the constraint mixture model is known. This knowledge is used to define the academic setting. It is called academic, since the simulation starts from a straight cylinder, which is only an idealized model of the geometry of an artery and because elastin is degraded in a well defined area.

To develop a suitable methodology to predict growth of an abdominal aortic aneurysm (AAA), elastin is degraded in a wedge shaped area, see Figure 3.24(b), since this led to the formation of a fusiform aneurysm, see Figure 3.25(b). The parameters listed in Table 3.1, an axial length of 150 mm, and a uniform growth factor $K_g^\sigma = 1$ are utilized for a growth and remodeling simulation starting at the homeostatic state that is described by a straight cylinder. This simulation is the reference simulation, which shall be reproduced.

The homeostatic variables λ_{pre}^k and σ_h^k have to be defined in advance. Hence, a preliminary simulation is performed. The pressure is applied to the inner surface of the cylinder and the homeostatic variables are computed as described in Section 3.3.3. To get rid of the effects of the fixation at the top and bottom of the cylinder, the values of the homeostatic variables that were computed in the middle of the cylinder are prescribed to the whole cylinder. Hence, the homeostatic variables are known for all following simulations.

In order to be as close to a more realistic setting as possible, three configurations are defined at important points in time: the flying start configuration, the intermediate configuration, and the predicted configuration. A sketch of the different configurations can be found in Figure 5.1. In the patient-specific case, two computed tomography (CT) scans of the developing aneurysm are known, as shown in Figure 1.3. To model the situation of the first CT scan, the simulation is stopped at time t_1 when an aneurysm has formed. This is the case after approximately eight years, i.e. $t_1 \approx 8$ y. The resulting geometry is called *flying start* configuration. It corresponds to

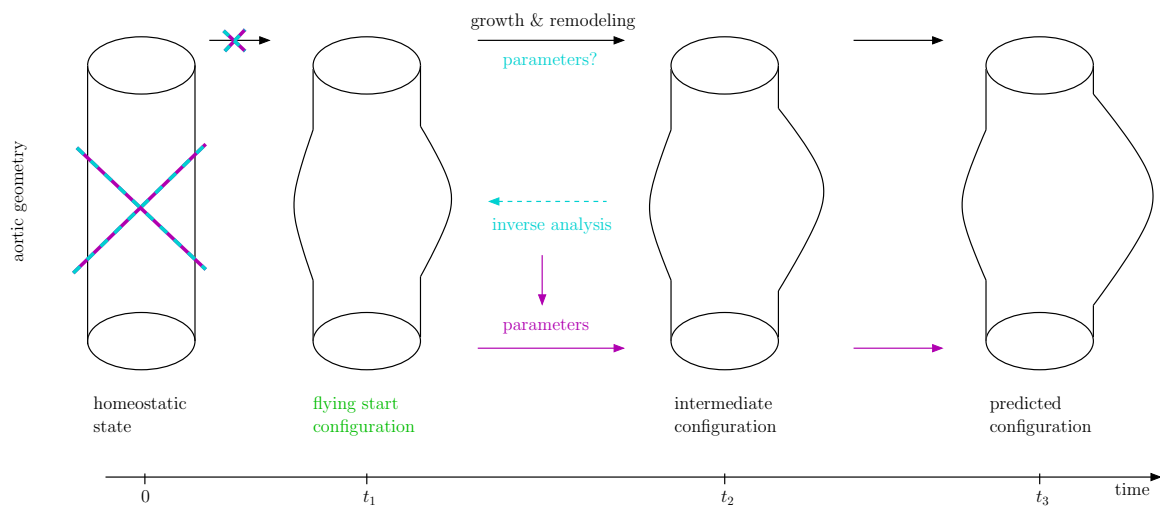


Figure 5.1: Scheme of the academic setting, three substantial steps are marked with colors: the altered flying start configuration (green), the inverse analysis of growth parameters (cyan), and the forward simulation to predict future growth (magenta)

the geometry created of the first CT scan. Hence, it will be the starting point of a new simulation that is used to reproduce the given growth process. Since the second CT scan is usually recorded one year after the first one, the simulation is again stopped at time $t_2 = t_1 + 1 \text{ y}$ to define the *intermediate* configuration. Finally, the *predicted* configuration is set at least another year later, depending how long one wants to look into the future ($t_3 = t_1 + 2 \text{ y}$).

These three configurations are defined by the reference simulation. Thus, the parameters of the growth model, e.g. growth factor, elastin content, and others, are known from the reference simulation. The history of the internal variables like collagen stretch and mass is also available. These quantities are unknown in a realistic setting, since the homeostatic state of a grown aneurysm as well as the growth parameters are not defined. Hence, when the flying start configuration is used as starting point for a new growth simulation, these quantities are unknown. Only the deformed geometry and the homeostatic variables from the forward simulation are utilized. Thus, the results of the simulation starting from the flying start configuration will differ from the results of the reference solution. Hence, the growth parameters, like growth factor K_g^σ and elastin content ι^e , have to be adapted to the altered situation to be able to reproduce the reference simulation. Since the influence of these parameters is only visible in the time course of the simulation, an inverse analysis is performed to determine them.

To determine growth parameters that are able to reproduce the reference solution, three different steps, which are shown in Figure 5.1, are conducted. The first step is to characterize the influence of the history of the internal variables on the growth process. This knowledge is then used to modify the history in the flying start configuration to be as close to the reference state as possible. Afterwards, the growth parameters will be inversely determined. The objective function is defined as the difference between the results from a simulation starting from the flying start configuration and the intermediate configuration of the reference simulation. The obtained growth parameters can be compared with the original chosen parameters to further quantify the influence of the flying start configuration. As last step the flying start configuration and the in-

versely determined parameters are used for a forward simulation to predict the future growth of the aneurysm. This grown configuration can then be compared to the original predicted configuration. This is only possible in the academic setting, since normally one does not know this state. The comparison is a good measure for the quality of the proposed framework and is used to validate it.

In order to compare the different simulations, the maximal diameters in x and y direction are examined. The diameters are defined by the difference of the x or y coordinates of the respective points marked in Figure 5.2. All points that are utilized are located on the outer surface of the aneurysm. These diameters are sensitive to changes in the growth process, since the deformation related to the growth process is large in the aneurysm sac. Additionally, the evolution of the diameter is a measure of the growth gradient. Hence, the diameters are a meaningful choice.

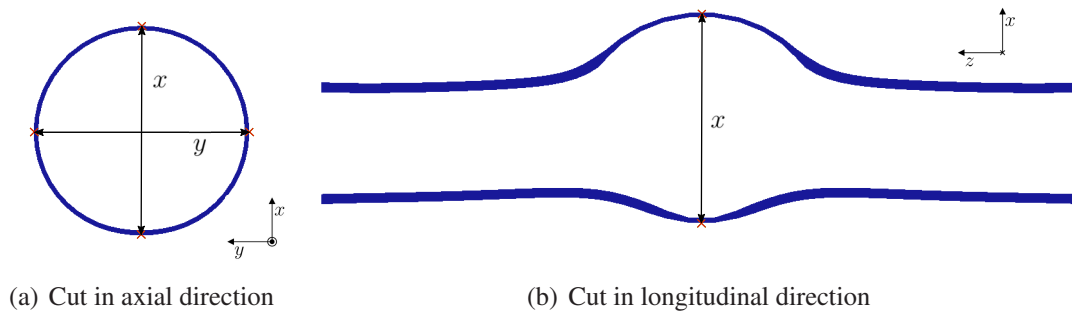


Figure 5.2: Slices of the flying start configuration, definition of the diameter in x and y direction

Remark: 5.1.1 *In the rest of the chapter the reference configuration Ω_R (see Section 2.1.1) is called material configuration to avoid confusions with the reference simulation.*

5.2 Flying start configuration

The flying start configuration plays an important role, since it is the starting point of the simulation that shall predict growth. Its geometry is defined by the deformed state of the reference solution at time t_1 . Since during the formation of the aneurysm, the wall gets very thin, see Figure 3.27, the thickness of the wall is taken over in the flying start configuration to exclude effects arising from a different wall thickness. A constant wall thickness gives completely different results. This information is not available in the patient-specific case. Hence, in this point the academic setting differs from the patient-specific case.

Since it is assumed that the history of the deformation, i.e. the mapping from the homeostatic state to the flying start configuration, is not known, differences compared to the reference simulation arise, when the simulation is started from the flying start configuration. These differences are discussed in the following section. The influence of the history variables is investigated in the second section. In the third section, methods to define an approximation of the history are introduced and their influence on the forward simulation of growth is examined.

5.2.1 Differences arising from the missing mapping to the homeostatic state at the flying start configuration

To get a better impression of the situation when the simulation is started from the flying start configuration without any modifications, the corresponding configurations and kinematic quantities are sketched in Figure 5.3. One important change compared to the case, which is shown in Figure 3.15, is the new material configuration $\tilde{\Omega}_R$ that is identical to Ω_{t_1} , since the deformation for $t < t_1$ is unknown. The quantities that change due to this new material configuration are marked with $\tilde{(\cdot)}$.

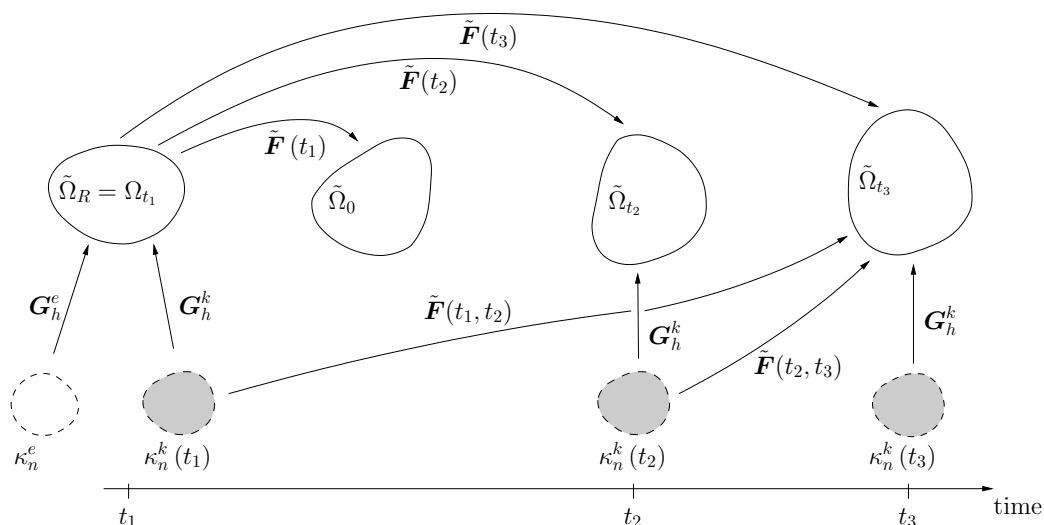


Figure 5.3: Scheme of different configurations and kinematic quantities after the simulation is started at the flying start configuration

In a first test, growth and remodeling is started without any special treatment. The deformed geometry of the reference solution at time t_1 is used as geometry for a new simulation. Hence, information about the past deformation is neglected and the history variables are fixed to the following values: $m^k(\tau) = m_0^k$ and $\lambda^k(\tau) = 1$ for $\tau \leq t_1$. The time interval $[t_1 - t_{lf}, t_1]$ is split into intervals of the length Δt to define distinct deposition times τ of the different fibers. The fiber directions are adapted to the new geometry. The elastin content $\iota^e = 1$ and the growth factor $K_g^\sigma = 1$ are assumed to be constant if not stated otherwise.

In Figure 5.4 one can see the evolution of the diameters over time. When the pressure is applied, the diameter is larger than the one of the original geometry. This reflects the neglect of the history of the deformation. Thus, the geometry already changes before growth starts. To get rid of the diameter change in the beginning, the modified updated Lagrangian formulation (MULF, Gee et al. [27, 28]) is used, while the pressure is applied. Hence, the displacements are zero in the beginning. It results in the green curve in Figure 5.4.

The slope of the black curve in Figure 5.4 is smaller than the one of the reference curve, which is shown in red. That means the growth gradient is too small. It seems that the wall is able to compensate more of the enlargement due to remodeling. Thus, the increase of the diameter is lower. When MULF is applied the slope decreases even more, but the growth problem starts from the exact geometry. The enlargement is too small in both simulations.

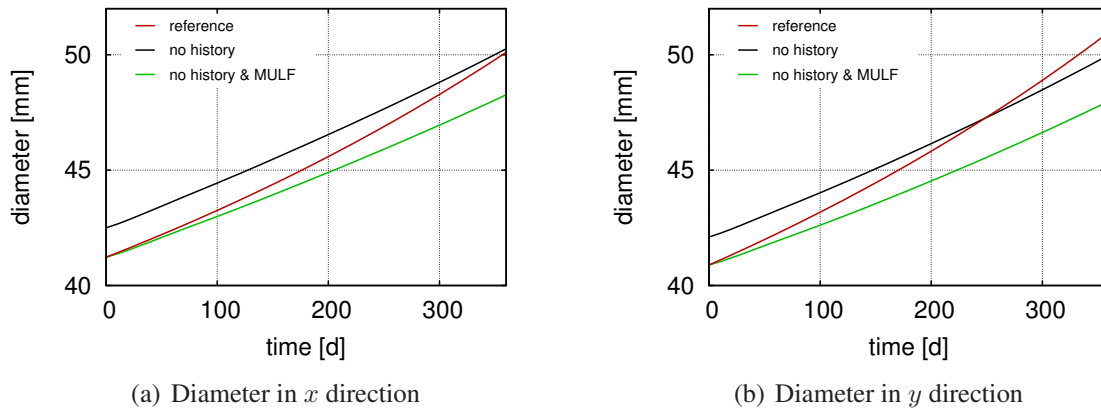


Figure 5.4: Evolution of diameters over time for a growing aneurysm that was started in the flying start configuration without an approximation of the history

In Figure 5.5 one can see slices of the deformed aneurysms in the intermediate configuration. In both cases the aneurysm sac translates in direction of the less damaged area in the bottom of the pictures. The simulation tends to straighten the healthy artery. It will be seen in the following sections that this translation is hard to correct. The resulting aneurysms of the restarted simulations have a slightly thicker wall, which is caused by the higher density production and the resulting lower enlargement of the aneurysm. The diameter change is underestimated in both cases. Summarizing, the neglected deformation in the flying start configuration has a large influence on the results of the growth problem. Thus, the flying start configuration has to be investigated in more detail.

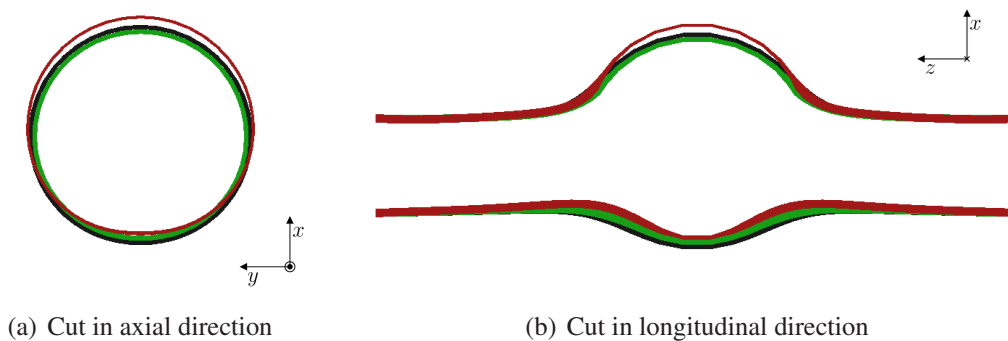


Figure 5.5: Slices of the intermediate configuration, red: reference solution, black: simulation starting from the flying start configuration, and green: MULF is used additionally

In the healthy part of the artery, elastin is not degraded and does not remodel. Hence, the complete deformation from the homeostatic state to the flying start configuration leads to stress in elastin. Since elastin is degraded in the sac of the aneurysm, the largest part of the deformation does not lead to stresses in elastin. Moreover, elastin does not influence the deformation there. In the other regions the deformation is small. Additionally, the stiffness of elastin is small com-

pared to the stiffness of the collagen fibers (see Table 3.1). Hence, its influence decreases even more. Thus, the effect of the past deformation on elastin is neglected in the following.

The fiber directions in the flying start configuration have to be newly defined, since those from the reference solution are defined for a straight cylinder. The original fiber direction transformed into the current configuration cannot be used, since it is assumed that the history of the deformation is not known. The axial and circumferential directions of the cylinder are projected tangentially to the outer surface of the deformed geometry. They coincide with the original axial and circumferential directions in the current configuration, since the principal axes of the deformation coincide with the axial and circumferential direction in the respective configuration. The diagonal fibers are oriented diagonally to these two newly defined fiber families. This assumption does not always lead to the original fiber directions, since the deformation in axial and circumferential direction may be different. Hence, the original diagonal fibers in the current configuration are oriented closer to the direction with the higher deformation. This effect is not further investigated, since its influence could not be quantified and a better approximation is not available.

When the simulation starts from the flying start configuration, the material configuration $\tilde{\Omega}_R$ is different than the material configuration Ω_R of the reference simulation. Hence, the densities that describe mass per reference volume are now defined with respect to a different configuration than before. In the following, this effect is further investigated.

To exclude other effects, it is assumed that only the densities are defined with respect to the new configuration and all other parameters are not affected. All quantities that are defined with respect to the new reference configuration are marked with $(\tilde{\cdot})$. For better illustration, a local volume increase is considered. Hence, the volume element dV in the old material configuration Ω_R is transformed into the volume element $d\tilde{V}$ in the new material configuration $\tilde{\Omega}_R$ with $dV < d\tilde{V}$. The density $\tilde{M}(t_1)$ is identical to the current density ρ and thus to the initial density ρ_0 , since the density remains constant during growth, i.e.

$$\tilde{M}(t_1) = \rho = \rho_0. \quad (5.1)$$

Since the simulation starts from the flying start configuration, a new basal mass production rate \tilde{m}_0^k is defined. It follows from (3.38) and (5.1) that it is identical to the original value, i.e.

$$\tilde{m}_0^k = \frac{\tilde{M}(t_1)}{a_m^k} = m_0^k, \quad (5.2)$$

but it is defined with respect to a different volume. The basal density production rate was originally defined such that the reference density, and hence the mass, remains constant during remodeling (3.38). That means for the special case here, the newly defined basal rate is defined such that it restores the locally increased mass during remodeling. It follows that the local mass production rate that is related to the basal density production rate is higher, yielding

$$\tilde{m}_0^k d\tilde{V} > m_0^k dV. \quad (5.3)$$

The new definition of the basal rate \tilde{m}_0^k influences the density production rate $\tilde{m}^k(t_1)$ that is defined as follows

$$\tilde{m}^k(t_1) = \tilde{m}_0^k \left[1 + \tilde{K}_g^\sigma \left(\frac{\tilde{\sigma}^k(t_1)}{\sigma_h^k} - 1 \right) \right], \quad (5.4)$$

where \tilde{K}_g^σ denotes an adapted growth factor. Since it was assumed that only the densities are affected by the restart, the growth stress $\tilde{\sigma}^k(t_1)$ that is defined in the current configuration has the same value as before, i.e. $\tilde{\sigma}^k(t_1) = \sigma^k(t_1)$. The local mass increase should be independent of the choice of the reference configuration, yielding

$$\tilde{m}^k(t_1) d\tilde{V} \stackrel{!}{=} m^k(t_1) dV. \quad (5.5)$$

From the definition of the density production rates, equations (3.42) and (5.4), it follows from (5.5) for the adapted growth factor that

$$\tilde{K}_g^\sigma = K_g^\sigma \underbrace{\frac{dV}{d\tilde{V}}}_{<1} + \frac{\overbrace{dV - d\tilde{V}}^{<0}}{\underbrace{\left(\frac{\sigma^k(t_1)}{\sigma_h^k} - 1\right) d\tilde{V}}_{\substack{>0 \\ <0}}} < K_g^\sigma. \quad (5.6)$$

That means a smaller growth factor \tilde{K}_g^σ than the reference growth factor K_g^σ is required to not overestimate the mass production, what explains the smaller enlargement of the diameter in Figure 5.4. The second term in (5.6) depends on the growth stress $\sigma^k(t_1)$. Hence, it is not possible to determine an adapted \tilde{K}_g^σ that ensures the same mass production for the complete time. This will influence the results of the inverse analysis, since the growth factor is determined there. To summarize, it is expected that the optimal growth parameter in the aneurysm sac, where the volume increases, will be smaller than the reference value.

Since the homeostatic state of a grown aneurysm is not known, the growth simulation has to be started differently than in the reference simulation. The equations developed in Section 3.3 can only be solved, when the history of the deformation is known at the beginning. Corresponding variables are for example the stretch $\lambda^k(\tau)$ and the density production rate $m^k(\tau)$ at time $\tau < t_1$. If the simulation starts from the homeostatic state, these quantities can be set to the homeostatic variables. This is also possible here, but it will lead to a different deformation, see Figures 5.4 and 5.5. Hence, the history of the deformation of the collagen fibers has to be approximated in the flying start configuration. In order to find a reasonable approximation, the influence of the history variables on the growth process has to be known.

5.2.2 Influence of history variables

In order to quantify the influence of different history variables, several simulations are performed. In each simulation, the history is manipulated differently, i.e. $\lambda^k(\tau)$ and $m^k(\tau)$ are modified for $\tau < t_1$. There are three basic modifications, which can be combined with each other:

1. Mass is modified such that the mass of the collagen fibers is equally distributed among all the fibers, i.e.

$$m_{\text{mod}}^k(\tau) = \frac{M(t_1) - (1 - \phi^c) \rho_0}{4 a_m^k} \quad \forall \tau \leq t_1, k \in \{1, 2, 3, 4\}. \quad (5.7)$$

During growth, the mass production varies for the different fiber directions. Hence, every direction has a different influence on the stresses. When the simulation is restarted, this information is lost. Each fiber family has to be treated equally. This effect is reproduced with this first modification.

2. For the stretch is assumed that the stretch of all collagen fibers is the same as the one of the newest fibers, i.e.

$$\lambda_{\text{mod}}^k(\tau) = \lambda^k(t_1) \quad \forall \tau \leq t_1, k \in \{1, 2, 3, 4\}. \quad (5.8)$$

Since the information about the past deformation is lost, the values of $\lambda^k(\tau)$ have to be approximated after the restart. The simplest method is to imprint no history, as it is depicted in Figure 5.3. That means all fibers have the same value $\lambda^k(\tau) = 1$. This corresponds to the modification given in (5.8) for a forward simulation, where it has to be incorporated that the deformation does not start from zero.

3. The stretch is linearly interpolated in deposition time between the stretch of the oldest and the newest fiber, i.e.

$$\lambda_{\text{mod}}^k(\tau) = \lambda^k(t_1 - t_{lf} + \Delta t) \frac{t_1 - \tau}{t_{lf} - \Delta t} - \lambda^k(t_1) \frac{t_1 - t_{lf} + \Delta t - \tau}{t_{lf} - \Delta t} \quad (5.9)$$

$$\forall \tau \leq t_1, k \in \{1, 2, 3, 4\}.$$

Another possibility to approximate the stretch history is to interpolate discrete values of the past deformation. These discrete values itself are approximated values of $\lambda^k(\tau)$ at given points in time. For a linear interpolation only one history value has to be known. It might be possible to get a good approximation of one history value. A method to compute an approximation is presented in the following section. Here, the effect of modifying the time course of the past stretch values is tested with a linear interpolation of the correct values of the oldest and the newest fiber existing at time t_1 .

The modifications described above are applied in the following way. The simulation is performed as usually until the time t_1 is reached. Hence, all history variables are known. Before the next time step $t_1 + \Delta t$ is computed, the history variables are modified as describe above. Afterwards, the simulation proceeds as if nothing happened.

In Figures 5.6(a)-(b) one can see the evolution of the diameters over time for four different modifications. The three modifications listed above are applied individually. Additionally, the first and second modification are combined. The diameters vary the most when the stretch is modified as described in the second modification. The difference arises mainly from a jump directly after the modification. In the case of the second modification, the change in the stretch history is large, since all values are reset. That means the increased resistance of the older fibers vanishes. Hence, the stress of the collagen fibers changes and leads to a different deformation. Since the difference of the individual curves to the reference solution is small compared to the diameter change, the difference is examined in more detail in Figure 5.6(c)-(d). The maximal relative difference is 2.5 percent. In the curves of the modified constant stretch history, one can see small oscillations due to the cosine survival function (3.39b). The third modification is nearly identical to the reference solution, its difference is almost constant over time. That means a linear

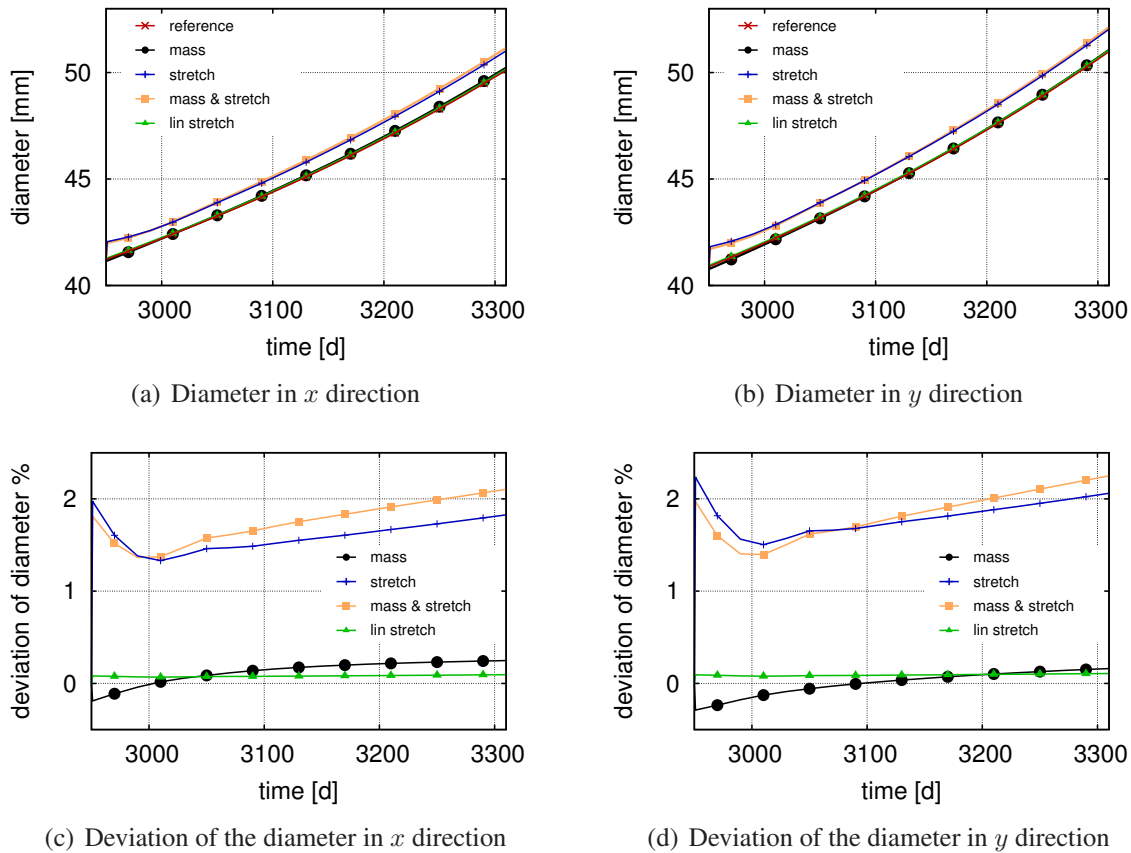


Figure 5.6: Evolution of diameters and deviation from the reference solution over time for different modifications of the history variables

interpolated stretch history may be a good choice to approximate the flying start configuration. In summary, stretch has the biggest influence of the history variables. This stems from the fact that here the formation of an aneurysm is driven by the remodeling process. Hence, the main focus will be on the stretch history.

5.2.3 Definition of the history

The starting point of the simulations within this section is the flying start configuration. The simulations performed within this section are identical to the simulation in Section 5.2.1 in the beginning. That means in particular that distinct deposition times τ are defined. Contrary to the previous simulation, the history variables $m^k(\tau)$ and $\lambda^k(\tau)$ are approximated before growth starts. These approximations are developed in the following.

In the elastic case, the deformation, hence the current configuration, is defined by the material of the solid, the applied pressure, the Dirichlet boundary conditions and the initial geometry. In the inelastic case here, the deformation is also influenced by the history variables. In the reference simulation, both effects are balanced and define the current configuration. In the flying start configuration, the solution of the boundary value problem (2.49) leads to a different current configuration, since e.g. the history of the stretches is different than in the reference solution. In

the ideal case, the history is adapted in such a way that the deformed geometry is identical to the initial geometry. This knowledge can be utilized to define the history variables. When the history is not adapted, the aneurysm deforms, when the pressure is applied. In the following, methods are developed to move this stretch into the history of the collagen fibers such that the stresses remain constant and the deformation is nearly zero afterwards.

The situation is slightly different when MULF is utilized. There, residual stresses are imprinted into the structure. A virtual deformation is applied to the structure, but the displacements are set to zero. Thus, reference and loaded configuration are identical. In the case of growth and remodeling, the residual stresses stem from the different stretch states of the collagen fibers. Hence, the computed virtual deformation should be shifted to the collagen fibers. Thus, the same methods can be applied.

All adaptations of the history that are presented in the following are applied after the solution of the respective time step t has been computed to not disturb the behavior of the Newton iteration. Thus, the adaptation has only an influence on the next time step, but the convergence of the Newton iteration is ensured.

To move the deformation into the history of the collagen fibers, the stretch at deposition time is adapted at time t_s . This time value is only an algorithmic quantity, since growth and remodeling starts for $t > t_s$. The simplest way of an adaptation is to use a constant value independent of the deposition time of the fiber, i.e. independent of τ , yielding

$$\lambda_{\text{new};\text{const}}^k(\tau) := \frac{1}{\lambda^k(t_s)} \quad (5.10)$$

for $\tau \leq t_s$. Here, the stretch in fiber direction at time t_s is utilized to define the history. From the definition of the total fiber stretch in (3.36b), follows:

$$\lambda^k(\tau, t_s) = \frac{\lambda_{\text{pre}}^k \lambda^k(t_s)}{1} = \frac{\lambda_{\text{pre}}^k}{\lambda_{\text{new};\text{const}}^k(\tau)}. \quad (5.11)$$

Hence, after the adaptation the fibers have the same stretch as before, i.e. $\lambda^k(\tau, t_s + dt) = \lambda^k(\tau, t_s)$, when the deformation is zero, i.e. $\lambda^k(t_s + dt) = 1$. In this case, the stress of collagen remains constant after the adaptation. Since collagen is the main load bearing constituent, the total deformation will be also nearly zero. That means the deformation has been shifted successfully to the history of the collagen fibers. Since there exist other constituents that are not affected by the adaptation, the deformation is not exact zero and the current configuration slightly differs from the initial geometry.

As discussed in the previous paragraph, the deformation of the whole structure will be close to zero after the adaptation. Thus, there is a jump in the deformation after the adaptation. This effect is challenging for the Newton method that is applied to solve the nonlinear system of equations. The Newton iteration utilizes an initial guess for the next time step that relies on the previous time step. Since the deformation is nearly zero after the adaptation, this initial guess might not be in the ratio for the optimal convergence of the Newton iteration. To make the adaptation more stable, this initial guess should be adapted too.

In the forward simulation of growth of an aneurysm, the deformation is high in the aneurysm sac when an aneurysm evolves. Hence, the deformation state, when the fibers are deposited, depends on the age of the fibers and thus the total stretch $\lambda^k(\tau, t)$. The oldest fiber of a fiber family has the

highest stretch and the youngest fiber is nearly not stretched. This is not reflected in the approach described previously, but it has an influence on the further evolution of the aneurysm. Hence, in a second variant the stretch is linear interpolated between the oldest and the newest fiber of a fiber family, while the pressure is applied, leading to

$$\lambda^k(\tau, t) = \left[(\lambda^k(t) - 1) \frac{t - \tau}{t_{lf}} + 1 \right] \lambda_{pre}^k \quad (5.12)$$

for $\tau \leq t$ and $t \leq t_s$. Hence, the stretch in every fiber depends on his age. At time t_s the stretch history is adapted similarly to the previous approach, the constant value $\lambda^k(t_s)$ in equation (5.10) is replaced by the actual stretch of the respective fiber, yielding

$$\lambda_{new;lin}^k(\tau) := \left[(\lambda^k(t_s) - 1) \frac{t_s - \tau}{t_{lf}} + 1 \right]^{-1} = [\lambda^k(\tau, t_s)]^{-1} \lambda_{pre}^k \quad (5.13)$$

for $\tau \leq t_s$. Additionally to the adaptation, the stretch is not interpolated any more for $t > t_s$, since the difference between the fibers is incorporated in the history. Again the deformation nearly vanishes after the adaptation for the same reasons as before. The linear approach is not applicable with the exponential survival function defined in equation (3.39c), since the difference of stretch between the oldest and the newest fiber is too high.

When the pressure is applied, the stress in the collagen fibers is defined. In a forward simulation, it is likely that the density of the fiber family with a higher stress than the other fiber families is higher, since more mass has been produced. Hence, the different stress values of the fiber families can be used to redistribute the total density such that the fiber families with higher stress have a higher portion of the total density. Within one fiber family the density is distributed evenly between all the fibers of different age. Since the relation between stress and density is defined through the density production rate (3.42), the following adaptation is used

$$m_{new}^k(\tau) := m_0^k \frac{m^k(t)}{\frac{1}{4} \sum_{l=1}^4 m^l(t)} = m_0^k \frac{1 + K_g^\sigma \left(\frac{\sigma^k(t)}{\sigma_h} - 1 \right)}{1 + K_g^\sigma \left(\frac{\sigma^1(t) + \sigma^2(t) + \sigma^3(t) + \sigma^4(t)}{4\sigma_h} - 1 \right)} \quad (5.14)$$

for $\tau \leq t$ with $t_m \leq t < t_s$. The quantity t_m denotes the time when the mass adaptation starts. In the rare case that $\sum_{l=1}^4 m^l(t) = 0$, the densities are not adapted. Equation (5.14) ensures that the total density remains constant.

In Figure 5.7 one can see the evolution of the diameter for the different approximations of the history. For a better comparison, the reference curve and the curve without modifications are also plotted. The largest difference occurs when MULF is not used, see Figures 5.7(a)-(b). The simulations with the approximated history start at nearly the same diameter contrary to the unaltered solution. In order to quantify the influence of the approximation of the history on the slope of the deformation, the solutions with MULF are helpful since all simulation start from the same point, Figures 5.7(c)-(d). The curve with the constant approximation is close to the unmodified curve. The slope of the curve is slightly higher. But compared to the difference to the reference solution, the improvement is negligible. The linear approximation is steeper in the beginning and has a different curvature. When all the original collagen fibers are degraded, the slope is close to

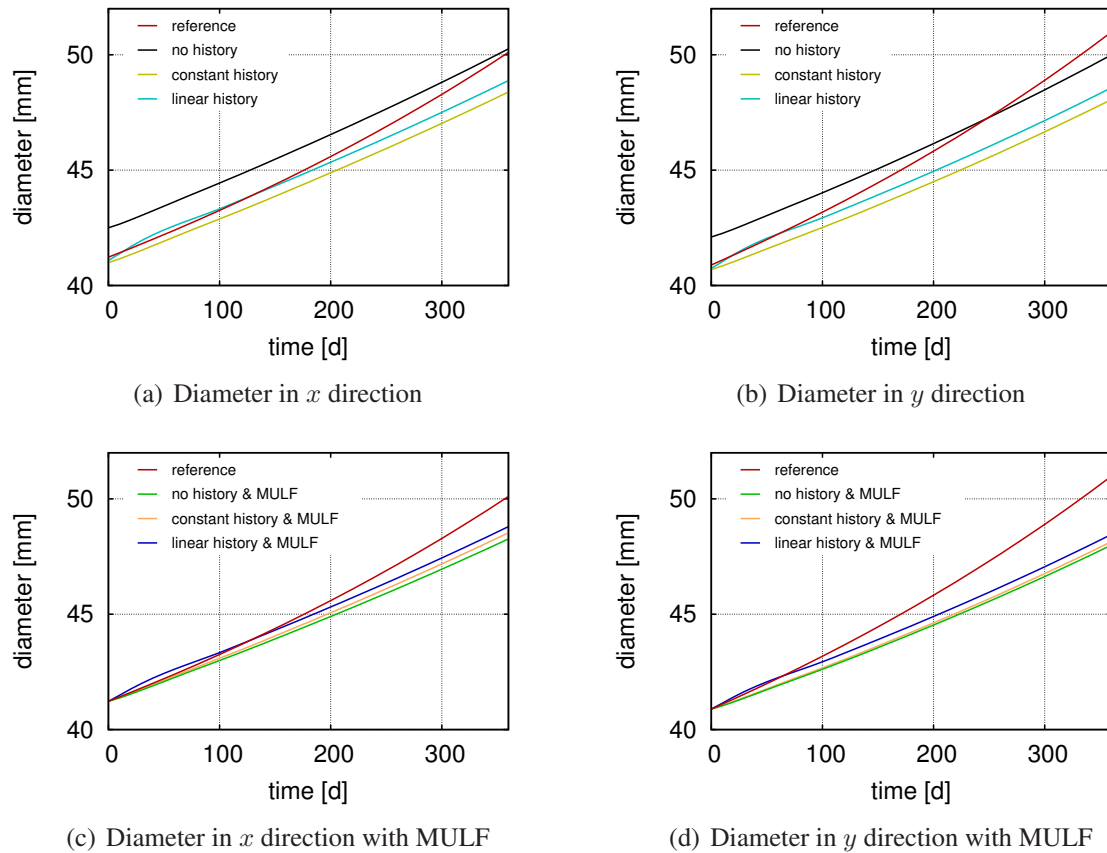


Figure 5.7: Evolution of diameters over time for different approximations of the history

the slope of the other curves. Due to the difference in the beginning, the linear approximation is the closest to the reference.

Summarizing, with the adaptation of the history the deviation of the deformed geometry, after the pressure has been applied, from the initial geometry could be minimized. Thus, the usage of MULF is not necessary any more. If the identity of initial and loaded geometry has to be guaranteed, the usage of MULF is recommended. The reproduction of the enlargement of the aneurysm is only marginally improved. As already discussed, the new reference volume for the density production rate has to be compensated by a smaller growth factor K_g^σ . Additionally, a modification of the elastin content ℓ^e of the wall could further improve the behavior.

Remark: 5.2.1 *The presented procedures are not meant to transfer the complete deformation from the homeostatic state to the flying start configuration. Since the collagen fiber families remodel continually, only a fraction of the whole deformation contributes to stress in the fibers. Hence, for the collagen fibers it is not necessary to know the complete deformation.*

5.3 Calibration of growth parameters

To calibrate the growth model to a given growth problem, an inverse analysis, as described in Chapter 4, is utilized. In the following sections, the results for different spatial parameter

abbreviation	number of patches	design variables	value of the other variable
V1.1	1	K_g^σ	$\iota^e = 1$
V1.2	1	ι^e	$K_g^\sigma = 1$
V1.3	1	ι^e	K_g^σ fixed to value from V1.1
V1.4	1	K_g^σ and ι^e	—
V2.1	3	K_g^σ	$\iota^e = 1$
V2.2	3	ι^e	K_g^σ fixed to value from V2.1
V2.3	3	K_g^σ and ι^e	—
V3.1	20	K_g^σ	$\iota^e = 1$
V3.2	20	ι^e	$K_g^\sigma = 1$
V3.3	20	K_g^σ and ι^e	—
V4.1	62	K_g^σ and ι^e	—

Table 5.1: Different variants of parameterizations and design variables

distributions are presented. The distributions are presented in ascending order of the number of patches. The growth factor K_g^σ and the elastin content ι^e are the design variables, which will be optimized separately or together. In Table 5.1 the different variants of the optimization are summarized.

To evaluate the objective function (4.1), the displacements of the reference solution presented in Section 5.1 at selected nodes are utilized. The selection of the nodes depends on the choice of the distribution of the optimization parameters. The respective displacements reflect the deformation from the flying start configuration to the intermediate configuration of the reference simulation. This corresponds to 360 days (≈ 1 year) of growth starting from the flying start configuration. In Figure 5.8 three variants of selected nodes and the respective displacements are depicted.

The elastin content ι^e describes the amount of elastin that has not been degraded, see equation (3.77). Thus, its value should be located in the interval $[0, 1]$. Since the method presented in Chapter 4 can only handle unconstrained optimization problems, a parameterization of the elastin content is used to ensure that the parameter ι^e lies in the interval $]0, 1[$, yielding

$$\iota^e = \frac{\text{atan}(p^e) + \frac{\pi}{2}}{\pi} \in]0, 1[, \quad (5.15)$$

respectively

$$p^e = \tan\left(\pi \iota^e - \frac{\pi}{2}\right) \in]-\infty, \infty[, \quad (5.16)$$

where p^e is the associated optimization parameter.

The growth factor K_g^σ has to be positive. Hence, it is parameterized with a quadratic function

$$K_g^\sigma = (p^K)^2 \in [0, \infty[, \quad (5.17)$$

where p^K is the corresponding optimization parameter.

To evaluate the gradient with Finite Differences within the optimization algorithm, n_p+1 forward simulation starting from the flying start configuration are computed. In each forward simulation, the history is newly defined. Therefore, the constant adaptation of the history defined in equation

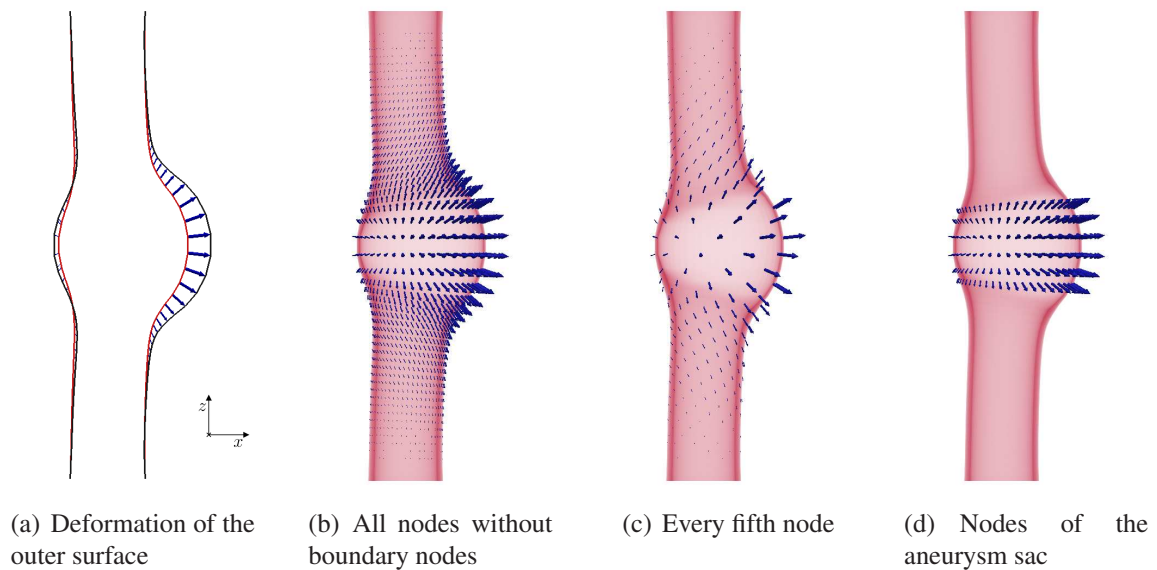


Figure 5.8: Different variants of selected nodes of the outer surface that are utilized to evaluate the objective function, the arrows indicate the measured displacement vectors

(5.10) is utilized, since this method is more stable than the linear one. To guarantee that the initial geometry and the loaded state coincide in the beginning, MULF is utilized.

As starting values for the optimization algorithm, the growth factor is set to a constant value of $K_g^\sigma = 1$ and the elastin content to $\iota^e = 0.5$, when the respective parameter is optimized. The parameterization of the elastin content led to the choice of 0.5, since the optimization algorithm should not be influenced by a start value on one branch of the tan function in equation (5.16).

5.3.1 Uniform parameters

As a first step in the optimization procedure, a spatially uniform parameter distribution is assumed. To maximize the influence of the parameters in the aneurysm sac, only displacements in the body of the aneurysm are monitored, as shown in Figure 5.8(d). The displacements in the healthy region are different than the displacements in the aneurysm sac. To reproduce the deformation of the healthy region, different parameter values as for the deformation of the aneurysm sac are required. Since the number of nodes in the healthy region is higher than the number of nodes in the aneurysm body, they would predominate the total behavior.

Three different sets of parameters are optimized: the growth factor and the elastin content alone and in the end both parameters together, see Table 5.1. The influence of the optimized parameters on the evolution of the diameter as well as the total deformation is investigated.

In Figure 5.9 one can see the convergence behavior of the optimization of the growth factor K_g^σ alone. The error decreases steeply in the beginning and reaches its minimal value after six iterations. The optimization parameter converges in the same way. The gradient slowly decreases in the beginning and decreases steeper in the end, until it is smaller than the required tolerance (logarithmic scale). That means the optimal parameter is roughly found after few iteration steps. When more iteration steps are performed, the parameters are more accurate.

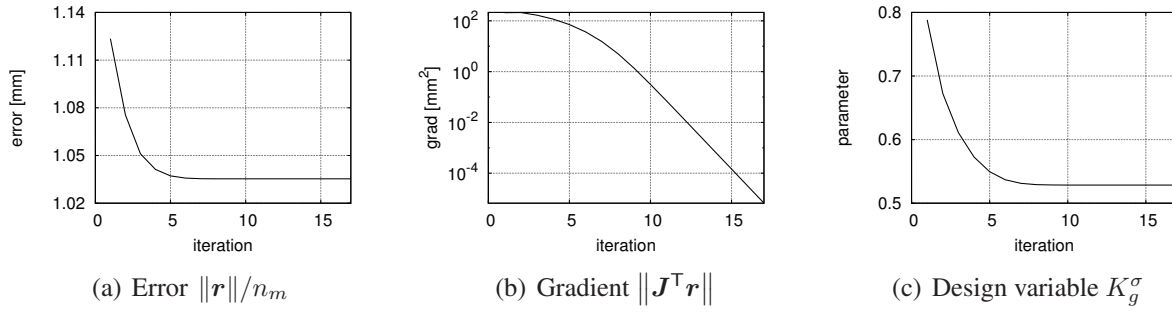


Figure 5.9: Convergence of the algorithm for the optimization of the growth factor K_g^σ

The optimal growth factor has the value $K_g^\sigma = 0.5285$. It is smaller than the reference value $K_g^\sigma = 1.0$. This was already predicted in Section 5.2.1, as a consequence of the new reference configuration for the density production. In Figure 5.10 one can see the resulting evolution of the diameters (black curve). The curve is closer to the reference than the curves from Figure 5.7. The evolution of the diameter in x direction is slightly overestimated, whereas the evolution of the diameter in y direction is still underestimated. It seems like the obtained solution cannot fit both curves and is a compromise.

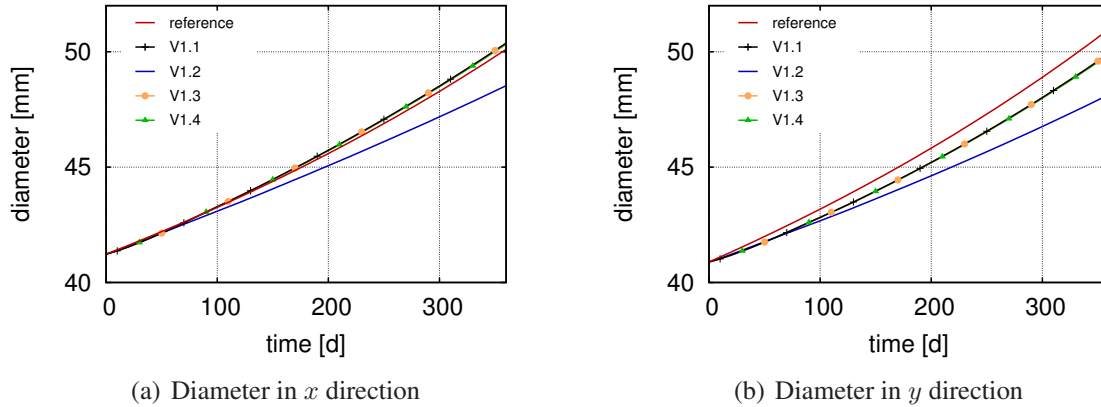


Figure 5.10: Evolution of diameters over time for growth simulations with parameters resulting from different optimization variants with a uniform parameter distribution

When solely the elastin content ι^e is optimized, the optimal result is $\iota^e = 1.0$ independent of the choice of the growth factor, which is fixed to the original value or to the previously computed optimal value. Hence, the resulting curves of the diameter evolution are identical to the curves without optimization, as shown in Figure 5.10 and Figure 5.4. For both variants the optimization algorithm converges after four iteration steps.

In a fourth inverse analysis, both parameters are optimized simultaneously. The optimization algorithm does not converge as fast as the previous ones. After twenty iteration steps, the prescribed tolerance of the norm of the gradient is not yet reached, but the first digits of the parameters do not change anymore. Hence, no more optimization steps are performed. The resulting

parameters are $K_g^\sigma = 0.5360$ and $\iota^e = 1.0$. The optimal value for the growth factor is close to the value that is obtained if K_g^σ is the only optimization parameter (V1.1).

If the parameters are used in a forward simulation, the resulting curves of the diameters over time are nearly identical, see Figure 5.10. Since the solutions lie so close together, only the deformed states resulting from the simulations with the parameters of the inverse analysis of the growth factor and the elastin content alone (V1.1 and V1.2) are plotted in Figure 5.11. The deformed state of the simulation with the parameters of the optimization of the elastin content alone (blue) corresponds to the deformed state of the solution without optimization. With a smaller growth factor, the wall gets thinner and leads to a greater enlargement of the aneurysm. The aneurysm sac again translates to the bottom compared to the reference solution, as was already observed in Figure 5.5. It seems like this problem can only be solved with spatially varying parameters. That means the errors resulting from the loss of the information of the past deformation in the flying start configuration make a nonuniform distribution of the parameters necessary, as was already depicted in equation (5.6).

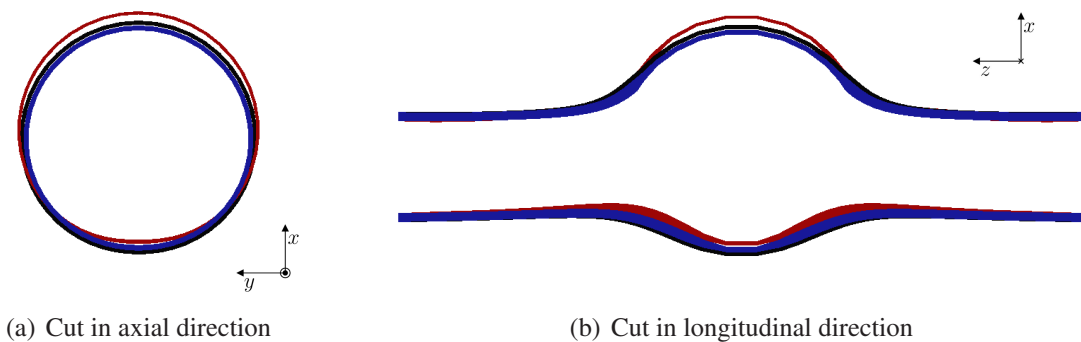


Figure 5.11: Slices of the deformed solution at the intermediate state with different parameters, red: reference solution, black: inversely determined growth factor (V1.1), and blue: inversely determined elastin content (V1.2)

Summarizing, all determined parameters do not improve the translation of the aneurysm sac, but the evolution of the diameters can be better approximated. Thus, the reproduction of the growth gradient is improved. The variation of the growth factor has the biggest influence, whereas an optimization of a constant elastin content makes no difference. A smaller growth factor partly compensates the errors that were made in the flying start simulation. The influence of this smaller growth factor on the long term behavior of the aneurysm will be investigated later.

5.3.2 Separation of healthy and diseased part

In a second step, the healthy and diseased parts of the geometry are treated differently. The geometry is divided into three patches, two healthy patches and one diseased patch, as depicted in Figure 5.12. The left part corresponds to the first healthy part, referred to as healthy 1, the right third is the healthy part, referred to as healthy 2 and in the middle one can see the diseased part. During the optimization routine, all parts are treated as separate patches, each of which has its own set of parameters. This should yield an improvement especially for the elastin content. To avoid jumps in parameter values at the patch boundaries, the smoothing methodology described

in Section 4.2.2 is applied. This time three variants of the optimization are performed, see Table 5.1. First, only the growth factor is optimized while the elastin content is held constant at $\iota^e = 1$. Then, the elastin content is optimized while the growth factor is held constant at the previously inversely computed value. In a third optimization, both, elastin content and growth factor, are design variables. Since now the aneurysm sac is treated separately, the deformation mismatch at the healthy part is included in the objective function. Therefore, every fifth node of the outer surface is evaluated, as can be seen in Figure 5.8(c).

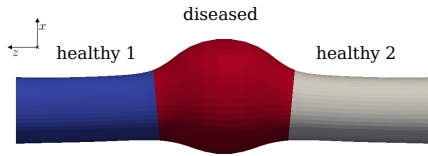


Figure 5.12: Example geometry: split into healthy and diseased part

		healthy 1	healthy 2	diseased
V2.1	K_g^σ	1.677	1.836	0.6239
V2.2	ι^e	0.8789	0.8732	0.0
V2.3	K_g^σ	1.866	1.814	0.5325
	ι^e	0.8694	0.8298	1.0

Table 5.2: Final parameters

The results of the optimization are given in Table 5.2. Each optimization reached after few iteration steps of the optimization algorithm a point, where the next optimization step did not lead to a decrease in the error. Hence, the optimization algorithm was aborted. Thus, the presented results are only a rough approximation of the optimal results. The same behavior is nearly always observed, when more than one parameter is optimized. Hence, all results presented in the following sections are only approximations of the optimal solutions. However, the results are sufficiently accurate to study the qualitative behavior of the aneurysms, which is the major objective of this work.

In all cases of the optimization, the growth factor is elevated in the healthy part compared to the reference value, whereas it is smaller in the diseased part. This corresponds to the elevated volume change in the aneurysm sac compared to the minimal change in the healthy part. When only the growth factor is optimized, the growth factor in the middle section is larger as the values of the uniformly determined parameters. In this case, also the symmetry of the healthy parts is lost in the inverse analysis. The evolution of the diameter in x direction is nearly identical to the reference curve, see Figure 5.13(a), whereas the evolution of the y diameter is even more underestimated than before, see Figure 5.13(b).

The inverse determination of the elastin content alone leads to a zero value in the diseased part. The value in the healthy part is also decreased, but they are nearly identical in both healthy parts. The evolution of the diameter in y direction is improved, and the evolution of the diameter in x direction is only slightly worse, as shown in Figure 5.13. Contrary to the simulations in the previous section, the inverse analysis of the elastin content leads to an improved behavior.

In the case of the optimization of both parameters together, the value of the growth factor in the middle section is nearly identical to the values of the uniformly determined parameters. On the other hand it leads to an unreasonable value for the elastin content ($\iota^e = 1.0$) in the diseased part. The other values are close to the values of the optimization variants V2.1 and V2.2. The evolution of the diameters is not improved compared to the optimal elastin content (V2.2), see Figure 5.13. In y direction it is slightly better than the evolution of the inverse defined growth

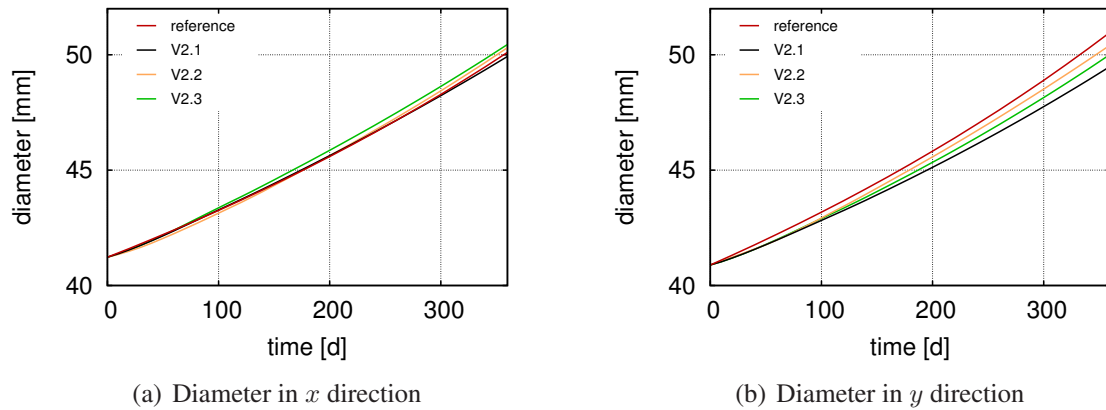


Figure 5.13: Evolution of diameters over time for growth simulations with parameters resulting from different optimization variants with three different patches

factor. All three sets of parameters lead not to an improvement of the translation of the aneurysm sac. Thus, they are not investigated in more detail.

5.3.3 Spatially varying parameters

Especially the diseased part of the aneurysm is of interest, since growth and remodeling mainly happens there. Hence, this area is better resolved. The single patch is split into 18 patches. Each patch consists of 40 elements. The resulting patch distribution can be seen in Figure 5.14. It is identical to the distribution shown from different angles in Figure 4.2. The transition is again smoothed with five steps. Three optimization problems are solved: growth factor and elastin content are optimized separately and then together, see Table 5.1. For the optimization of the elastin content, the growth factor is fixed to its original value $K_g^\sigma = 1.0$. This optimization variant is performed to test if the influence of the elastin content on the solution increases when it varies over the domain.

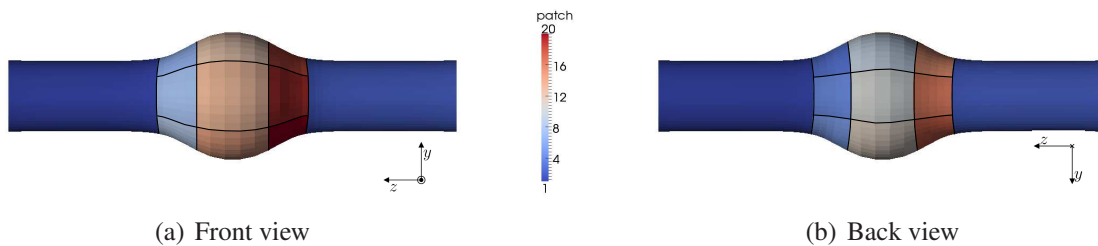


Figure 5.14: Definition of 20 patches for the reference aneurysm

In Figure 5.15 one can see the resulting distribution of the elastin content. In the left pictures, one can see the distribution for the optimization of the elastin content ι^e alone, in the right pictures, both parameters are optimized. Both distributions are quite similar, but the solution on the right is not symmetric since the values from two patches differ from the symmetric pattern. This problem stems from the parameterization of the elastin content with the tangent function.

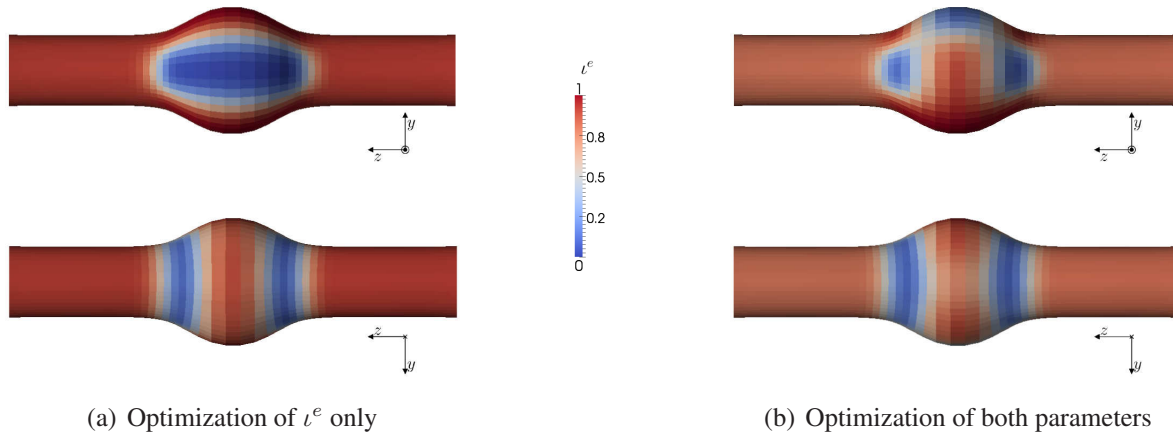


Figure 5.15: Obtained distribution of the elastin content ι^e for 20 patches, top row: front view, and bottom row: back view

The limit $\iota^e \approx 1.0$ corresponds to large values of the optimization parameter, e.g. $p^e \approx 10^{20}$. This leads to a bad conditioning of the linear system of equations (4.4) that defines the update of the optimization parameters. Thus, the parameter p^e sometimes oscillates between large positive and negative numbers.

The elastin content is mainly decreased in the aneurysm sac. The optimization of both parameters also leads to values smaller than one in the healthy part, but they are still higher than in most parts of the diseased area. The patterns at the front and back of the aneurysm are quite different. At the front, where the main part of the aneurysm bulges out, elastin is completely degraded in the front three patches. This amplifies the enlargement in this direction. Next to these patches, the elastin content is higher. At the back, the elastin content is elevated in the middle, where the enlargement after the flying start is too high. The value in the center patch is slightly lower for the optimization of both parameters compared to the value of the optimization of solely ι^e . At the transition to the healthy parts, elastin is partially degraded.

In Figure 5.16 the final distribution of the growth factor is shown. When the elastin content is fixed to one and the growth factor is optimized, a peak value at the back of the aneurysm occurs. The value there is twice as large as the values in the rest. This peak vanishes when the elastin content is optimized too. In the front of the aneurysm the final value is lower than the optimal parameter from the previous section. One can clearly see the influence of the separation of the optimization parameters at the front and back of the aneurysm. Summarizing, the variation of the growth factor between patches is smaller than the variation of the elastin content. Nevertheless, it is reasonable to include the elastin content despite its large variation in the optimization process, since it reduced the outlier of the growth factor in the back of the aneurysm.

The influence of the parameter distribution on the evolution of the diameters can be seen in Figure 5.17. The variation of the elastin content alone has again nearly no influence on the evolution. Thus, it is not reasonable to optimize the elastin content alone. The solution with the inverse determined growth factor matches the evolution of the diameter in x direction quite well in the beginning. In the end it gets worse. The solution from the optimization of both parameters is underestimating the enlargement constantly, but gives the best results at the final point of time.

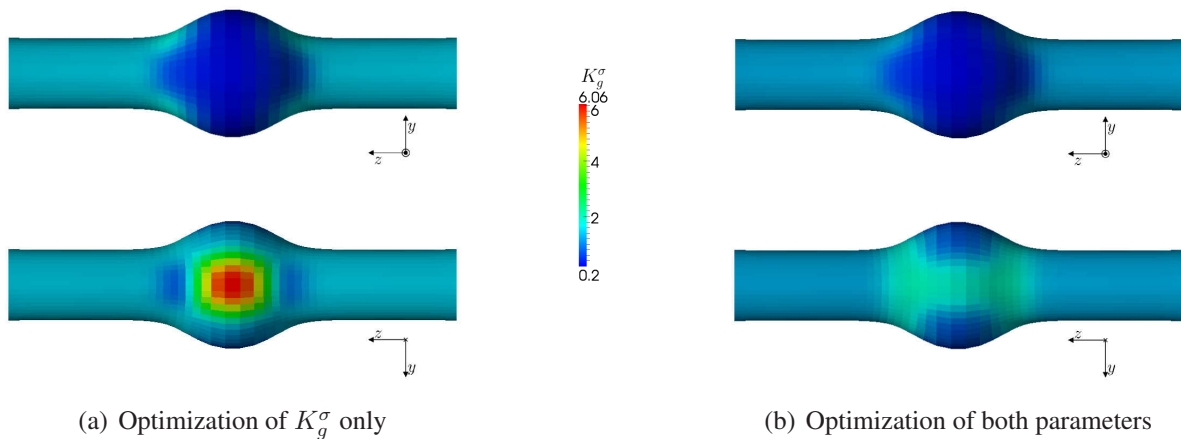


Figure 5.16: Obtained distribution of the growth factor K_g^σ for 20 patches, top row: front view, and bottom row: back view

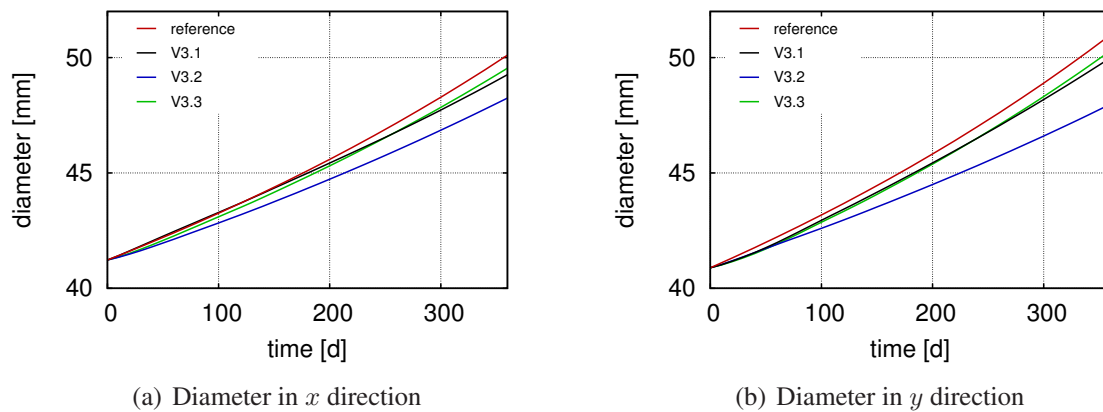


Figure 5.17: Evolution of diameters over time for growth simulations with parameters resulting from different optimization variants with 20 different patches

It is also most promising for the prediction of growth, since the slope of the curve is close to the slope of the reference.

In Figure 5.18 one can see the deformed shapes of the aneurysms at the final state. The solution from the inverse determination of only the elastin content still shows the translation to the bottom, whereas the other results can reproduce the expansion of the aneurysm without that translation. The elevated growth factor in the back of the aneurysm, see Figure 5.16, what corresponds to the bottom in Figure 5.18, compensates the translation. The black shape is nearly completely hidden by the green shape. These two shapes are close to the reference shape. Some local deviation could not be reflected, since the representation of the optimization variables is not detailed enough.

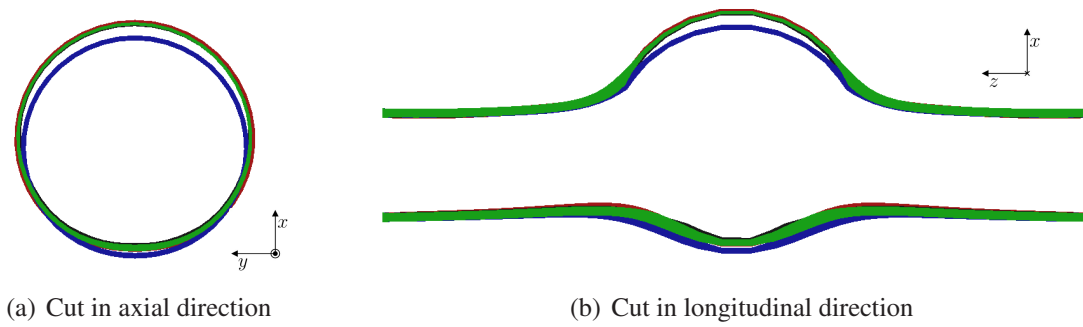


Figure 5.18: Slices of the deformed solution at the intermediate state with different parameters, red: reference solution, black: inversely determined growth factor (V3.1), blue: inverse elastin content (V3.2), and green: both parameters are inversely determined (V3.3)

Higher resolution with a finer mesh

To get an even higher resolution than with the 18 patches the diseased part is split into 60 patches, as shown in Figure 5.19. Hence, the whole structure consists now of 62 patches. Since for the previous example already few elements were part of one patch, the mesh was refined to get a reasonable number of elements per patch. The new mesh consists of 14400 elements, where especially the part in the middle has been refined. Since the different mesh size influences the result of the simulation (see Section 3.3.7), a new reference simulation has been computed. The flying start configuration is defined at the same time t_1 as before.

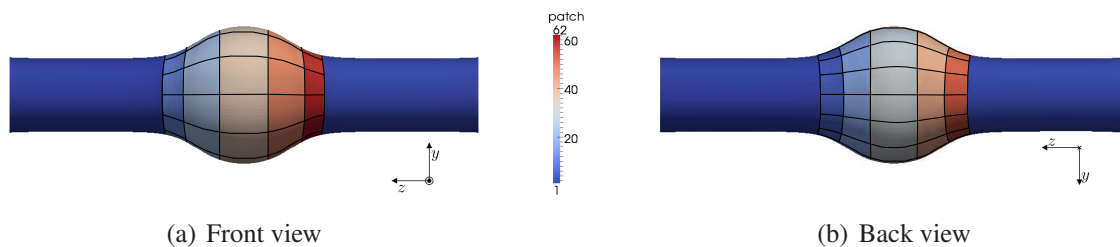


Figure 5.19: Definition of 62 patches for the reference aneurysm with a finer mesh

Since the optimization of both parameters led to the best results for the coarse patches, only an inverse analysis of both parameters together is performed. Thus, 125 forward simulation have to be computed simultaneously. In Figure 5.20 one can see the resulting distribution of the parameters. The elastin content ι^e in the healthy part is smaller than in parts of the aneurysm sac, but the values in the healthy part are similar to the values in the healthy part in Figure 5.15(b). The distribution of the elastin content jumps especially at the back of the aneurysm, but nearly always two neighboring patches have a similar value. In the center of the back, where the wall has to be strengthened to circumvent the translation to the bottom, the elastin content is one. In a nearly circular area around it, the elastin content is decreased. In the front, the elastin content is zero in the middle. In the other patches of the front the elastin content is higher. Two patches stand out, since they have a smaller value than the patches around them.

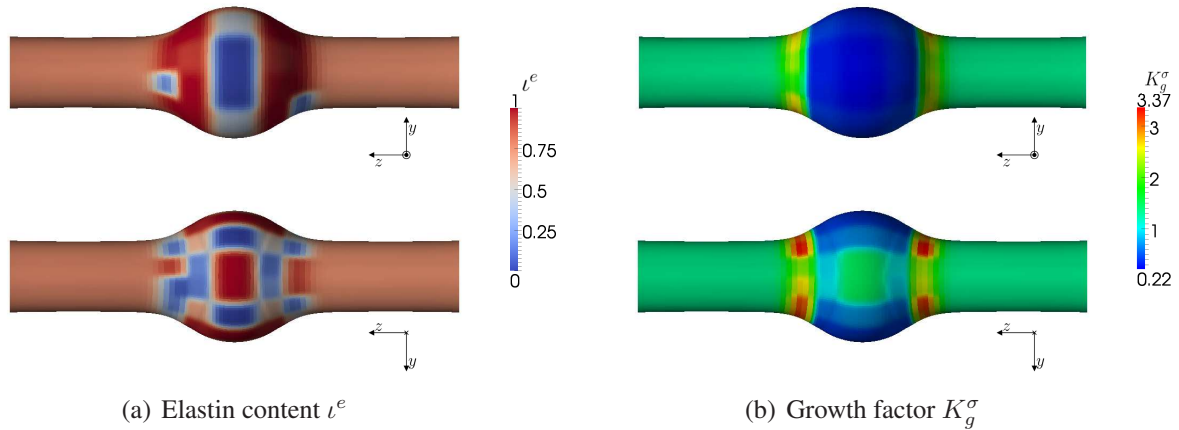


Figure 5.20: Obtained distribution of the elastin content ι^e and the growth factor K_g^σ for 62 patches, top row: front view, and bottom row: back view

The growth factor K_g^σ is similarly distributed as with the coarse resolution depicted in Figure 5.16(b). The minimal value that is constant throughout the aneurysm sac is nearly the same as before. The value at the center of the back is slightly smaller than before. The main difference occurs at the transition from the sac to the healthy part, the growth factor is increased in one row of patches. In this ring, the maximal value of all growth factors is located at the back of the aneurysm. This increase leads to a strengthening of the wall around the aneurysm sac and localizes the expansion.

To get a better insight of the influence of the optimized parameters on the time course of the enlargement, the evolution of the diameters is shown in Figure 5.21. The evolution of the diameter in x direction is nearly identical to the reference. A difference of only 0.5 % in diameter was achieved. In the end, the enlargement is slightly overestimated. Whereas, the diameter in y direction is underestimated throughout the whole simulation. The difference increases at the beginning, but at the end it remains constant and the slope of the curves is similar. Compared

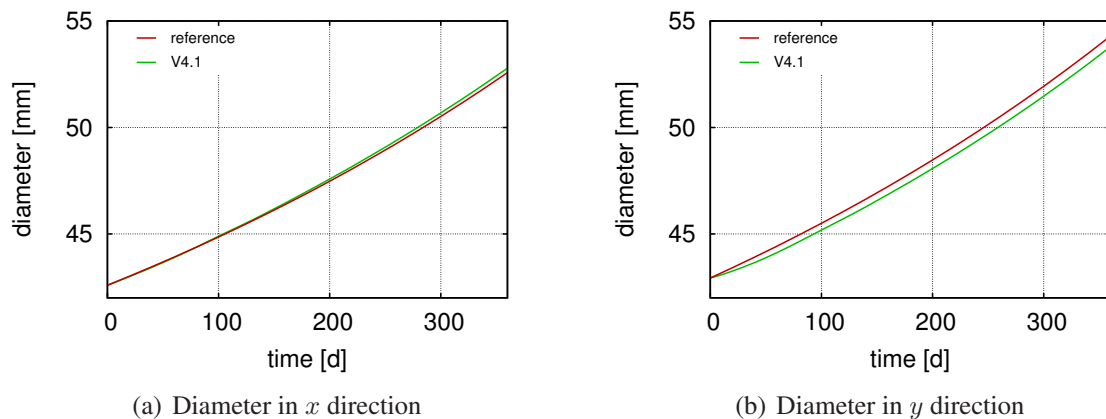


Figure 5.21: Evolution of diameters over time for a growth simulation with parameters obtained by the optimization of both parameters with 62 different patches

to the results from the coarse mesh, the aneurysm gets larger, as has already been shown in Section 3.3.7. The higher resolution fits the evolution better than the previous results shown in Figure 5.17.

The improved behavior can also be seen in the slices of the deformed geometries in the intermediate configuration, as shown in Figure 5.22. The deformed geometry is nearly identical to the reference solution. At the transition between the sac and the healthy part, where the growth factor is elevated, the wall is thicker than the wall of the reference. A thickening of the wall also occurs at the bottom of the aneurysm. In the axial cut, one can see a slight movement of the aneurysm to the left. A loss of the symmetry of the enlargement has already been observed in Figure 5.18.

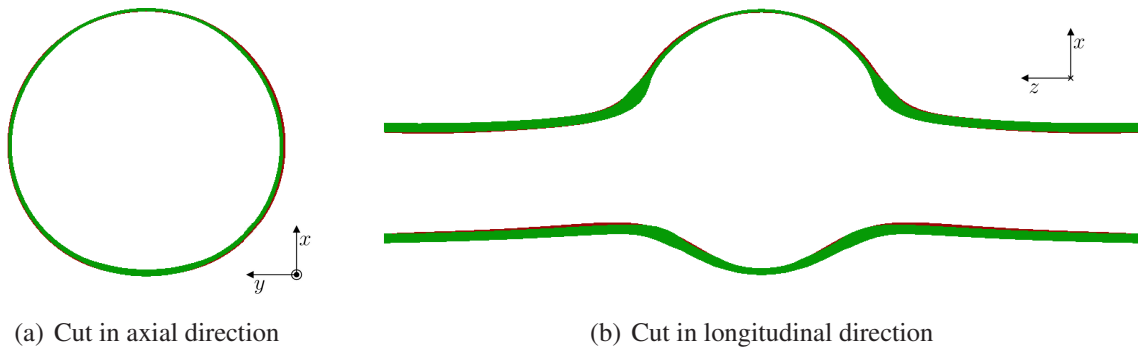


Figure 5.22: Slices of the deformed solution at the intermediate state with different parameters, red: reference solution and green: both parameters are inversely determined (V4.1)

5.4 Validation of predicted results

In the previous section, parameters were determined to fit the growth model to the given growth of an aneurysm within one year. In the most cases, the parameters differed from the reference value. For example, the best uniform parameter $K_g^\sigma = 0.5285$ is smaller than the reference value of $K_g^\sigma = 1.0$. In the following section, the influence of this variation of the parameters on long term growth is investigated to validate the proposed framework. Therefore, the best values of each parameterization have been selected. For the uniform parameter, the inverse analysis of the growth factor alone is chosen (V1.1, $K_g^\sigma = 0.5285$), for the split into healthy and diseased part, the successive optimization of growth factor and elastin content is used (V2.2, first two rows of Table 5.2) and for the twenty patches, the optimization of both parameters together is chosen (V3.3, Figures 5.15(b) and 5.16(b)). In a subsequent study, the influence of the parameters of the higher resolution with the fine mesh is investigated. With these optimal parameters a growth simulation over two years starting from the flying start configuration is performed and compared to the respective reference solution.

In Figures 5.23(a)-(b) one can see the evolution of the diameters in x and y direction. Because the curves lie so close together, the relative difference to the reference solution is plotted in Figures 5.23(c)-(d). The uniform solution and the solution with the three different patches fit the evolution of the diameter in x direction well, see Figure 5.23(c). The deviation is less than one

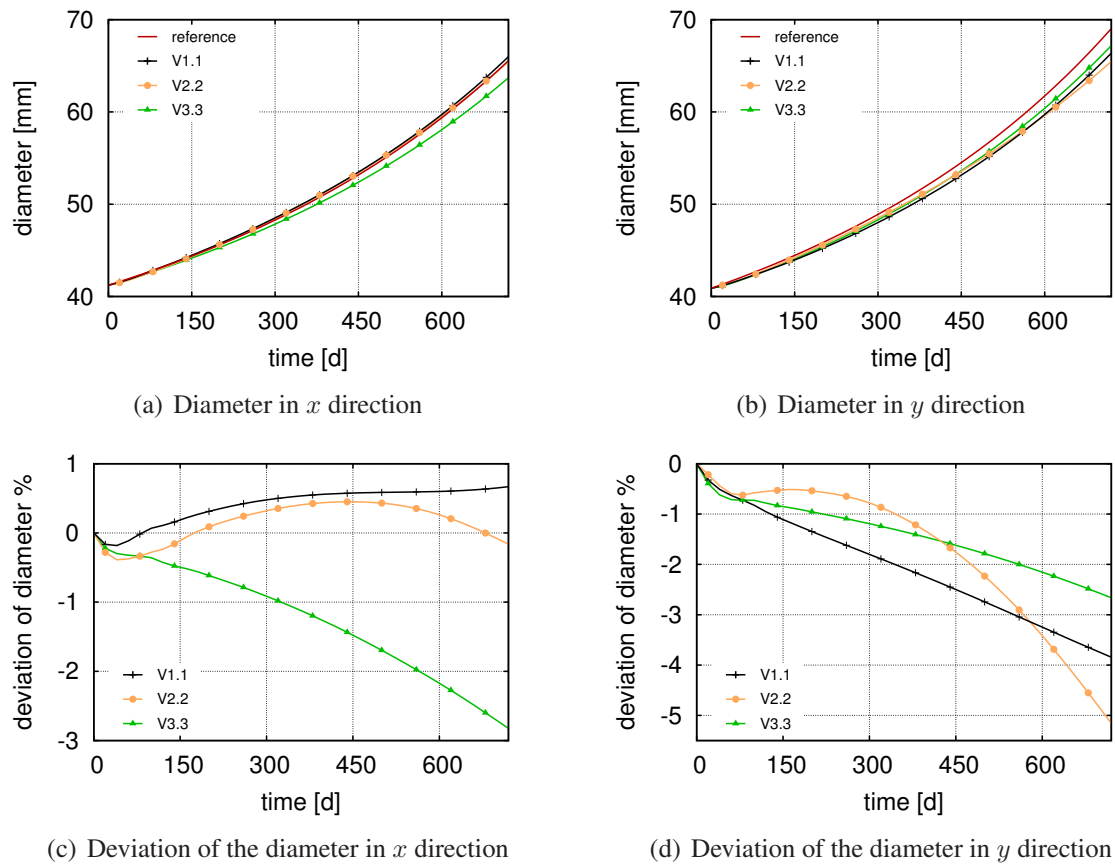


Figure 5.23: Evolution of diameters and deviation from the reference solution over time for selected inversely determined parameters for growth of two years

percent. The twenty patch solution provides the worst fit to the diameter in x direction and underestimates the enlargement. In the end, the discrepancy is three percent. Since the difference increases with time, the prediction gets worse, when a longer period of growth is considered. The deviation from the diameter in y direction, see Figure 5.23(d), is higher for the first two variants. The maximal difference at the end is approximately five percent. The difference increases with increasing time for the solution from the separation of healthy and diseased part. Hence, the capability to predict the correct growth decreases with increasing time. Summarizing, the enlargement is underestimated for all parameters. The prediction gets worse for longer time scales, but the maximal difference of five percent is small. Thus, the smaller growth factor does not lead to an overestimation of the enlargement.

Since the evolution of the diameters holds no information about the deformation of the whole body occurring during growth, the final shape of the aneurysm is sketched in Figure 5.24. All solutions except the twenty patch solution show a translation to the bottom and cannot reproduce the shape of the aneurysm, as was already seen at the final point of the inverse analysis, i.e. Figure 5.11. Due to the high growth factor at the bottom of the aneurysm, as shown in Figure 5.16(b), the twenty patch solution has a thicker wall there. This effect is more visible than before, since the wall gets very thin in the rest of the aneurysm. The aneurysm also translates in y direction,

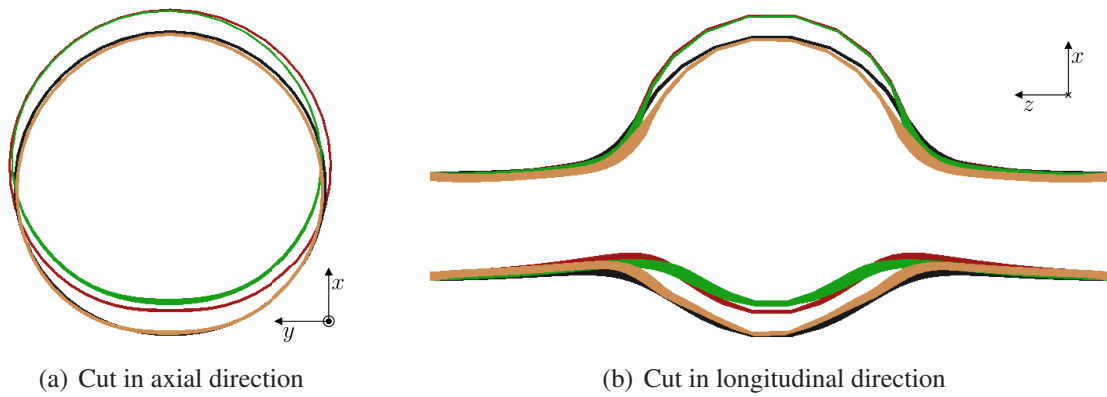


Figure 5.24: Slices of the solution with parameters determined by inverse analysis, red: reference solution, black: uniform growth factor K_g^σ (V1.1), orange: V2.2, and green: V3.3

what can be seen in the cut in axial direction. Due to the asymmetry of the optimal elastin content ι^e , see Figure 5.15(b), the wall is asymmetric weakened. Thus, the aneurysm bulges out into this direction.

The best results in the intermediate configuration were obtained with the higher resolution of the finer mesh. Hence, its capacity to predict the evolution of the aneurysm is also investigated. In Figure 5.25 one can see the evolution of the diameters over time for a time period of two years. Again, the evolution of the diameter in x direction can be reproduced, see Figure 5.25(a). The expansion is slightly overestimated, what leads to a relative error of 0.75 percent. The difference to the reference is constantly increasing in time, see Figure 5.23(c). Thus, the prediction is getting worse for longer time periods. In y direction, see Figure 5.25(b), the enlargement is constantly underestimated. After ca 100 days of growth, the variation of the error over time is still relatively small, see Figure 5.23(d). Compared to the other optimization results, see Figure 5.23(b), the reproduction of the diameter in y direction is much better. The maximal relative difference is less than one percent.

Contrary to the evolution of the diameters, the deformed geometry of the optimized solution is slightly different to the reference solution, as shown in Figure 5.26. At the center of the aneurysm sac, the radial increase is higher. Hence, the expansion in x direction is overestimated. The thickening of the wall at the transition between healthy and diseased part gets larger compared to the intermediate configuration, as depicted in Figure 5.22. Again, the final shape matches the reference solution the best compared to the other optimization variants.

Not only the shape of the final aneurysm is important but also its state. Hence, in Figures 5.27 and 5.28, the distribution of the change of the reference density and the von Mises stress of the predicted results ($t = t_3$) is shown for the 62 patches and the reference solution. For the density, the density change is plotted, since the density is referred to the reference volume. This volume is different for the obtained solution and the reference solution, since the reference solution starts from a straight cylinder, whereas the obtained solution starts from the flying start configuration. Since $M(t_1)$ and $M(t_3)$ are both referred to the same volume, this effect is canceled out, when both values are divided by each other. Hence, the quotients are comparable for both solutions. At the back of the aneurysm, the density increase is elevated for the solution with the optimized parameters, since the growth factor is there elevated too, see Figure 5.20(b). For the same reason,

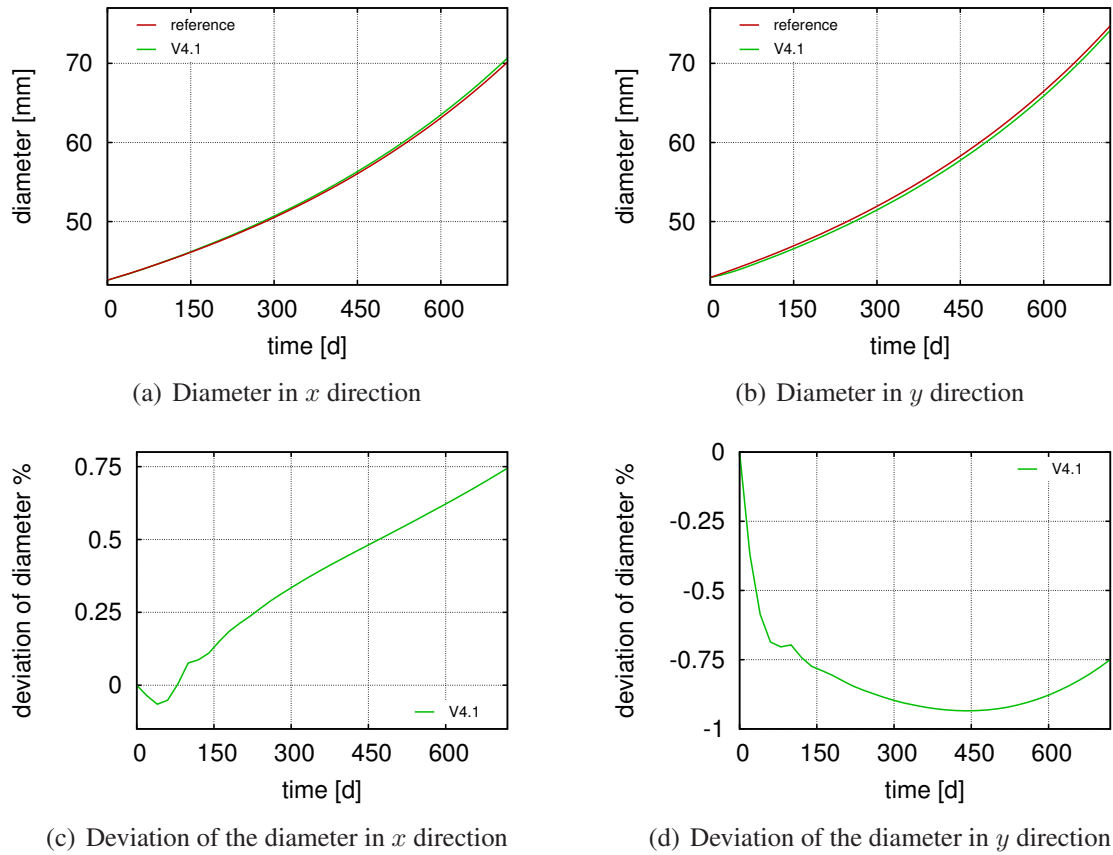


Figure 5.25: Evolution of diameters over time for a growth simulation of two years with parameters obtained by the optimization of both parameters with 62 different patches

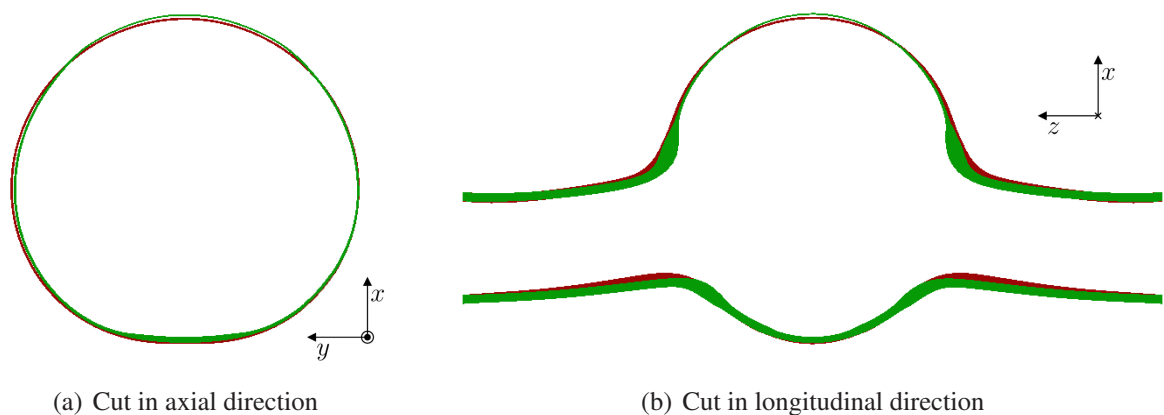
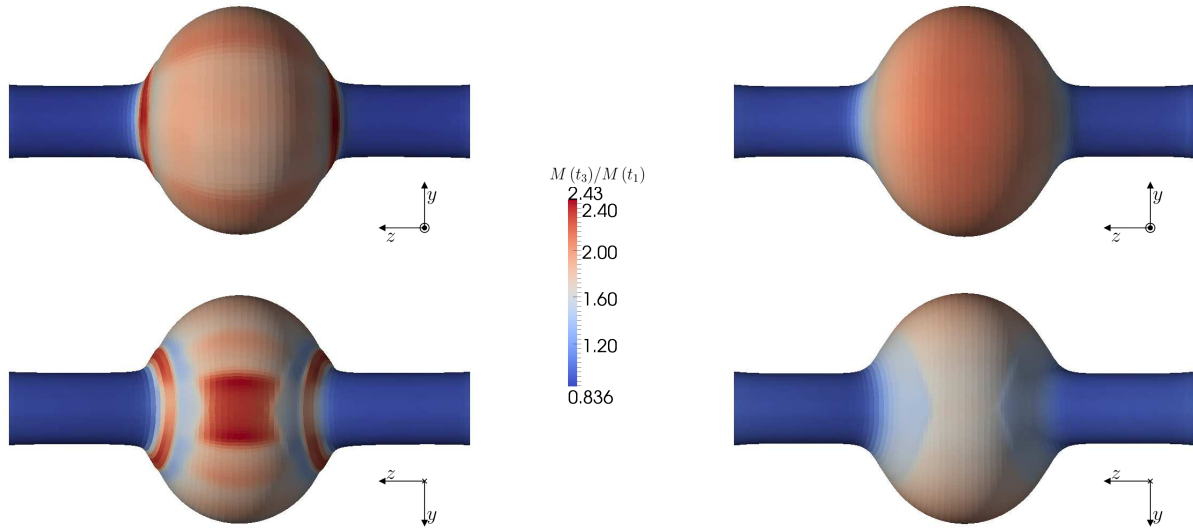


Figure 5.26: Slices of the solution with different parameters for the fine mesh, red: reference solution and green: both parameters are inversely determined

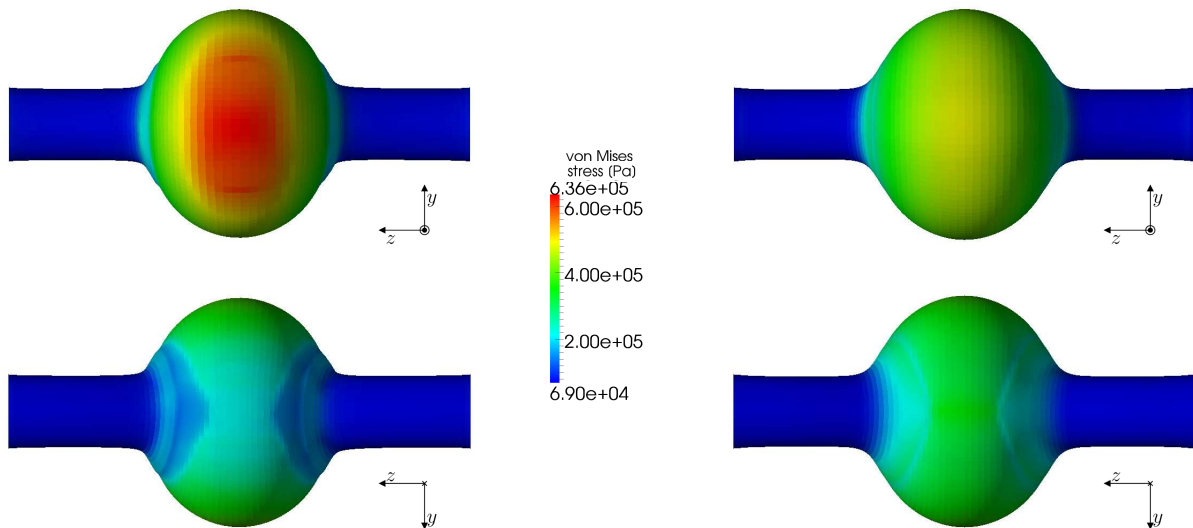


(a) Optimization of both parameters with 62 patches

(b) Reference solution

Figure 5.27: Relative change of the referential density at the predicted state, i.e. $t = t_3$

the density increase is higher at the transition between the healthy and the diseased part. The maximum value is located there. The density change in the aneurysm sac is lower compared to the reference. The cause is a lower growth factor in this area. In both figures, the boundary of the initial degradation of elastin, as shown in Figure 3.24(b), is visible at the back.



(a) Optimization of both parameters with 62 patches

(b) Reference solution

Figure 5.28: Von Mises stress at the predicted state, i.e. $t = t_3$

The maximal stress in the optimized solution is higher as in the reference solution, as shown in Figure 5.28. In both cases, it is located in the aneurysm sac. This higher stress value stems from the fact that the simulation that starts from the flying start configuration has to bulge out more to compensate the translation to the bottom. The increase of the growth factor in the bottom of the aneurysm leads to lower stresses in this region. This higher growth factor was needed to compensate the translation to the bottom. It has to be stressed again that the translation influences the stress at the final state.

In summary, the optimized solutions are able to approximate the evolution of the diameters. The enlargement is slightly underestimated in the most cases. The ability to predict the behavior of the reference solution decreases the longer the simulation lasts, but the representation of the parameters with 62 patches gives a good prediction. The final shape of the aneurysm can only be approximated by spatially distributed growth parameters that compensate the effects arising from the flying start configuration. This compensation leads to an altered stress state.

6 Patient-specific case

In the previous chapter, a methodology for determining growth parameters to fit a given growth process has been developed. This methodology is now exemplarily applied to a patient-specific case, where two computed tomography (CT) scans of one patient are available. At the time of the first CT scan, the male patient was 62 years old. The second CT scan was recorded two years later. In the first section, the derivation of the computational model from the CT scan is briefly described. With patient-specific geometries certain challenges come along. These challenges are investigated in the second section. Subsequently, the growth model is calibrated to the measured displacement field. The obtained parameters are utilized to compute a growth simulation over a longer period of time. Finally, two modifications of the optimization procedure are discussed.

6.1 Derivation of a computational model

If surgery is necessary, computed tomography (CT) scans are made to plan the surgery. In some cases, follow up scans are available, where the patient has not been operated. Medical imaging data utilized in this work was provided by the university hospital Klinikum rechts der Isar of the Technische Universität München. In the following section, a brief summary of the steps required to create a computational model of the images is presented. For a more detailed explanation of this topic, the reader is referred to Maier [64].

As first step, the different anatomical structures, the lumen and the intraluminal thrombus (ILT), are segmented. Subsequently, the three dimensional geometry of the lumen and the ILT is reconstructed from the 2D CT data. The aneurysm wall cannot be reconstructed, since the resolution of the CT scans is not high enough (Reeps et al. [80]).

As next step, the geometry is discretized. For a pure structural simulation, the lumen is not considered, since it represents the fluid domain. The ILT is meshed in Harpoon (Sharc Ltd, Manchester, UK) with a hexahedron-dominant mesh. The element edge length is set to 1 mm. Afterwards, the aneurysm wall is extruded from the ILT surface, if available. Otherwise, the luminal surface is utilized. The Extrusion can be performed with a constant wall thickness or a variable one as proposed in Maier [64]. During the extrusion, a discretization of the wall arises from the extrusion of the surface mesh of the initial surface. Hence, the whole geometry is discretized.

As last step, the behavior of the tissue has to be described. Thus, strain energy functions (SEFs) for every component of the geometry are specified. The aneurysm wall is modeled in the same way as in the previous chapter, see equation (3.34) and Table 3.1. That means the aneurysm wall consists of an elastic ground substance and four collagen fiber families. The ILT is modeled with the following SEF

$$W^{ILT} = c (\bar{I}_1 - 2\bar{I}_2 - 3) + \kappa \beta_2^{-2} (\beta_2 \ln J + J^{-\beta_2} - 1) \quad (6.1)$$

with the scalar $\beta_2 = -2$ and c a stress-like parameter (Gasser et al. [26], Maier [64]). The bulk modulus κ is defined by the Poisson's ratio $\nu = 0.48$ and the parameter c as follows $\kappa = \frac{8c}{(1-2\nu)}$. The material parameter c depends on the position in the ILT. At the luminal surface the value 2.62 kPa is set, in the middle of the ILT the value 1.98 kPa and at the outer surface the value 1.73 kPa. In between these three values, the material parameter is linearly interpolated. Hence, c , and thus κ , vary within the ILT.

In order to solve the boundary value problem (2.49), boundary conditions have to be specified. The surfaces at the top and bottom, where the aneurysm has been cut, are fixed in all directions. Thus, all displacements of the ILT and the wall are set to zero at these surfaces. The constant inner pressure is applied orthogonal at the luminal surface, i.e. either at the ILT or directly at the wall, when no ILT exists. The pressure $P = 13.322$ kPa is always referred to the current configuration.

6.2 Challenges of patient-specific geometries

The simulations in the previous chapter were based on idealized geometries. That simplified some things that are more complex for patient-specific geometries. In the following sections, these problems will be investigated. First, the fiber directions are specified. Second, the homeostatic variables are set. In the end, stress peaks are further examined.

6.2.1 Determination of fiber directions

Two of the four fiber directions are aligned with the axial and the circumferential direction, as sketched in Figure 3.8. For a straight cylinder, these directions are defined through the cylindrical coordinates. This is not the case for a patient-specific geometry. In Figure 6.1, one can see a sketch of the geometry of the aneurysm of the 62 year old patient and the respective centerline.

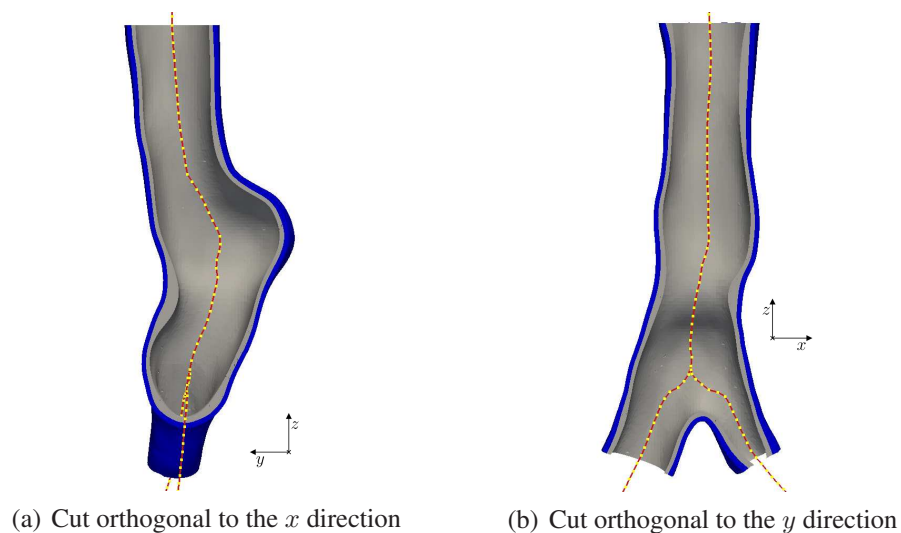


Figure 6.1: Sketch of the geometry and the corresponding centerline of an aneurysm of a 62 years old male patient, grey: ILT, and blue: aneurysm wall

The centerline is represented by distinct points. The line is only drawn for better visualization. Especially in the aneurysm sac, a definition of the axial direction is not straight forward. An additional difficulty arises with the bifurcation of the artery at the bottom of the aneurysm. In the following, a procedure to determine a reasonable distribution of the fiber directions is presented. For each structural element of the spatial discretization of the wall, four fiber directions, as defined in Figure 3.8, are computed. The aneurysm wall is discretized with linear elements with straight edges that originate from an extrusion of the thrombus surface. Thus, the inner and outer surface are almost parallel to each other. That means the tangential directions, i.e. axial and circumferential direction, are nearly identical throughout the element. Hence, the fiber directions are set constant within one element. In a first step, the fibers are geometrically defined. Afterwards, the fiber distribution is improved.

Geometric definition of the fiber directions

The geometric computation of the fiber directions is based on the discrete centerline given in Figure 6.1. For each element, the closest point of the centerline to the element center is computed. It is assumed that the direction of the centerline at this point corresponds to the axial direction of the element. The radial direction is set to the difference vector between the point of the centerline and the element center. The circumferential direction is now computed such that the three directions yield an orthogonal system. As last step, the circumferential and axial directions are projected in the tangential space of the outer surface of the aneurysm. The radial direction is adapted to obtain again an orthogonal system. Finally, all directions are normalized. When this local orthonormal coordinate system is defined, the fiber directions can be computed. For a straight cylinder, the proposed procedure yields the exact fiber directions.

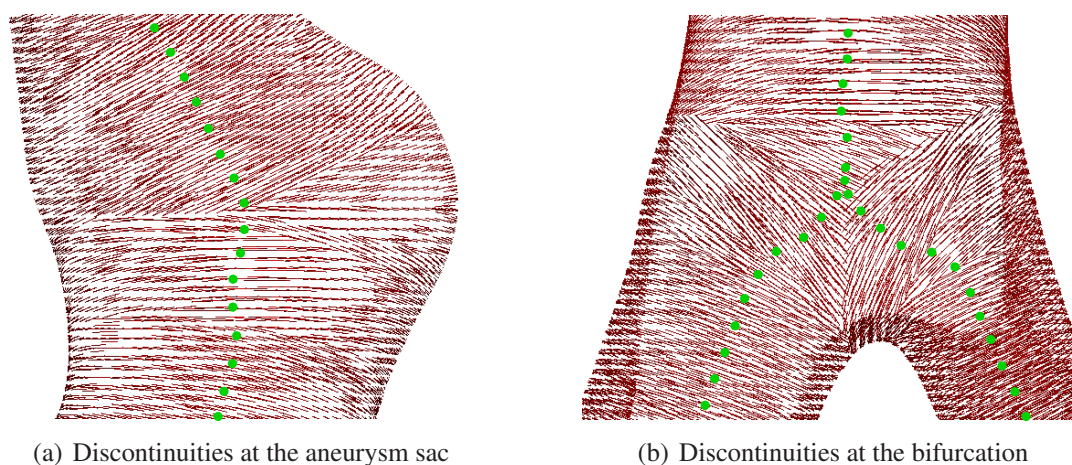


Figure 6.2: Circumferential fiber directions for the geometrically defined directions, green dots depict the discrete centerline

In Figure 6.2 one can see the resulting circumferential fibers at two special places of the aneurysm, i.e. the aneurysm sac and the bifurcation. The fiber distribution is discontinuous in both cases. To illustrate the origin of these discontinuities, the discrete points of the centerline are also sketched in Figure 6.2. In the aneurysm sac, the high curvature in axial direction is critical. Since the centerline is represented with discrete points, the curvature leads to large differences in the axial

directions of two neighboring points. In Figure 6.2(a) one can see wedges of several elements, where the fibers are nearly aligned. The elements in these wedges correspond to the same point of the centerline. At the boundary of two wedges, there is a jump to the next point of the centerline. At the bifurcation, the transfer between the two branches causes problems, see Figure 6.2(b). At the position of the kink, the closest points of the centerline jump from one branch to the other for neighboring elements. Since the axial direction of the two branches is different, this transfer leads to discontinuities. These discontinuities generate artificial jumps of the von Mises stress, as shown in Figure 6.3. Thus, the fiber directions have to be revised.

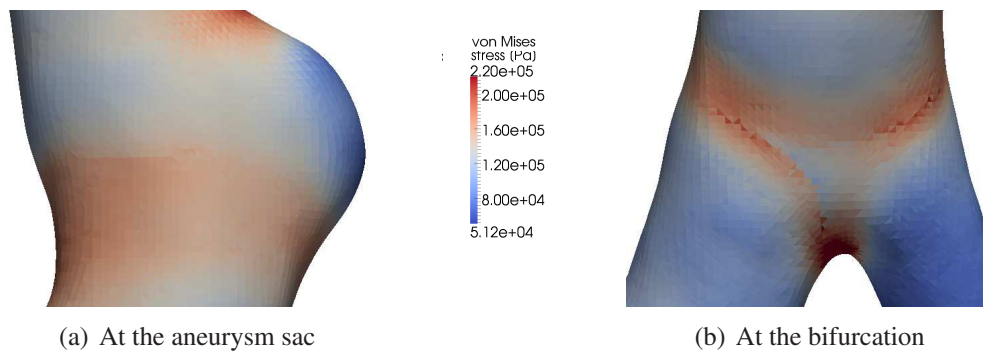


Figure 6.3: Discontinuities of the von Mises stress resulting from the geometrically defined fiber directions

Aligning the fiber directions with the principal stresses

Hariton et al. [36, 37] present a strategy for modeling stress-driven collagen remodeling. The strategy is utilized to determine the directions of two helical collagen fiber families in the arterial wall that is modeled with the Holzapfel-Gasser-Ogden material defined in equation (2.48). They assume that the preferred directions of the two fiber families are located between the directions of the two maximal principal stresses. The fiber angle in equation (2.47) depends on the quotient of the two highest principal stress values. That means the two highest principal stress directions play the role of the circumferential and axial direction. Since the principal stress directions are orthogonal, the third principal stress directions corresponds to the radial direction. This correlation between principal stress directions and local coordinate system is utilized in the proposed strategy that proceeds as described in the following. The fiber directions are computed in an iterative way. Starting point is an isotropic material. The resulting stresses are used to compute the initial fiber directions. These fiber directions lead to a new stress distribution and the fiber directions are adapted to these changes until the stress field is converged.

In the following paragraph, the correlation between principal stress directions and local coordinate system is investigated in more detail. The directions of the principal stresses are defined by the load. The aneurysm is loaded with a constant pressure at the inner surface. For a thin walled cylinder that is fixed in axial direction this leads to compression in radial direction. Since the cylinder is fixed in axial direction, the stretch in circumferential direction is the highest. Thus, the lowest principal stress is in radial direction and the highest in circumferential direction. The middle principal stress coincides with the axial directions. This relation even holds, when the geometry is not an exact cylinder. Hence, the correlation between principal stresses and local coordinate system is reasonable.

The procedure presented above is adapted to the problem given here. As starting point of the iterative process, the geometrical fiber directions are used. During the adaptation, the circumferential and axial fiber directions are aligned with the first and second principal stress direction, respectively. The other two fiber directions are defined diagonal to the others. Since the aneurysm does not have the straight shape of a cylinder, the principal directions do not always fulfill the requirements. For example, sometimes the second principal direction has a radial component. Hence, the final fibers are projected on the outer surface. To get rid of the boundary effects at the clamped surfaces at the ends of the aneurysm, the aneurysm is extruded there. More details regarding these corrections can be found in Heinrich [40]. In Figure 6.4 one can see the resulting fiber directions in the same regions as in Figure 6.2. The discontinuities are gone and a reasonable distribution of the fiber directions is defined. The proposed procedure is applicable to all sorts of aneurysms.

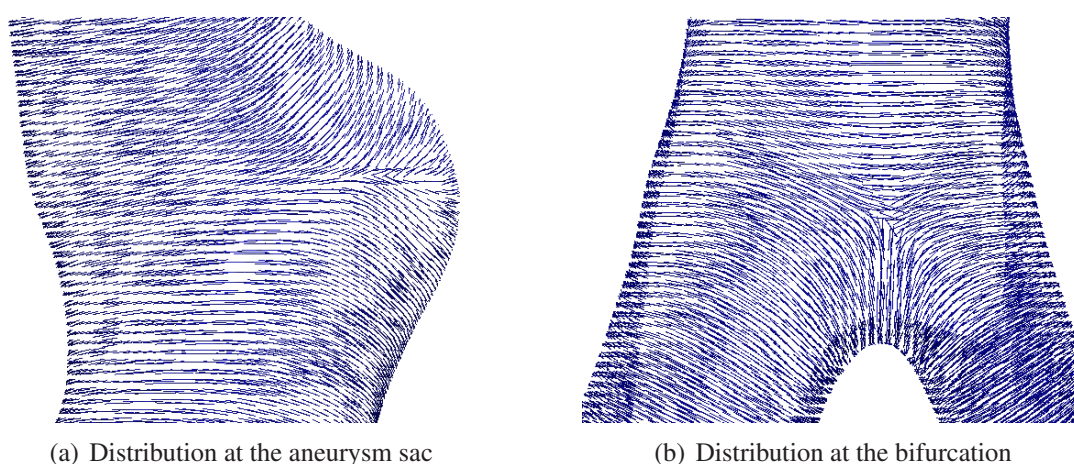


Figure 6.4: Circumferential fiber directions of the final fiber distribution

6.2.2 Homeostatic variables

The simulations in Chapter 5 start from a straight cylinder, see Figure 5.1, that represents the homeostatic state. Thus, the prestretch λ_{pre}^k and the homeostatic stress σ_h^k can be computed, as proposed in Section 3.3.3. Since the homeostatic state of the patient-specific geometry is not known, the homeostatic variables have to be defined differently. For the given patient-specific geometry, a long piece of the healthy artery at the top of the aneurysm is included, as shown in Figure 6.1. Hence, it can be utilized to determine the homeostatic variables.

The procedure to define homeostatic variables that is presented in Section 3.3.3 is utilized for the patient-specific geometry. Therefore, the pressure is applied at the inner surface of the aneurysm and the homeostatic variables are adapted as defined in equation (3.63). For the initial prestretch the value $\lambda_{pre}^k = 1.05$ is chosen. The applied procedure yields homeostatic variables for the whole geometry, which are not always reasonable. Thus, a part of the healthy artery at the top, as depicted in Figure 6.5(a), is extracted from the rest of the aneurysm to determine the homeostatic variables. In Figures 6.5(b) and 6.5(c) one can see the distribution of the homeostatic variables of the circumferential fiber family in the extracted area. The variation of the prestretch

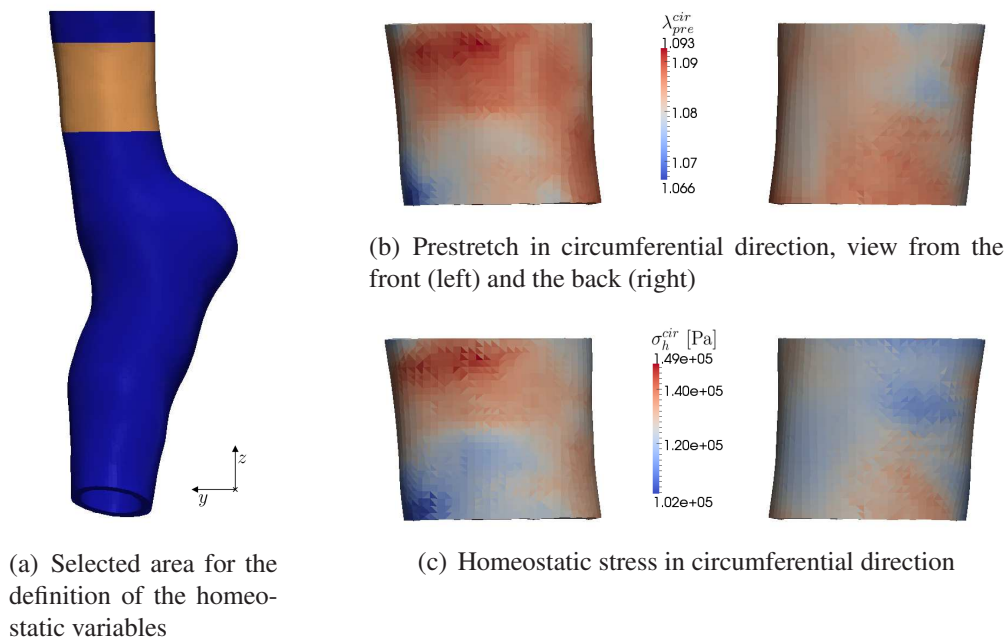


Figure 6.5: Computation of the homeostatic variables as proposed in Section 3.3.3 and distribution of the resulting homeostatic variables in circumferential direction

is comparable to the variation of the prestretch in the patient-specific artery that is depicted in Figure 3.18(c). The homeostatic values of the other fiber directions have similar distributions. In order to get a constant homeostatic value for the complete geometry, the computed values are averaged over the selected region. The resulting values are summarized in Table 6.1. The value in axial direction is the smallest, since the aneurysm is fixed in axial direction. The value of the diagonal direction lies in between the other two values. No distinction between the two different diagonal fiber families is made.

	cir	axi	dia
λ_{pre}^k	1.08	1.04	1.06
σ_h^k	121.0 kPa	62.2 kPa	93.3 kPa

Table 6.1: Final homeostatic variables for all fiber directions for the patient-specific aneurysm

Remark: 6.2.1 *The values of the computed homeostatic variables at the thinner branches at the bottom of the aneurysm are smaller than the values in Table 6.1. Since it is not possible to define a smooth and reasonable transition between the three branches, the thinner branches are not treated separately and the same homeostatic values as in the rest of the aneurysm are prescribed.*

6.2.3 Stress peaks

In the patient-specific case, the geometry is defined by CT scans. Hence, complex geometries may be generated. The first difficulty is to get a mesh with the required quality. Distorted ele-

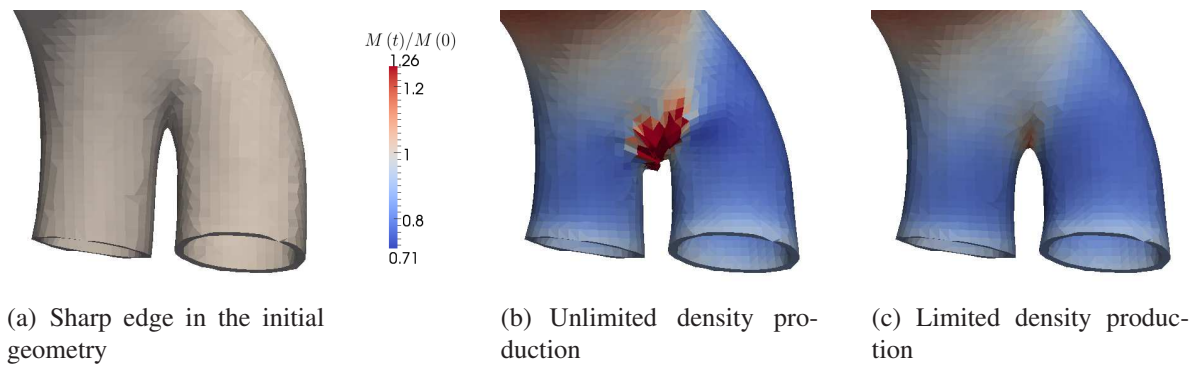


Figure 6.6: Initial and deformed geometries after one year of growth with buckling at the bifurcation, colors depict the relative reference density, the maximum of the color scale is defined by the 99th percentile of the picture in the middle

ments can lead to stress peaks. Additionally, critical geometries, such as kinks and wholes, cause stress peaks too. Often, both problems occur in the same places. A local refinement and smoothing of the mesh may reduce the stress peaks. The effort for this modification of the mesh has to be balanced to the improvement of the results. Sometimes, stress peaks may be acceptable depending on their position. Hence, a safety mechanism should be included in the growth and remodeling model to achieve reasonable results even when stress peaks occur.

No problems with stress peaks arise for the patient-specific geometry utilized within this chapter. However, the bifurcation at the bottom of the aneurysm of a different patient (67 years old, male) has a sharp edge, as shown in Figure 6.6(a), and some elements are distorted in this area. In the zone around the edge, a stress peak occurs. If the mass production is not limited, these stress peaks lead to a large increase in density, see Figure 6.6(b). After one year of growth, the density is maximally increased by a factor of 6000. In 99 percent of the wall, the increase is less than a factor of 1.3. Thus, the problem is local in a few elements. The large density increase leads to an increase in volume in these elements. Hence, the wall is buckling and leads to higher distorted elements. This effect amplifies the stress peaks. Thus, a factor like 6000 can arise.

In Section 3.3.1, a solution has been presented. The mass production rate $m^k(t)$ defined in equation (3.42) is restricted to the interval $[0, m_{max}^k]$. In Figure 6.6(c) one can see the deformed shape for the choice $m_{max}^k = 4m_0^k$. The buckling has vanished and the density increase has reasonable values. The influence of the limiting value is restricted to a few elements. The major part of the geometry is not affected, since the mass production is lower there. Hence, with a small reasonable modification of the mass production rate the problem with stress peaks could be solved and an additional safety mechanism is included in the growth model.

6.3 Calibration of growth parameters

With the methods presented in the previous section, it is possible to compute a growth and remodeling simulation starting at the patient-specific geometry. The only component that is missing is the history of the deformation. Since the patient-specific geometry is challenging, it is not possible to utilize one of the methods presented in Section 5.2.3 to approximate the history.

The convergence of the Newton iteration is destroyed after the adaptation. Hence, in the following sections, the history variables are set to the same values as in the homeostatic state, i.e. $\lambda^k(\tau) = 1$ and $m^k(\tau) = m_0^k$. The time interval $[t_1 - t_{lf}, t_1]$ is split into intervals of the length Δt to define distinct deposition times τ of the different fibers. To ensure that the loaded geometry is identical to the reference geometry, the modified updated Lagrangian formulation (MULF, Gee et al. [27, 28]) is utilized.

Since the reference geometry is not symmetric, it is difficult to capture all aspects of the growth process in two dimensional pictures. In order to quantify important aspects of the growth process, two orthogonal cutting planes are defined. The intersection of the cutting planes with the initial geometry is sketched in Figure 6.7. The two cutting planes correspond to axial and longitudinal cuts through the aneurysm sac. Thus, important aspects of the growth process are registered with these two cuts. The bar in the figure indicates the length of 20 mm, which corresponds approximately to the diameter of the main artery.

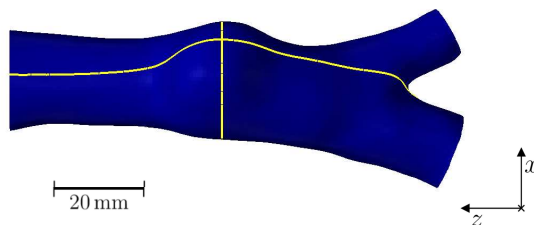


Figure 6.7: Intersection of cutting planes with the geometry and definition of a length scale

In order to calibrate the growth model to the given growth problem, the two CT scans have to be transformed into a displacement field. The resulting displacement field is presented in the following section. Subsequently, three variants of the optimization, which are listed in Table 6.2, are performed. They are ordered with increasing number of patches. The same design variables as in Section 5.3 are utilized with the same parameterization, as defined in equations (5.15) and (5.17). Since the optimization of both parameters together led to the best results for the spatially distributed parameters (see Section 5.3.3), the optimization algorithm that is utilized in the following sections is restricted to the optimization of both parameters together, i.e. growth factor K_g^σ and elastin content ι^e , when more than one patch is defined. In the last section, the evolution of the diameter is investigated in more detail for all optimization variants together.

abbreviation	number of patches	design variables	value of the other variable
P1	1	K_g^σ	$\iota^e = 1$
P2	20	K_g^σ and ι^e	—
P3	74	K_g^σ and ι^e	—

Table 6.2: Different variants of parameterizations and design variables for the patient-specific geometry

6.3.1 Measured displacement field

From the first CT scan of the 62 year old patient, the geometry for the flying start configuration is determined, see Figure 6.1. The inner wall of the aneurysm is covered with a thin layer of ILT. A second CT scan depicts the growth of the aneurysm after the time period of two years. In order to determine parameters to fit the given growth process, a displacement field that represents a mapping of the first CT scan to the second CT scan is required. To compute this displacement field for the outer surface, the image registration method presented in Section 4.1.2 is utilized. The obtained nodewise displacement field can be utilized to evaluate the objective function in equation (4.1) that is the basis of the optimization algorithm. Therefore, only a selection of nodes is evaluated to reduce the noise in the displacement field that results from the measurements. Similar to Figure 5.8(c), every fifth node may be selected or only the nodes in the middle are considered. The choice of the selection depends on the spatial distribution of the growth parameters.

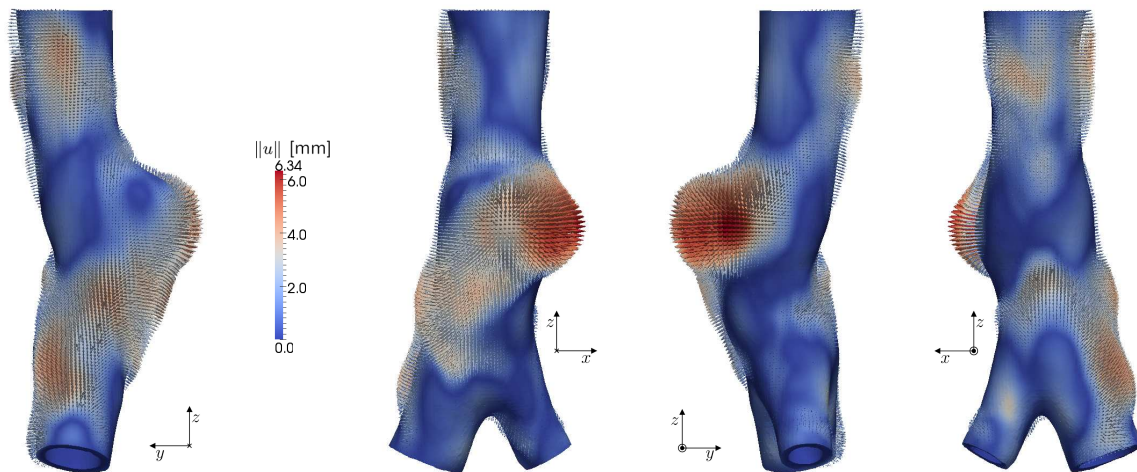


Figure 6.8: Displacement field that represents a mapping from the first CT scan to the second CT scan, the data is provided by Sebastian Kehl, Mechanics and High Performance Computing Group, Technische Universität München

The resulting displacement field is sketched in Figure 6.8. The arrows represent the displacement vectors and the color indicates the displacement magnitude. The maximum displacement magnitude is 6.34 mm, what corresponds to nearly one-third of the diameter of the healthy artery at the top. The maximum displacements are located in the aneurysm sac, which bulges further out. The displacements in the rest are considerably smaller. In two other regions, an expansion can be observed. One of these regions is located sideways and below the sac. The other one is located at the healthy artery at the top close to the boundary. The expansion in this area will be hard to reproduce, since the geometry is fixed at all ends.

To get a more detailed impression of the measured growth, the cutting planes that are defined in Figure 6.7 are utilized. The respective slices of the initial geometry that corresponds to the flying start configuration and the deformed outer surface resulting from the measured displacement field, the intermediate configuration, are sketched in Figure 6.9. The position of the respective other cut is also drawn in each picture to get a better impression of the exact position of the cutting planes and to be able correlate both cuts to each other. The enlargement of the aneurysm

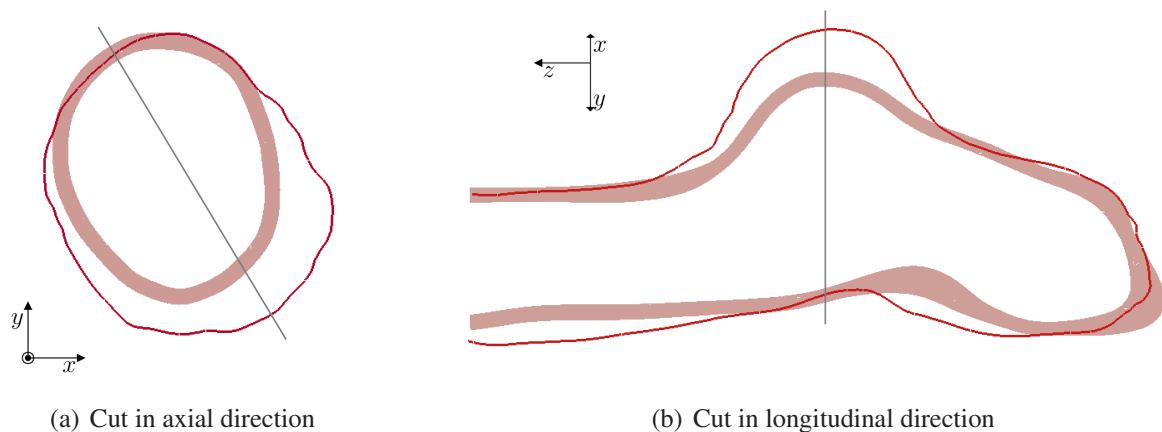


Figure 6.9: Slices of the initial geometry (rose) and the deformed outer surface resulting from the measured displacements (red), position of the cutting planes

sac is again highlighted. The diameter is increased by approximately one-fifth of its original value. The back of the aneurysm slightly moves in direction of the sac. This movement is not visible in Figure 6.8, since the arrows point inwards. The increase of the diameter of the main artery that was pointed out in the previous paragraph can be observed in the longitudinal cut. The other expansion below and sideways of the sac is not illustrated in the slices, since it is located in between the cutting planes. Hence, the slices are not suitable to depict all aspects of the growth of the aneurysm, but the contained information is sufficient to describe the main factors.

6.3.2 Uniform parameters

Within this section it is assumed that the growth parameters are constant over the whole domain. During the optimization within the academic setting, see Section 5.3.1, it was observed that the optimization of a uniform elastin content leads to the same results as when it is not included in the optimization. Hence, the elastin content is fixed to $\iota^e = 1$. To maximize the influence of the deformation of the aneurysm sac on the final parameter value, only nodes in the middle of the geometry are evaluated in the objective function. The so defined optimization problem results in a growth factor with the following value: $K_g^\sigma = 1.898$.

In Figure 6.10 one can see slices of the deformed aneurysm after two years of growth and of the deformed outer surface, when the measured displacement field is applied. For a better comparison of the improvement of the fit of the growth process after the inverse analysis, slices of the deformed outer surface that results of a growth simulation with $K_g^\sigma = 1$ are also depicted. In the axial cut, the results of the two simulations with different growth factors are nearly identical. The locality of the aneurysm sac in longitudinal direction is increased for the inversely defined growth factor. The shape of the grown aneurysm is better approximated. Nevertheless, both simulations underestimate the radial enlargement of the aneurysm sac. In the academic example, a smaller growth factor led to a larger enlargement of the aneurysm. Hence, a smaller growth factor than one would have been expected to induce a larger enlargement in this area. But a smaller growth factor does not lead to an improvement, what the optimization algorithm confirms.

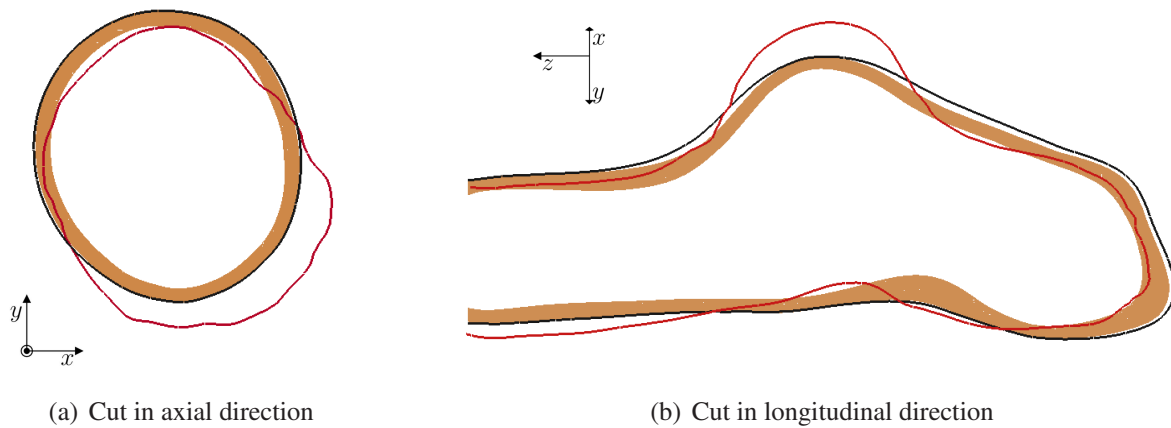


Figure 6.10: Slices of the deformed outer surface resulting from the measured displacements (red) and of the deformed solution at the intermediate configuration for different parameters: orange: uniform inverse growth factor $K_g^\sigma = 1.898$, and black: fixed growth factor $K_g^\sigma = 1$

The evolution of the diameter over time and the final value of the diameter is investigated in more detail in a subsequent section. In the patient-specific case the reference time curve is not known, contrary to the academic setting where the reference curve was known. Thus, it is not reasonable to plot the time curve of the evolution of the diameter for the uniform parameter alone, since it cannot be quantified. Hence, the results of all optimization variants are investigated together to yield a brief comparison of the results.

6.3.3 Spatially varying parameters with 20 patches

In order to better reproduce the enlargement of the aneurysm sac, the area around the sac is split into 18 patches. The patch distribution is shown in Figure 6.11. In contrast to the patch distributions in the academic example, see Figures 5.14 and 5.19, the boundaries between the patches are not straight lines, they have an irregular shape. This is a result of the unstructured mesh in contrast to the structured mesh in the academic example. Hence, it is even more important to

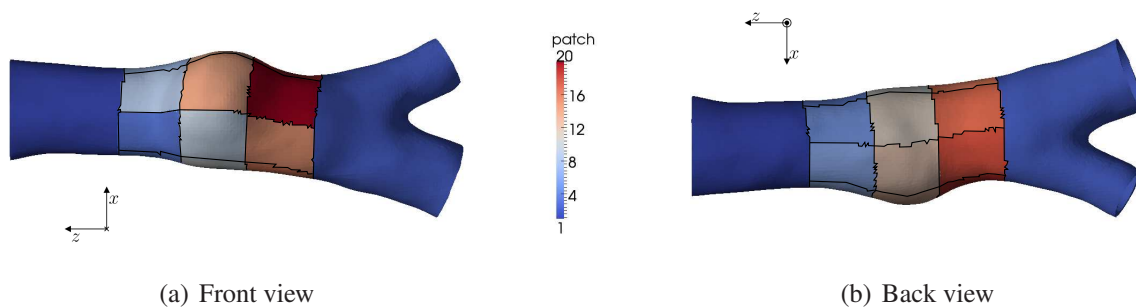


Figure 6.11: Definition of 20 patches for the patient-specific aneurysm

smooth the parameter values at the patch boundaries. Five smoothing steps are applied to the patchwise parameters.

Within the optimization algorithm, every fifth node of the outer surface is evaluated in the objective function. Both parameters, growth factor and elastin content, are design variables. In Figure 6.12 one can see the obtained distribution of both parameters. The irregular patch boundaries were smoothed by the smoothing operator, they are not visible in the final parameter distribution. In the back of the aneurysm sac the elastin content is the highest, i.e. $\iota^e = 1$. The minimum value is located in the patch at the aneurysm sac where the apex lies. The elastin content in the healthy arteries is smaller than one, i.e. $\iota^e = 0.56$ respectively $\iota^e = 0.33$.

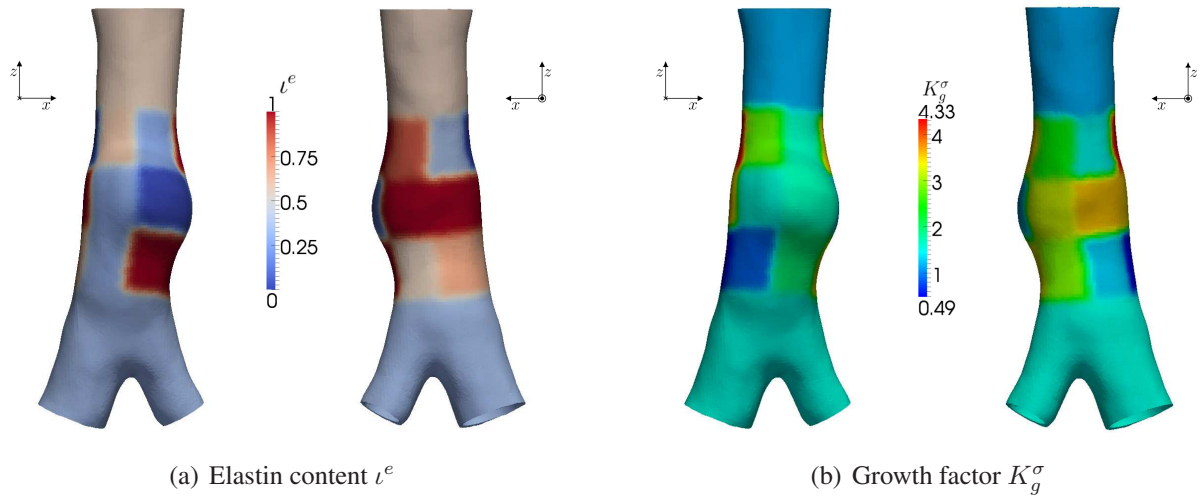


Figure 6.12: Obtained distribution of the elastin content ι^e and the growth factor K_g^σ for 20 patches, in each picture the left column depicts the front view, and the right column the back view

The maximum of the growth factor is located at the side of the aneurysm. The value at the back of the aneurysm is elevated similarly to the elevated value in the academic example, as shown in Figure 5.20(b). The minimum value is not located in the aneurysm sac but sideways and below of the sac. This area corresponds to a region where the measured displacements are elevated, as depicted in Figure 6.8. In this area a smaller growth factor leads to a larger enlargement. The value in the aneurysm sac, $K_g^\sigma = 1.684$, is smaller compared to most of the other patch values. It is also slightly smaller compared to the uniform value $K_g^\sigma = 1.898$.

In Figure 6.13 one can see the deformed geometry resulting from a growth simulation with the obtained parameter distribution. The deformed outer surface of the simulation with the inversely defined uniform growth factor is also sketched for a better comparison. The enlargement of the aneurysm sac is larger than the enlargement with the uniform growth factor, but it is still smaller than the measured displacements in this area. In the back of the aneurysm, the solution with the spatially varying parameters fits the measured displacements slightly better than the solution with the uniform parameter. In the other regions that are depicted in the slices, the change of the shape of the outer surface is small compared to the spatial variation of the growth factor, i.e. $K_g^\sigma \in [0.49, 4.33]$, and the local difference to the uniform value $K_g^\sigma = 1.898$.

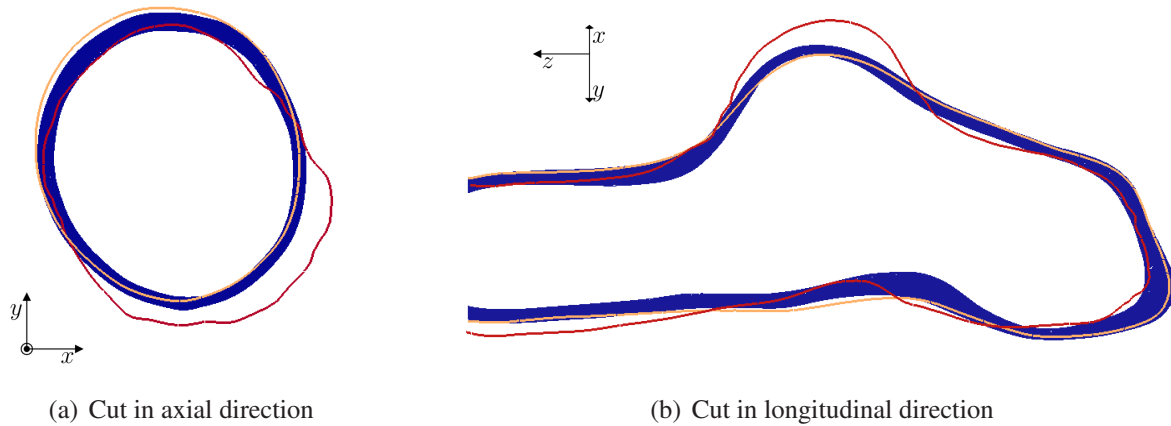


Figure 6.13: Slices of the deformed outer surface resulting from the measured displacements (red) and of the deformed solution at the intermediate configuration for different parameters: blue: inversely determined K_g^σ and ι^e with 20 patches, and orange: uniform inverse growth factor

6.3.4 Spatially varying parameters with 74 patches

Since a higher number of patches led to an improved approximation of the growth process in the academic example, as shown in Section 5.3.3, the number of patches is further increased. Every patch except the two patches of the healthy artery is divided into four new patches. The resulting 74 patches are depicted in Figure 6.14. The patch boundaries consist again of irregular shaped lines. To evaluate the Jacobian matrix as proposed in equation (4.5), 149 forward simulations have to be computed in each optimization step. With the help of nested parallelization all forward simulations can be computed simultaneously.

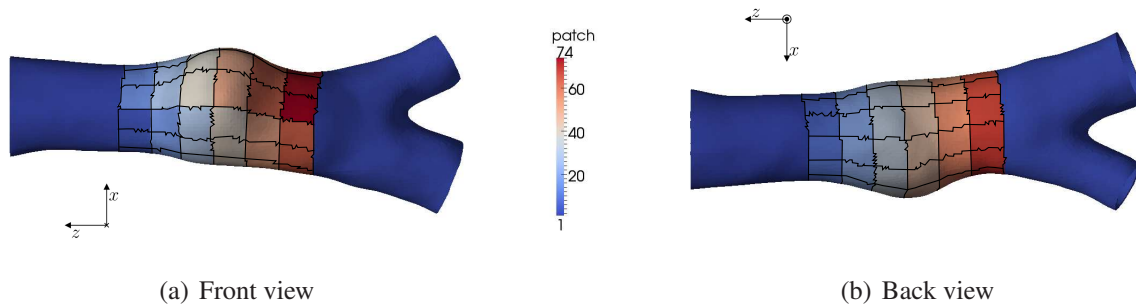


Figure 6.14: Definition of 74 patches for the patient-specific aneurysm

For the inverse determination of the parameters, again every fifth node of the outer surface is evaluated in the objective function. The final distribution of the elastin content can be seen in Figure 6.15. At the side of the aneurysm body the elastin content is elevated. In the sac of the aneurysm, it is decreased. All in all, there is no clear pattern visible. In one third of the patches the elastin content is nearly one and in one third it is nearly zero. In the last third of the patches the value lies in between. The elastin content in the healthy artery is reduced to a value of

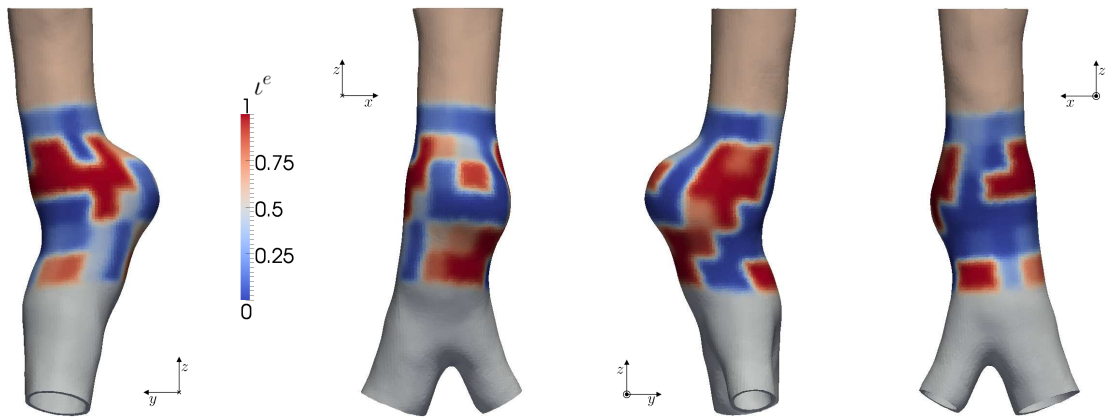


Figure 6.15: Obtained distribution of the elastin content l^e for 74 patches

approximately 0.5, the value of the upper patch is slightly higher and the value in the lower patch is slightly lower. The same qualitative behavior is observed with less patches, as shown in Figure 6.12(a).

In order to get a better correlation between the values of the elastin content of the different patches an additional regularization term can be included in the optimization problem. In the same way the well-posedness of the optimization problem is ensured during image registration, which is performed to obtain the measured displacement field. There an elastic regularization term is added to the actual optimization function, see equation (4.7). This approach leads to an additional algorithmic parameter within the optimization algorithm, the regularization factor, that has to be chosen carefully.

In Figure 6.16 one can see the spatial distribution of the growth factor. The maximum value of the color scale was reduced to a value such that a variation between most of the patches is visible. In two patches outliers were detected. Their values are $K_g^\sigma = 14.186$ and $K_g^\sigma = 16.199$. The outliers are located at the side of the aneurysm. The elastin content is zero in the respective patches. The minimum of the growth factor is located in the same spot as the minimum of the

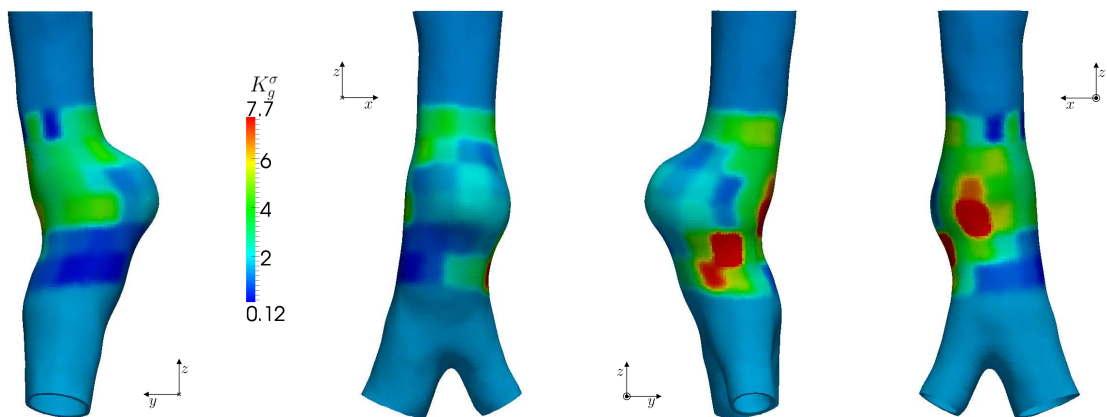


Figure 6.16: Obtained distribution of the growth factor K_g^σ for 74 patches

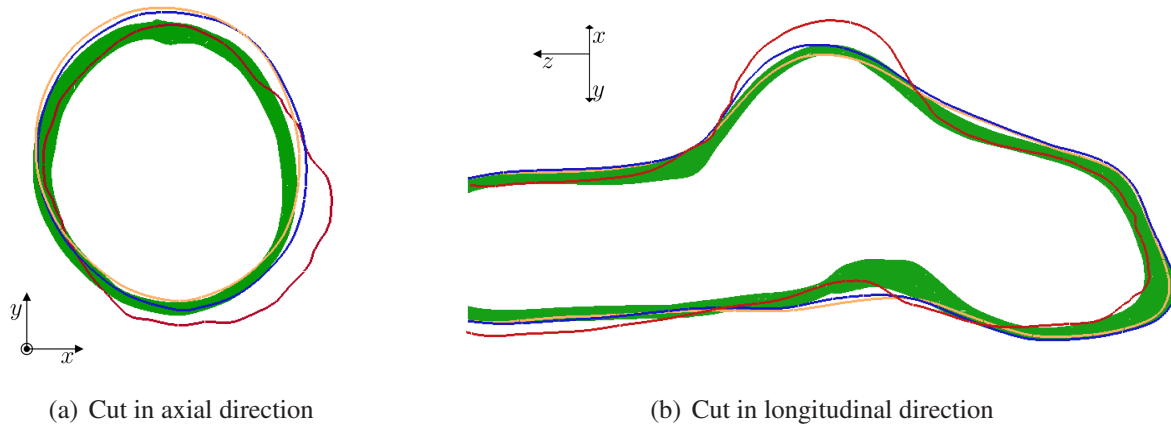


Figure 6.17: Slices of the deformed outer surface resulting from the measured displacements (red) and of the deformed solution at the intermediate configuration for different parameters: inversely determined K_g^σ and ι^e with 74 patches (green) and 20 patches (blue), and orange: uniform inverse growth factor

20 patch distribution, where the measured displacement magnitude is increased. The minimum value is smaller than before. The value in the aneurysm sac is approximately 1.99, which is higher than the uniform value $K_g^\sigma = 1.898$ and the value $K_g^\sigma = 1.684$ that was determined with 20 patches.

In Figure 6.17 one can see the resulting shape of the aneurysm after two years of growth. The deformed outer surfaces resulting from the parameter distributions of the previous optimization variants (P1 and P2) are also sketched to be able to better quantify the changes related to the different parameter distributions. The radial enlargement of the aneurysm sac is not improved. The maximum value is still smaller than the measured enlargement. The deformation at the back of the aneurysm can be better approximated. The back moves further in direction of the aneurysm sac. In the axial cut, it is visible that the aneurysm translates to the bottom left corner of the picture compared to the other solutions with the inversely determined parameters. The solution with the newly defined parameters better approximates the target shape of the aneurysm. This translation is related to the outlier patches of the growth factor, since one of these patches is located at the top right part of the wall sketched in the slice of the axial cut.

Since the refinement of the patches does not lead to an improvement of the radial enlargement in direction of the aneurysm sac, no further refinement is performed. It seems like the enlargement cannot be increased with a different distribution of the growth parameters. The small enlargement originates from a different source. The remodeling process is not yet dominating the growth process similar to the example of the formation of a saccular aneurysm in Section 3.3.7, where the enlargement was small in the beginning until a certain threshold was reached, see Figure 3.26(a). The density increase in the wall is still able to partially compensate the enlargement.

6.3.5 Investigation of the diameter

So far only the deformed shape of the aneurysm after growth of two years has been investigated. Within this section the time course of the development as well as the final values are further examined. The diameter of the aneurysm that is evaluated at the intersection line of the longitudinal and axial cutting planes as sketched in Figure 6.18(a) is a good measure of the growth gradient. Its evolution over time is plotted in Figure 6.18(a) for all three variants of the optimization listed in Table 6.2. In the beginning, especially the time curve of P3 oscillates (green curve). This oscillation reflects the influence of the missing history in the flying start configuration. The slope of all curves decreases with increasing time.

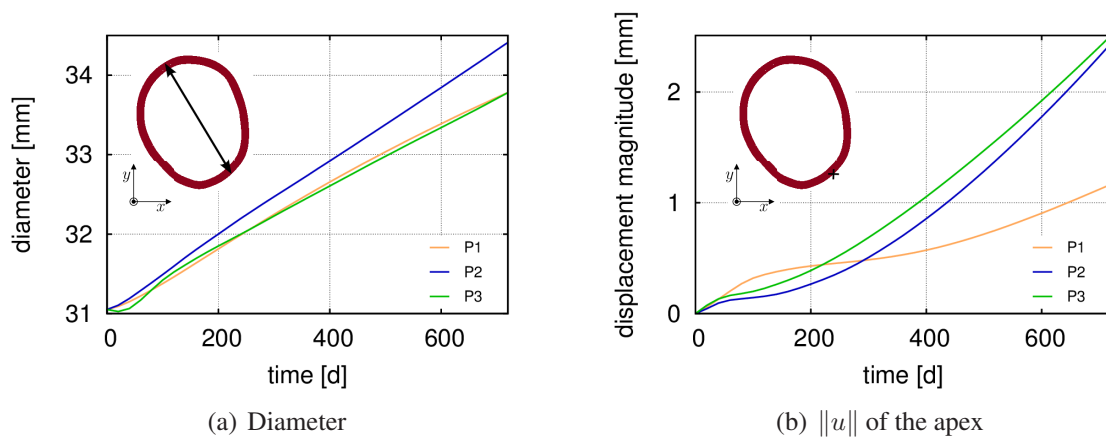


Figure 6.18: Definition of the diameter and position of the apex, evolution of diameter and displacement magnitude of the apex over time for growth simulations with parameters resulting from different optimization variants (see Table 6.2)

The simulation with the parameters from the 20 patch optimization (P2, blue curve) leads to the highest values. Thus, it is the closest to the measured diameter of the real grown aneurysm after two years of growth. The other two solutions have a nearly identical value at the end. This is surprising, since the solution with the most patches should fit the diameter the best. This behavior results from the better approximation of the deformation at the back of the aneurysm, see Figure 6.17, what results in a decrease of the diameter, since the back deforms in direction of the aneurysm sac. To exclude the influence of the back of the aneurysm, the displacement magnitude of the apex that reflects the enlargement of the aneurysm sac is also investigated.

The position of the apex and the evolution of the displacement magnitude at the apex over time are plotted in Figure 6.18(b). The influence of the missing history in the beginning is now visible in all three time curves. It has the largest influence when the uniform growth factor is utilized (orange curve). Hence, the displacement magnitude is the smallest, what corresponds to the observations in the previous sections. The other two time curves resemble each other. The solution with the highest number of patches leads to larger values. With increasing time, the curve of the solution with 20 patches gets closer to the green curve. Thus, the slope of the curve is higher in the end and will lead to larger values of the displacement magnitude, when the aneurysm grows for a longer period of time.

	diameter	deviation	$\ u\ $	deviation
measured	35.83 mm	—	5.666 mm	—
P1	33.78 mm	−5.7%	1.166 mm	−79%
P2	34.41 mm	−4.0%	2.438 mm	−57%
P3	33.78 mm	−5.7%	2.509 mm	−56%

Table 6.3: Final values of the diameter and the displacement magnitude of the apex for different optimization variants (see Table 6.2) and deviation from the measured value

To get more detailed information about the quality of the results at the final time, i.e. $t = t_2$, the values of the two quantities that are introduced in the previous paragraphs are listed in Table 6.3 for all optimization variants and for the measured displacement field. In all cases, the diameter is underestimated. In the best fit, a relative difference of 4 percent is achieved. Contrary to this small difference, the difference of the displacement magnitude at the apex is larger. The smallest relative difference is 56 percent. This is a higher value than the average deviation from the diameter, which cannot be solely explained by the difference of the order of magnitude of the respective absolute reference values. The better approximation of the diameter partially results from a compensation of the lower enlargement of the aneurysm sac by the approximation of the behavior at the back of the aneurysm, see Figure 6.17. The difficulties with the approximation of the enlargement of the aneurysm sac have already been seen in the slices of the final geometry, see Figure 6.17, but now they are also quantitatively described. Due to the latest development of the proposed methodology, a few challenges arising from the patient-specific application are yet to be resolved. In the previous and the following sections, valuable insights are gained that will be required for future improvements, which will be proposed at the end of this chapter.

6.4 Growth over a longer period of time

Within this section, growth of the patient-specific aneurysm over a period of four years is investigated in more detail. The growth parameter distribution that results from the optimization with the 74 patches (P3) is utilized. The capacity of a growth simulation with these parameters to predict the actual growth of the aneurysm is limited, since the enlargement of the aneurysm sac after two years of growth could not be reproduced. Nevertheless, the simulation is computed, since the results in the rest of the aneurysm were promising. Additionally, the simulation is utilized to get a better insight into the growth process and to be able to identify quantities that may help to improve the results of the optimization.

The reference values after two years of growth are also sketched to compare the results. After the initial variation due to the missing history, the diameter increases nearly linearly over time. After four years of growth, the diameter is larger than the reference value for two years of growth. This is the same for the displacement magnitude of the apex, where the difference at the end is even larger, since the slope of the curve is increasing with increasing time. Hence, the model is basically capable to reproduce the enlargement of the aneurysm sac, which is defined by the measured displacements. The enlargement is just too slow in this area. That means the enlargement has to be locally accelerated, since the enlargement in other regions was well ap-

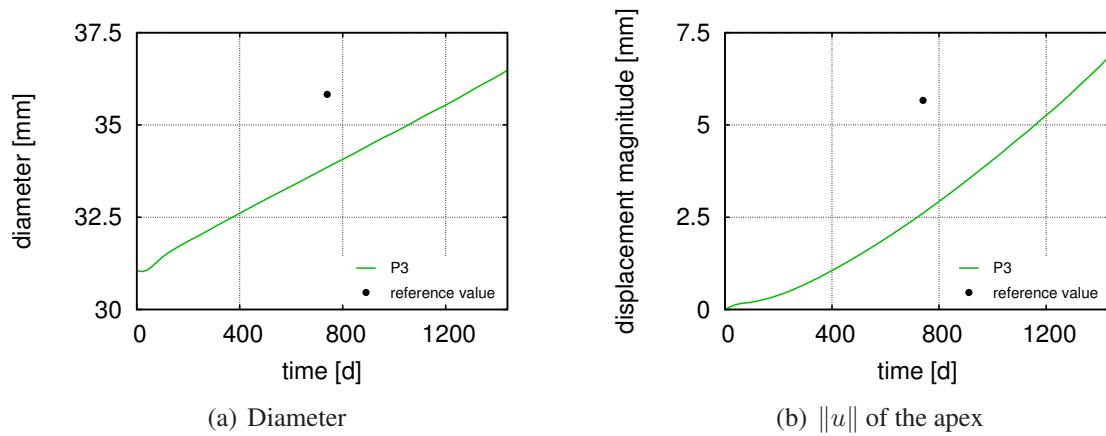


Figure 6.19: Evolution of diameter and displacement magnitude of the apex over time for the final parameter distribution with 74 patches and respective reference values

proximated. This can be achieved in different ways, for example the geometry may be adapted locally or other parameters of the growth model that have not been considered yet may be utilized as design variables in the optimization process. Two potential modifications will be discussed in the next section.

Up to now only the evolution of the diameter and the displacement magnitude over time are investigated. These quantities yield no information about the deformation of the whole aneurysm. Hence, slices of the deformed shape of the aneurysm after growth of four years are shown in Figure 6.20. For a better comparison, the deformed outer surface after two years of growth and the outer surface resulting from the measured displacements are also sketched. Both pictures confirm that the diameter is nearly identical to the measured diameter after two years of growth. The radial enlargement orthogonal to the diameter is larger as would be expected for growth

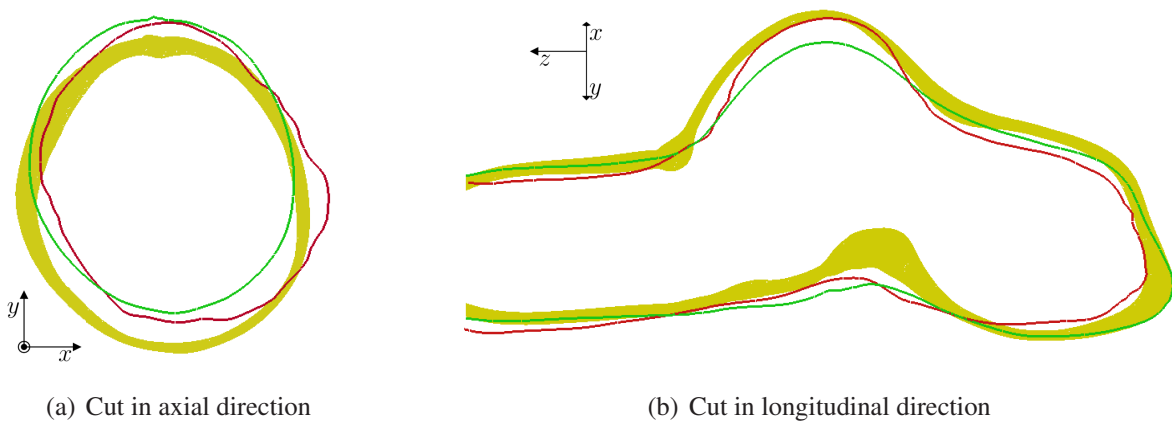


Figure 6.20: Slices of the deformed outer surface resulting from the measured displacements (red) and of the deformed solution after two (green) and four (yellow) years of growth for the inversely determined parameters with 74 patches

after twice the time period of the measured displacements. Hence, it is again highlighted that the adaptations of the optimization process have to lead to local changes of the deformation.

In the longitudinal cut, two regions stand out because of the thickness of the wall. At the transition between healthy and diseased part on top of the aneurysm, the wall gets thicker due to growth. At the back of the aneurysm, the increased thickness has several reasons. The thickness of the ILT is high there from the beginning, see Figure 6.9. Since the wall bulges out into the direction of the aneurysm sac in this area, the thickness is more emphasized. Additionally, a relatively high growth factor leads to a thickening of the wall next to the thick ILT.

To get a better impression of the growth process, the change of the reference density is plotted in Figure 6.21. There are areas where the mass increase is higher compared to the rest of the aneurysm. The growth factor in these areas is often higher than the growth factor in the surroundings, see Figure 6.16. The patches with outliers of the growth factor do not stand out alone, since the density is also increased in the adjacent patches. In the transition between the bulge of the aneurysm and the healthy artery, the aneurysm wall starts to buckle. There, strips of density increase and density decrease lie close together.

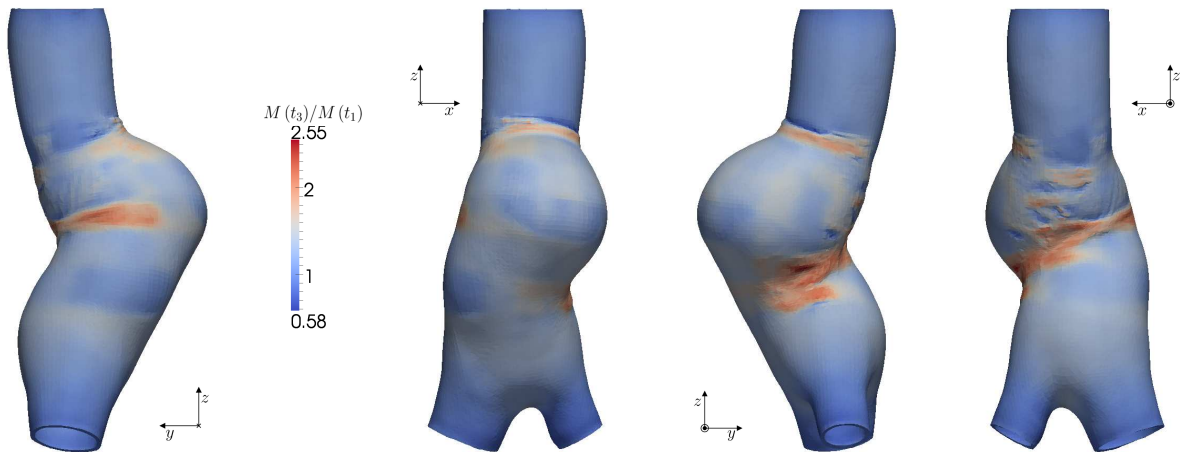


Figure 6.21: Relative change of the referential density at the predicted state, i.e. $t = t_3$

To investigate how growth influences stress, the von Mises stress in the flying start configuration and in the predicted configuration after four years of growth are sketched in Figure 6.22. The maximum value of the color scale is defined by the 99th percentile of the von Mises stress of the initial loaded state, i.e. 205 kPa. The 99th percentile after four years of growth is 3.5 percent smaller, its value is 198 kPa. Hence, the maximum stress decreases slightly after growth. The stress peak on top of the aneurysm at the transition to the healthy artery in the flying start configuration moves upward during growth and gets slightly smaller. A minimum of stress arises next to it. The stress pattern in this region matches the buckling that was observed in Figure 6.21. In other areas of the aneurysm, stress peaks evolve during growth. For example at the side of the aneurysm where the density increase was already elevated, the stress is elevated too, as shown in the left pictures of Figure 6.21 and Figure 6.22. Additionally, the stress is elevated in the region sideways and below the aneurysm sac, where the growth factor has its minimum value, see Figure 6.16. Thus, the tissue is not able to compensate as much of the increase of stress with an increase of mass as it could with a higher growth factor similar to the other patches.

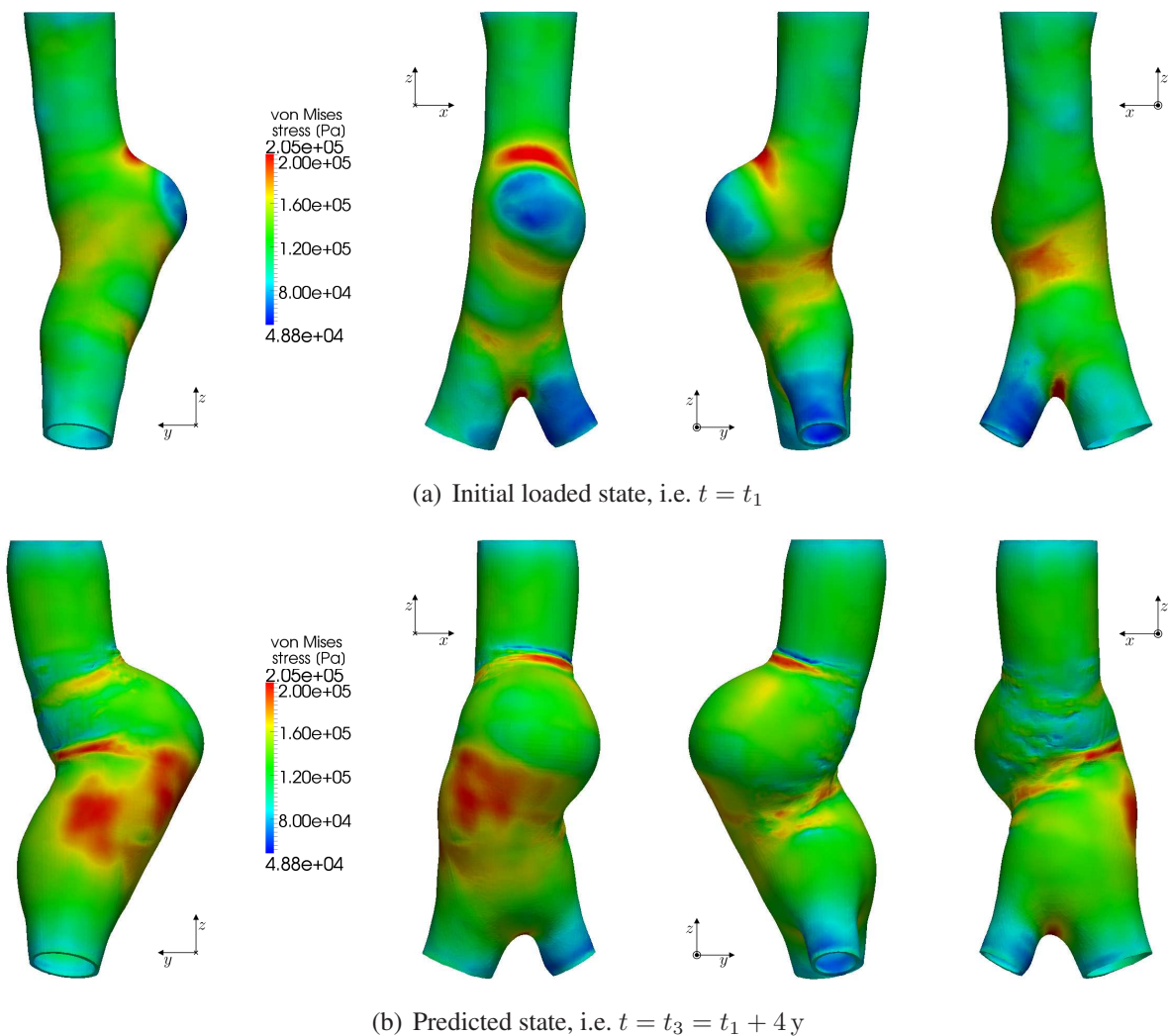


Figure 6.22: Von Mises stress at different points in time

The adaptation of the growth parameters to the larger enlargement in this area results in higher stresses.

6.5 Potential modifications in the optimization process

In the preceding sections, it has become apparent that the presented optimization process has to be modified to better approximate the growth of the presented patient-specific geometry. Two potential modifications are discussed within this section. In the academic example, the wall of the aneurysm sac was thinner than the wall in the rest of the aneurysm, see Figure 5.2. Up to now it was assumed that the thickness of the wall of the patient-specific aneurysm is constant. Hence, the thickness of the wall could be adapted similarly to the academic setting. Since it is difficult to predict the proper thickness distribution beforehand, the thickness would have to be included in the optimization process as a design variable. This would lead to a new type of

design variable, since the thickness is a geometric quantity and not a material parameter. Thus, the geometry would have to be adapted during the optimization process.

Additionally to the modification of the geometry, the remaining parameters of the growth model should be reconsidered. For example a reduction of the lifetime of collagen could accelerate remodeling, since the oldest fibers that have the highest stretch are faster degraded. However, the influence of a local variation of the lifetime on the simulation results is difficult to quantify, since it is manifold. To evaluate stress, equation (3.48) is discretized in time resulting in equation (3.51). Therefore, the time interval $[t - t_{lf}, t]$ is split into discrete intervals $[t_l, t_{l+1}]$. This split has to be performed globally, since only one time step size Δt can be utilized in the simulation. Thus, a local variation of t_{lf} will not influence this split.

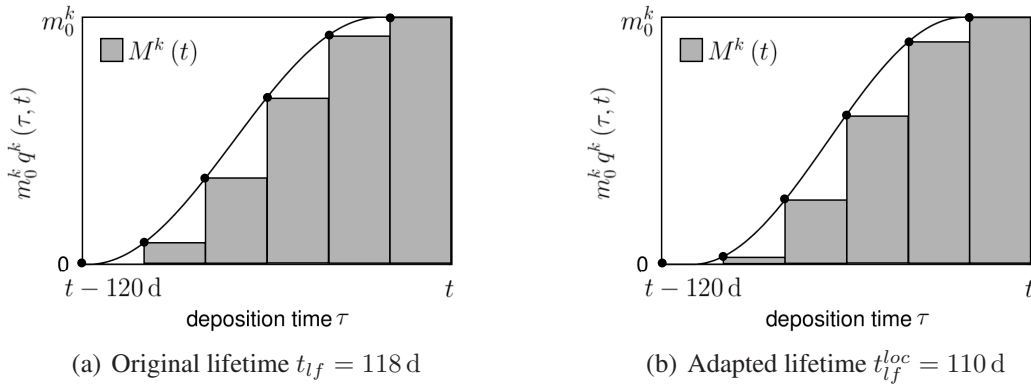


Figure 6.23: Discrete integration over time to compute the reference density $M^k(t)$ for different lifetimes of collagen with a time step size of $\Delta t = 20$ d

In Figure 6.23 the integration over time to compute the reference density is sketched for a large time step $\Delta t = 20$ d for two different values of the lifetime of collagen, i.e. $t_{lf} = 118$ d and $t_{lf}^{loc} = 110$ d. The large time step size is chosen to emphasize the influence of the discretization in time. If the difference between the reduced local lifetime from the global lifetime is smaller than the time step size, i.e. $t_{lf} - t_{lf}^{loc} < \Delta t$, the oldest fibers will still be degraded at the same point in time. Just the value of $q^k(t_l, t)$ changes, as it is depicted in Figure 6.23. Hence, the basal density production rate has to be adapted locally, since the basal density production rate is defined in equation (3.38) such that the density remains constant during remodeling. Otherwise, the initial reference density varies within the aneurysm. The density production will be influenced to, since it depends on the basal density production rate, see equation (3.42). Thus, it cannot be guaranteed that a local adaptation of the lifetime leads to the desired result.

7 Summary and outlook

A three-dimensional computational method to predict the growth of an aneurysm was developed in the present work. The method consists of the following three essential components that were incorporated in the finite element framework BACI: the computational growth model, the characterization of the initial state, and the calibration of the growth model by solving an optimization problem. To the best of the author's knowledge, this is the first methodology that calibrates the computational growth model not only to accurately reproduce the given growth process but also to predict the future development of a patient-specific aneurysm.

The first step is a three-dimensional constraint mixture model that was developed to model growth and remodeling. Biological relevant examples showed the capabilities of the proposed model. Among others, the computational growth model was able to induce the formation of an aneurysm after an initial loss of elastin. The stability of the homeostatic state led to a local enlargement of the artery, which was restricted to a region close to the initial degradation zone. In the second step, an academic example that was as close as possible to a realistic setting was defined to characterize the initial state. The example consists of the formation of an aneurysm after an initial loss of elastin in an idealized artery. This simulation was utilized as reference. After a pronounced aneurysm arose, the deformed geometry is taken as the starting point for a new growth simulation, where the past deformation is neglected to mimic the patient-specific case. With this setting it was feasible to quantify the influence of the missing mapping from the healthy artery to the aneurysm on the development of the aneurysm and on the growth parameters. For example, it was predicted that the optimal growth factor would deviate from the reference value. Moreover, an approximation of the history of the deformation was developed and its influence on the development of the aneurysm was quantified. The adaptation of the history ensured the similarity of the initial geometry and the initial loaded configuration. Hence, no special treatment of the prestress of the patient-specific geometry was necessary.

In the third step, a novel idea for parameterization of the design variables was introduced to represent the spatial distribution of the growth parameters. With the help of the optimization algorithm, the growth model was calibrated to match the reference simulation after one year of growth. The increasing complexity of the spatial distribution of the growth parameters improved the reproduction of the reference solution. The best result approximated the diameter with more than 99 percent accuracy. Furthermore, the prediction of the enlargement with the determined parameters matched the enlargement of the reference aneurysm. The deviation of the diameter from the reference value was less than one percent after two years of growth. Hence, the proposed methodology was validated, since the prediction of growth was correct. Density change and stress distribution of the final state were not in agreement with the reference results due to the lack of information about the deformation preceding the initial state.

To use the proposed growth and remodeling approach for patient-specific geometries, collagen fiber directions had to be defined. A procedure that yields a reasonable distribution of fiber directions was developed and successfully applied to the patient-specific geometry of an aneurysm

of a 62 years old male patient. Moreover, a small section of the healthy artery adjacent to the aneurysm was utilized to define homeostatic variables for the whole geometry. Additional safety mechanisms were included in the growth and remodeling model to increase the stability of the algorithm. For the calibration of the growth model, image registration was utilized to define a displacement field that depicts the deformation between two consecutive computed tomography (CT) scans. The solution of an optimization problem with the resulting displacement field as reference solution yielded spatial distributions of the growth parameters. The simulations with the determined parameters were able to partially reproduce the displacement field. The deviation of the diameter from the measured value was four percent for the best fit. The parameters that fit best for the displacement field are used in the finite element simulation to gain insights into the further development of the patient-specific aneurysm and to characterize the predicted state after four years of growth.

In summary, growth of the reference aneurysm has been successfully reproduced under realistic conditions. Due to the latest development of the proposed methodology, a few challenges arising from the patient-specific application are yet to be resolved, but valuable insights are gained that will be required for future improvements. Some issues were already emphasized at several places within the main part of this thesis and possible remedies were proposed. The stability of the definition of the history can be increased such that it is also applicable to patient-specific geometries. The optimization process can be modified to improve the reproduction of the given growth process. The growth model itself can be extended by accounting for nutrients that are available during growth. The concentration of the nutrients can be modeled as a scalar transport problem (Yoshihara et al. [111]).

Currently, the measured displacement field and the growth parameters are determined by solving two separate optimization problems. The image registration that defines the measured displacement field is performed independently of the growth model; it is assumed that the structure deforms elastically to fit the requested deformation. The procedure is improved when the growth and remodeling model is included in the image registration. That means during image registration the growth parameters and the displacement field are determined at once. In such a case, the resulting optimization problem will not be in the form of a least squares problem. Hence, the Levenberg-Marquardt algorithm cannot be applied, and a new optimization algorithm that also accounts for the transient behavior of the growth problem has to be utilized.

In patient-specific simulations, the results are subjected to uncertainties that originate from various sources. For example, it is hard to access the exact constitutive properties that correspond to a specific patient. In the simulations computed within this work, the constitutive parameters, the wall thickness of the aneurysms, and the measured displacement field are some of the potential sources of uncertainties. To obtain a more reliable prediction and to quantify the influence of these uncertainties on the prediction, an uncertainty quantification method is necessary, which is applicable to large biomechanical problems like the one recently presented in Biehler et al. [11]. Finally, the proposed methodology should be applied to many patient-specific examples to obtain further insights into the development of different abdominal aortic aneurysms and to better quantify the capabilities of the methodology. The time span between the first two CT scans should preferably be larger than one year to better calibrate the growth model, since the missing history influences the time course of the development especially in the beginning. At best, the methodology can be further validated with a patient specific example where at least three consecutive CT scans exist.

A Appendix

A.1 Wall shear stress

In this chapter, the wall shear stress dependent term $-K_g^\tau \left(\frac{\tau_w^k(t)}{\tau_{w;h}} - 1 \right)$ in the mass density production rate (3.42) is further investigated. Therefore, a digression in fluid mechanics is needed, since wall shear stress (WSS) is a fluid quantity.

A.1.1 Wall shear stress in fluid mechanics

In order to solve the fluid equations analytical, a simplified geometry is examined. The artery is modeled as a straight circular tube with radius R . In the following, a fully-developed incompressible axisymmetric flow (Hagen-Poiseuille flow) through the cylinder is assumed. The fluid is considered as Newtonian, which is not always the case for blood (Katritsis et al. [52]). Because of the symmetry of the problem, only the equation of the Navier-Stokes equations in cylindrical coordinates that denotes the equilibrium in axial direction remains (Schlichting and Gersten [84]) yielding

$$\mu \left(\frac{d^2 u}{dr^2} + \frac{1}{r} \frac{du}{dr} \right) = \frac{dp}{dz} \quad (\text{A.1})$$

with u denoting the velocity of the fluid in axial direction z , μ dynamic viscosity, and p pressure. The velocity u only depends on the radial position r , i.e. $u = u(r)$. As boundary condition a no-slip condition at $r = R$ is applied. The analytical solution of this problem is defined as follows

$$u(r) = \frac{dp}{dz} \frac{1}{4\mu} (r^2 - R^2). \quad (\text{A.2})$$

Since the flow is fully developed, the pressure gradient is independent of z and can thus be replaced by the difference of pressure at the inlet p_1 and outlet p_2 , leading to

$$u(r) = \frac{p_1 - p_2}{4\mu L} (R^2 - r^2) \quad (\text{A.3})$$

with L denoting the axial length of the cylinder. The volumetric flow rate Q can be expressed as

$$Q = \frac{\pi R^4 (p_1 - p_2)}{8\mu L}. \quad (\text{A.4})$$

Equations (A.3) and (A.4) lead to the following equation for the velocity

$$u(r) = \frac{2Q}{\pi R^4} (R^2 - r^2). \quad (\text{A.5})$$

For a Newtonian fluid the shear stress is defined as

$$\tau_{12} = \mu \frac{du}{dr} = \frac{4\mu Q}{\pi r^3}. \quad (\text{A.6})$$

The maximal value is located at the wall and is called *wall shear stress*

$$\tau_w = \frac{4\mu Q}{\pi R^3}. \quad (\text{A.7})$$

A.1.2 Application to growth

In this section, the consequences for the growth model are investigated. Since only a structural simulation is performed, there exists no information about the volumetric flow rate. Thus, it is assumed to be constant. With this assumption the quotient between current and homeostatic WSS simplifies to

$$\frac{\tau_w(t)}{\tau_{w;h}} = \frac{4\mu Q \pi R_i^3}{\pi r_i^3 4\mu Q} = \left(\frac{R_i}{r_i} \right)^3 \quad (\text{A.8})$$

with R_i denoting the undeformed and r_i the deformed inner radius of the structure. This equation is only defined at the inner surface of the vessel wall. The endothelial cells sense there the changes in flow and trigger the growth of the vessel. Hence, WSS is defined to be constant throughout the wall. If the blood pressure is altered and the radius increases, the quotient is smaller than one. In this case, a mass increase is expected, which leads to the minus in front of K_g^τ in the mass production rate equation (3.42).

For more complex geometries, equation (A.8) can be evaluated with the help of a centerline to estimate the WSS. This value is not exact, since equation (A.7) only holds for a flow in a cylindrical tube. For true values, one has to perform a fluid-structure interaction simulation that is not practicable. For abdominal aortic aneurysms, WSS does not play an important role, since the arterial wall is shielded from the flow by the intraluminal thrombus. Thus, the endothelial cells cannot sense WSS and this term is omitted in the density production. The shape of a healthy artery is close to a cylinder. Hence, equation (A.8) can be used in these examples. But one has to keep in mind that blood is generally not Newtonian and the flow is pulsative, which contradicts two basic assumptions at the beginning of the derivation of equation (A.8).

Another possibility to include WSS in the mass production rate is the ratio $C(t)$ of constrictors to dilators, which is also part of the active stress in smooth muscle cells (Valentín et al. [103]). The ratio is defined as

$$C(t) = C_B - C_S \left(\frac{\tau_w(t)}{\tau_{w;h}} - 1 \right) \quad (\text{A.9})$$

with C_B denoting the basal constrictor to dilator ratio and C_S a scaling factor. $\frac{C(t)-C_B}{C_B}$ is minus the wall shear stress term in the mass production rate and can replace this term. Thus, the minus in front of K_g^τ vanishes.

A.2 Derivatives for the implicit integration within the constraint mixture model

In this chapter, several derivatives that are needed to solve the linearizations of the equations in Section 3.3.2.2 are given. For the local Newton iteration to compute stress and density production in a Gauss point, the linearization of the stress equation (3.59) is used. There are two derivatives missing:

$$\begin{aligned} \frac{\partial m^k}{\partial \mathbf{S}_{ij}^g} &= \frac{\partial \left\{ m_0^k \left[1 + K_g^\sigma \left(\frac{\sigma^k(\mathbf{S}^g)}{\sigma_h} - 1 \right) - K_g^\tau \left(\frac{\tau_w}{\tau_{w;h}} - 1 \right) \right] \right\}}{\partial \mathbf{S}_{ij}^g} \\ &= \frac{m_0^k K_g^\sigma}{2\sigma_h \sigma^k(t) (\lambda^k(t))^2 \det \mathbf{C}} \left[(\mathbf{C} \mathbf{a}_0^k)_i (\mathbf{C} \mathbf{S}^g \mathbf{C} \mathbf{a}_0^k)_j + (\mathbf{C} \mathbf{S}^g \mathbf{C} \mathbf{a}_0^k)_i (\mathbf{C} \mathbf{a}_0^k)_j \right], \quad (\text{A.10}) \end{aligned}$$

$$\frac{\partial \mathbf{S}^g}{\partial m^k} = \frac{\partial \mathbf{S}^k}{\partial m^k} + \frac{\partial \mathbf{S}^{vol}}{\partial m^k} = \frac{q^k(t, t) \Delta t}{\rho_0} \left[\frac{\partial \Psi^k(I_4^k(t, t))}{\partial I_4^k(t, t)} \left(\frac{\lambda_{pre}^k}{\lambda^k(t)} \right)^2 \mathbf{A}_0^k - \kappa J \mathbf{C}^{-1} \right]. \quad (\text{A.11})$$

The second derivative depends on the choice of the growth stress \mathbf{S}^g . The result given here is only valid for $\sigma^g = \sigma$. To compute the constitutive matrix \mathbb{C}^g defined in equation (3.61) the derivative of the density production rate with respect to the Cauchy-Green tensor is required, yielding

$$\begin{aligned} \frac{\partial m^k}{\partial \mathbf{C}_{ij}} &= \frac{m_0^k K_g^\sigma}{2\sigma_h} \left[\frac{(\mathbf{a}_0^k)_i (\mathbf{S}^g \mathbf{C} \mathbf{S}^g \mathbf{C} \mathbf{a}_0^k)_j + (\mathbf{S}^g \mathbf{C} \mathbf{S}^g \mathbf{C} \mathbf{a}_0^k)_i (\mathbf{a}_0^k)_j + (\mathbf{S}^g \mathbf{C} \mathbf{a}_0^k)_i (\mathbf{S}^g \mathbf{C} \mathbf{a}_0^k)_j}{\sigma^k(t) (\lambda^k(t))^2 \det \mathbf{C}} \right] \\ &\quad - \frac{m_0^k K_g^\sigma}{2\sigma_h} \sigma^k(t) \left(\frac{(\mathbf{a}_0^k)_i (\mathbf{a}_0^k)_j}{(\lambda^k(t))^2} + \mathbf{C}_{ij}^{-1} \right). \quad (\text{A.12}) \end{aligned}$$

A.3 Definition of the elastin degradation area for the formation of an aneurysm

In this chapter, the exact definition of the degradation areas shown in Figure 3.24 and used to trigger growth of an aneurysm is given. The first two functions depend on the axial position z that is located in the interval $[-75, 75]$ and the azimuthal angle ϕ . This angle is defined as $\phi = \text{atan2}\left(\frac{y}{x}\right)$, since the center of the cylinder corresponds to the origin. For simplicity the units are omitted in the following. The axial position is given in mm and the angle in radians. For the rectangular shape, see Figure 3.24(a), the following function is used

$$\iota_{\text{rect}}^e = 1.0 - f_{\text{rect}}^z(z) f_{\text{rect}}^\phi(\phi) \quad (\text{A.13})$$

with

$$f_{\text{rect}}^z(z) = \begin{cases} 1 & \text{for } -12 \leq z \leq 12 \\ \frac{1}{2} [1 - \cos\left(\frac{z+16}{4}\pi\right)] & \text{for } -16 \leq z < -12 \\ \frac{1}{2} [1 + \cos\left(\frac{z-12}{4}\pi\right)] & \text{for } 12 < z \leq 16 \\ 0 & \text{else} \end{cases} \quad (\text{A.14})$$

and

$$f_{\text{rect}}^\phi(\phi) = \begin{cases} 1 & \text{for } -0.5\pi \leq \phi \leq -0.25\pi \\ \frac{1}{2} [1 - \cos\left(\frac{\phi+0.55\pi}{0.05\pi}\right)] & \text{for } -0.55\pi \leq \phi < -0.5\pi \\ \frac{1}{2} [1 + \cos\left(\frac{\phi+0.25\pi}{0.05\pi}\right)] & \text{for } -0.25\pi < \phi \leq -0.2\pi \\ 0 & \text{else} \end{cases}. \quad (\text{A.15})$$

The elastin content for the wedge shaped area, see Figure 3.24(b), has a similar form, i.e.

$$\iota_{\text{wedge}}^e = 1.0 - f_{\text{wedge}}(z, \phi) \quad (\text{A.16})$$

with

$$f_{\text{wedge}}(z, \phi) = \begin{cases} 1 & \text{for } -12g(\phi) \leq z \leq 12g(\phi) \\ \frac{1}{2} \left[1 - \cos\left(\frac{z+16g(\phi)}{4g(\phi)}\pi\right) \right] & \text{for } -16g(\phi) \leq z < -12g(\phi) \\ \frac{1}{2} \left[1 + \cos\left(\frac{z-12g(\phi)}{4g(\phi)}\pi\right) \right] & \text{for } 12g(\phi) < z \leq 16g(\phi) \\ 0 & \text{else} \end{cases} \quad (\text{A.17})$$

and

$$g(\phi) = 1 - \frac{3|\phi|}{4\pi}. \quad (\text{A.18})$$

The elastin content for the circles, see Figure 3.24(c), is defined through two circles around the coordinates $(12, 0, 10)$ and $(-12, 0, -10)$. If the distance of the Gauss point to one of the centers is smaller than 10 the elastin content is zero, if it is larger than 15 for both circles it is one. Between the two radii a transition with the cos function similar to (A.14) is applied.

Bibliography

- [1] Alford, P.W., Humphrey, J.D. and Taber, L.A., Growth and remodeling in a thick-walled artery model: effects of spatial variations in wall constituents, *Biomechanics and Modeling in Mechanobiology* **7**, 245–262, 2008.
- [2] Ambrosi, D. and Guillou, A., Growth and dissipation in biological tissues, *Continuum Mechanics and Thermodynamics* **19**, 245–251, 2007.
- [3] Ambrosi, D., Ateshian, G.A., Arruda, E.M., Cowin, S.C., Dumais, J., Goriely, A., Holzapfel, G.A., Humphrey, J.D., Kenkemer, R., Kuhl, E., Olberding, J.E., Taber, L.A. and Garikipati, K., Perspectives on biological growth and remodeling, *Journal of the Mechanics and Physics of Solids* **59**, 863–883, 2011.
- [4] Ambrosi, M. and Mollica, F., On the mechanics of a growing tumor, *International Journal of Engineering Science* **40**, 1297–1316, 2002.
- [5] Ateshian, G.A. and Humphrey, J.D., Continuum mixture models of biological growth and remodeling: Past successes and future opportunities, *Annual Review of Biomedical Engineering* **14**, 97–111, 2012.
- [6] Baek, S., Rajagopal, K.R. and Humphrey, J.D., Competition between radial expansion and thickening in the enlargement of an intracranial saccular aneurysm, *Journal of Elasticity* **80**, 13–31, 2005.
- [7] Baek, S., Rajagopal, K.R. and Humphrey, J.D., A theoretical model of enlarging intracranial fusiform aneurysms, *Journal of Biomechanical Engineering* **128**, 142–149, 2006.
- [8] Baek, S., Gleason, R.L., Rajagopal, K.R. and Humphrey, J.D., Theory of small on large: Potential utility in computations of fluid-solid interactions in arteries, *Computer methods in applied mechanics and engineering* **196**, 3070–3078, 2007.
- [9] Baek, S., Zambrano, B.A., Choi, J. and Lim, C.-Y., Growth prediction of abdominal aortic aneurysms and its association of intraluminal thrombus, In *11th. World Congress on Computational Mechanics*, 2014.
- [10] Bel-Brunon, A., Kehl, S., Martin, C., Uhlig, S. and Wall, W.A., Numerical identification method for the non-linear viscoelastic compressible behavior of soft tissue using uniaxial tensile tests and image registration - application to rat lung parenchyma, *Journal of the Mechanical Behavior of Biomedical Materials* **29**, 360–374, 2014.
- [11] Biehler, J., Gee, M.W. and Wall, W.A., Towards efficient uncertainty quantification in complex and large scale biomechanical problems based on a bayesian multi fidelity scheme, *Biomechanics and Modeling in Mechanobiology* **14**, 489–513, 2015.

- [12] Bonet, J. and Wood, R.D., *Nonlinear Continuum Mechanics for Finite Element Analysis*, Cambridge University Press, 2008.
- [13] Cardamone, L., Valentín, A., Eberth, J.E. and Humphrey, J.D., Origin of axial prestretch and residual stress in arteries, *Biomechanics and Modeling in Mechanobiology* **8**, 431–446, 2009.
- [14] Cardamone, L., Valentín, A., Eberth, J.F. and Humphrey, J.D., Modelling carotid artery adaptations to dynamic alterations in pressure and flow over the cardiac cycle, *Mathematical Medicine and Biology* **27**, 343–371, 2010.
- [15] Carmo, M., Colombo, L., Bruno, A., Corsi, F.R.M., Roncoroni, L., Cuttin, M.S., Radice, F., Mussini, E. and Settembrini, P.G., Alteration of elastin, collagen and their cross-links in abdominal aortic aneurysms, *European Journal of Vascular and Endovascular Surgery* **23**, 543–549, 2002.
- [16] Chase, A.J. and Newby, A.C., Regulation of matrix metalloproteinase (matrixin) genes in blood vessels: A multi-step recruitment model for pathological remodelling, *Journal of Vascular Research* **40**, 329–343, 2003.
- [17] Choke, E., Cockerill, G., Wilson, W.R.W., Sayed, S., Dawson, J., Loftus, I. and Thompson, M.M., A review of biological factors implicated in abdominal aortic aneurysm rupture, *European Journal of Vascular and Endovascular Surgery* **30**, 227–244, 2005.
- [18] Cowin, S.C., The specific growth rates of tissues: A review and a re-evaluation, *Journal of Biomechanical Engineering* **133**, 041001, 2011.
- [19] de Souza Neto, E.A., Perić, D., Dutko, M. and Owen, D.R.J., Design of simple low order finite elements for large strain analysis of nearly incompressible solids, *International Journal of Solids and Structures* **33**, 3277–3296, 1996.
- [20] Epstein, M. and Maugin, G.A., Thermomechanics of volumetric growth in uniform bodies, *International Journal of Plasticity* **16**, 951–978, 2000.
- [21] Figueroa, C.A., Baek, S., Taylor, C.A. and Humphrey, J.D., A computational framework for fluid-solid-growth modeling in cardiovascular simulations, *Computer Methods in Applied Mechanics and Engineering* **198**, 3583–3602, 2009.
- [22] Fridez, P., Zulliger, M., Bobard, F., Montorzi, G., Miyazaki, H., Hayashi, K. and Stergiopoulos, N., Geometrical, functional, and histomorphometric adaptation of rat carotid artery in induced hypertension, *Journal of Biomechanics* **36**, 671–680, 2003.
- [23] Fung, Y.C., *Biomechanics: Motion, Flow, Stress, and Growth*, Springer, 1990.
- [24] Garikipati, K., The kinematics of biological growth, *Applied Mechanics Reviews* **62**, 030801, 2009.
- [25] Garikipati, K., Arruda, E.M., Grosh, K., Narayanan, H. and Calve, S., A continuum treatment of growth in biological tissue: The coupling of mass transport and mechanics, *Journal of the Mechanics and Physics of Solids* **52**, 1595–1625, 2004.

-
- [26] Gasser, T.C., Görgülü, G., Folkesson, M. and Swedenborg, J., Failure properties of intraluminal thrombus in abdominal aortic aneurysm under static and pulsating mechanical loads, *Journal of Vascular Surgery* **48**, 179–188, 2008.
- [27] Gee, M.W., Reeps, C., Eckstein, H.H. and Wall, W.A., Prestressing in finite deformation abdominal aortic aneurysm simulation, *Journal of Biomechanics* **42**, 1732–1739, 2009.
- [28] Gee, M.W., Förster, Ch. and Wall, W.A., A computational strategy for prestressing patient-specific biomechanical problems under finite deformation, *International Journal for Numerical Methods in Biomedical Engineering* **26**, 52–72, 2010.
- [29] Gleason, R.L., Taber, L.A. and Humphrey, J.D., A 2-D model of flow-induced alterations in the geometry, structure, and properties of carotid arteries, *Journal of Biomechanical Engineering* **126**, 371–381, 2004.
- [30] Göktepe, S., Abilez, O.J. and Kuhl, E., A generic approach towards finite growth with examples of athlete’s heart, cardiac dilation, and cardiac wall thickening, *Journal of the Mechanics and Physics of Solids* **58**, 1661–1680, 2010.
- [31] Göktepe, S., Abilez, O.J., Parker, K.K. and Kuhl, E., A multiscale model for eccentric and concentric cardiac growth through sarcomerogenesis, *Journal of Theoretical Biology* **265**, 433–442, 2010.
- [32] Goriely, A. and Ben Amar, M., On the definition and modeling of incremental, cumulative, and continuous growth laws in morphoelasticity, *Biomechanics and Modeling in Mechanobiology* **6**, 289–296, 2007.
- [33] Haber, E. and Modersitzki, J., A multilevel method for image registration, *SIAM Journal of Scientific Computing* **27**, 1594–1607, 2006.
- [34] Haber, E., Heldmann, S. and Modersitzki, J., A computational framework for image-based constrained registration, *Linear Algebra and its applications* **431**, 459–470, 2009.
- [35] Haftka, R.T. and Gürdal, Z., *Elements of Structural Optimization*, Kluwer Academic Publishers, 1992.
- [36] Hariton, I., deBotton, G., Gasser, T.C. and Holzapfel, G.A., Stress-driven collagen fiber remodeling in arterial walls, *Biomechanics and Modeling in Mechanobiology* **6**, 163–175, 2007.
- [37] Hariton, I., deBotton, G., Gasser, T.C. and Holzapfel, G.A., Stress-modulated collagen fiber remodeling in a human carotid bifurcation, *Journal of Theoretical Biology* **248**, 460–470, 2007.
- [38] Hayenga, H.N., Thorne, B.C., Peirce, S.M. and Humphrey, J.D., Ensuring congruency in multiscale modeling: Towards linking agent based and continuum biomechanical models of arterial adaptation, *Annals of Biomedical Engineering* **39**, 2669–2682, 2011.

- [39] He, C.M. and Roach, M.R., The composition and mechanical properties of abdominal aortic aneurysms, *Journal of Vascular Surgery* **20**, 6–13, 1994.
- [40] Heinrich, V., *Bestimmung von Faserrichtungen für patientenspezifische abdominale Aortenaneurysmen*, Bachelor's thesis, Lehrstuhl für Numerische Mechanik, Technische Universität München, 2013.
- [41] Heroux, M.A., Bartlett, R.A., Howle, V.E., Hoekstra, R.J., Hu, J.J., Kolda, T.G., Lehoucq, R.B., Long, K.R., Pawlowski, R.P., Phipps, E.T., Salinger, A.G., Thornquist, H.K., Tuminaro, R.S., Willenbring, J.M., Williams, A. and Stanley, K.S., An overview of the Trilinos project, *ACM Transactions on Mathematical Software* **31**, 397–423, 2005.
- [42] Himpel, G., Kuhl, E., Menzel, A. and Steinmann, P., Computational modelling of isotropic multiplicative growth, *Computer Modeling in Engineering and Sciences* **8**, 119–134, 2005.
- [43] Holzapfel, G.A., *Nonlinear Solid Mechanics: A Continuum Approach for Engineering*, John Wiley & Sons Ltd, 2001.
- [44] Holzapfel, G.A., Gasser, T.C. and Ogden, R.W., A new constitutive framework for arterial wall mechanics and a comparative study of material models, *Journal of Elasticity* **61**, 1–48, 2000.
- [45] Humphrey, J.D., Vascular adaption and mechanical homeostasis at tissue, cellular, and sub-cellular levels, *Cell Biochemistry and Biophysics* **50**, 53–78, 2008.
- [46] Humphrey, J.D. and Rajagopal, K.R., A constrained mixture model for growth and remodeling of soft tissues, *Mathematical Models and Methods in Applied Science* **12**, 407–430, 2002.
- [47] Humphrey, J.D. and Rajagopal, K.R., A constrained mixture model for arterial adaptations to a sustained step change in blood flow, *Biomechanics and Modeling in Mechanobiology* **2**, 109–126, 2003.
- [48] Humphrey, J.D. and Taylor, C.A., Intracranial and abdominal aortic aneurysms: Similarities, differences, and need for a new class of computational models, *Annual Review of Biomedical Engineering* **10**, 221–246, 2008.
- [49] Kadoglou, N.P. and Liapis, C.D., Matrix metalloproteinases: contribution to pathogenesis, diagnosis, surveillance and treatment of abdominal aortic aneurysms, *Current Medical Research and Opinion* **20**, 419–432, 2004.
- [50] Karšaj, I., Sorić, J. and Humphrey, J.D., A 3-D framework for arterial growth and remodeling in response to altered hemodynamics, *International Journal of Engineering Science* **48**, 1357–1372, 2010.
- [51] Karypis, G. and Kumar, V., A parallel algorithm for multilevel graph partitioning and sparse matrix ordering, *Journal of Parallel and Distributed Computing* **48**, 71–95, 1998.

- [52] Katritsis, D., Kaiktsis, L., Chaniotis, A., Pantos, J., Efstathopoulos, E.P. and Marmarelis, V., Wall shear stress: Theoretical considerations and methods of measurement, *Progress in Cardiovascular Diseases* **49**, 307–329, 2007.
- [53] Kelley, C.T., Liao, L.Z., Qi, L., Chu, M.T., Reese, J.P. and Winton, C., Projected pseudo-transient continuation, *SIAM Journal on Numerical Analysis* **46**, 3071–3083, 2008.
- [54] Kroon, M. and Holzapfel, G.A., A model for saccular cerebral aneurysm growth by collagen fibre remodelling, *Journal of Theoretical Biology* **247**, 775–787, 2007.
- [55] Kroon, M. and Holzapfel, G.A., Modeling of saccular aneurysm growth in a human middle cerebral artery, *Journal of Biomechanical Engineering* **130**, 051012, 2008.
- [56] Kroon, M. and Holzapfel, G.A., A theoretical model for fibroblast-controlled growth of saccular cerebral aneurysms, *Journal of Theoretical Biology* **257**, 73–83, 2009.
- [57] Kwon, S.T., Rectenwald, J.E. and Baek, S., Intracac pressure changes and vascular remodeling after endovascular repair of abdominal aortic aneurysms: Review and biomechanical model simulation, *Journal of Biomechanical Engineering* **133**, 011011, 2011.
- [58] Langille, B.L., Remodeling of developing and mature arteries: Endothelium, smooth muscle, and matrix, *Journal of Cardiovascular Pharmacology* **21**, S11–S17, 1993.
- [59] Lee, E.H., Elastic-plastic deformation at finite strain, *Journal of Applied Mechanics* **36**, 1–6, 1969.
- [60] Lehoux, S., Castier, Y. and Tedgui, A., Molecular mechanics of the vascular responses to haemodynamic forces, *Journal of Internal Medicine* **259**, 381–392, 2006.
- [61] Levenberg, K., A method for the solution of certain nonlinear problems in least squares, *Quarterly of Applied Mathematics* **2**, 164–168, 1944.
- [62] Longo, G.M., Xiong, W., Greiner, T.C., Zhao, Y., Fiotti, N. and Baxter, B.T., Matrix metalloproteinases 2 and 9 work in concert to produce aortic aneurysms, *The Journal of Clinical Investigation* **110**, 625–632, 2002.
- [63] Lubarda, V.A. and Hoger, A., On the mechanics of solids with a growing mass, *International Journal of Solids and Structures* **39**, 4627–4664, 2002.
- [64] Maier, A., *Computational Modeling of Rupture Risk in Abdominal Aortic Aneurysms*, PhD thesis, Lehrstuhl für Numerische Mechanik, Technische Universität München, 2012.
- [65] Maier, A., Gee, M.W., Reeps, C., Eckstein, H.-H. and Wall, W.A., Impact of calcifications on patient-specific wall stress analysis of abdominal aortic aneurysms, *Biomechanics and Modeling in Mechanobiology* **9**, 511–521, 2010.
- [66] Maier, A., Gee, M.W., Reeps, C., Pongratz, J., Eckstein, H.-H. and Wall, W.A., A comparison of diameter, wall stress, and rupture potential index for abdominal aortic aneurysm rupture risk prediction, *Annals of Biomedical Engineering* **38**, 3124–3134, 2010.

- [67] Marquardt, D.W., An algorithm for least-squares estimation of nonlinear parameters, *Journal of the Society for Industrial and Applied Mathematics* **11**, 431–441, 1963.
- [68] Martufi, G. and Gasser, T.C., Turnover of fibrillar collagen in soft biological tissue with application to the expansion of abdominal aortic aneurysms, *Journal of the Royal Society Interface* **9**, 3366–3377, 2012.
- [69] Martufi, G., Auer, M., Roy, J., Swedenborg, J., Sakalihasan, N., Panuccio, G. and Gasser, T.C., Multidimensional growth measurements of abdominal aortic aneurysms, *Journal of Vascular Surgery* **58**, 748–755, 2013.
- [70] Matsumoto, T. and Hayashi, K., Mechanical and dimensional adaptation of rat aorta to hypertension, *Journal of Biomechanical Engineering* **116**, 278–283, 1994.
- [71] Modersitzki, J., *Numerical Methods for Image Registration (Numerical Mathematics and Scientific Computation)*, Oxford University Press, 2004.
- [72] Mohar, B., The Laplacian spectrum of graphs, *Graph theory, combinatorics, and applications* **2**, 871–898, 1991.
- [73] Narayanan, H., Arruda, E.M., Grosh, K. and Garikipati, K., The micromechanics of fluid-solid interactions during growth in porous soft biological tissue, *Biomechanics and Modeling in Mechanobiology* **8**, 167–181, 2009.
- [74] Newby, C.A., Matrix metalloproteinases regulate migration, proliferation, and death of vascular smooth muscle cells by degrading matrix and non-matrix substrates, *Cardiovascular Research* **69**, 614–624, 2006.
- [75] Ockert, S., Böckler, D., Allenberg, J. and Schumacher, H., Rupturiertes abdominelles aortenaneurysma, *Gefäßchirurgie* **12**, 379–391, 2007.
- [76] Ogden, R.W., Large deformation isotropic elasticity: On the correlation of theory and experiment for compressible rubberlike solids, *Proceedings of the Royal Society A* **328**, 567–583, 1972.
- [77] Raghavan, M.L. and Vorp, D.A., Toward a biomechanical tool to evaluate rupture potential of abdominal aortic aneurysm: identification of a finite strain constitutive model and evaluation of its applicability, *Journal of Biomechanics* **33**, 475–482, 2000.
- [78] Rausch, S.M.K., *Computational and Experimental Modeling of Lung Parenchyma*, PhD thesis, Lehrstuhl für Numerische Mechanik, Technische Universität München, 2012.
- [79] Rausch, S.M.K., Martin, C., Bornemann, P.B., Uhlig, S. and Wall, W.A., Material model of lung parenchyma based on living precision-cut lung slice testing, *Journal of the Mechanical Behavior of Biomedical Materials* **4**, 583 – 592, 2011.
- [80] Reeps, C., Gee, M., Maier, A., Gurdan, M., Eckstein, H.H. and Wall, W.A., The impact of model assumptions on results of computational mechanics in abdominal aortic aneurysm, *Journal of Vascular Surgery* **51**, 679–688, 2010.

-
- [81] Reeps, C., Maier, A., Pelisek, J., Härtl, F., Grabher-Meier, V., Wall, W.A., Essler, M., Eckstein, H.-H. and Gee, M.W., Measuring and modeling patient-specific distribution of material properties in abdominal aortic aneurysm wall, *Biomechanics and Modeling in Mechanobiology* **12**, 717–733, 2013.
- [82] Rodriguez, E.K., Hoger, A. and McCulloch, A.D., Stress-dependent finite growth in soft elastic tissue, *Journal of Biomechanics* **27**, 455–467, 1994.
- [83] Sakalihasan, N., Limet, R. and Defawe, O.D., Abdominal aortic aneurysm, *The Lancet* **365**, 1577–1589, 2005.
- [84] Schlichting, H. and Gersten, K., *Boundary layer theory*, Springer, 1999.
- [85] Scott, R.A.P. and The Multicentre Aneurysm Screening Study Group, The multicentre aneurysm screening study (MASS) into the effect of abdominal aortic aneurysm screening on mortality in men: a randomised controlled trial, *The Lancet* **360**, 1531–1539, 2002.
- [86] Sheidaei, A., Hunley, S.C., Zeinali-Davarani, S., Raguin, L.G. and Baek, S., Simulation of abdominal aortic aneurysm growth with updating hemodynamic loads using a realistic geometry, *Medical Engineering & Physics* **33**, 80–88, 2011.
- [87] Skalak, R., Dasgupta, G., Moss, M., Otten, E., Dullemeijer, P. and Vilmann, H., Analytical description of growth, *Journal of Theoretical Biology* **94**, 555–557, 1982.
- [88] Skalak, R., Zargaryan, S., Jain, R.K., Netti, P.A. and Hoger, A., Compatibility and the genesis of residual stress by volumetric growth, *Journal of Mathematical Biology* **34**, 889–914, 1996.
- [89] Skalak, R., Farrow, D.A. and Hoger, A., Kinematics of surface growth, *Journal of Mathematical Biology* **35**, 869–907, 1997.
- [90] Smith, B.F., Bjorstad, P.E. and Gropp, W., *Domain decomposition: Parallel multilevel methods for elliptic partial differential equations*, Cambridge University Press, 2004.
- [91] Sussman, T. and Bathe, K.-J., A finite element formulation for nonlinear incompressible elastic and inelastic analysis, *Computers & Structures* **26**, 357–409, 1987.
- [92] Taber, L.A., Biomechanics of growth, remodelling, and morphogenesis, *Applied Mechanics Review* **48**, 487–545, 1995.
- [93] Taber, L.A., A model for aortic growth based on fluid shear and fiber stresses, *Journal of Biomechanical Engineering* **120**, 348–354, 1998.
- [94] Taber, L.A. and Eggers, D.A., Theoretical study of stress-modulated growth in the aorta, *Journal of Theoretical Biology* **180**, 343–357, 1996.
- [95] Taber, L.A. and Humphrey, J.D., Stress-modulated growth, residual stress, and vascular heterogeneity, *Journal of Biomechanical Engineering* **123**, 528–535, 2001.
- [96] Thompson, D'Arcy W., *On growth and form*, Cambridge University Press, 1942.

- [97] Thompson, R.W. and Parks, W.C., Role of matrix metalloproteinase in abdominal aortic aneurysms, *Annals of the New York Academy of Sciences* **800**, 157–174, 1996.
- [98] Thorne, B.C., Hayenga, H.N., Humphrey, J.D. and Peirce, S.M., Toward a multi-scale computational model of arterial adaptation in hypertension: verification of a multi-cell agent-based model, *Frontiers in Physiology* **2**, 20, 2011.
- [99] Valentín, A. and Holzapfel, G.A., Constraint mixture models as tools for testing competing hypotheses in arterial biomechanics: A brief survey, *Mechanics Research Communications* **42**, 126–133, 2012.
- [100] Valentín, A. and Humphrey, J.D., Parameter sensitivity study of a constrained mixture model of arterial growth and remodeling, *Journal of Biomechanical Engineering* **131**, 101006, 2009.
- [101] Valentín, A. and Humphrey, J.D., Evaluation of fundamental hypotheses underlying constrained mixture models of arterial growth and remodelling, *Philosophical Transactions of the Royal Society A* **367**, 3585–3606, 2009.
- [102] Valentín, A. and Humphrey, J.D., Modeling effects of axial extension on arterial growth and remodeling, *Medical and Biological Engineering and Computing* **47**, 979–987, 2009.
- [103] Valentín, A., Cardamone, L., Baek, S. and Humphrey, J.D., Complementary vasoactivity and matrix remodelling in arterial adaptations to altered flow and pressure, *Journal of the Royal Society Interface* **6**, 293–306, 2009.
- [104] Valentín, A., Humphrey, J.D. and Holzapfel, G.A., A multi-layered computational model of coupled elastin degradation, vasoactive dysfunction, and collagenous stiffening in aortic aging, *Annals of Biomedical Engineering* **39**, 2027–2045, 2011.
- [105] Valentín, A., Humphrey, J.D. and Holzapfel, G.A., A finite element-based constrained mixture implementation for arterial growth, remodeling, and adaptation: Theory and numerical verification, *International Journal for Numerical Methods in Biomedical Engineering* **29**, 822–849, 2013.
- [106] Vande Geest, J.P., Wang, D.H.J., Wisniewski, S.R., Makaroun, M.S. and Vorp, D.A., Towards a noninvasive method for determination of patient-specific wall strength distribution in abdominal aortic aneurysms, *Annals of Biomedical Engineering* **34**, 1098–1106, 2006.
- [107] Wall, W.A. and Gee, M.W., BACI: A parallel multiphysics simulation environment, Technical report, Institute for Computational Mechanics, Technische Universität München, 2010.
- [108] Watton, P.N. and Hill, N.A., Evolving mechanical properties of a model of abdominal aortic aneurysms, *Biomechanics and Modeling in Mechanobiology* **8**, 25–42, 2009.
- [109] Watton, P.N., Hill, N.A. and Heil, M., A mathematical model for the growth of the abdominal aortic aneurysm, *Biomechanics and Modeling in Mechanobiology* **3**, 98–113, 2004.

- [110] Wilson, J.S., Baek, S. and Humphrey, J.D., Importance of initial aortic properties on the evolving regional anisotropy, stiffness, and wall thickness of human abdominal aortic aneurysms, *Journal of the Royal Society Interface* **9**, 2047–2058, 2012.
- [111] Yoshihara, L., Coroneo, M., Comerford, A., Bauer, G., Klöppel, T. and Wall, W.A., A combined fluid-structure interaction and multi-field scalar transport model for simulating mass transport in biomechanics, *International Journal for Numerical Methods in Engineering* **100**, 277–299, 2014.
- [112] Zeinali-Davarani, S., Raguin, L.G., Vorp, D.A. and Baek, S., Identification of in vivo material and geometric parameters of a human aorta: toward a patient-specific modeling of abdominal aortic aneurysm, *Biomechanics and Modeling in Mechanobiology* **10**, 689–699, 2011.
- [113] Zeinali-Davarani, S., Sheidaei, A. and Baek, S., A finite element model of stress-mediated vascular adaptation: application to abdominal aortic aneurysms, *Computer Methods in Biomechanics and Biomedical Engineering* **14**, 803–817, 2011.
- [114] Zienkiewicz, O.C., Taylor, R.L. and Zhu, J.Z., *The Finite Element Method: Its Basis and Fundamentals*, Elsevier Butterworth-Heinemann, 2005.

Curriculum vitae

Name: Susanna Sabine Tinkl
Geburtsdatum: 1.1.1985
Geburtsort: Landsberg am Lech
Eltern: Prof. Dr. Werner und Adelheid Tinkl, geb. Greisel
Nationalität: Deutschland
Familienstand: ledig

1991 - 1995 Grundschule Kaufering
1995 - 2004 Dominikus-Zimmermann-Gymnasium in Landsberg am Lech
Juni 2004 Zeugnis der Allgemeinen Hochschulreife
2004 - 2009 Studium der Technomathematik an der Technischen Universität München
Mai 2007 Aufnahme in die Studienstiftung des deutschen Volkes
März 2009 Abschluss als Diplom Technomathematikerin
2009 - 2014 Wissenschaftliche Mitarbeiterin am Lehrstuhl für Numerische Mechanik, Technische Universität München

Reports of the Institute for Computational Mechanics at Technische Universität München

- 29 (2015) **Susanna Tinkl:**
Towards a predictive computational growth model for aneurysms.
- 28 (2015) **Sudhakar Yogaraj:**
An embedded interface finite element method for fluid-structure-fracture interaction.
- 27 (2015) **Ursula Rasthofer:**
Computational Multiscale Methods for Turbulent Single and Two-Phase Flows.
- 26 (2015) **Tobias Wiesner:**
Flexible Aggregation-based Algebraic Multigrid Methods for Contact and Flow Problems.
- 25 (2015) **M. Hamman de Vaal:**
Computational Modeling, Clinical Comprehension and Improvement of Aortic Manipulation.
- 24 (2014) **Jakob Huemer:**
Einfluss instationärer aerodynamischer Kräfte auf die Fahrdynamik von Personenkraftwagen.
- 23 (2014) **Robert Metzke:**
Modeling and experimental investigation of the mechanobiological environment associated with alveolar pneumocytes.
- 22 (2014) **Shadan Shahmiri:**
A hybrid ALE-fixed-grid approach for fluid-structure interaction.
- 21 (2014) **Caroline Danowski:**
Computational modelling of thermo-structure interaction with application to rocket nozzles.
- 20 (2014) **Kei Müller:**
Simulation of self-assembly and mechanics of transiently crosslinked, semiflexible biopolymer networks.
- 19 (2014) **Mahmoud Ismail:**
Reduced dimensional modeling of the entire human lung.
- 18 (2013) **Florian Henke:**
An extended finite element method for turbulent premixed combustion.
- 17 (2012) **Markus Gitterle:**
A dual mortar formulation for finite deformation frictional contact problems including wear and thermal coupling.
- 16 (2012) **Andreas Maier:**
Computational modeling of rupture risk in abdominal aortic aneurysms.
- 15 (2012) **Georg Bauer:**
A coupled finite element approach for electrochemical systems.

- 14 (2012) Alexander Popp:**
Mortar methods for computational contact mechanics and general interface problems.
- 13 (2012) Thomas Klöppel:**
A finite element model for the human red blood cell.
- 12 (2012) Sophie Rausch:**
Computational and experimental modeling of lung parenchyma.
- 11 (2011) Christian Cyron:**
Micromechanical continuum approach for the analysis of biopolymer networks.
- 10 (2011) Lena Wiechert:**
Computational modeling of multi-field and multi-scale phenomena in respiratory mechanics.
- 9 (2010) Peter Gamnitzer:**
Residual-based variational multiscale methods for turbulent flows and fluid-structure interaction.
- 8 (2010) Axel Gerstenberger:**
An XFEM based fixed grid approach to fluid-structure interaction.
- 7 (2009) Ulrich Küttler:**
Effiziente Lösungsverfahren für Fluid-Struktur-Interaktions-Probleme.
- 6 (2009) Moritz Frenzel:**
Advanced structural finite element modeling of arterial walls for patient-specific geometries.
- 5 (2007)* Christiane Förster:**
Robust methods for fluid-structure interaction with stabilised finite elements.
- 4 (2004)* Tobias Erhart:**
Strategien zur Numerischen Modellierung transienter Impaktvorgänge bei nichtlinearem Materialverhalten.
- 3 (2004)* Michael Gee:**
Effiziente Lösungsstrategien in der nichtlinearen Schalenmechanik.
- 2 (2003)* Volker Gravemeier:**
The variational multiscale method for laminar and turbulent incompressible flow.
- 1 (2001)* Daniel Mok:**
Partitionierte Lösungsverfahren in der Strukturdynamik und der Fluid-Struktur-Interaktion.

*This dissertation was supervised by Prof. Dr.-Ing. Wolfgang A. Wall at the Institute for Structural Mechanics at the University of Stuttgart and is published in the respective report series.